UNIVERSITY OF SOUTHAMPTON

FACULTY OF ENGINEERING, SCIENCE AND MATHEMATICS

SCHOOL OF CHEMISTRY

Synthesis and Characterisation of Lanthanide and other Inorganic Framework Materials

By

Jessica Rouse

Thesis for the degree of Doctor of Philosophy

January 2010

UNIVERSITY OF SOUTHAMPTON

ABSTRACT

FACULTY OF ENGINEERING, SCIENCE AND MATHEMATICS

SCHOOL OF CHEMISTRY

Doctor of Philosophy

Synthesis and Characterisation of Lanthanide and other Inorganic Framework Materials

By Jessica Rouse

Five new cerium (IV) fluoride and fluoride–arsenate framework structures have been synthesised through hydrothermal techniques using CeF_4 as a fluoride source. $Cs[Ce^{IV}{}_2F_8[F.H_2O]]$ (**I**) consists of layers, formed from linked $Ce(F,O)_n$ polyhedra cross-linked by hydrogen bonding that defines channels containing the caesium ions. $[(NH_4)_5(H_2O)_2][Ce^{IV}{}_4(AsO_4)_6(H_2O)F_3]$ (**II**), has an open framework structure with large channels filled with NH_4^+ cations and H_2O molecules. $Ce^{IV}[AsO_4]F$ (**III**) and $Ce^{IV}[AsO_4]F[H_2O]$ (**IV**) exhibit two types of bridging (Ce–O–Ce and Ce–F–Ce) bonds between $Ce(O,F)_n$ polyhedra, and $(NH_4)[Ce^{IV}F_2(AsO_4)]$ (**V**), is isostructural with the previously reported fluoride-phosphate $(NH_4)[Ce^{IV}F_2(PO_4)]$.

The use of metal tetra-fluorides (MF_4; M = Zr, Hf) in hydrothermal reactions, has led to the production of new structures that incorporate either phosphate or arsenate oxotetrahedra linking metal oxo-fluoro polyhedra. This new synthetic pathway has provided a safer route to formation that does not require the addition of the dangerous HF reagent. Seven new zirconium and four hafnium arsenate or phosphate materials have been identified including $Zr^{IV}(HAsO_4)(AsO_4)(NH_4)$ (**VI**) a three-dimensional framework with NH_4^+ within the channels, $Zr^{IV}(AsO_4)F(H_2O)$ (**VII**) exhibits Zr-F-Zr linkages, $Zr^{IV}(HAsO_4)_2$ a novel three-dimensional framework (**VIII**) and $Zr^{IV}{}_2(AsO_4)_3(NH_4)(H_2O)$ (**IX**) analogous to the mineral Langbeinite. Organic amines included in the reaction mixture can template the frameworks and form cavities, as observed within the channels of $Hf^{IV}{}_2F(HAsO_4)(AsO_4)_2[Temp\text{-}H_n]_{1/n}(H_2O)_{1.5}$ (**XIII**) (Temp = ethylenediamine/diethylenetriamine). The substitution of fluoride ions for oxygen in the metal polyhedral unit has produced variations in the dimensionality of the materials formed as fluoride is more frequently incorporated as terminating species, reducing framework dimensionality. The controlled addition of these fluoride species, has provided a route to the rational design of one, two and three-dimensional framework structures.

Hexagonal lanthanide phosphates ($Ln^{III}PO_4.nH_2O$) with the mineral Rhabdophane structure type were synthesised through hydrothermal techniques and analysed upon heating where a distinct increase in the *a*-axis lattice length was observed upon dehydration of the structure. Variable-temperature X-ray diffraction, EDX, TGA and fluorescence studies were undertaken to illustrate the interaction between the lanthanide cations and the water molecules that reside within the channels of the framework.

TABLE OF CONTENTS

LIST OF TABLES AND FIGURES

CHAPTER 3: CERIUM FLUORIDE FRAMEWORKS **Page**

CHAPTER FOUR: ZIRCONIUM ARSENATE FRAMEWORKS **Page**

CHAPTER FIVE: HAFNIUM PHOSPHATE AND ARSENATE FRAMEWORKS **Page**

ABBREVIATIONS

DABCO	1, 4-diazabicyclo[2.2.2]octane
PIP	Piperazine
EDA	Ethylenediamine
DETA	Diethylenetriamine
OAD	Oxalic acid dihydrate
TEA	Tetraethylammonium hydroxide
TMAOH	Tetramethylammonium hydroxide
TMAC	Tetramethylammonium chloride
PHEN	1, 10-Phenanthroline
PXD	Powder X-ray diffraction
SXD	Single crystal X-ray diffraction
TGA	Thermogravimetric analysis
IR	Infra-red
EDX	Energy dispersive X-ray spectroscopy
BV	Bond valence
AlPO	Aluminium Phosphate
GaPO	Gallium phosphate

DECLARATION OF AUTHORSHIP

I, Jessica Rouse, declare that the thesis entitled

Synthesis and Characterisation of Lanthanide and Inorganic Framework Materials

and the works presented in it are my own. I confirm that:

- This work was done wholly or mainly while in candidature for a research degree at this university;
- Where any part of this thesis has previously been submitted for a degree or any other qualification at this University or any other institution, this has been clearly stated;
- Where I have consulted the published work of others, this is always clearly attributed;
- Where I have quoted from the work of others, the source is always given. With the exception of such quotations, this thesis is entirely my own work;
- I have acknowledged all main sources of help;
- Where the thesis is based on work done by myself jointly with others, I have made clear exactly what was done by others and what I have contributed myself;
- Parts of this work have been published as:

J. Rouse, M. T. Weller, *Dalton Trans*., **2009**, 46, 10330

J. Rouse, K. V. Redrup, E. Kotsapa, M. T. Weller, *Chem. Comm.*, **2009**, 46, 7209

Signed:

Date:

ACKNOWLEDGEMENTS

The production of this research thesis has been a long personal journey and without certain people it is an accomplishment that I do not think I would have completed.

First, many thanks are due to my supervisor Mark Weller, who has guided me throughout this project and encouraged me along the way. Thank you for the opportunity to express my passion for science through 'creating a colourful life'. It was a truly fulfilling addition to this PhD project, and has kept me motivated when the research has been tough, thinking of all of the bright young minds that we have encouraged to pursue a career in this fascinating area of science.

The Southampton crystallography department, especially Mark Light and Peter Horton, have been helpful throughout and provided time on machines to document the new structures within this thesis. Thanks are due for your guidance and patience as there always seemed to be so many problems with my crystals and the machines whenever I went near them!

Massive thanks should be given to the Weller group (past and present) for their amazing motivation, which has made the last three years thoroughly enjoyable and memorable! Thanks to the crazy Greek and Italian that have made this experience personally worthwhile and to Kate who helped me through this journey, providing amazing insight into the world of crystals and also the gym! Valeska and Jenny thank you for the proof-reading of thesis (I must owe you both so many beers by now). I know it wasn't easy but we got there in the end!

Thanks are due to Daniel and my mum who have helped me through this experience encouraging me when I thought I would never have my first 'Eureka' moment, and congratulating me when I did. Without you both this experience would have been less exciting and I don't know whether I would have been motivated enough to finish my journey. The inspiration you both gave me academically and personally to do something more than the average University student is priceless.

Thanks to everyone for helping me achieve the unachievable...the finish line...and Dan finally the conversations where nothing makes sense are over! Love to you all.

CHAPTER ONE

INTRODUCTION

1.0 Introduction

The research presented within this thesis has focussed upon the production of new open framework structures with the aim of producing new materials that might possess useful properties. Research interest in this area of science has been driven by the number of new and unusual materials that solvothermal synthesis produces. One problem with the systematic application of this synthetic procedure has been in understanding the 'black box' reactions involved, thereby allowing optimisation of the conditions for the fabrication of useful materials. As a result a large number of reactions were undertaken involving small changes in the reaction conditions as these can lead to major alterations in the crystal structure formed as well as changes in crystal morphology. A programme of work was undertaken involving systematic studies of the synthetic conditions to investigate this area fully. This chapter initially describes early studies of zeolite materials that developed the foundations for framework synthesis, before discussing alternative building units that form the basis of current research into three-dimensional structures.

1.1 Framework Materials

Inspiration within science often originates from nature, as for example, when considering the natural forms of the aluminosilicate zeolites. The word zeolite was first applied to stilbite[1], a naturally occurring aluminosilicate discovered by Baron Cronstedt, that was found to release steam upon being heated by the sun. These 'boiling stones' were found to be formed from three-dimensional microporous aluminosilicates that included size and shape specific channels or pores, and that typically contained water molecules within their frameworks. The pore sizes and shapes within a zeolite are defined throughout the crystal[2]. Over 40 naturally occurring zeolites and more than two hundred synthetic aluminosilicates have been discovered to date[3]. Naturally occurring zeolites have been found to contain water molecules as well as cations such as Mg^{2+}, Ca^{2+}, Na^{+} and K^{+} [4] within the framework channels and pores. Attempts to replicate these natural zeolites in the laboratory have involved the addition of Group 1 and 2 hydroxides in the solvothermal reaction media; the presence of these hydroxides increases the solubility of the reagents, and allows the zeolite framework to form with increased rate.

Zeolite structures are built from AlO_4 and SiO_4 tetrahedral building units (TO_4, T = Al/Si). Löweinstein's rule[5] of aluminium avoidance states that under mild hydrothermal conditions Al-O-Al linkages are forbidden within zeolite frameworks. Therefore, the linkages within these structures where the Al:Si ratio is 1:1, must all be Al-O-Si. Extensive research has been undertaken in this area of science as a result of the wide variety of structures that can be obtained by varying the aluminium and silicon ratios. The Si/Al ratio must be a minimum of 1:1, which causes the Si and Al centred tetrahedra to alternate within the framework (Löweinstein's rule). The bonding within aluminosilicates is based upon corner-sharing of the silicate and alumina tetrahedra though oxygen anions. The tetrahedral species are linked to produce a number of ring formations (4, 6, 8 secondary bonding units, *etc.*) and a variety of bond angles (120-180 °) of the *T*-O-*T* species, which enables multiple structure types to form. The size of the pores varies widely resulting from the synthesis methods (temperature, pH, ratio, *etc.*). Investigations into the zeolites have highlighted important properties such as reversible dehydration, which proceeds without the collapse of the aluminosilicate structure. The removal of water molecules enables alternative gas and solvent molecules to be adsorbed into the framework[6].

Synthetic zeolites have been extensively produced since the 1950's as a result of the industrial interest in the properties and bulk quantities of the materials that can be prepared. The aluminosilicates produced demonstrated a number of possible industrial applications, such as adsorption, ion-exchange and catalysis. The specific nature of the pores was found to facilitate the adsorption process, for example Zeolite A adsorbed small molecules, such as water. Ion exchange reactions were found to alter the cation within the aluminosilicate framework (e.g. from Na^+ to the smaller Ca^{2+}), and create additional space within the channels. This space allows larger molecules such as methanol to enter the same framework[3]. The specific nature of the differing zeolite structures has provided many practical applications industrially, such as drying agents.

The cations contained within aluminosilicates were found to readily undergo ion exchange at room temperature in view of their weak interactions with the framework. This reaction led to the use of zeolites as water softeners in washing powders, where Ca^{2+} ions removed from the water are exchanged for Na^+. More recently, materials have been synthesised for use in the preparation of safe drinking water, whereby transition metal ions such as Fe^{2+} (as a result of the metal leaching from the soil and pipe corrosion[7]), can be removed from the water.

The catalytic properties of aluminosilicates have been highlighted with the acidic zeolites, where the cations are H^+. These materials offer shape and size selectivity and active protonated

sites. Once molecules have been adsorbed into the cavities, the acidic zeolites perform catalytic functions in dehydration and rearrangement reactions. The reaction products can then leave the zeolite framework, though this process may be subject to selectivity. This ability of zeolites to control various catalytic processes is of great industrial significance. One application has been the use of faujasite (zeolite Y), in the catalytic cracking of crude oil within the petrochemical industry. The depleting worldwide reserves of this important natural resource have led to further research into alternative cracking materials, such as ITQ-21[8], which is a fluorinated, silicon germinate framework that bonds to organic cations. ITQ-21 was specifically designed to optimise the catalytic processes and to reduce petrochemical wastage. This cutting edge research highlights the continuing importance of zeolites and similar chemical structures to current industrial processes.

More recently, significant attention has been given to materials that offer similar structural archetypes to zeolites. This has created opportunities for alternative building blocks to replace the aluminium and silicon tetrahedra. These studies initially concentrated on the aluminophosphates (AlPOs). Flannigan and his co-workers supplied the most significant initial discoveries within this area in the 1980's[9]. The AlPOs were synthesised under mild hydrothermal conditions similar to those of the aluminosilicates that involved organic templates and quaternary ammonium salts (NR_4^+). These organic reagents acted in a structure directing fashion or alternatively as templating agents that the AlPOs form around, and were thus surrounded by the framework. The organic templates are commonly housed within the channels and pores of the AlPOs, and produce structural motifs specific to these reagents. The bonding observed within the compounds consists of Al-O-P linkages, in agreement with Löweinstein's rule and avoiding Al-O-Al bonds. A number of AlPOs formed that were structurally similar to the zeolites and resulted from comparable bonding of the phosphate and silicon tetrahedra. One example is the zeolite framework gismondite (GIS), which exhibits tetrahedral units within its framework. A fluorinated AlPO was discovered that displayed a GIS structure type[10]. The coordination of the aluminium was tetrahedral and octahedral within this compound, which coordinated (AlO_4F_2), to the framework of $[H_2Me_2]$ $[Al_2P_2O_8F]$. Research on AlPO has also produced structures exhibiting topologies not known for aluminosilicate zeolites. VPI-5 ($[(H_2O)_{42}][Al_{18}P_{18}O_{72}]$) discovered in the late 1980s, has large 18-ring channels with a pore diameter of 12-13 Å[11] and no zeolite equivalent (Fig. 1.1).

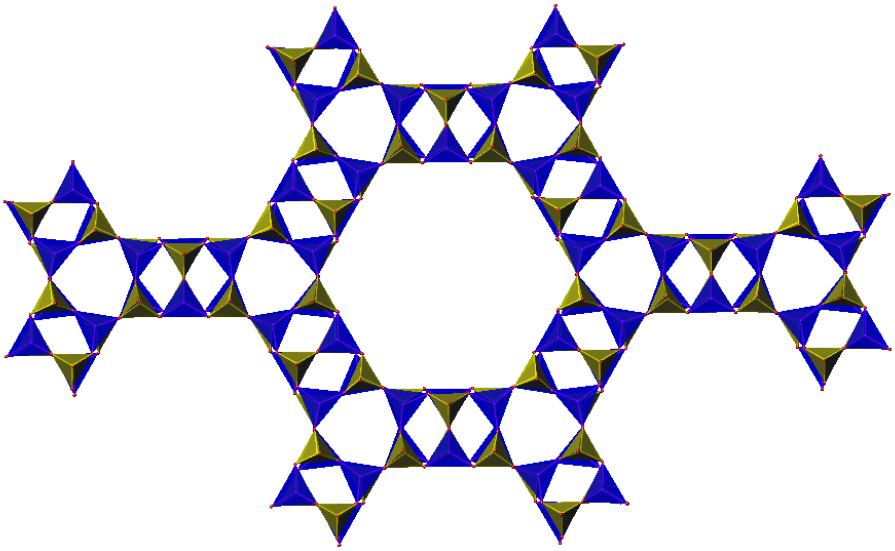

***Figure 1.1**: 18-ring channels within the aluminophosphate VPI-5*[11]

AlPO-21 is an example of a three-dimensional AlPO structure that contains aluminium in tetrahedral as well as trigonal bipyramidal coordination, encapsulating an organic template ion[12].

Gallophosphates (GaPOs) were the next extension of the aluminosilicate family which incorporated alternative building units to the original aluminium and silicon. In this case gallium formally replaces the aluminium in the structure of AlPOs. Isotypic structures of the aforementioned aluminophosphates could be obtained by introducing the chemically similar gallium cation and examples reported included the isostructural AlPO-12 and GaPO-12[13]. These compounds are formed from tetrahedral PO_4 and five-coordinate GaO_5 building units.

New GaPOs have also been produced with structural archetypes unique to gallium, such as the open-framework $GaPO_4$-C3 with 8-ring channels[14], synthesised using hydrothermal methods. This compound exhibited gallium in the tetrahedral and distorted trigonal bipyramidal form with protonated triethylamine ions. These examples of GaPOs and AlPOs have highlighted the role of the interchangeable *T* units in preparing novel three-dimensional frameworks.

The phosphate groups have also been replaced within these families by the chemically similar arsenate ion to produce aluminium and gallium arsenates. Structures such as that of $Al_3As_3O_{12}C_4H_{12}NOH$ are constructed from arsenate tetrahedra linked through aluminium centred tetrahedra and distorted bipyramids[15]. The introduction of the slightly larger arsenate ion (in

comparison with the phosphate) did not alter the tetrahedral bonding environment. Arsenate analogues of the phosphate materials have the potential to form as a result of their similar chemistry. Reaction conditions that involve arsenate rather than phosphate may require moderate alterations to accommodate their differences in size[16].

The formation of synthetic zeotypes, AlPOs and GaPOs originally proceeded within hydrothermal vessels that contained water as the reaction solvent. The next major step forward was the introduction of nonaqueous reaction media which often modified the crystallinity of the products and the reaction pathway. Aluminosilicate zeolite structures are normally produced in alkaline hydrothermal conditions[17], while AlPOs form in acidic reaction media[18]. Synthetic procedures that use solvents to substitute the water within the reaction solution are termed solvothermal. Research has shown that the choice of solvent is very important. Strong interactions between the reaction media and the template ions, affects their structure directing roles, as the solution may form hydrogen bonds with the template. TO_4 species commonly require the organic templates for framework formation, thus strong interactions with the solvent inhibit the manufacture of reaction products. Ethylene glycol and alcohol media have been used by research groups when investigating alternative reaction media for zeolite synthesis.

The inclusion of alternative solvents such as alcohols in general has been shown to have a large effect on improving the crystallinity of the reaction products, although this area has received less research interest than the typical hydrothermal reaction route[18]. New frameworks structures have also resulted from this research. Aluminophosphate structures such as AlPO-HDA, a compound that was found to contains 12 and 8-membered rings, formed within an ethylene glycol reaction solvent[19]. The presence of the organic template hexanediamine was essential to this synthesis. Gallophosphates that form in solvothermal conditions were first observed in the early 1990s in the presence of ethylene glycol[20]. This route to formation has produced a greater understanding of the frameworks possible by altering the reaction conditions.

A further step forward in research of particular interest to this study, is the use of fluoride ions. These anions can act as mineralisers in aqueous solutions associated with the formation of microporous materials. Their presence leads to improved crystallinity through the formation of larger single crystals; this is attributed to the presence of fluoride ions acting to slow the rate of nucleation[21]. Solvothermal reactions have often failed to produce crystals that are a suitable size for analysis *via* single-crystal diffraction studies. The fluoride route, developed by Guth *et al.*[21] in the preparation of zeolites, AlPOs and GaPOs, involved the addition of a *B*F species (B = H/NH_4/Na

etc.) in the reaction mixture. The formation of new structures has often depended upon the inclusion of fluoride ions. Reactions that involve aluminium and silicon species for the formation of zeolites normally occur in alkaline media, but the introduction of fluoride ions reduces the reaction pH from alkaline to almost neutral ranges. The solubility of silicon was increased as a consequence of the formation of intermediary phases such as hexafluorosilicates. New frameworks can be produced in the newly accessible lower alternative pH ranges that are not formed under normal alkaline conditions.

The presence of large quantities of fluoride ions within a reaction medium can lead to their inclusion in the framework, substituting oxygen anions within the polyhedral species. The AlPOs and GaPOs that incorporated fluoride ions exhibited new bonding types. Ferey *et al.* undertook a thorough investigation of the oxyfluorinated phosphates denoted ULM-*n* in the early 1990's, which focussed upon the design of novel frameworks encapsulating fluoride ions within the building blocks[22]. Gallium structures exhibited the fluorinated building units GaO_4F and GaO_4F_2, which replaced GaO_5 or GaO_6. Examples such as ULM-16[22] demonstrated Ga-F-Ga bridges between gallium centres (Fig 1.2) through a mixture of octahedral and hexameric units.

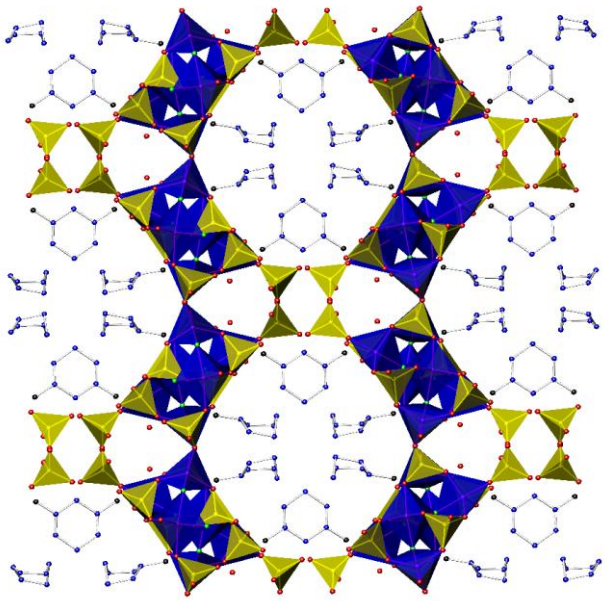

***Figure 1.2**: The 16-ring channels within ULM-16[22] ($Ga_4(PO_4)_4F_2.1.5NC_6H_{14}.0.5H_2O.0.5H_3O$) with encapsulated cyclohexylamine [Key: Yellow polyhedra – PO_4, blue hexamers – GaO_4F, blue octahedra – GaO_4F_2]*

The products of these reactions were found to exhibit a mixture of both terminal and bridging fluorine bonding, for example MIL-12[23] has the polyhedron unit GaO_2F_4. Strong hydrogen bonding interactions between the terminal Ga-F and H-N units are prevalent within the ULM class, which led to an increase in the Ga-F bond lengths resulting from these interactions.

1.2 Metal Framework Materials

The incorporation of alternative building units to those originally found within the zeolite materials has introduced many possibilities. Metal frameworks are one area of science that has received significant research interest. The metal species provide bonding spheres that are not all formed from tetrahedral units. The polyhedral groups form in 3, 4, 5, and 6 atom coordination spheres, dependent upon the metals selected. The metal cations within these frameworks also formed mixed valence states within the same compound[24]. The research presented in this section highlights scientific studies of molybdenum, vanadium, tin, iron, cobalt and titanium framework chemistry.

Molybdenum and vanadium phosphates were amongst the first metal species employed in the search for novel zeotypes. The reactions initially concentrated on high temperature solid-state syntheses. Although these studies were successful, the metal phosphates produced did not exhibit significant ion exchange capacities. As a result, hydrothermal reaction pathways replaced high temperature methods[25]. These initial syntheses, undertaken by Haushalter, formed molybdenum phosphate that incorporated organic templates within their frameworks[26]. These compounds displayed tunnels and cages, built from phosphate tetrahedra and molybdenum octahedra. Frameworks such as $[Mo_2O_2(PO_4)_2(H_2PO_4)]^-$ were found to exhibit sorption properties, resulting from the phosphate group's ability to re-orientate into a variety of shapes within the voids, that left around 25% of space within the structure[27]. These compounds are less rigid than the aluminosilicate zeolites, leading to applications in ion exchange.

Studies of vanadium phosphates have been undertaken that have incorporated cations (such as K^+ and Cs^+) within their three-dimensional structures. One such example is $Cs[V^{III}_2(PO_4)(HPO_4)_2(H_2O)_2]$[28], which houses Cs^+ cations housed within its channels, vanadium in an octahedral environment (VO_6), and exhibits corner-sharing bonding with PO_4 tetrahedral groups.

Fluoride ions have been incorporated into reactions that produce aluminosilicate zeolites, AlPOs and GaPOs, and thus their application within metal framework syntheses is unsurprising. This research has provided materials such as the vanadium compound ULM-7 ($(H_3N(CH_2CH_2)NH_3[(V^{v}O_2)_2(PO_4)F]$), synthesised by Ferey *et al.*[29]. The material was constructed from VO_4F, VO_5 and PO_4 building units that formed V_2O_8F dimers (Fig. 1.3), with fluoride ions linked to terminal positions. The organic template was housed within the channels of the framework, with hydrogen bonding interactions between the terminal fluoride anions and the ethylenediamine.

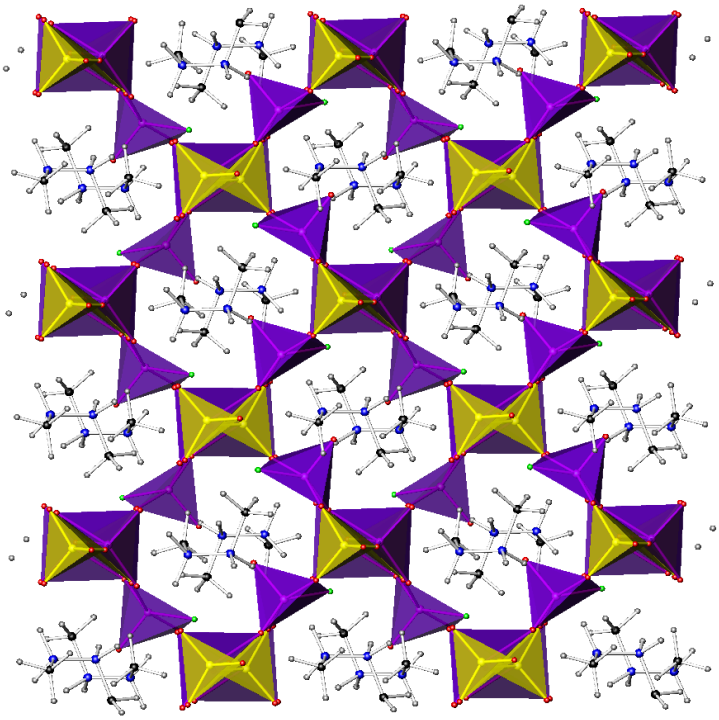

***Figure 1.3**: The structure of ULM-7[29] viewed down the c-axis [Key: Purple polyhedra – VO_5/VO_4F; yellow tetrahedra – PO_4; ethylenediamine within channels]*

Systematic studies into tin phosphates have produced open-framework structures. As a result it has been documented that the tin will typically bond in a trigonal pyramidal (SnO_3) or square planar form (SnO_4). The addition of an organic template commonly leads to its incorporation into the structure[30]. The first tin framework $[(NH_4)(Sn_3O)_2(PO_4)_3]$ (synthesised

through hydrothermal methods) was produced by Cheetham *et al.*[31], denoted as SnOPO-1. The structure was formed from SnO_3 and PO_4 units with NH_4^+ cations within the channels, which resulted from the breakdown of the organic template (1, 4-diaminobutane). Alternative templating units such as diaminobutane have been integrated into tin frameworks, for example the compound $[H_3N(CH_2)_4NH_3]_{0.5}[Sn_4P_3O_{12}]$ (Fig. 1.4), which consists of SnO_3 and PO_4 units. The tin species were fully connected to the framework, whereas the phosphate groups displayed terminal oxygen ions that pointed into the channels, forming interactions with the organic groups[32]. This research group undertook investigations into the removal of the template to form a microporous structure, which resulted in a collapse of the framework. This is a common feature of these compounds, where the bonding interactions between the framework and the template provide stability and their removal can result in structural collapse. Metal frameworks that do not follow this trend have the potential to provide scientists with a number of applications, such as small molecule stores.

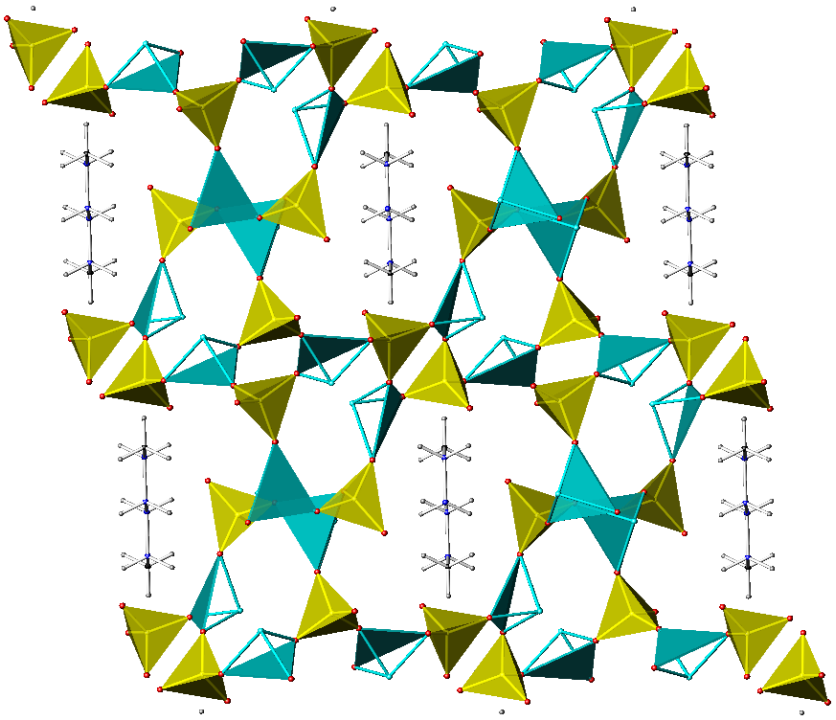

***Figure 1.4**: Tin phosphate framework $[H_3N(CH_2)_4NH_3]_{0.5}[Sn_4P_3O_{12}]$[32] viewed down the b-axis [Key: blue trigonal pyramidal – SnO_3; yellow tetrahedra – PO_4; diaminobutane within channels]*

Scientific studies of tin phosphates have continued to expand and there have been recent developments of materials such as $[H_2DACO]_{0.5}[Sn^{II}_4(PO_4)_3]$ (DACO = 1, 5-diazacyclooctane)[33]. This compound was constructed of SnO_3 and PO_4 units forming a three-dimensional structure that housed protonated template anions.

Research into iron phosphates has been driven by the number of open-framework structures that have formed, such as $[NH_3(CH_2)_2NH_3]_{1.5}(Fe_3PO_4(HPO_4)_3(C_2O_4)_{1.5}].xH_2O$, which exhibits reversible hydration[34]. Ferey *et al.* produced the first iron phosphate containing organic cations within its pores. This material incorporated fluoride ions into the metal coordination sphere, a result of the addition of HF into the reaction mixture[35]. The Fe-F bonds were found to be elongated as was the case for all ULM compounds. This effect was attributed to the strong interaction of the fluoride ions with the organic template A later development in the iron phosphate system was ULM-15[36] which formed around 1, 3-diaminopropane and contained fluoride within the polyhedra. As a result of these studies iron phosphate and arsenate materials have attracted interest for their magnetic properties, as the compounds are able to form antiferro or ferromagnetic compounds[37] (where unpaired electrons are aligned parallel (ferro), or antiparallel which gives a zero overall charge).

Systematic studies on iron phosphates also found them to be suitable battery materials. $LiFePO_4$ is well researched[38], although depleting worldwide lithium reserves have led to the investigation of alternative sodium iron phosphates. Recent studies have included fluoride ions in the reaction mixture, which formed A_2FePO_4F, (A = Li/Na). As a result these compounds have provided alternative forms of this battery material, and offer scope for the replacement of lithium by sodium. These structures also incorporate fluoride into the framework, which can aid movement of ions from between the layers of the materials[39].

Studies of the cobalt phosphates have found 4, 5, and 6 atom polyhedral units around the metal centre. The three-dimensional framework of $Co_5(OH_2)_4(HPO_4)_2(PO_4)_2$ was the product of a hydrothermal synthesis[40], and this material exhibited anti-ferromagnetic behaviour. Cobalt compounds can also exhibit ferromagnetic susceptibility as established for the 12-membered channel structure of $[enH_2][Co_{3.5}(PO_4)_3]$[41]. Research into analogues of the Edingtonite family of aluminosilicate zeolites has been undertaken using cobalt. These materials incorporate a small amount of aluminium or gallium within the cobalt phosphate framework[42]. Figure 1.5 illustrates the structure of ACP-EDI1 $[(NH_3CH_2CH(NH_3)CH_3)_2(AlCo_4P_5O_{20})]$, which houses 1, 2-diaminopropane molecules within 10-ring channels. Aluminium ions were found on some of the cobalt sites as a

result of the presence of aluminium nitrate within the reaction mixture. The cobalt was in a tetrahedral coordination environment, which allowed similar structural archetypes to those observed in the aluminosilicates. Metal tetrahedral groups are found infrequently within transition metal frameworks.

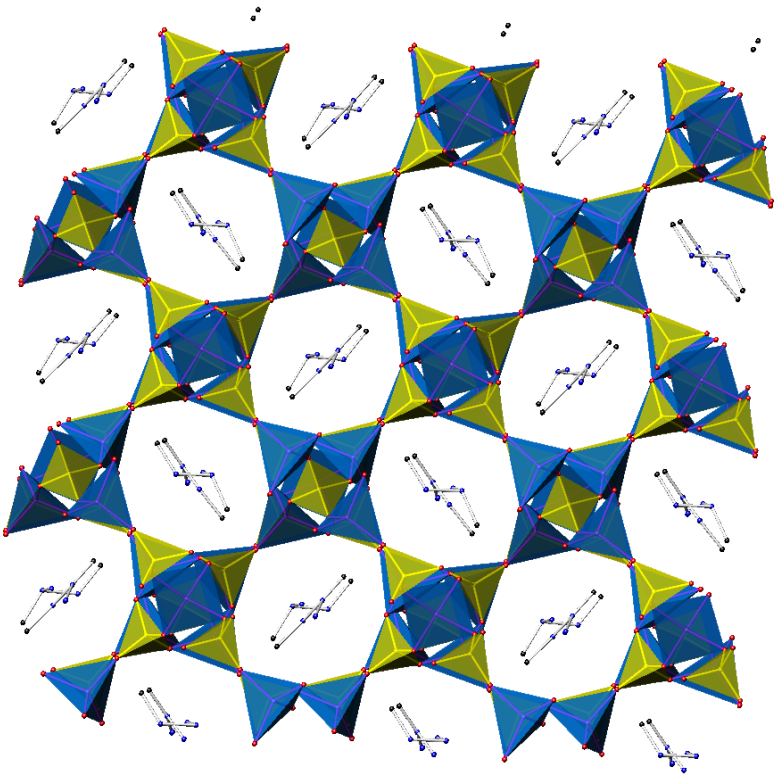

***Figure 1.5**: [$(NH_3CH_2CH(NH_3)CH_3)_2(AlCo_4P_5O_{20})$][42], Cobalt phosphate based zeolite with Edingtonite-type framework viewed through the c-axis [Key: Yellow tetrahedra – PO_4; blue tetrahedra - $CoO_4/AlPO_4$; 1,2-diaminopropane within channels]*

Titanium phosphates have recently undergone syntheses that involve the fluoride route, through the addition of HF in hydrothermal reactions. The powder and crystalline products provided tiny crystallites. These were too small for analysis through single crystal diffraction techniques and so powder diffraction methods were applied. The first structure MIL-6, $Ti_2(PO_4)_2F_4.N_2C_2H_{10}$, was a layered oxyfluorinated compound[43]. The fluoride anions were present at the terminal sites within the titanium octahedra, which formed interactions with the ethylenediamine species within the channels. Further fluorinated phosphates produced by this

research group, such as $Ti^{III}Ti^{IV}F(PO_4).(H_2O)_2$ (MIL-15)[44], exhibited mixed valence titanium octahedra. The titanium octahedra were connected through bridging bonds (Ti-F-Ti bonds and Ti-O-P-O-Ti), with the metal fluoride bonds forming a more three-dimensional structure. The presence of fluoride anions in the terminal positions has been found to discourage three-dimensional frameworks by inhibiting continuation of the bonding.

1.3 Lanthanide Structures

Framework syntheses have evolved, as a result of the introduction of alternative starting materials such as the lanthanide reagents. These rare-earth materials have potential applications in ion exchange, fluorescence, sensors and ionic conduction[45,46]. Lanthanide building units form larger polyhedra than those found within transition metal phosphate and arsenates structures. The coordination spheres in lanthanide materials tend to comprise of 7, 8 or 9 atoms, producing entirely new microporous materials.

Hexagonal lanthanide phosphates were first isolated in the 1950s by Mooney[47], an example is $Ln PO_4.nH_2O$, which exhibits tunnels when viewed through the *c*-axis. The high thermal and chemical stability of this family of phosphates has provided many applications including nuclear waste storage materials[48] and luminescent lamps[49]. In more recent years the proton conductivity of monoclinic $LaPO_4$ was investigated as a high temperature fuel cell[50] electrolyte.

The zeolite-type material MUF-1 was the first example of an actinide or lanthanide zeotype structure[51]. The hydrothermal synthesis of $(C_4N_2H_{12})U_2O_4F_6$ yielded UO_2F_5 polyhedral building units through the incorporation of HF into the reaction mixture, which formed a three-dimensional structure that housed piperazine molecules. Four of the fluoride anions within the polyhedra were linked to further uranium species *via* bridging bonds. The fifth fluoride ion was terminally connected to the polyhedra and was involved in hydrogen bonding with the piperazine molecules. The mixture of terminal and bridging species attached to the lanthanide unit is typical of structures with high fluoride ion content.

A significant amount of research has been undertaken within this thesis incorporating the element cerium, and it is important to highlight recent advances in this field. Hydrothermal studies of lanthanides have received less scientific interest than other transition metals, and so research in

this area tends to be relatively recent. Cerium oxyfluoride, YU-1, was produced using this synthetic technique, however the oxotetrahedral species that are commonly found[52] were not incorporated into this framework. The structure was formed from CeO_6F_2 cages with fluoride ions present at the terminal polyhedral positions. The fluoride species pointed into the channels of the framework that encapsulated NH_4^+ cations. Hydrogen bonding was found to exist between the terminal F^- and NH_4^+ ions. An additional crystal phase formed within this synthesis, the fluorinated $NH_4CeF_2PO_4$ structure, which accounted for the presence of the phosphate groups[53]. The material was constructed from CeO_4F_4 building units, where the fluoride ions within the polyhedra were linked *via* bridging Ce-F-Ce bonding.

Recent studies into lanthanide frameworks, have resulted in structures similar to the zeolites, that do not include tetrahedral species[54]. The compound $[Ln_2(imidc)_2(H_2O)_3](H_2O)_n]$ (Fig. 1.6) exhibits 4,5-imidazoledicarboxylic acid (imidc) and water molecules connected directly to the lanthanide (Ln = Gd^{III} and Er^{III}) cations. The structure is formed from spheres that contain lanthanide cations linked to eight ions (oxygen and nitrogen). The compound was stable after the removal of the water molecules from within the channels. Adsorption measurements were completed and these indicated that sorption of water molecules was possible, although alternative cations were not, which displays the selectivity of the compound.

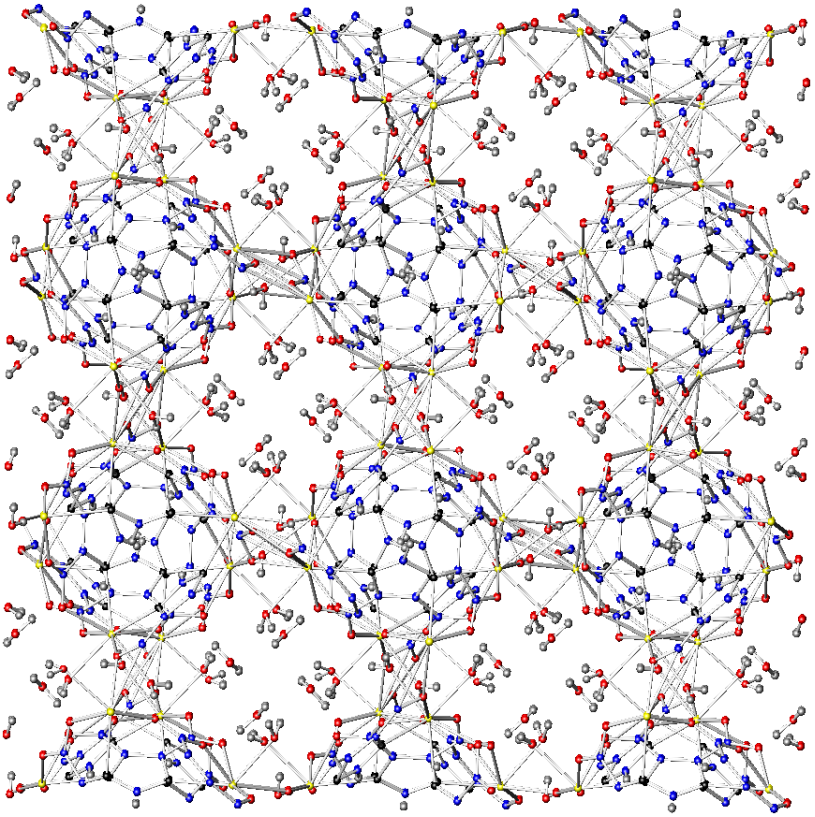

Figure 1.6: *$[Ln_2(imidc)_2(H_2O)_3](H_2O)_n]$[54] viewed down the c-axis [Key: yellow sphere – Ln, red sphere – oxygen, black sphere – nitrogen, blue sphere – carbon, grey sphere – hydrogen]*

The first organically templated cerium phosphate was discovered in 2002 by Yu *et al.*[55], and contains ethylenediamine within its layers ($[enH_2]_{0.5}[Ce^{III}(PO_4)(HSO_4)(OH_2)]$). The structure of this material is illustrated in Figure 1.7. The cerium polyhedra are formed of CeO_9 units, linked to PO_4 and SO_4 tetrahedra (from the starting material $Ce(SO_4)_2.2(NH_4)_2SO_4.4H_2O$) through Ce-O-*T* bonding (*T* = S or P). The reaction proceeded without the incorporation of HF (included within previous syntheses that produced YU-1), which led to a layered structure housing ethylenediamine. The relative acidity of the reaction was found to aid the inclusion of ethylenediamine molecules (previously only ammonium cations were incorporated), by reducing the competition from these NH_4^+ species.

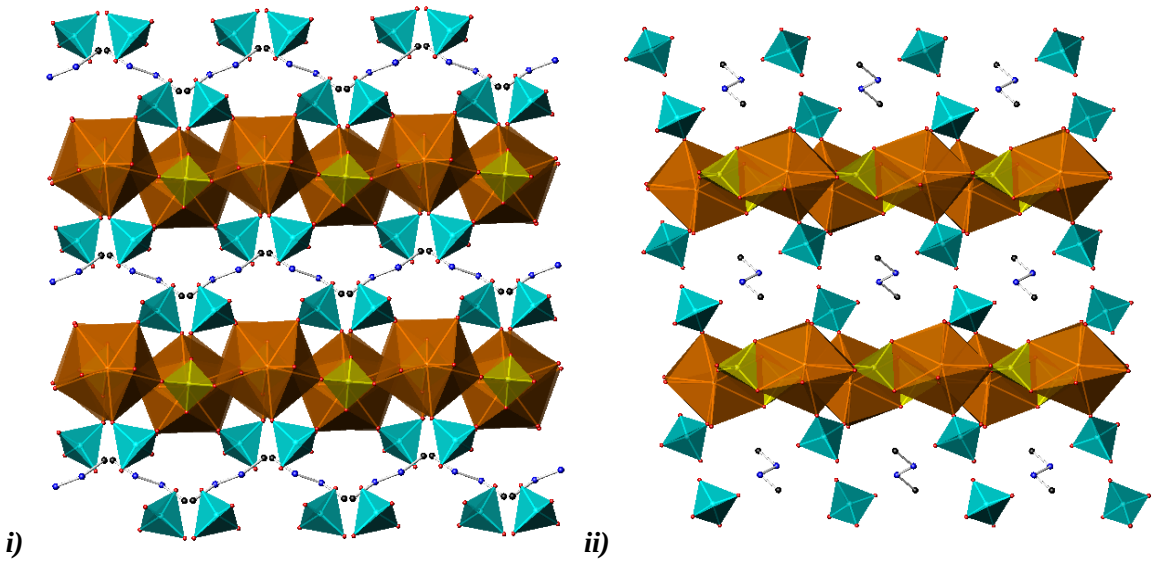

***Figure 1.7**: The view down the **i)** a and **ii)** b-axis for $[enH_2]_{0.5}[Ce^{III}(PO_4)(HSO_4)(OH)_2]$[55] [Key: orange polyhedra – CeO_9; blue tetrahedra – SO_4; yellow tetrahedra – PO_4, en between layers]*

Cerium materials can incorporate organic template groups and oxotetrahedral species into the framework, and have also been found with fluoride ions within the cerium coordination sphere. The compound $[(CH_2)_2(NH_3)_2]_{0.5}[Ce^{IV}F_3(HPO_4)]$ (Fig. 1.8), was the first layered cerium structure to form of this type[56]. The reaction synthesis proceeded in water but the inclusion of HF produced an acidic medium. This reaction system, coupled with a low reaction temperature increased the probability of including the organic template. The presence of fluoride ions bonded to the cerium polyhedra produced the new building unit, CeO_3F_5, which was attached to the framework through Ce-O-P bonding between the polyhedral and tetrahedral units. The cerium species were connected to one another through mixed Ce-F-Ce and Ce-O-Ce bridging bonds. The remaining fluoride ions were linked to the cerium centre in terminal positions, which pointed towards the ethylenediamine molecules. The template species formed distinct hydrogen bonds with the terminal fluoride ions.

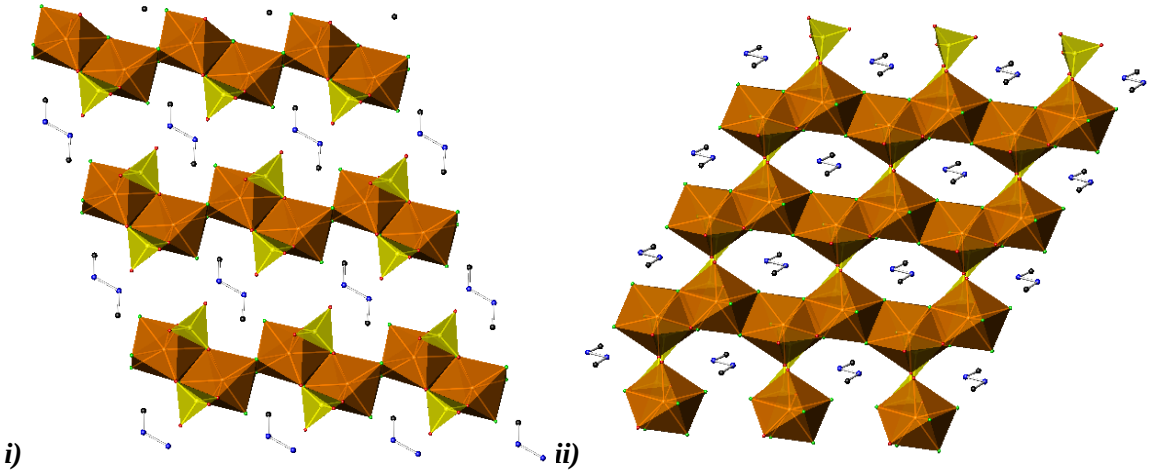

***Figure 1.8**: View down the **i)** a and **ii)** c-axis for[$(CH_2)_2(NH_3)_2]_{0.5}[Ce^{IV}F_3(HPO_4)]$[56] [Key: orange polyhedra - CeO_3F_5, yellow tetrahedra – PO_4, ethylenediamine between layers]*

The incorporation of fluoride ions within lanthanide phosphate and arsenate materials has not been limited to cerium structures. The yttrium fluoride phosphate, $NaYFPO_4$, initially formed in 2000[57], was the product of a hydrothermal synthesis, which included NaF rather than HF as the fluoride source. The presence of fluoride ions within this structure charge-balanced the Group 1 cations (Na^+). The lanthanide building unit that formed (YO_6F_2) was also found within the framework of YU-1. The yttrium polyhedra were linked through bridging fluoride anions, which produced edge-sharing bonding, opposed to their terminal positions within YU-1. This led to a three-dimensional structure, housing sodium cations within its channels (Fig. 1.9).

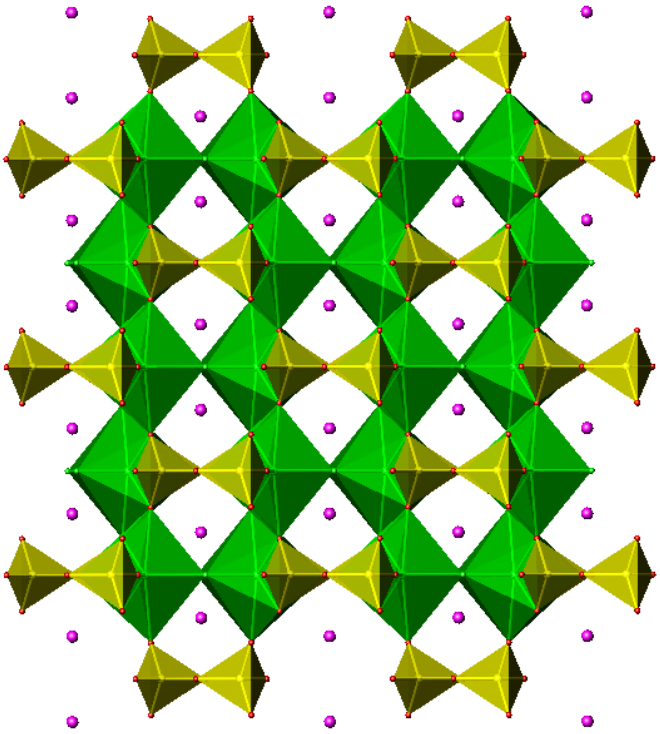

***Figure 1.9**: Structure of $NaYFPO_4$[57] viewed down the a-axis [Key: green polyhedra – YO_6F_2, yellow tetrahedra – PO_4, purple sphere – Na^+ cations]*

The majority of the compounds presented within this section have included phosphate oxotetrahedral units in the framework. Arsenate analogues also form, although alterations to the reaction conditions are typically required. High temperature solid-state reactions have produced the cerium and ytterbium arsenates $CeAsO_4$ and $YbAsO_4$[58,59]. These compounds are constructed from LnO_8 octahedra (*Ln* = Ce/Yb) and AsO_4 tetrahedra, with the *Ln* species in the +3 oxidation state. The reactivity of the arsenate sources and their toxicity has resulted in a small number being documented in the literature.

The larger coordination spheres available to the lanthanide species have increased the number of frameworks that can form. Lanthanide cations have incorporated both F^- and O^{2-} ions within their polyhedra. The fluoride ions have been found to form bridging and terminal links to the structure, and this diverse bonding has produced layered and three-dimensional frameworks.

1.4 Zirconium phosphates and arsenates

Research undertaken by Clearfield found zirconium phosphates to form both layered and pillared structures, which led to significant academic and industrial interest. His research efforts centred upon the synthesis and ion exchange properties of these materials[60].

Zirconium phosphate and arsenate materials typically have an oxidation state of +4. The two-dimensional structures α-Zr(HTO_4)$_2$.H_2O[61] and γ-Zr(TO_4)(H_2TO_4)$_2$.$2H_2O$[62] (Fig. 1.10) are well researched and form both phosphate and arsenate analogues. These structure have been produced for a variety of metal cations when in the +4 state (α = Ti, Sn, Pb and γ = Ti *etc.*). The ZrO_6 octahedral units are connected in layers through Zr-O-P linkages originating from the PO_4 tetrahedra. These layered structures have potential applications in ion exchange (α-type)[63], as well as intercalation chemistry, with materials such as the alkylamines and γ-zirconium phosphate[64].

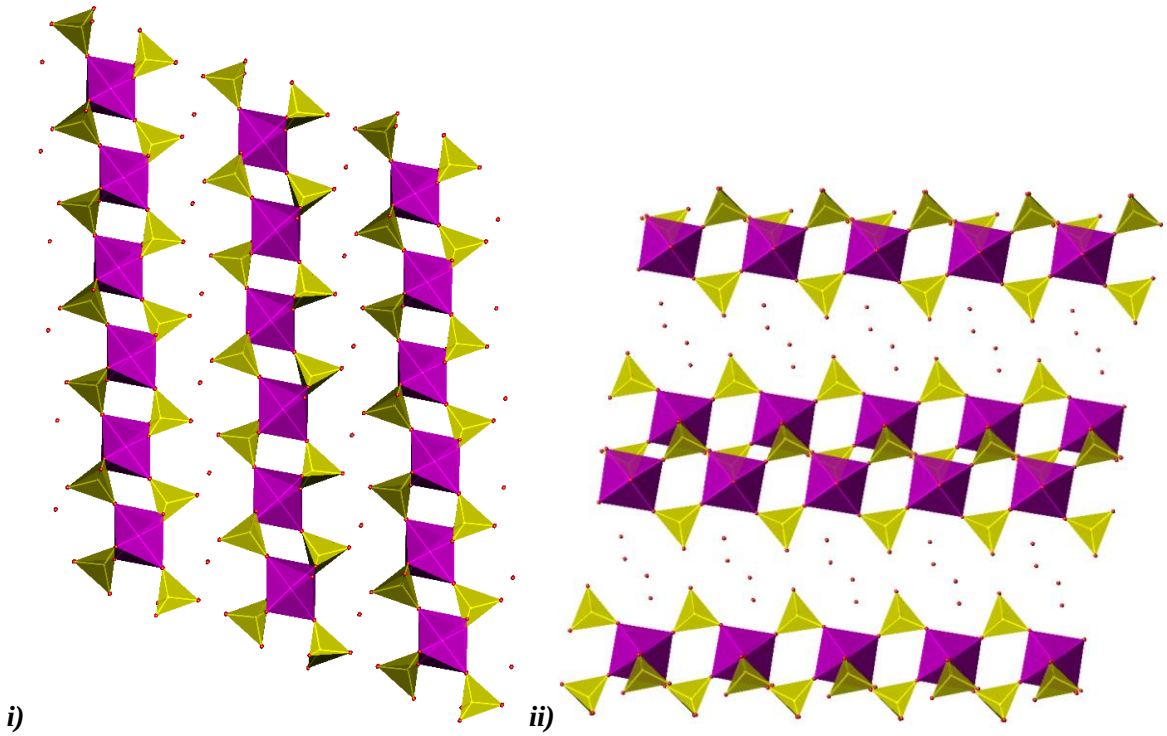

i) ***ii)***

***Figure 1.10**: **i)** α[61] and **ii)** γ[62] layered zirconium phosphates viewed down the b-axis [Key: Purple octahedra - ZrO_6, yellow tetrahedra – PO_4/HPO_4, red sphere – H_2O molecules]*

The introduction of the fluoride route has been fundamental to the production of one, two and three-dimensional zirconium frameworks. Hydrothermal reactions typically include a zirconium starting material (e.g. $ZrOCl_2$) mixed with a phosphate source and in some cases an organic template is added. One-dimensional chains of $[NH_4]_3[Zr(OH)_2(PO_4)(HPO_4)]$[65] were formed through the addition of NH_4F, but fluoride anions were not incorporated into the material. The introduction of fluoride ions (in the form of HF/NH_4F), has led to the production of structures that incorporate these anions. The layered $Zr(PO_4)F(OSMe_2)$ synthesised by Clearfield *et al.*[66], and the three-dimensional $[(enH_2)_{0.5}][Zr_2(PO_4)_2(HPO_4)F].H_2O$ synthesised by Kemnitz[67] are both examples of structures that include fluoride ions once HF is introduced into the reaction. These materials exhibit the fluoride ions linked to the framework through the zirconium octahedra (ZrO_5F), in the terminal positions. Alternative reaction conditions such as nonaqueous syntheses (solvents such as ethylene glycol replace water), have been relatively successful, for example in the synthesis of $[NH_4]_2[H_3N(CH_2)_2NH_3]_2[Zr_3(OH)_6(PO_4)_4]$[68]), however, the hydrothermal route remains the more common method of formation. Wloka undertook research into the formation of zirconium fluoride compounds that also incorporate organic template ions[69,70]. The three-dimensional zirconium phosphates include template species, such as ethylenediamine and diaminocyclohexane within their channels. Research into this area is ongoing, and examples such as the recent discovery of ZrPOF-4[70] and ZrPOF-pyr ($((C_5H_6N)_4(H_2O)_2[Zr_{12}P_{16}O_{60}(OH)_4F_8])$ in 2007 have demonstrated the continued scientific interest[71] (Fig. 1.11). ZrPOF-pyr was the product of a hydrothermal synthesis that included HF. Zirconium octahedra were found to form ZrO_6, ZrO_5F and ZrO_4F_2 building units. The fluorinated octahedra displayed bridging and terminal fluoride species within the structure. This framework was constructed from 10-ring channels that housed pyridinium ions. The terminal fluoride anions exhibited hydrogen bonding interactions with the pyridinium units.

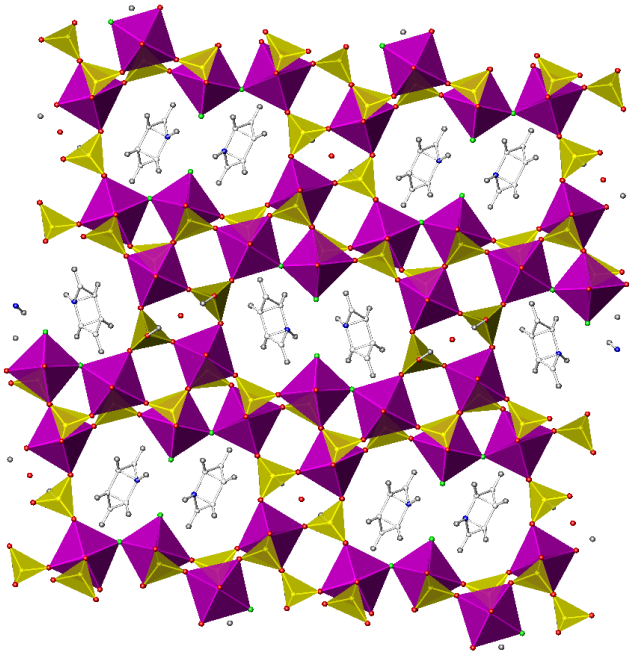

***Figure 1.11**: Channels viewed down the c-axis of ZrPOF-pyr[71] [Key: purple octahedra – ZrO_6, ZrO_5F and ZrO_4F_2; yellow tetrahedra – PO_4; pyridine within channels]*

The Nasicon structures of zirconium, $AM_2(PO_4)_3$ (*A* = Group 1 or 2 cation; *M* = Zr, Ti, Ge *etc.*), have received much research interest, driven by their potential applications in areas such as ion exchange with lithium and sodium[72]. Systematic studies of Nasicon structures have found them to exhibit promise in many applications, such as the fields of low thermal expansion and electrolytes[73]. These three-dimensional materials are constructed from MO_6 and TO_4 units that corner share through the oxygen ions.

1.5 Hafnium phosphates and arsenates

There has been limited research into the hydrothermal production of hafnium phosphate and arsenate materials, in comparison with other Group 4 metals such as titanium and zirconium. The chemistry of hafnium is similar to that of zirconium, and thus analogous materials have formed.

Layered hafnium phosphates such as the α-$Hf_2(HPO_4)_2.H_2O$ have performed ionic exchange reactions with cations such as lithium[74]. The 'α' material has been analysed *via* neutron powder diffraction to identify the hydrogen positions within the structure[75]. It has been established that the 'α' layered phosphates of hafnium, zirconium and titanium are isotypic, and form channels within the framework that house water molecules. The orientation of the water molecules was different within the hafnium material when compared to the other structures (zirconium and titanium), although the hydrogen bonding (between terminal OH groups on the HPO_4 units and H_2O within the channels) was found to be the same.

The γ-$M(PO_4)(H_2PO_4).2H_2O$ (*M* = Zr/Hf *etc.*) is another well known layered structure. This hafnium phosphate was recently produced through hydrothermal methods and was characterised through single crystal X-ray analysis (resulting from the success of the zirconium and titanium compounds[76]). The difference between the two layered structures is that the 'γ' version incorporates two types of phosphate groups (PO_4 and H_2PO_4), whereas the 'α' structure includes only one (HPO_4), which leads to alternative connectivity. The PO_4 groups are linked through all four oxygen sites, whereas the H_2PO_4 groups possess terminal OH groups with exchangeable protons.

In view of their chemical and thermal stability, the alpha and gamma hafnium phosphates have been investigated as intercalation hosts. The presence of H_xPO_4 groups within both structures enables guest species to enter the layers, which are then able to accept protons on these terminal sites. These compounds have formed with the intercalation of amines such as methylpiperidine[77] and piperidine[78], and have the potential to interact with many more. The layered phosphates have received further research interest as a result of their abilities to act as molecular sieves, ion and proton conductors[76].

The hafnium Nasicon structure exhibits bonding that is isotypic to the zirconium compound, although it has not been explored in as much detail. The incorporation of alternative cations to the typical Group 1 and 2 ions has recently been investigated, producing materials such as the copper hafnium phosphate ($Cu^IHf_2(PO_4)_3$)[79]. This material was the product of high temperature (900 °C) reactions within sealed quartz tubes (an alternative to the hydrothermal synthesis), and houses copper in the +1 oxidation state

Recent research studies have witnessed hafnium ions being doped into structures, such as the iron phosphates that have applications in nuclear waste management systems[80]. The

incorporation of hafnium into β-$Zn_3(PO_4)_2$ has potential as a long-lasting phosphorescence material[81], with applications in road signs and low level lighting. The hafnium replaces one of the zinc sites within the structure, which accounts for this effect.

Hafnium arsenate compounds have received less research interest than the phosphates. Frameworks incorporating an organic template ion are very rare, and one of the first materials to be isolated was by Redrup in 2009[82] ($Hf^{IV}_2F_8(AsO_4)(DABCO\text{-}H_2)(NH_4)$). The chemistry of hafnium is significantly underdeveloped in comparison to the zirconium and titanium compounds; however the versatility of the material lends itself to many similar uses as found for other Group 4 and 5 metals.

1.6 Scope of work

The aim of this research project was to synthesise new metal or lanthanide open frameworks with the potential for industrial applications such as catalysis, ion exchange and as actinide hosts. Within these known and novel structures the bonding was found to be both tetrahedral and polyhedral, bound by edge and corner-sharing atoms. The different structural building units revealed a variety of compounds, some of which exhibit entirely new frameworks.

Chapter Two details the experimental methods and theory applied in order to understand and complete this research.

Chapter Three discusses five new cerium fluoride structures. Currently, there are very few examples found in the literature. A variety of structure types have been identified, highlighting the versatility of these materials and their potential applications.

Chapter Four describes six zirconium frameworks synthesised using ZrF_4. The majority do not incorporate fluoride ions, and were found to be three-dimensional.

Chapter Five explains the novel hafnium arsenate and phosphate structures with varying dimensionalities. This chapter examines the types of bonding observed in these materials.

Chapter Six explicates the introduction of amine templating techniques to Group 4 metals combined with oxotetrahedral species to demonstrate the ease with which these compounds can form three-dimensional porous structures, without the direct use of HF in the synthesis method.

Chapter Seven explores the known hydrated hexagonal lanthanide phosphate phase in terms of its water content and change in lattice size upon thermal exposure. This material is an actinide host and so further understanding of the structure will aid in producing more advanced nuclear waste management materials.

Chapter Eight discusses the main findings of this research thesis and offers some conclusions.

1.7 References

(1) Kasture, M. W.; Mirajkar, S. P.; Joshi, V. V.; Choudhari, A. L.; Shiralkar, V. P. *Journal of Inclusion Phenomena and Molecular Recognition in Chemistry* **1997**, *29*, 1-13.

(2) Vansant, E. F. *Pore size engineering in zeolites*; John Wiley, **1990**.

(3) Weller, M. T. *Inorganic Materials Chemistry*; Oxford University Press, **1994**.

(4) Vezzalini, G.; Quartieri, S.; Galli, E.; Alberti, A.; Cruciani, G.; Kvick, A. *Zeolites* **1997**, *19*, 323-325.

(5) Cheetham, A. K.; Day, P. *Solid-State Chemistry Techniques*; Claredon Press Oxford, **1987**.

(6) Dutta, D.; Chatterjee, S.; Ganguly, B. N.; Pillai, K. T. *Journal of Applied Physics* **2005**, *98*, 7.

(7) Kim, J. S.; Zhang, L.; Keane, M. A. *Separation Science and Technology* **2001**, *36*, 1509-1525.

(8) Corma, A.; Diaz-Cabanas, M.; Martinez-Triguero, J.; Rey, F.; Rius, J. *Nature* **2002**, *418*, 514-517.

(9) Wilson, S. T.; Lok, B. M.; Messina, C. A.; Cannan, T. R.; Flanigen, E. M. *Journal of the American Chemical Society* **1982**, *104*, 1146-1147.

(10) Paillaud, J. L.; Marler, B.; Kessler, H. *Chemical Communications* **1996**, 1293-1294.

(11) Davis, M. E.; Saldarriaga, C.; Montes, C.; Garces, J.; Crowder, C. *Nature* **1988**, *331*, 698-699.

(12) Bennett, J. M.; Cohen, J. M.; Artioli, G.; Pluth, J. J.; Smith, J. V. *Inorganic Chemistry* **1985**, *24*, 188-193.

(13) Parise, J. B. *Inorganic Chemistry* **1985**, *24*, 4312-4316.

(14) Yang, G. D.; Feng, S. H.; Xu, R. *Journal of the Chemical Society-Chemical Communications* **1987**, 1254-1255.

(15) Li, L.; Wu, L. X.; Chen, J. S.; Xu, R. R. *Acta Crystallographica Section C-Crystal Structure Communications* **1991**, *47*, 246-249.

(16) Shannon, R. D. *Acta Crystallographica Section A* **1976**, *32*, 751-767.

(17) Bhatia, S. *Zeolite catalysis: principles and applications*; CRC Press, **1990**.

(18) Morris, R. E.; Weigel, S. J. *Chemical Society Reviews* **1997**, *26*, 309-317.

(19) Yu, J.; Sugiyama, K.; Zheng, S.; Qiu, S.; Chen, J.; Xu, R.; Sakamoto, Y.; Terasaki, O.; Hiraga, K.; Light, M.; Hursthouse, M. B.; Thomas, J. M. *Chemistry of Materials* **1998**, *10*, 1208-1211.

(20) Kan, Q. B.; Glasser, F. P.; Xu, R. R. *Journal of Materials Chemistry* **1993**, *3*, 983-987.

(21) Caullet, P.; Paillaud, J. L.; Simon-Masseron, A.; Soulard, M.; Patarin, J. *Comptes Rendus Chimie* **2005**, *8*, 245-266.

(22) Loiseau, T.; Ferey, G. *Journal of Materials Chemistry* **1996**, *6*, 1073-1074.

(23) Loiseau, T.; Ferey, G. *Acta Crystallographica Section C-Crystal Structure Communications* **2005**, *61*, M315-M317.

(24) Korzenski, M. B.; Schimek, G. L.; Kolis, J. W. *Journal of Solid State Chemistry* **1998**, *139*, 152-160.

(25) Cheetham, A. K.; Ferey, G.; Loiseau, T. *Angewandte Chemie-International Edition* **1999**, *38*, 3268-3292.

(26) Haushalter, R. C.; Mundi, L. A. *Chemistry of Materials* **1992**, *4*, 31-48.

(27) Mundi, L. A.; Strohmaier, K. G.; Haushalter, R. C. *Inorganic Chemistry* **1991**, *30*, 153-154.

(28) Haushalter, R. C.; Wang, Z. W.; Thompson, M. E.; Zubieta, J. *Inorganic Chemistry* **1993**, *32*, 3700-3704.

(29) Riou, D.; Ferey, G. *Journal of Solid State Chemistry* **1994**, *111*, 422-426.

(30) X., D. Z.; Wang, C.; Sun, X. M.; Li, Y. D. *Inorganic Chemistry* **2002**, *41*, 869-873.

(31) Natarajan, S.; Cheetham, A. K. *Journal of Solid State Chemistry* **1997**, *134*, 207-210.

(32) Natarajan, S.; Cheetham, A. K. *Chemical Communications* **1997**, 1089-1090.

(33) Fan, L. Q.; Wu, J. H.; Huang, Y. F.; Lin, J. L. *Bulletin of the Korean Chemical Society* **2009**, *30*, 965-968.

(34) Choudhari, A. L.; Natarajan, S.; Rao, C. N. R. *Chemistry of Materials* **1999**, *11*, 2316+.

(35) Cavellec, M.; Riou, D.; Ninclaus, C.; Greneche, J. M.; Ferey, G. *Zeolites* **1996**, *17*, 250-260.

(36) Cavellec, M.; Greneche, J. M.; Riou, D.; Ferey, G. *Microporous Materials* **1997**, *8*, 103-112.

(37) Meng, H.; Li, S.; Liu, L.; Cui, Y. J.; Li, G. H.; Pang, W. Q. *Materials Letters* **2005**, *59*, 3861-3865.

(38) Takahashi, M.; Tobishima, S.; Takei, K.; Sakurai, Y. *Journal of Power Sources* **2001**, *97-98*, 508-511.

(39) Ellis, B. L.; Makahnouk, W. R. M.; Makimura, Y.; Toghill, K.; Nazar, L. F. *Nat Mater* **2007**, *6*, 749-753.

(40) Zhangang, H.; Jun, P.; Aixiang, T.; Xueliang, Z. *Journal of Solid State Chemistry* **2006**, *179*, 3209-3213.

(41) Choudhari, A. L.; Neeraj, S.; Natarajan, S.; Rao, C. N. R. *Angewandte Chemie-International Edition* **2000**, *39*, 3091-3093.

(42) Bu, X. H.; Gier, T. E.; Feng, P. Y.; Stucky, G. D. *Chemistry of Materials* **1998**, *10*, 2546-2551.

(43) Serre, C.; Ferey, G. *Journal of Materials Chemistry* **1999**, *9*, 579-584.

(44) Serre, C.; Guillou, N.; Ferey, G. *Journal of Materials Chemistry* **1999**, *9*, 1185-1189.

(45) Patra, C. R.; Bhattacharya, R.; Patra, S.; Basu, S.; Mukherjee, P.; Mukhopadhyay, D. *Clinical Chemistry* **2007**, *53*, 2029-2031.

(46) Rao, R. P.; Devine, D. J. *Journal of Luminescence* **2000**, *87-9*, 1260-1263.

(47) Mooney, R. C. L. *Acta Crystallographica* **1950**, *3*, 337.

(48) Volkovich, V. A.; Griffiths, T. R.; Thied, R. C. *Physical Chemistry Chemical Physics* **2003**, *5*, 3053-3060.

(49) Riwotzki, K.; Meyssamy, H.; Schnablegger, H.; Kornowski, A.; Haase, M. *Angewandte Chemie-International Edition* **2001**, *40*, 573-576.

(50) Harley, G.; Yu, R.; De Jonghe, L. C. *Solid State Ionics* **2007**, *178*, 769-773.

(51) Halasyamani, P. S.; Walker, S. M.; O'Hare, D. *Journal of the American Chemical Society* **1999**, *121*, 7415-7416.

(52) Yu, R. B.; Wang, D.; Kumada, N.; Kinomura, N. *Chemistry of Materials* **2000**, *12*, 3527-+.

(53) Yu, R. B.; Wang, D.; Takei, T.; Kumada, N.; Koizumi, H.; Kinomura, N. *Journal of Solid State Chemistry* **2001**, *157*, 180-185.

(54) Maji, T. K.; Mostafa, G.; Chang, H. C.; Kitagawa, S. *Chemical Communications* **2005**, 2436-2438.

(55) Wang, D.; Yu, R.; Xu, Y. H.; Feng, S. H.; Xu, R. R.; Kumada, N.; Kinomura, N.; Matsumura, Y.; Takano, M. *Chemistry Letters* **2002**, 1120-1121.

(56) Yu, R.; Wang, D.; Isiwata, S.; Saito, T.; Azuma, M.; Takano, M.; Chen, Y.; Li, J. *Chemistry Letters* **2004**, *33*, 458-459.

(57) Zhizhin, M. G.; Olenev, A. V.; Spiridonov, F. M.; Komissarova, L. N.; D'Yachenko, O. G. *Journal of Solid State Chemistry* **2001**, *157*, 8-12.

(58) Brahim, A.; Mongi, F. T.; Amor, H. *Acta Crystallographica Section E-Structure Reports Online* **2002**, *E58*, i98-i99.

(59) Kang, D. H.; Hoss, P.; Schleid, T. *Acta Crystallographica Section E-Structure Reports Online* **2005**, *E61*, i270-i272.

(60) Clearfield, A. *Industrial & Engineering Chemistry Research* **1995**, *34*, 2865-2872.

(61) Clearfield, A.; Smith, D. *Inorganic Chemistry* **1969**, *8*, 431-436.

(62) Bortun, A. I.; Clearfield, A.; Suarez, M.; Llavona, R.; Rodriguez, J. *Materials Chemistry and Physics* **1998**, *55*, 152-154.

(63) Clearfield, A.; Duax, W. L.; Medina, A. S.; Smith, G. D.; Thomas, J. R. *The Journal of Physical Chemistry* **1969**, *73*, 3424-3430.

(64) Rodriguez, J.; Suarez, M.; Rodriguez, M. L.; Llavona, R.; Arce, M. J.; Salvado, M. A.; Pertierra, P.; Garcia-Granda, S. *European Journal of Inorganic Chemistry* **1999**, 61-65.

(65) Wang, D.; Yu, R. B.; Takei, T.; Kumada, N.; Kinomura, N.; Onda, A.; Kajiyoshi, K.; Yanagisawa, K. *Chemistry Letters* **2002**, 398-399.

(66) Poojary, D. M.; Zhang, B. L.; Clearfield, A. *Journal of the Chemical Society-Dalton Transactions* **1994**, 2453-2456.

(67) Kemnitz, E.; Wloka, M.; Trojanov, S.; Stiewe, A. *Angewandte Chemie-International Edition in English* **1996**, *35*, 2677-2678.

(68) Wang, D.; Yu, R. B.; Kumada, N.; Kinomura, N. *Chemistry of Materials* **2000**, *12*, 956-960.

(69) Wloka, M.; Troyanov, S. I.; Kemnitz, E. *Journal of Solid State Chemistry* **1998**, *135*, 293-301.

(70) Wloka, M.; Troyanov, S. I.; Kemnitz, E. *Journal of Solid State Chemistry* **2000**, *149*, 21-27.

(71) Dong, J. X.; Liu, L.; Li, J. P.; Li, Y.; Baerlocher, C.; McCusker, L. B. *Microporous and Mesoporous Materials* **2007**, *104*, 185-191.

(72) Catti, M.; Comotti, A.; Di Blas, S. *Chemistry of Materials* **2003**, *15*, 1628-1632.

(73) Chakir, A.; El Jazouli, A.; de Waal, D. *Materials Research Bulletin* **2003**, *38*, 1773-1779.

(74) Tomita, I.; Magami, K.; Watanabe, H.; Suzuki, K.; Nakamura, T. *Bulletin of the Chemical Society of Japan* **1983**, *56*, 3183-3184.

(75) Salvado, M. A.; Pertierra, P.; GarciaGranda, S.; Garcia, J. R.; Rodriguez, J.; FernandezDiaz, M. T. *Acta Crystallographica Section B-Structural Science* **1996**, *52*, 896-898.

(76) Suarez, M.; Barcina, L. M.; Llavona, R.; Rodriguez, J.; Salvado, M. A.; Pertierra, P.; Garcia-Granda, S. *Journal of the Chemical Society-Dalton Transactions* **1998**, 99-102.

(77) Barcina, L. M.; Vega, A.; Suarez, M.; Llavona, R.; Rodriguez, J. *Solvent Extraction and Ion Exchange* **1998**, *16*, 861-873.

(78) Rodriguez, M. L.; Barcina, L. M.; Villa-Garcia, M. A.; Anillo, A.; Llavona, R.; Suarez, M.; Rodriguez, J. *Solvent Extraction and Ion Exchange* **1999**, *17*, 1371-1384.

(79) Ahmamouch, R.; Arsalane, S.; Kacimi, M.; Ziyad, M. *Materials Research Bulletin* **1997**, *32*, 755-761.

(80) Karabulut, M.; Yuksek, M.; Marasinghe, G. K.; Day, D. E. *Journal of Non-Crystalline Solids* **2009**, *355*, 1571-1573.

(81) Peng, Z. F.; Xu, Z.; Luo, C. Q.; Yu, J. B.; Zhang, G. B. *Luminescence* **2008**, *23*, 14-16.

(82) Redrup, K. V. *Synthesis and Characterisation of new Framework Materials, University of Southampton* **2009**.

CHAPTER TWO

EXPERIMENTAL TECHNIQUES

2.0 Introduction

The synthetic techniques employed within this research study predominantly involved solvothermal methods. Alternative reaction routes were employed (sealed tube reactions, flux *etc.*) but the new structures obtained came from the aforementioned route. The reaction products were analysed using a variety of techniques common to solid state chemistry. These methods have assisted in the successful identification and characterisation of the reaction products. The following techniques were applied within this research project and they are discussed in greater detail later in this chapter.

Single crystal X-ray diffraction (SXD) enabled characterisation of new crystal structures, and this was the primary method of analysis applied to identify the solvothermal products.

Powder X-ray diffraction (PXD) was undertaken in the identification of powdered phases. The method has facilitated measurement of the purity of the samples, demonstrating whether secondary phases were present within reaction products.

Thermogravimetric analysis (TGA) determined the temperature at which the water or ion content of a structure was released. The decomposition temperatures of samples were established where possible. This technique provided important supplementary information to identify the expected molecules and ions present within new structures.

Energy Dispersive X-ray Microanalysis (EDX) and Scanning Electron Microscopy (SEM) were completed on reaction products to provide an understanding of the morphology of crystals, which was not possible using a laboratory microscope. This process provided the elemental composition within the bulk sample of powders and specific crystals from crystalline samples, establishing whether certain elements (such as fluorine) were present.

Infrared Spectroscopy (IR) was undertaken to clarify the presence or absence of ions and molecules (such as H_2O/NH_4) within the materials studied.

Fluorescence spectroscopy was completed on hydrated and dehydrated phosphate materials to ascertain whether the samples produced different levels of electronic emissions and highlight any differences between hydrated and dehydrated samples.

2.1 Synthesis Methods

Inert reagents used within solid-state methods can attain improved reactivity through alterations to the synthetic procedures. These reaction conditions will typically involve longer heating times, repeated grinding and elevated temperatures. These processes aid in the ion mobility within the solid reaction. Thorough grinding of reagents with a pestle and mortar and the production of pellets increases the number of reaction sites and thus the reactivity of the solids. The disadvantage of solid-state reactions is that the more thermodynamically stable product is typically formed. The synthetic methods employed in this research thesis are described below.

2.1.1 Solvothermal synthesis

Hydrothermal syntheses were completed in Teflon-lined steel autoclaves with volumes of 23/45 mL (Fig. 2.1), provided by the Parr Instrument Company. The autoclaves used within this research project had a maximum working temperature of 250 °C (523K) and an operating pressure of 8000kPa (1200psig). These closed vessels are constructed to withstand high pressures, and fitted with safety valves. If the pressure exceeds the maximum operating level it will be released through two holes in the side of the stainless steel screw cap.

Figure 2.1*: Image of Teflon-lined steel Parr autoclaves (23 mL on left and 45 mL on right)*

Solvothermal syntheses are reactions that proceed with alternative solvents to water within the autoclaves. This research project has included various alternative solvents such as ammonia, ethanol, acetone, hydrochloric acid, sodium hydroxide and isopropanol. Heating hydrothermal autoclaves in ovens increases the pressure within the vessels and the water or solvent remains in its liquid form above its typical boiling point (100 °C for water). These conditions mimic the natural formation of materials such as the zeolites, which take place in porous basalt rocks under high temperatures and pressures.

High pressure and temperature conditions encourage the growth of single crystals where other methods fail. The main advantage of this synthesis over solid-state methods is the improved mobility of the ions when in solution. This increased mobility allows reactions to proceed at lower temperatures or for shorter periods of time, reducing the synthetic efforts needed to form products.

A supercritical fluid has properties that incorporate both a liquid and a gas, when water reaches this point it exists as hydrogen bonded clusters. The critical point within a hydrothermal reaction can be affected by factors such as temperature and pressure. The properties that water molecules exhibit are similar to gases, almost non-polar and with a lowered density. There is no surface tension within these fluids as there is no phase boundary between the liquid and gas phase. The solvating ability of supercritical fluids increases with their density as long as the temperature is kept at a constant value. Density is directly linked to pressure, and so as the pressure within the hydrothermal bombs is increased, so is the solubility. When the density of these fluids is constant then the temperature will increase its solubility. However, just before the critical point is reached the solubility of the reagents can be greatly reduced as the temperature is increased. The solubility will often drop sharply around this point and then continue to rise again. External pressure sources can be used to create more extreme reaction conditions, closer to the supercritical state, although this has not been completed within this research project.

Zeolite synthesis often employs the use of organic templating ions within the reaction solution. These large cations can be used as a site for the aluminosilicate framework to crystallise around, without which dense structures would form. The amine filled cavities or channels that the framework grows around can be rendered empty through heating of the material as the template decomposes. The zeolite framework will remain intact as long as it was not dependent upon these ions, in which case its removal causes structural collapse. This technique can be applied in the search for novel nanoporous materials that incorporate metal polyhedra and oxotetrahedral species such as the compounds described within this research thesis. The incorporation of these ions can

lead to the formation of interesting and unusual bonding motifs, with a variety of practical applications.

Solvothermal syntheses have certain disadvantages. Parr autoclaves are expensive, and it is not possible (with the current experimental set up) to observe the growth of the crystals within the hydrothermal vessel, which can be useful in understanding new materials. The closed hydrothermal system can be affected by many factors, for example pH, temperature, reagent concentrations, pressure and solvent filling levels.

Solvothermal methods provide advantageous routes of formation for novel compounds, which may not form through alternative synthetic techniques. Reactions proceed at lower temperatures as a result of the increased pressure within the system. Solvothermal conditions increase the solubility of starting materials and additional reagents such as alkali hydroxides or metal salts can be introduced to the reaction, binding to the solid to make it more soluble. Templated compounds do not form readily through general solid-state reactions as the elevated temperatures cause decomposition of their structures, hydrothermal methods allow their investigation.

2.1.2 Molten Flux synthesis

This experimental method proceeds with all starting materials in the solid phase within a sealed vessel (hydrothermal bomb or sealed tube) to prevent the evaporation of the starting materials. The reagents are ground in order to produce a homogenous system, and heated to a temperature at which point one of the reagents (the flux medium) melts. The reaction proceeds in the liquid state, increasing the ion mobility within the system, thus encouraging alternative synthetic products to form compared to standard solid-state reactions. The flux medium is involved in the reaction and can be incorporated into the product, which can be difficult with unreactive sources using techniques such as hydrothermal synthesis. Boric acid, H_3BO_3, was used within this research project as a flux medium, which melts at 180 °C (453 K). Reaction times and pressures are reduced and grindings are not necessary, an improvement upon solid-state methods.

2.2 Introduction to X-ray Diffraction

The initial problem that arises from synthetic reactions is characterisation of the products. A powdered sample will require powder X-ray diffraction (PXD) analysis to determine the bulk phase. Every compound has a unique powder diffraction pattern, some of which can be found in databases such as the JCPDF, which is an exhaustive list of over 500,000 unique X-ray diffraction patterns. The use of programmes such as EVA[1], part of the Bruker Diffrac Plus Evaluation Suite of programmes, enable quick analyses of samples and identification of known phases. If the products of the reaction were determined to be good quality single crystals of a suitable size and without twinning problems, then single crystal X-ray diffraction analysis (SXD) was undertaken. This technique provides structural information for a specific crystal, by using X-rays to determine the geometry of the unit cell and its contents.

The discovery of X-rays by Röntgen in the late 1800's led Max von Laue to conclude that the wavelengths of X-rays have the same order of magnitude as interatomic spacing's ($\sim 10^{-10}$ m). The Laue equations described three conditions for incident radiation to be diffracted by a crystal lattice. This description was then simplified by W.H. Bragg and W.L. Bragg, who were able to explain the phenomenon of crystals 'reflecting' X-rays at specific angles of incidence, which will be discussed further within this section.

2.2.1 X-ray Diffraction

Single crystals consist of regular arrangements of atoms that pack together in a three-dimensional (3D) framework or lattice. The smallest repeating unit within these structures is called the unit cell, which exhibits the full translational and rotational symmetry of the crystal lattice. Unit cell parameters are measured using the lengths *a*, *b*, and *c*, which corresponds to the axis of *x*, *y* and *z*, with angles α, β and γ (Fig. 2.2). Crystals are made up of a regular arrangement of these unit cells so the environment of each lattice point is identical.

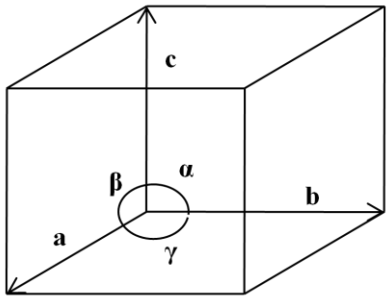

Figure 2.2: *The unit cell defined by a, b, c and α, β, γ*

The specific angles and lengths within a unit cell provide it with unique characteristics that enable classification into groups based upon symmetry. There are seven crystal systems and these are listed in Table 2.1. The different types of lattices within these systems are centred and non-centred. The non-centred P (primitive) lattice contains one lattice point per cell. Centred lattices contain more than one lattice point per unit cell (two or four) as a result of the translational symmetry within the cell. Centred lattices form; I (body centred with 2 lattice points); A, C (side centred with two lattice points) and F (face centred with four lattice points). The combination of these lattice points with the crystal systems gives rise to the 14 Bravais lattices. The unit cell contents can possess one of 32 point group symmetries that are consistent with the translational symmetry of the Bravais lattices. The combination of these point and translational symmetries lead to additional symmetry elements such as glide planes and screw axes and distribution of these amongst the 14 Bravais lattices leads to a total of 230 space groups. The translational symmetry within centred cells produces systematic absences within diffraction patterns. For a non-centred primitive lattice generally all reflections are observed. A body-centred cell with atoms at (x, y, z) will also have corresponding lattice points at (x + ½, y + ½, z + ½). Systematic absences will be observed when $h + k + l$ is even, as the atoms from one motif will scatter out of phase as others scatter in phase, thus cancelling out the reflections. All other translational symmetry elements such as glide planes produce similar systematic absences which enable space-group determination.

Crystal System	Bravais Lattice	Lattice Parameters	Point Groups
Triclinic	P	$a \neq b \neq c$; $\alpha \neq \beta \neq \gamma \neq 90°$	$1, \bar{1}$
Monoclinic	P, C	$a \neq b \neq c$; $\alpha = \gamma = 90° \neq \beta > 90°$	2/*m*, *m*, 2
Orthorhombic	P, C, I, F	$a \neq b \neq c$; $\alpha = \beta = \gamma = 90°$	*mmm*, *mm*2, 222
Tetragonal	P, I	$a = b \neq c$; $\alpha = \beta = \gamma = 90°$	4/*mmm*, $\bar{4}2m$, 4*mm*, 422, 4/*m*, -4, 4
Rhombohedral	R	$a = b = c$ $\alpha = \beta = \gamma \neq 90°$	$\bar{3}m$, 3*m*, 32, $\bar{3}$, 3
Hexagonal	P	$a = b \neq c$; $\alpha = \beta = 90°, \gamma = 120°$	6/*mmm*, $\bar{6}m2$, 6*mm*, 622, 6/*m*, $\bar{6}$, 6
Cubic	P, I, F	$a = b = c$ $\alpha = \beta = \gamma = 90°$	$m\bar{3}m$, $\bar{4}3m$, 432, $m\bar{3}$, 23

Table 2.1*: The seven crystal systems, 14 Bravais lattices, and the point groups assigned to the crystal systems*

Structures that have a three-dimensional form can be regarded as having layers or planes that stack together. These planes are equally spaced from one another as well as parallel. This regular distance is referred to as the *d*-spacing. The origin of every cell is a lattice point, which must lie on a set of lattice planes.

The Miller indices refer to the reciprocal of the points at which the *a, b* and *c*-axes of the lattice planes are intercepted, denoted *h, k* and *l* from a defined origin. If a Miller index is equal to zero then the plane is parallel to that axis. The Bragg equation (Equation 2.1) describes the scattering that is observed from a given crystal as reflections from a set of these lattice planes. The path difference between two waves when they are scattered by atoms in the lattice planes separated by d_{hkl}, is given by AB+BC, equal to $2d\sin\theta$ (for reflection AB=BC). For constructive interference to be observed the lattice planes *hkl* must exhibit scattering at the angle 2θ (if the incident beam

strikes the lattice plane at angle θ it must also be reflected at angle θ), satisfying Bragg's law (Fig. 2.3). The integer *n* must be a whole number of wavelengths.

$$n\lambda = 2d_{hkl}\sin\theta \qquad (2.1)$$

λ = wavelength, *d* = spacing between planes, θ = angle of incidence

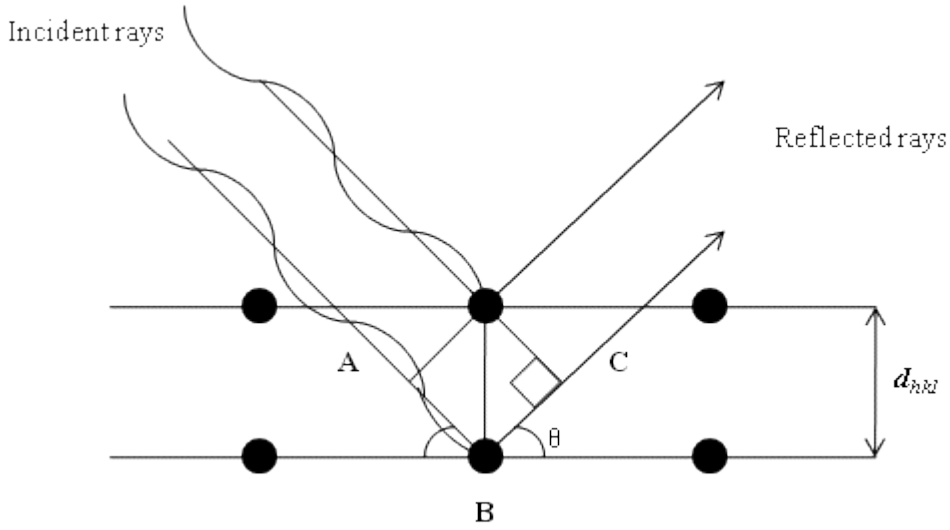

Figure 2.3*: Bragg's law exhibiting the diffraction of X-rays from the crystal lattice planes*

Atoms can act as point scatterers when exposed to X-ray radiation. Incoming X-ray beams are scattered by the electron clouds that surround the atom or crystal in question. The resultant constructive or destructive interference provides us with a pattern that is specific to that group of atoms. It is the regular spacing of these point scatterers in the crystal lattice that leads to constructive interference and allows interpretation of the subsequent diffraction pattern.

X-rays are generated when high energy electrons are fired at a specific metal target and collide with this matter. Electric currents are applied to a tungsten filament to generate electrons, which are then accelerated by voltages from 30-60 kV. The electrons will hit a metal target (copper for the powder diffraction examples and a rotating molybdenum anode in the case of single crystal). The product is a broad spectrum consisting of white radiation as a result of the electrons collisions with the target that has slowed them down or caused them to stop, and monochromatic X-rays, required for the experiment. The generated electrons have enough energy to ionize some of the electrons from the metals 1*s* (K) shell. Electrons from the outer orbitals such as 2/3*p* will drop

down to fill the vacant inner shell, and this energy of transition has a characteristic value, creating an emission of X-rays. The two possible transitions from the L (2*p*) and M (3*p*) shells produce Kα and Kβ radiation respectively. Kα is a more frequent transition to Kβ, and is the more intense emission needed for the diffraction experiments. These transitions are actually doublets of Kα_1, Kα_2; Kβ_1 and Kβ_2. In order to obtain the desired Kα lines the beam is monochromated either by a crystal (PXD: D5000 = Ge) or pseudo mirrors (SXD) to filter out the unwanted radiation.

The interaction of X-rays with a given crystal or powder sample will involve either absorption or scattering. If they are scattered the ions within the crystal act as point scatterers, and the X-ray photons will be emitted in all directions. Atoms or ions within a crystal or polycrystalline powder will have different scattering capabilities (scattering factors) dependent upon the number of electrons present. The atoms within the sample will begin to interact with one another as they scatter electrons and cause emissions of X-rays. X-ray diffraction patterns will be produced when point scatterers interact with one another in a constructive manner, creating distinct peaks within the diffraction spectrum.

2.2.2 Single Crystal X-ray Diffraction (SXD)

Single crystal X-ray diffraction generates more information than its powder equivalent (three-dimensional as opposed to effectively one-dimensional). The quantity of unique data (reflections) required within a collection (known as the asymmetric unit) is dependent upon the level of symmetry of a particular crystal. If there are fewer symmetry elements then the asymmetric unit will contain more unique reflections and a longer data collection will be required to gather enough information for structural characterisation.

The intensity of reflections that are the product of constructive interference is linked to the electron density of individual atoms. The electron density at a point (*x, y, z*) in the unit cell contributes to every measured reflection. The summation of these contributions through the electron density equation will produce an electron density map (Equation 2.2).

$$\rho_{xyz} = \frac{1}{V} \sum_{hkl} |F_{hkl}| . \exp[i\emptyset_{hkl}] . [-2\pi i(h_x + k_y + l_z)] \qquad (2.2)$$

ρ = electron density, F_{hkl} = structure factor

The contribution from each reflection is described by its structure factor F_{hkl} ($I_{hkl} \propto F_{hkl}^2$). The relative intensities of reflections can be measured within a diffraction experiment, providing information about the square of the scattering factor. Each atom has a unique scattering factor (f_j). The structure factor is a combination of all scattering factors within a unit cell, which forms Equation 2.3. The structure factor is a complex number which comprises both the amplitude and the phase. The amplitude can be directly measured although the phase cannot, and so the electron density equation does not provide a direct pathway to the structure solution. However, if the structure is known (*i.e.* positions of the atoms) then the complete structure factor including both amplitude and phase can be calculated through the structure factor equation.

$$F(hkl) = \sum_{j=1}^{N} f_j \exp\left[2\pi i\left(hx_j + ky_j + lz_j\right)\right] \quad (2.3)$$

F = structure factor; f = scattering factor

Equation 2.2 and 2.3 are related by a Fourier transform – the forward Fourier transform is the diffraction experiment (going from the unknown structure to its measurable diffraction pattern) and the reverse Fourier transform, which computes the structure from its observable diffraction pattern. The phase of a unit cell cannot be calculated accurately without the application of further mathematics, such as Patterson (when heavy atoms are present) and direct methods. In order to solve a crystal structure these must first be applied to counteract the phase problem.

A.L. Patterson discovered his answer to the phase problem in the early 1900's, which can be applied to structures that contain a number of atoms with very large atomic mass when compared to the remainder within the structure. Patterson methods avoid the phase problem by utilising the electron density equation that ignores the phase angle (assuming that all reflections are in phase) to produce a three-dimensional map. This map represents the vectors between atoms relative to one another not to the origin of the unit cell. The electron density of atoms affects their ability to scatter X-rays; therefore the heavy atoms will produce larger diffraction peaks, increasing the intensity of the vector between two atoms. The data provides us with positions of the heavy atoms, and from this the lighter atoms can be deciphered. Once the approximate atom positions are isolated the structure factor can be calculated, and the refinement completed.

If the structure contains atoms with similar atomic numbers then the Patterson method breaks down, as the diffraction peaks are too similar, and 'direct-methods' will be applied. This statistical method is dependent upon the atoms having similar scattering capabilities and a degree of randomness in their distribution; most organic molecules will be solved in this way. Direct methods apply basic assumptions regarding the nature of electron density to derive probabilistic relationships between phases of a number of strong reflections. The most likely candidates can then be used to obtain a starting model.

Once the phase problem has been solved by either Patterson or direct-methods and the atom placement within the unit cell is known, a least squares refinement is begun to improve the accuracy of the specific atoms positions within the structure. The '*R*' (residual) factor is a measurement of the difference between the observed and calculated structure factors (Equation 2.4).

$$R = \frac{\sum ||F_o| - |F_c||}{\sum |F_o|} \tag{2.4}$$

R = residual factor, F_o = observed structure factor, F_c = calculated structure factor

This *R*-factor provides an insight into the extent to which the refinement model (F_c) is in agreement with the measured data (F_o). By simply placing the heavy atoms into a refinement an *R*-factor of 0.2-0.3 (20-30 %) could be achieved, but to publish a level of 0.05 or less would be anticipated. Generally an *R*-factor of greater than 0.05 would suggest that the crystal quality is low or an atom has been incorrectly assigned within the structure. The *R*-factor has an associated degree of error, as it explains the differences between calculated and observed intensities of complex structures, when four or more parameters are observed for each atom using just one number. The weighted *R*-factor (wR_2) and GooF (goodness of fit or S) will be quoted alongside this figure to counteract this problem.

$$wR_2 = \frac{[\sum w(F_o - F_c)^2]^{1/2}}{(\sum \sqrt{w(F_o)^2})} \tag{2.5}$$

wR_2 = weighted reliability factor, w = assigned weight

The value of wR_2 (Equation 2.5) is typically larger than R, as R is based upon F alone, whereas the former is derived from F^2. The *S* value (Equation 2.6) should be as close to unity as possible, as it describes the differences in F as well as the number of reflections and parameters within the refinements.

$$S = \frac{[\sum w(F_o - F_c)^2]^{1/2}}{N-P} \quad (2.6)$$

S = Goodness of fit, *N* = number of observed data, *P* = number of parameters

The measurement of single crystal reflection intensities can be systematically affected if the X-rays are significantly absorbed by the crystal; these errors are eliminated by absorption corrections. Similarly, the scattering factor needs to be modified to include thermal motion. The low scattering power of hydrogen atoms means that they contribute little to the diffraction pattern and are difficult to locate. The process of least squares refinement outputs parameter values (such as atomic positions), which have an associated estimated standard deviation (ESD) or uncertainty, this ESD is propagated through the derived parameters such as bond lengths and angles.

Single crystal X-ray diffraction was completed on the University of Southampton's two Bruker-Nonius KappaCCD diffractometers. A Bruker-Nonius FR951 rotating anode X-ray generator enables these two machines to function, and runs with a molybdenum target. One window uses confocal focusing mirrors, to produce focused monochromatic X-rays, and the other a graphite monochromator. The machines are capable of working at temperature of 80-500 K, through the incorporation of Oxford cryosystems cryostreams. The Kα radiations produced through the use of the molybdenum target is λ = 0.71703 Å, and the data collections were completed at 120 K for all of the systems analysed within this thesis.

A typical single crystal experiment would involve isolating a suitable single crystal, which did not exhibit twinning under the microscope and polarised light completely. This crystal would then be mounted onto a glass fibre attached to a brass pip with silicone grease, which hardens as it is exposed to lower temperatures and does not interact with the generated X-rays. The pip is attached to the goniometer, and centred in the X-ray path (Fig. 2.4). A 'quick scan' (10-60 sec) is run to check that the crystal produces a diffraction pattern with well defined diffraction and does not include smearing or twinning of the spots. The presence of rings within a scan would suggest the sample is a powder rather than a single crystal, and an amorphous sample would not show any

diffracted reflections but a very broad amorphous scattered background. Weaker diffraction spots will cause the data collection to be lengthy, so an alternative crystal may be sought. The crystal sample is checked for the quality as high quality data will aid speedy analysis and ultimately give a better structure solution with better statistics.

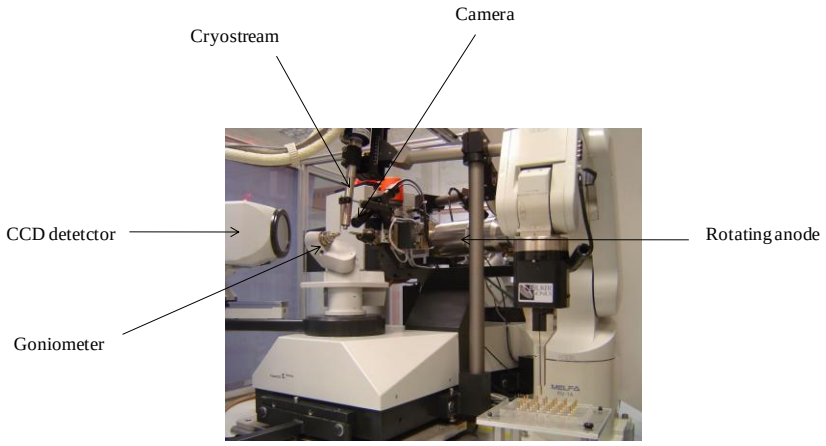

***Figure 2.4**: Photograph of one of the Bruker-Nonius Kappa CCD (courtesy of the National Crystallography Service, University of Southampton)*

Once a suitable single crystal has been isolated a unit cell will be run on the sample, which consists of four phi and phi/chi scans lasting from 2-10 minutes dependent upon the crystals ability to diffract. The unit cell is calculated using DirAx[3,4] and the programme offers an idea of how well the data fits to that cell with a number associated with fitting and non-fitting parameters. The unit cell measurements produce an understanding of the type of crystal, and whether twinning or bad quality data will require an alternative example to be selected. A database of known unit cell parameters is compared against the values obtained to check whether a full dataset is needed[5]. The software package COLLECT[6] is used for full data collections of the crystals, suggesting the length of time required and the number of frames needed, whilst recording all of the reflections present within the asymmetric unit. Once the data has been gathered an absorption correction is applied on the data using SADABS[7]. This method is a so called 'multi-scan' technique that uses the large redundancy of the data set to correct for adsorption. In cases where absorption is very strong, a more rigorous analytical correction may be applied, this requires the composition of the crystal to be known and a face index description of the crystal shape. The data would then be transferred to a different computer and all analyses within this research thesis were completed using the WinGX[8] programme that utilised XPREP[9] and SHELX-97[10] packages.

2.2.3 Powder X-ray Diffraction (PXD)

Powder X-ray diffraction is a fundamental technique to solid-state chemistry. A powdered sample should contain an infinite number of crystallites, ordered randomly throughout. X-rays are diffracted by the planes of atoms within the polycrystalline sample as long as the angle of the lattice planes is appropriate. The variations in the orientation of the crystallites within the sample produces cones of diffraction rather than the spots observed for single crystal diffraction. This experimental technique offers rapid determination of the bulk phase present within these crystalline solids.

The Siemens D5000 diffractometer was used to characterise the powder samples within this research project, it uses a Bragg Brentano $\theta/2\theta$ geometry. The diffractometer uses a Cu target that after monochromation *via* a Ge crystal gives a $K\alpha_1$ peak with a wavelength of $\lambda = 1.54056$ Å. The beam is focussed through a germanium crystal primary monochromator. Samples were ground before mounting upon a Perspex or aluminium sample holder. The aperture slits within these data collections were a 2 mm pre-sample slit, 2 mm post-sample slit and 0.2 mm detector slit. The computer interface which begins the data collection can control the range of 2θ studied, step size and the length of time needed for characterisation of the powder. The angle of incidence is always set to hit the sample surface at θ and the detector is set at 2θ (Fig. 2.5). Once a powder pattern had been recorded it was analysed through programmes such as DIFFRAC^{plus} evaluation Package[1].

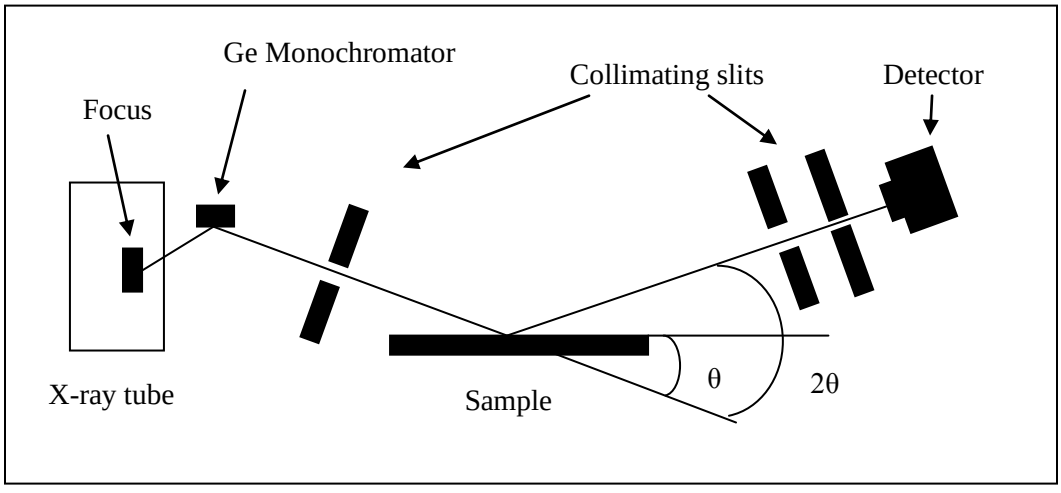

***Figure 2.5**: Diagram of the D5000 diffractometer*

2.3 Thermogravimetric analysis (TGA) and Differential scanning calorimetry (DSC)

DSC and TGA analysis are both thermoanalytical techniques. TGA analysis provides information on the change in weight of a sample in relation to the temperature. It can provide details on the contents of a structure and how this changes when exposed to variations in temperature, such as the loss of ions or whether structures exhibit phase changes a certain temperatures. The quantity of molecules and ions within structures can be calculated from the data obtained. It provides us with information in terms of how much energy is required to cause the molecules or ions to leave the structure. TGA can be carried out under atmospheric gas or a gas such as nitrogen, to temperatures of up to 1200 °C to analyse the structures. The atmosphere under which the TGA is undertaken can affect the rate of reaction. This research project incorporated atmospheric gas in all TGA measurements to ensure the results were comparable. The samples analysed through TGA measurements are heated as a function of temperature and time at a rate that is constant until the thermal decomposition begins. Thermal decomposition usually takes place over a range of temperatures, until a second constant mass is observed. The change in mass from the initial weight to the plateaued weight is the overall mass that has been lost from the substance.

DSC is an analytical technique that provides information on materials that experience phase changes without loss of mass upon heating. A reference material is used to calculate these energy changes, and has relative stability over the temperatures that the sample is being analysed in order that calculated measurements can easily be made. The temperatures of the sample and reference material are maintained throughout the experiment. The quantity of heat required may increase or decrease in order that the sample and reference material are kept at a constant temperature. This allows quantitative analysis of the enthalpy changes that can be observed for given samples. If a change in crystal structure, (decomposition, melting *etc.*) of a sample occurs either more or less energy in the form of heat is required to flow to the sample in order that the temperature is kept the same as the reference material. This will be apparent in the data experiment as a positive (exothermic) or negative (endothermic) peak when temperature is plotted against energy change.

DSC and TGA are often required jointly in experimental analysis as some phase changes can only be seen *via* the DSC when there is no change in mass. Changes can also be observed *via* cooling as well as heating from DSC analysis, creating awareness of reversible processes such as the level of hydration.

Within this research thesis the TGA analysis was completed on a Polymer Laboratories STA 1500 simultaneous thermogravimetric analysis system (Fig. 2.6). Typical experiments would involve 50 mg of a sample, weighed through the microbalance. The samples were heated at a rate of 10 °C/min to 800 °C in atmospheric air to measure their weight loss and thermal stability. TGA analysis was used to observe the loss in mass of cations and molecules within the majority of materials within this project, as phase change information was not required. For this reason the DSC data have been removed for clarity in the majority of cases.

Figure 2.6: *TGA instrument*

2.4 Energy Dispersive X-ray Microanalysis (EDX) and Scanning Electron Microscopy (SEM)

EDX analysis enables the elemental content within a sample to be identified. EDX spectroscopy investigates the elements within the sample through the use of electromagnetic radiation, electrons hit the sample and the X-ray emissions are recorded.

In its ground state a sample contains unexcited electrons within their respective elemental electron shells. These electrons are bound to the nucleus and cannot move. An incident beam of highly charged electrons is aimed at the sample. These electrons may collide with an electron from an inner shell of the sample (1s) and excite it so that it is ejected from the electron shell. An electron from a higher-energy electron shell (2p/3p) will then be released to the lower empty electron shell left by the ejected electron. The energy difference associated with the movement of electrons from a higher to a lower electron shell is measured in the form of an emitted X-ray/photon, which has energy that is characteristic of the parent element. Measuring these specific X-rays enables EDX data to be collected.

Scanning electron microscopy (SEM) scans a high-energy beam of electrons over the surface of a sample. The beam of primary electrons can interact with the sample in a number of ways. The generation of low energy secondary electrons can be produced as a result of the primary electrons beam hitting atoms at the surface of the material. This interaction illustrates the topographical nature of the sample, resulting from the contrast within the image. The narrow beam diameter produces high resolution images at the samples surface. The second interaction is a result of the primary electrons being backscattered by the sample. The back-scattered electron signal is characteristic of atomic number and thus the elements present can be characterised. Heavy elements such as cerium will back scatter electrons more readily than their lighter counterparts. This analytical method can study the size, shape, texture and surface features of powders and single crystals, which optical microscopes are often not powerful enough to reveal.

SEM-EDX combines these two analytical processes and has been applied within this research thesis. This technique creates an understanding of the morphology of the particles or crystals formed whilst also providing information on the elemental composition of the reaction product. The data is measured is semi-quantitative, as the instrument detects all wavelengths simultaneously, creating a rapid analysis of the crystals or powders but the values obtained are not accurate because of difficulties in calibration for variations in matrix and overlapping peaks.

SEM-EDX microanalysis was carried out within this research project on a JEOL JSM-5910 Scanning Electron Microscope. This machine was fitted with an Oxford Instruments Inca Energy 300 Energy-Dispersive X-ray Spectrometry analysis system. This is a type of scanning-electron microscope with a resolution of 3nm.

2.5 Bond Valence Theory

Organic and inorganic structures use bond valence theory to describe the type of bonding, for example single, double, triple and so forth. Bond valence theory has been used in this research thesis to analyse the bonding within the structures and theorise whether an oxygen or fluorine atom is attached at specific sites, or if there is a need for hydrogen ions to be attached to oxygen anions forming hydroxide or water molecules. These factors are often difficult to observe through SXD analysis alone as hydrogen ions often cannot be located and the differences between the sizes of an oxygen or fluoride anion are minimal.

Bond valence theory relies upon the oxidation state of ions within a structure. Pauling's electrostatic valence rule uses the sums of anions and neighbouring cations to equalise the charge of the atom in question. The valence rule is a modification of bond valence, which can be used when structures are not truly ionic in bonding. The formal charge of the anion and the bond valence are replaced by the number of electrons that take part in the bonding. This theory has been developed by Pauling[11] when applied to metals and compounds that contain more than one metal element. Byström and Wilhlemi applied the theory to oxides and this was later added to by Zachariasen[12]. Brown[9], Brese and O'Keefe[13] were authors of definitive papers on the matter, which form the basis of the calculations that are made today.

$$\upsilon_{ij} = \exp\left[(R_{ij}-d_{ij})/b\right] \tag{2.7}$$

$$\Sigma_j \upsilon_{ij} = V_i \tag{2.8}$$

υ_{ij} = valence of bond between two atoms *i* and *j*; V_i = valence; R_{ij} = bond valence parameter[13], d = bond length, b = universal constant (0.37 Å)[9];

Equation 2.7 must be completed for every ion that bonds to the site where the valence value is required. Equation 2.8 describes how the sum of the bond valences around each site will produce a value that is equal to the oxidation state of the ion in question. In this thesis for example the cerium source used was Ce^{+4}; if the V_i value was found to vary between 3 and 4 then we would consider there to be a mixed valence at those cation sites within the framework. The valences for oxygen and fluorine anions were often essential for this research. Their similar atomic masses make them difficult to differentiate through diffraction analysis alone. Bond valence calculations can indicate the presence of mono rather than divalent anions. The valence has also been observed to be very low (0.2-0.5) at some terminal oxygen sites, less than expected for monovalent anions. In these cases it is assumed that two hydrogen ions are required to stabilise the weakly bound water molecule to the framework.

The disadvantages of bond valence analyses are that it cannot be used on sites that have mixed occupancies. If the shape of the ions within SXD refinements are not truly spherical, the bond valence will be marginally inaccurate as the bond lengths will be taken from the centre of the ellipsoids rather than at the edge, producing an altered bond length to that which is truly observed.

2.6 Infrared (IR) Vibrational Spectroscopy

Within solids atoms vibrate at a frequency between $10^{12} – 10^{13}$ Hz. If these solids absorb radiation at a frequency appropriate to them then they can be excited into higher energy states. An IR spectrum is a plot of absorption as a function of frequency. The frequency of this incident radiation can be varied, allowing us to understand the amount of radiation which is absorbed or transmitted by the sample. A large variety of peaks are observed in IR spectra, all corresponding to a specific vibrational transition. Functional groups can be isolated from these peaks and this is the reason for analysis of the majority of compounds within this thesis. Peaks found in the range of 3000-3500 cm^{-1} are characteristic of an OH group of some kind. The specific position and the intensity of the peak will provide an insight as to whether the OH is a water molecule, if hydrogen bonding is observed, the quantity of OH and where it resides within the structure. The IR spectral features of inorganic solids are not as well characterised as for organic functional groups, however for the purpose of this thesis, it was not an issue as functional groups such as NH_4, H_2O, OH^- *etc.* were the primary concerns.

The discs were prepared by grinding milligrams amounts of a sample and mixing it with dry KBr until a fine powder was formed. This mixture was then placed within a pellet press. The translucent pellet was then transferred to the IR machine and the beam from the spectrometer was passed through it, and a spectrum recorded. A Perkin-Elmer Instruments Spectrum-One FT-IR Spectrometer was used in the range of 4000-150 cm^{-1} for the analyses and the data was interpreted using the Spectrum software.

2.7 Solid State Fluorescence Spectroscopy

Luminescence is a term which denotes the emission of light from a material after it has absorbed energy. Fluorescence is a form of photoluminescence, where a photon is absorbed producing an electronic excited state, that subsequently relaxes with re-emission of a photon. Electrons can undergo various forms of promotion such as from low to high vibrational energy levels within the same and adjacent atoms. Each element has characteristic transitions, which will result in photons emitted at a certain wavelength. The energy of these emitted photons are sensitive to the bonding environments of the atoms in question, which can allow changes in structure to be observed within the spectra.

Ground powder samples were mounted in a recessed aluminium holder with a quartz window. A reference cell that contained barium sulphate was used to produce a background spectrum before analysis could begin. Fluorescence spectra were collected using a PerkinElmer LS 45 fluorescence spectrometer in a diffuse rectangular mode. Spectra were recorded in the range 400-800 nm.

2.8 References

(1) *Diffrac^{plus} Evaluation Package, Regents of the University of California, Sun Microsystems Inc., 2004*.

(2) Clegg, W.; Blake, A. J.; Gould, R. O.; Main, P. *Crystal Structure Analysis Principles and Practise*; Oxford University Press, **2001**.

(3) Duisenberg, A. J. M. *Journal of Applied Crystallography* **1992**, *25*, 92-96.

(4) Duisenberg, A. J. M.; Hooft, R. W. W.; Schreurs, A. M. M.; Kroon, J. *Journal of Applied Crystallography* **2000**, *33*, 893-898.

(5) Fletcher, D. A.; McMeeking, R. F.; Parkin, D. *Journal of Chemical Information and Computer Sciences* **1996**, *36*, 746-749.

(6) Hooft, R. W. W. *COLLECT data software Nonius B.V* **1998**.

(7) Sheldrick, G. M. *SADABS Version 2.10. Bruker AXS Inc, Madison, Wisconsin, USA* **2003**.

(8) Farrugia, L. J. *Journal of Applied Crystallography* **1999**, *32*, 837-838.

(9) Brown, I. D.; Altermatt, D. *Acta Crystallographica Section B-Structural Science* **1985**, *41*, 244-247.

(10) Sheldrick, G., *Programmes for Crystal Structure Analysis, Release 97-2*, **1997**

(11) Pauling, L. *Journal of the American Chemical Society* **1947**, *69*, 542-533.

(12) Zachariasen, W. H. *Acta Crystallographica* **1963**, *16*, 385-389.

(13) Brese, N. E.; O'Keeffe, M. *Acta Crystallographica Section B-Structural Science* **1991**, *47*, 192-197.

CHAPTER THREE

CERIUM FLUORIDE FRAMEWORKS

3.0 Introduction

The initial aim of this research was to produce novel cerium arsenate and phosphate frameworks *via* the introduction of large quantities of fluorine into the reaction, using the reagent CeF_4. The intention was to produce new and interesting three-dimensional lanthanide compounds with potential applications, in areas such as ionic exchange, actinide hosts[1] due to their high thermal stability and low solubility in water[2], lasers[3] and fuel cells[4]. It was hoped that this investigation would supply a reaction pathway that would provide, as an alternative approach to standard solvothermal syntheses. It was hoped that a greater understanding of the role of the fluoride ions and their affect on the structures formed could be gained through the use of CeF_4 instead of HF.

Hydrofluoric acid (HF) is an industrially useful tool as a fluorine source in areas such as the pharmaceutical and oil sectors. HF is often used within hydrothermal reactions and its addition is required to promote crystal growth by acting as a mineraliser within the solution. The main issue in the use of HF in bulk reactions is that it is extremely corrosive and a poison. Its ability to penetrate the skin and enter the bloodstream means that exposure can be fatal or require amputation even in small doses. HF interacts with the calcium and magnesium cations within the bloodstream forming calcium fluoride. An antidote gel, calcium gluconate, must be carried by all users when in contact with HF, as simply washing the solution from the skin will not suffice. For this reason, alternative fluorine sources such as CeF_4 could remove the potential risk associated with direct use of HF in solvothermal syntheses. If alternative reagents could replace HF or reduce the quantities required, there would be a great reduction to these health and safety risks.

Amine templating is a method that is commonly used in solvothermal synthesis. The amine acts as a templating ion, directing the crystallisation of the structures around itself, causing structures to form that are specific to the size and shape of the template. The presence of organic templates will alter the pH of the reaction solution, which can increase the relative solubility of the reagents.

A literature review undertaken at the beginning of this study revealed that very few compounds are known that incorporate cerium, oxotetrahedral species and in some cases organic materials within their channels. This suggested that this would be an interesting area of study with many new materials and areas of interest yet to be discovered. Examples of non-fluorinated structures synthesised without the use of a fluorine source include $[enH_2]_{0.5}[Ce^{III}(PO_4)(HSO_4)(OH_2)]$[5], and the fluorinated compound $[(CH_2)_2(NH_3)_2]_{0.5}[Ce^{IV}F_3(HPO_4)]$[6]

was produced as a result of the addition of HF to the reaction. The presence of these materials suggested that this area could provide results in the search for novel zeotypes. The use of CeF_4 as opposed to HF in a reaction was intended to provide an alternative fluoride source, that in low concentrations would produce non-fluorinated frameworks and in high concentrations fluorinated cerium structures. These materials were hoped to have applications such as ion exchange, catalysis and as actinide hosts.

The nature of lanthanide elements, with their ability to contain larger bonding motifs in the polyhedral unit, creates possibilities for more uncommon framework structures to form. Lanthanides are relatively safe materials to use and so large scale replication could be possible on an industrial scale.

The fluorine within these reactions was obtained from the starting material $Ce^{IV}F_4$. Initial synthetic methods used $Ce^{III}F_3$, which is not presented within this research thesis in detail, as a result of the lack of success. The variation in oxidation state from +3 to +4 created a more reactive starting material, which incorporated larger volumes of fluorine into the reaction mixture. It was not known whether the fluorine would aid the reaction mechanism by acting as a mineraliser, promoting crystal growth, or as a catalyst for framework formation, where other starting materials such as oxides, sulphates, carbonates and other halide groups had failed.

In this study a number of reactions were completed before any novel structures were formed. The synthetic process was altered through the ratios of starting materials; pH (*via* addition of NH_3 or amine templates), solvents (H_2O, HCl, CH_3CH_2OH, NH_3, NaOH (l)), temperatures and reaction lengths to aid the formation of analysable crystals. Reactions that obtained powder and crystal are detailed in Table 3.1 to provide an understanding of the reaction conditions that favoured certain materials formation. The table also details alternative reaction conditions that were completed throughout the research project. A large number of powdered phases were produced, as well as amorphous and single crystal phases. It is the single crystal results that are described within this chapter.

This chapter is focused on the structures that included cerium and fluoride ions, and occasionally other elements (Cs, O *etc.*). A total of five novel structures have been synthesised, characterised and are discussed herein. The fifth compound, $(NH_4)[Ce^{IV}F_2(AsO_4)]$, is listed last rather than after the second material $[(NH_4)_5(H_2O)_2][Ce^{IV}{}_4(AsO_4)_6(H_2O)F_3]$ (as both materials formed in the same reaction vessel), as it is isostructural to the phosphate polymorph $(NH_4)[Ce^{IV}F_2(PO_4)]$ discovered by Ranbo Yu *et al*[7].

***Table 3.1**: Synthetic conditions for a number of cerium reactions (all Parr autoclaves 23 mL)*

Reaction No.	Reagents	Temp (°C)	Time (days)	Single crystal/powder	Product(s)	Thesis section
1	CeF_4 (0.2 g); H_3AsO_4 (0.131 g); CsOH (0.278 g); H_2O (11 mL)	140	14	Elongated octahedra single crystals	$CsCe_2F_8[F.H_2O]]$ (**I**)	3.1
2	CeF_4 (0.2 g); $NH_4H_2AsO_4$ (0.44 g); H_2O (12 mL); pH 6	175	5	Thick needle single crystals	$[(NH_4)_5(H_2O)_2][Ce_4(AsO_4)_6(H_2O)F_3]$ (**II**)	3.2
3	CeF_4 (0.1 g); H_3AsO_4 (0.19 g); RbOH (0.24 g); H_2O (11 mL);	140	14	Rod single crystals	$Ce(AsO_4)F$ (**III**)	3.3
4	CeF_4 (0.1 g); H_3AsO_4 (0.19 g); RbOH (0.24 g); H_2O (11 mL);	140	14	Diamond single crystals	$Ce(AsO_4)F(H_2O)$ (**IV**)	3.4
5	CeF_4 (0.2 g); $NH_4H_2AsO_4$ (0.44 g); H_2O (12 mL); pH 6	175	5	Hexagonal plate single crystals	$[NH_4]CeF_2(AsO_4)$ (**V**)	3.5
6	$Ce(SO_4)_2.xH_2O$ (0.3 g); H_3PO_4 (0.08 g); NaF (0.04 g); H_2O (11 mL)	175	12	Multi-phase powder	$Ce(PO_3)_4$; $NaPO_3$; $NaCe_2(PO_4)_3$	3.6
7	$Ce(SO_4)_2.xH_2O$ (0.3 g); H_3PO_4 (0.26 g); NaF (0.04 g); H_2O (11 mL)	175	12	Single phase powder	Na_2HPO_4; $CeHPO_4$	3.6
8	$Ce(SO_4)_2.xH_2O$ (0.3 g); H_3PO_4 (0.08 g); NaF (0.12 g); H_2O (11 mL)	175	12	Multi-phase powder	$NaPO_3$; $Ce(SO_4)_2$	3.6
9	$Ce(SO_4)_2.xH_2O$ (0.6 g); H_3PO_4 (0.08 g); NaF (0.04 g); H_2O (11 mL)	175	12	Multi-phase powder	$Ce(SO_4)_2.4H_2O$; $NaH_2PO_2.H_2O$	3.6
10	CeF_3 (0.3 g); H_3PO_4 (0.45g); H_2O (11 mL)	175	14	Powder	CeF_3	3.6
11	CeF_3 (0.3 g); H_3PO_4 (0.45g); ethanol (11 mL)	175	14	Multi-phase powder	CeF_3; $Ce(PO_4)/.xH_2O$	3.6
12	CeF_3 (0.3 g); $NH_4H_2PO_4$ (0.35 g); NaF (0.09 g); H_2O (11 mL)	200	14	Powder	CeF_3	3.6
13	CeF_4 (0.2 g); $NH_4H_2PO_4$ (0.3 g); Acetone (11 mL)	175	5	Multi-phase powder	$CePO_4$, CeF_3, ammonium phosphates	3.6
14	CeF_4 (0.2 g); $NH_4H_2PO_4$ (0.3 g); Ethanol (11 mL)	175	5	Amorphous	n/a	3.6
15	CeF_4 (0.2 g); $NH_4H_2PO_4$ (0.3 g); NH_3 (11 mL)	175	5	Multi-phase powder	$(NH_4)_2Ce(PO_4)_2.H_2O$ ammonium phosphates	3.6
16	CeF_4 (0.2 g); $NH_4H_2PO_4$ (0.3 g); NaOH (11 mL)	175	5	Multi-phase powder	NaF, $(NH_4)Ce(PO_4)_2.H_2O$	3.6
17	CeF_4 (0.2 g); $NH_4H_2PO_4$ (0.3 g); DABCO (0.1 g); H_2O (11 mL)	140	7	Multi-phase powder	CeF_3, $CePO_4.H_2O$, organic phases	3.6

18	CeF_4 (0.2 g); H_3AsO_4 (0.13 g); TEA (0.12 g); H_2O (11 mL)	140	7	Multi-phase powder	CeF_3, $CeAsO_4$	3.6
19	CeF_4 (0.2 g); H_3AsO_4 (0.13 g); PYR (0.05 g); H_2O (11 mL)	140	7	Multi-phase powder	As_2O_5, $CeAsO_4$	3.6
20	CeF_4 (0.1 g); H_3PO_4 (0.05g); KOH (0.05 g); H_2O (11 mL)	140	10	Amorphous	n/a	3.6
21	CeF_4 (0.1 g); H_3PO_4 (0.05g); RbOH (0.09 g); H_2O (11 mL)	140	10	Multi-phase powder	$Rb_2(H_2PO_3)_2$, $CePO_4$	3.6
22	CeF_4 (0.1 g); H_3PO_4 (0.05g); CsOH (0.14 g); H_2O (11 mL)	140	10	Multi-phase powder	$CePO_4$, CsH_2PO_4	3.6
23	CeF_4 (0.1 g); H_3PO_4 (0.05g); $Ba(OH)_2$ (0.08 g); H_2O (11 mL)	140	10	Multi-phase powder	BaF_2, $Ba(HPO_4)$, $CePO_4$	3.6
24	CeF_4 (0.3 g); H_3PO_4 (0.68g); H_2O (11 mL)	175	5	Multi-phase powder	$Ce(HPO_4)_2$, $Ce(PO_3)_4$	3.6
25	CeF_4 (0.5 g); H_3PO_4 (0.05g); H_2O (11 mL)	175	5	Multi-phase powder	$CePO_4$ H_3PO_4 CeO_2	3.6

3.1 Compound I: Hydrated Caesium Cerium Fluoride - $Cs[Ce_2^{IV}F_8[F,H_2O]]$

3.1.1 Synthesis

Compound **I**, $Cs[Ce_2^{IV}F_8[F,H_2O]]$ was synthesised *via* hydrothermal methods. CeF_4 (0.2 g, 0.09 mmol, Aldrich 99.9%), H_3AsO_4 (0.131 g, 0.92 mmol, 75% wt. BDH chemicals) and CsOH (50% wt, 0.278 g, 1.85 mmol, Aldrich) were stirred in H_2O (11 mL). The reaction mixture was transferred to a 23 mL Teflon-lined Parr autoclave and heated at 140 °C for 14 days. The autoclave was allowed to cool slowly to room temperature, and the solid product removed from the solution by filtration, washed with warm water and left to dry in air at 80 °C for 3 hours.

3.1.2 Results and Discussion

Compound **I** was crystallised from reactions aimed at incorporating caesium into cerium arsenate structures. The reaction product was ratio specific in order for the small, block-shaped colourless crystals to form (Fig. 3.1). Tables 3.2 and A.3.1 (see Appendix), show the details of the crystal structure and atomic positions.

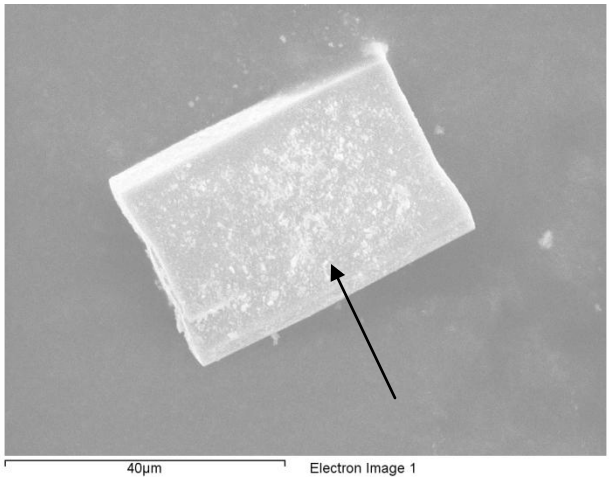

Figure 3.1: *SEM image of $Cs[Ce_2^{IV}F_8[F,H_2O]]$crystals*

Table 3.2: *Details of single crystal data collection for $Cs[Ce^{IV}_2F_8[F,H_2O]]$(Compound I)*

Molecular Formula	**$CsCe_2^{IV}F_8[F,H_2O]]$**
Formula Weight (g)	601.71
Crystal Appearance	Colourless block
Crystal Size (mm)	0.02 x 0.02 x 0.01
Crystal System	Monoclinic
Space Group	*C2/c*
Lattice Parameters	a = 15.4579(5) Å, α = 90°
	b = 6.9826(2) Å, β = 117.938(2)°
	c = 8.5656(2) Å, γ = 90°
V (Å^3)	816.79(10)
Z	4
Temperature (K)	120
Theta range (°)	3-27.5
Calculated density (mg/m^3)	4.9
Wavelength (Å)	Mo *K*α (λ = 0.71073)
Number of Reflections Measured	Total – 4230, Unique - 719
R_1 [I>2σ (I)]^a	0.029
***R*1(all data)**	0.031
wR_2	0.101
Goodness of fit indicator	1.185

Compound **I** crystallised in the monoclinic *C2/c* space group, and its structure is shown in Figure 3.2. The basic framework of **I** was identified in the initial stages of the structure refinement; further analysis, was carried out using information from the EDX analysis and bond valence sums[8,9].

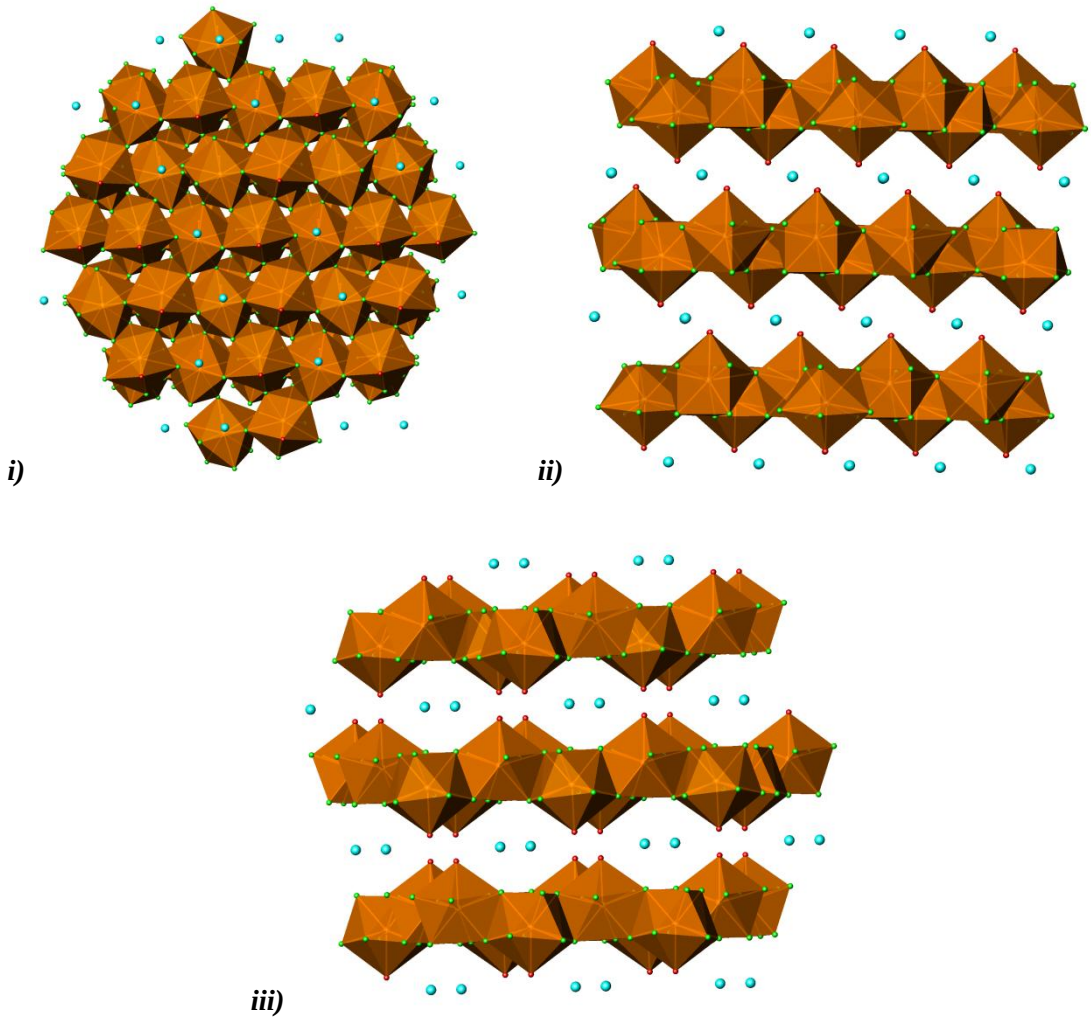

***Figure 3.2**: Structure of **I** viewed down the **i)** a, **ii)** b and **iii)** c-axis. [Key: orange polyhedra - CeF_8X (X = H_2O/F), blue sphere – Cs^+ cation, green sphere – F^- anion, red sphere - H_2O/F]*

The structure of **I** (Fig. 3.2) consists of layers of cerium-centred polyhedra, CeF_8X (X = F/H_2O) with 8 bridging anions and one terminal unit, denoted X, that points into the channels containing the caesium cations. The orientation of the terminal X alternates in adjacent cerium-centred polyhedra, and has a similar bond length with cerium (2.28 Å) to the other bonding anions (average bond lengths to Ce = 2.30(5) Å). Bond valence (BV) calculations (Table 3.3) illustrated that the anions attached to the cerium polyhedra lacked electron density and were assumed to be monovalent anions. The BV values were marginally lower when the sites were assumed to be fluoride ions, and the ions assumed to exist at each site are shown in Table 3.3.

Table 3.3: *Bond lengths and bond valence calculations for O/F anions within cerium polyhedra of* ***I***

Atoms	Bond	Ce-F/O bond length (Å)	υ_{ij}	Total υ_{ij}
F1	F1-Ce1	2.24(4)	0.51	0.77
	F1-Ce1	2.41(4)	0.26	
F2	F2-Ce1	2.29(5)	0.46	0.90
	F2-Ce1	2.30(5)	0.44	
F3	F3-Ce1	2.27(4)	0.47	0.93
	F3-Ce1	2.29(4)	0.45	
F4	F4-Ce1	2.26(4)	0.49	0.87
	F4-Ce1	2.35(4)	0.38	
O1/F5	O1-Ce1	2.28(6)	0.51	0.51

A lack of electron density was observed at the O1 site (BV at site if ion is O = 0.51; F = 0.47) compared with the other ions within the cerium polyhedra that had average bond valences of 0.88(6). The much lowered bond valence suggested the need for extra electron density in the form of an H_2O molecule at this site, rather than an OH/F anion. In order for the structure to charge balance the terminal O1 unit is thought to alternate between a H_2O molecule and an F^- anion, which was investigated *via* further techniques such as IR. The O1/F5 site has been split within the single crystal refinement with a shared occupancy of fluorine and oxygen, thus becoming O1 and F5 within the data tables.

Table 3.4: *Bond lengths and bond valence values for Ce within* ***I***

Atoms	Ce-O/F bond length (Å)	Ce-O/F Bond Valence
F1	2.25(4)	0.51
F1	2.41(4)	0.33
F2	2.28(4)	0.46
F2	2.30(4)	0.43
F3	2.27(4)	0.48
F3	2.29(4)	0.45
F4	2.26(4)	0.49
F4	2.35(4)	0.38
O1/F5	2.28(6)	0.5
Total		**4.03**

Elemental analysis was completed on single crystals of compound **I**. The presence of Ce, Cs, O and F were found within the crystals. The approximate elemental contents were 16 % Ce, 8 % Cs, 6 % O and 71 % F (see Appendix A.3.2). These proportions show us that the assumed molecular formula is not dissimilar to the elemental content, having in the region of 1Cs:2Ce:1O:9F. It also identified oxygen anions within the material, in agreement with F and H_2O at the O1/F5 site.

Hydrogen bonds were assumed to exist along the vector associated with the terminal O1/F5 (deduced to be H_2O/F) sites, even though the hydrogen atoms could not be placed within the SXD refinement. The O1/F5 sites pointed toward one another across the channels of **I** and are close enough to suggest such bonding (Fig. 3.3). The average donor-acceptor length between the terminal sites is 2.66 Å. If present this bonding creates hydrogen bonded channels within the structure of **I** (Fig. 3.3.*ii*), with the caesium cations then trapped within these donor-acceptor bonded tunnels. The channels are approximately 7.16 Å wide by 6.35 Å long, large enough to accommodate caesium cations.

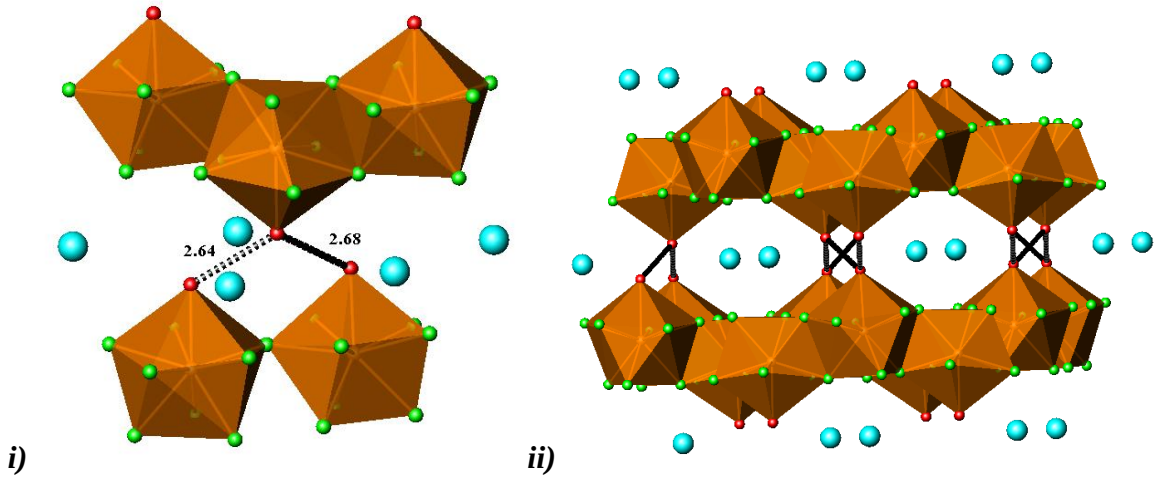

***Figure 3.3**: Hydrogen bonded tunnels (black dotted lines) within structure **I** [lengths in Å]*

The structure of **I** was comprised of distorted nine-coordinate, CeF_8X (*X*= H_2O, F) edge-sharing polyhedra, linked in chains observed down the *b* and the *c*-axes (Fig. 3.2.*ii* and 3.2.*iii*). The Cs^+ cations were found within the channels running parallel to the *b* and *c*-axis, between the cerium chains. The nine-coordinate polyhedra are distorted, which compensates for the mixture of mono and divalent anions and the bond lengths of Ce-O/F that vary from 2.2-2.4 Å.

Bridging bonding was observed between the cerium centres and eight of the fluoride ions within the polyhedral unit, which produced edge-sharing of the polyhedra *via* Ce-F-Ce connectivity's. Attempts to synthesise analogues of this compound with other Group 1 and 2 ions were unsuccessful, which indicated that the formation of this structure is dependent upon the presence and size of the large caesium cations within the channels.

TGA analysis (Fig. 3.4) showed an initial mass loss between 211-266 °C. Calculations have shown a mass loss approximately equivalent to half a H_2O molecule per formula unit. There was a continued loss of mass after this initial point until 535 °C was reached, which contributed to a total loss of 8 % of the structures mass. This was believed to be a result of the continued loss of the terminal fluorine and H_2O molecules within structure **I**. From roughly 535 °C onwards a sharp decline in mass was observed, attributed to the ongoing decomposition of the crystal, no longer stabilised *via* the hydrogen bonding between the chains.

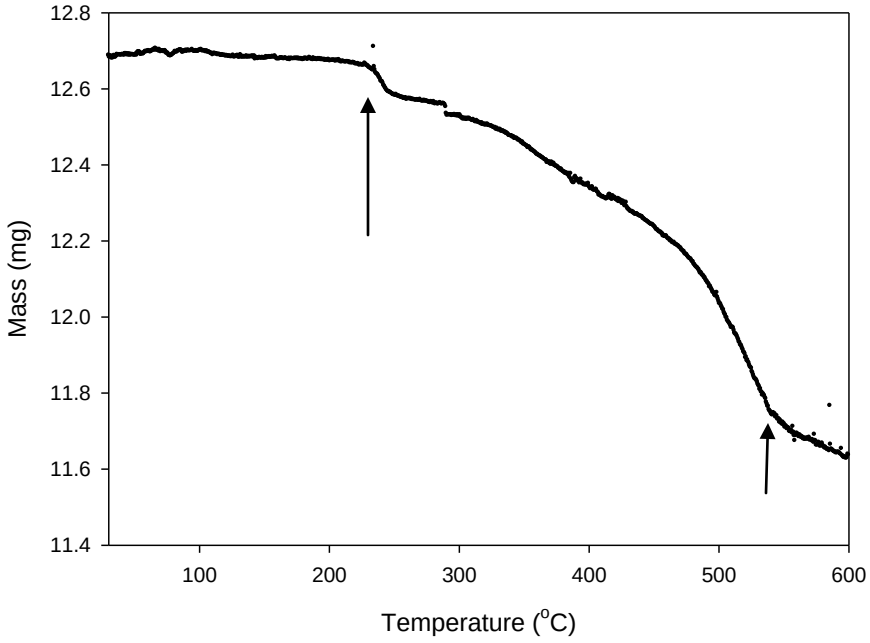

***Figure 3.4**: Mass vs. temperature graph for **I** (mass losses indicated by arrows)*

IR analysis showed the presence of water within the sample, and showed bands at 3434.6 and 1384.8 cm^{-1} (see Appendix A.3.3), linked to the stretching and bending regions of water molecules, which highlighted that this molecule was present within the structure of **I**.

3.2 Compound II: Hydrated Cerium Fluoro Arsenate $[(NH_4)_5(H_2O)_2][Ce^{IV}_4(AsO_4)_6(H_2O)F_3]$

3.2.1 Synthesis

Single crystals of both $[(NH_4)_5(H_2O)_2][Ce^{IV}_4(AsO_4)_6(H_2O)F_3]$ (**II**) and $NH_4Ce^{IV}F_2(AsO_4)$ (**V**) were obtained from a single hydrothermal reaction. CeF_4 (0.2 g, 0.09 mmol, 99.9% Aldrich) and $NH_4H_2AsO_4$ (0.44 g, 2.77 mmol, 99 % Aldrich) were dissolved individually in 6 mL of H_2O, and the two solutions mixed. The pH of the liquid was altered to 6.3 using NH_3 solution (35 %), and the reaction was transferred to a 23 mL Teflon-lined Parr autoclave. The autoclave was heated at 175 °C for 5 days and then cooled slowly to room temperature. The solid filtrate was filtered, washed with warm water and left to dry in air at 80 °C for 3 hours.

3.2.2 Results and Discussion

Structure **II** formed as long thick colourless needles that can be seen in Figure 3.5 below. The crystals were isolated under a polarising microscope and the structural data for this compound can be seen in Tables 3.5 below and A.3.4 in the Appendix.

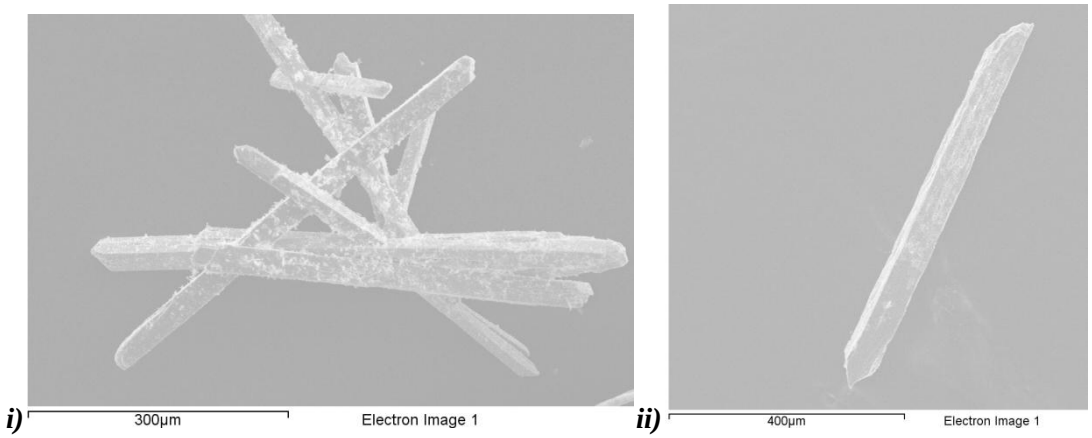

Figure 3.5: *SEM images of* ***i)*** *grouped and* ***ii)*** *single crystals of* $[(NH_4)_5(H_2O)_2][Ce^{IV}_4(AsO_4)_6(H_2O)F_3]$

***Table 3.5**: Details of single crystal data collection for $[(NH_4)_5(H_2O)_2][Ce^{IV}_4(AsO_4)_6(H_2O)F_3]$(**II**)*

Molecular Formula	**$[(NH_4)_5(H_2O)_2][Ce^{IV}_4(AsO_4)_6(H_2O)F_3]$**
Formula Weight (g)	1595.26
Crystal Appearance	Thick colourless needles
Crystal Size (mm)	0.1 x 0.1 x 0.5
Crystal System	Triclinic
Space Group	$P\bar{1}$
Lattice Parameters	a = 9.3894(3) Å, α = 91.234(2)°
	b = 9.5285(3) Å, β = 104.024(2)°
	c = 18.4963(5) Å, γ = 114.293(2)°
V (Å^3)	1449.51(8)
Z	2
Temperature (K)	120
Theta range (°)	3-25.03
Calculated density (mg/m^3)	3.655
Wavelength (Å)	Mo *K*α (λ = 0.71073)
Number of Reflections Measured	Total – 30092, Unique - 5106
R_1 [$I>2\sigma(I)$][a]	0.0291
***R*1(all data)**	0.0330
wR_2	0.0829
Goodness of fit indicator	1.192

Compound **II** crystallised as thick colourless needles (Fig. 3.5) and was the minor product in the synthesis at this reaction pH (the major product being compound **V)**. Initial refinements on the structure of **II** showed four distinct eight-coordinate Ce polyhedra that had one terminal site. BV calculations (based on either O^{2-} or F^- on each anion site) were completed on the terminal ion sites (eventually assigned as F1, F2, F3 and O1), which were shown to have similar low bond valence values (BV (O) = F1 - 0.65, F2 - 0.54, F3 - 0.62; BV (F) = F1 - 0.59, F2 - 0.49, F3 - 0.57) as anticipated for monovalent rather than divalent ions. The BV values using R_{ij} for F^- are

significantly below unity as these ions exhibited hydrogen bonding with the ammonia cations and water molecules (Table 3.6). The exceptionally long bond length for the final terminal ion O1 (Ce-O = 2.56 Å) and much lower bond valence value in comparison to other terminal sites (BV (O) = 0.24; BV (F) = 0.22), suggested that this anion is different from F1, F2 and F3, and likely to be a water molecule (although hydrogen could not be located as part of the SXD structure determination).

Table 3.6: *Bond lengths and bond valence calculations for O/F anions within the cerium and arsenate polyhedra of* $[(NH_4)_5(H_2O)_2][Ce^{IV}{}_4(AsO_4)_6(H_2O)F_3]$ ***(II)***

Atoms	Ce-O/F bond	As-O bond	Ce-O/F bond length (Å)	As-O bond length (Å)	υ_{ij} Ce-O/F	υ_{ij} As-O	Total υ_{ij}
O11	Ce1-O11	As1-O11	2.31(4)	1.69(4)	0.47	1.23	1.7
O12	Ce3-O12	As1-O12	2.30(5)	1.69(4)	0.48	1.23	1.71
O13	Ce4-O13	As1-O13	2.18(4)	1.69(4)	0.66	1.23	1.89
O14	Ce3-O14	As1-O14	2.30(5)	1.69(4)	0.48	1.23	1.71
O21	Ce4-O21	As2-O21	2.35(4)	1.70(4)	0.42	1.20	1.62
O22	Ce2-O22	As2-O22	2.24(4)	1.69(4)	0.56	1.29	1.85
O23	Ce1-O23	As2-O23	2.28(4)	1.68(4)	0.51	1.27	1.78
O24	Ce2-O24	As2-O24	2.17(4)	1.70(4)	0.68	1.20	1.88
O31	Ce1-O31	As3-O31	2.38(4)	1.68(4)	0.39	1.27	1.92
	Ce4-O31		2.52(4)		0.26		
O32	Ce4-O32	As3-O32	2.41(4)	1.68(5)	0.36	1.27	1.63
O33	Ce2-O33	As3-O32	2.43(4)	1.68(4)	0.34	1.27	1.61
O34	Ce2-O34	As3-O34	2.33(4)	1.69(4)	0.44	1.29	2.03
	Ce2-O34		2.47(4)		0.30		
O41	Ce4-O41	As4-O41	2.43(4)	1.68(4)	0.34	1.27	1.87
	Ce1-O41		2.52(4)		0.26		
O42	Ce1-O42	As4-O42	2.45(4)	1.69(4)	0.32	1.29	1.61
O43	Ce3-O43	As4-O43	2.45(4)	1.69(4)	0.32	1.29	1.61
O44	Ce3-O44	As4-O44	2.40(4)	1.68(4)	0.37	1.27	1.92
	Ce3-O44		2.50(4)		0.28		
O51	Ce4-O51	As5-O51	2.28(4)	1.69(5)	0.51	1.29	1.8
O52	Ce3-O52	As5-O52	2.19(4)	1.69(4)	0.65	1.29	1.94
O53	Ce3-O53	As5-O53	2.39(4)	1.69(4)	0.38	1.29	1.67
O54	Ce1-O54	As5-O54	2.30(5)	1.69(4)	0.48	1.29	1.78
O61	Ce1-O61	As6-O61	2.20(4)	1.69(4)	0.63	1.29	1.92
O62	Ce2-O62	As6-O62	2.29(4)	1.70(4)	0.49	1.20	1.69
O63	Ce4-O63	As6-O63	2.38(4)	1.68(4)	0.39	1.27	1.66
O64	Ce2-O64	As6-O64	2.30(4)	1.70(4)	0.48	1.20	1.68
O1	Ce2-O1	n/a	2.56(4)	n/a	0.24	n/a	0.24
F1	Ce4-F1	n/a	2.19(4)	n/a	0.59	n/a	0.59
F2	Ce1-F2	n/a	2.25(4)	n/a	0.50	n/a	0.50
F3	Ce3-F3	n/a	2.20(4)	n/a	0.57	n/a	0.57

EDX analysis showed the presence of Ce, As, F and O within compound **II** and the determined percentages of Ce (21.4%) and F (16.8%) (see Appendix A.3.5) were in a ratio of Ce1.28:F1.0. These values were in agreement with the refined structure of **II** (ratio Ce1.33:F1). The overall framework stoichiometry with this anion site assignment is thus $\mathbf{[}Ce^{IV}{}_4(AsO_4)_6(H_2O)F_3\mathbf{]}^{5-}$. Seven non- framework species were located and were assigned as 5 x N (NH_4^+) and 2 x O (H_2O) in order to charge balance the framework. The hydrogen ions could not be isolated *via* SXD and due to the mixed nature of the reaction product it was not possible to use techniques such as neutron powder diffraction to isolate these positions.

The structure of **II** is a three-dimensional framework consisting of four distinct distorted eight-coordinate cerium-centred polyhedra (1 x CeO_7OH_2 and 3 x CeO_7F), arsenic-centred AsO_4 tetrahedra, with large channels that house NH_4^+ cations and H_2O molecules (Fig. 3.6). Five corner sharing AsO_4 tetrahedra bond to each cerium polyhedron at the oxygen sites, and these arsenic units are fully coordinated to the framework.

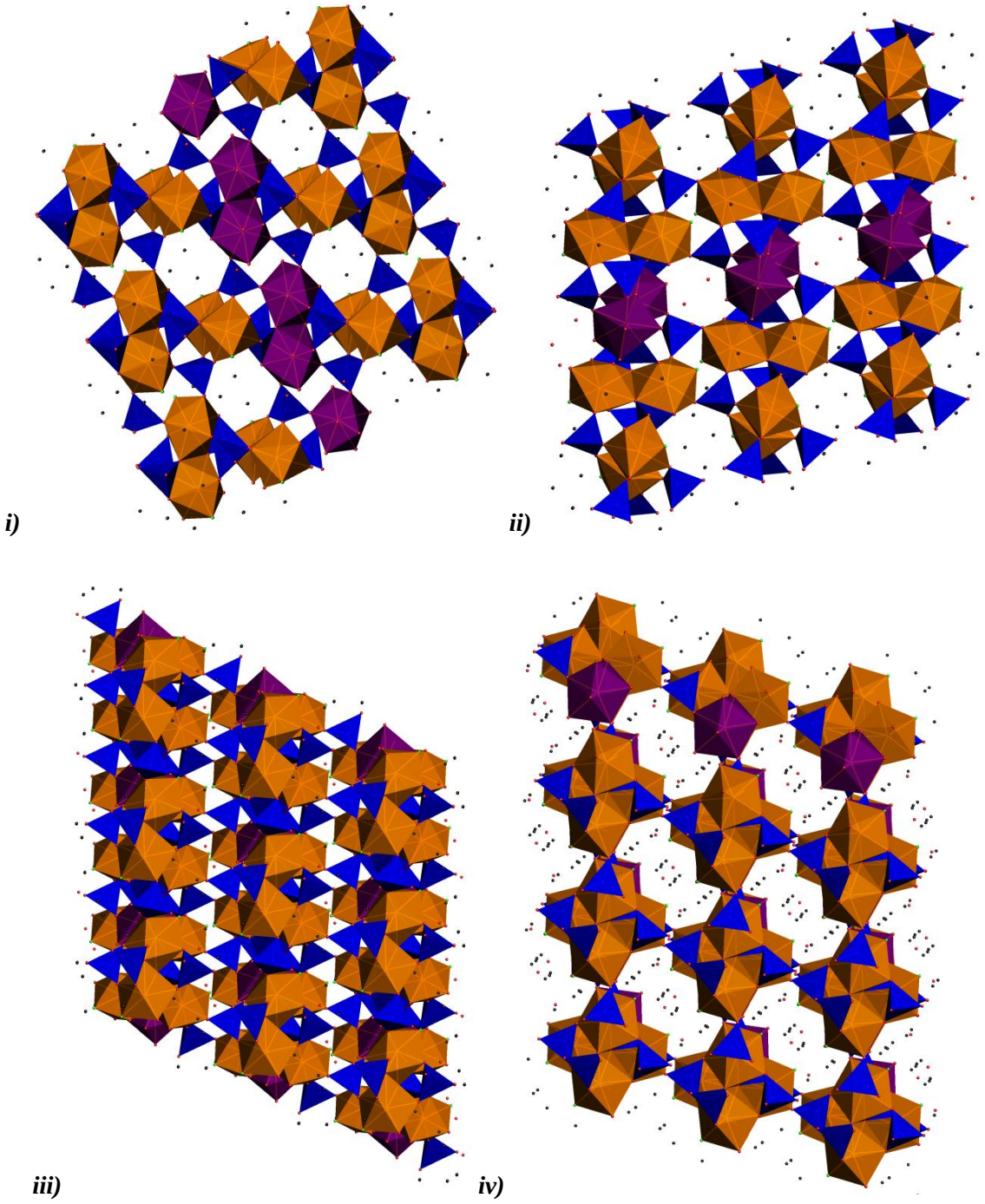

Figure 3.6: *Structure of* ***II*** *viewed down the* ***i)*** *a,* ***ii)*** *b,* ***iii)*** *c-axis, and* ***iv)*** *through the channels. [Key: orange – CeO_7F polyhedra, purple – CeO_8 polyhedra, blue – AsO_4 tetrahedra, red – H_2O molecule, black – NH_4^+ cation]*

The cerium polyhedra exhibited bridging edge-sharing bonding with one another. Ce2 (CeO_7OH_2) bridged to a further Ce2; Ce3 (CeO_7F) bridged to an alternative Ce3, and Ce4 bridged to Ce1 (both CeO_7F). The edge-sharing bonding occurred at the oxygen sites within the two polyhedra, causing this bonding type. The remaining terminal site within the polyhedron is a fluorine ion or water molecule that points into the channels of the framework. The four terminal atoms (F1, F2, F3, and O1) are orientated so that the Ce-F/O vector points towards the centre of the channels.

Four of the oxygen ions within the cerium polyhedra (O31, O34, O41 and O44) (Fig. 3.7) are triply bridging once to an arsenate ion, and twice to two cerium cations; this bonding motif is also found in compounds **III** and **IV** discussed later in this chapter.

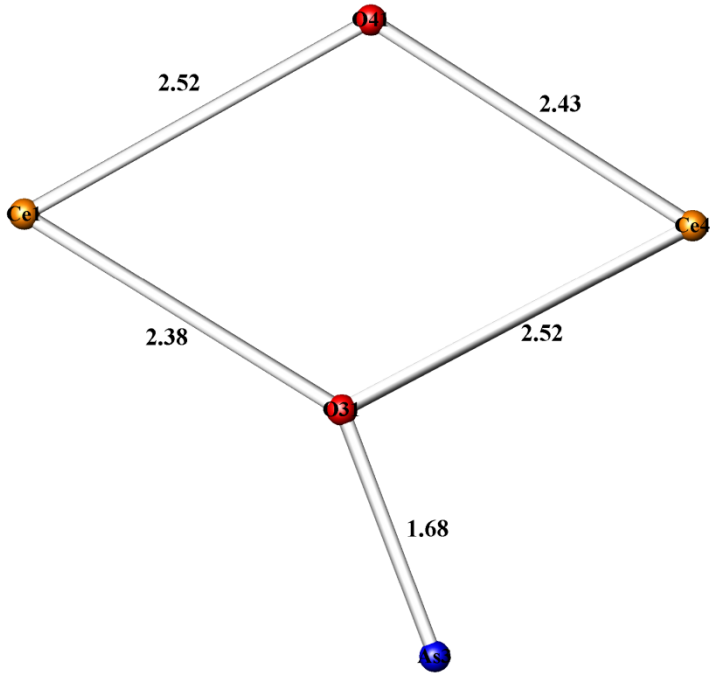

Figure 3.7: *Three-coordinate bonding between O31 and Ce1, Ce4 and As3 (lengths in Å)*

The cavities observed within compound **II** are approximately 12 Å long by 6 Å wide (at their narrowest point). The cerium polyhedra exhibit two types of edge-sharing bonding *via* Ce-O-Ce and Ce-O-As bridging bonds.

Table 3.7: *Bond lengths and bond valence values for Ce within* ***II***

Atoms	Ce-O/F bond length (Å)	Ce-O/F Bond Valence
Ce1 – O11	2.31(4)	0.47
Ce1 – O23	2.28(4)	0.5
Ce1 – O31	2.38(4)	0.38
Ce1 – O41	2.52(4)	0.26
Ce1 – O42	2.45(4)	0.32
Ce1 – O54	2.3(4)	0.49
Ce1 – O61	2.2(4)	0.63
Ce1 – F2	2.25(4)	0.5
Total		**3.55**
Ce2 – O1	2.56(5)	0.24
Ce2 – O22	2.25(4)	0.55
Ce2 – O24	2.17(4)	0.68
Ce2 – O33	2.43(4)	0.34
Ce2 – O34	2.33(4)	0.44
Ce2 – O34	2.43(4)	0.34
Ce2 – O62	2.3(4)	0.48
Ce2 – O64	2.3(4)	0.48
Total		**3.55**
Ce3 – O12	2.3(5)	0.48
Ce3 – O14	2.3(5)	0.48
Ce3 – O43	2.45(4)	0.32
Ce3 – O44	2.40(5)	0.37
Ce3 – O44	2.5(4)	0.28
Ce3 – O52	2.19(4)	0.65
Ce3 – O53	2.39(4)	0.38
Ce3 – F3	2.2(4)	0.57
Total		**3.52**
Ce4 – O13	2.18(4)	0.66
Ce4 – O21	2.35(5)	0.42
Ce4 – O31	2.52(4)	0.26
Ce4 – O32	2.41(4)	0.36
Ce4 – O41	2.43(4)	0.34
Ce4 – O51	2.28(4)	0.51
Ce4 – O63	2.48(4)	0.3
Ce4 – F1	2.19(4)	0.6
Total		**3.43**

The bond valence values for cerium within compound **II** are all around 3.5 (Table 3.7). This suggests that the cerium has moved away from the ideal +4 oxidation state. However, these figures are still closer to 4 than 3, which suggested +4 is the most likely form of cerium. Studies could be performed to clarify this assumption, but this was beyond the scope of this study.

The four distinct eight-coordinate cerium polyhedra within compound **II** are shown in Figure 3.8. The bond lengths vary greatly within the polyhedra, a result of the mixed mono and

divalent nature of the bonding. The Ce-F bond lengths observed in **II** are on average shorter than the observed Ce-O bond lengths (Ce-F = 2.21(3) Å; Ce-O = 2.35(10) Å (Fig. 3.8)), compared to their expected values (Ce-O = 2.49 Å, Ce-F = 2.47 Å). The deviation of these bond lengths from their expected values results in distortion of the polyhedra, and a lower than expected bond valence for cerium (Table 3.7).

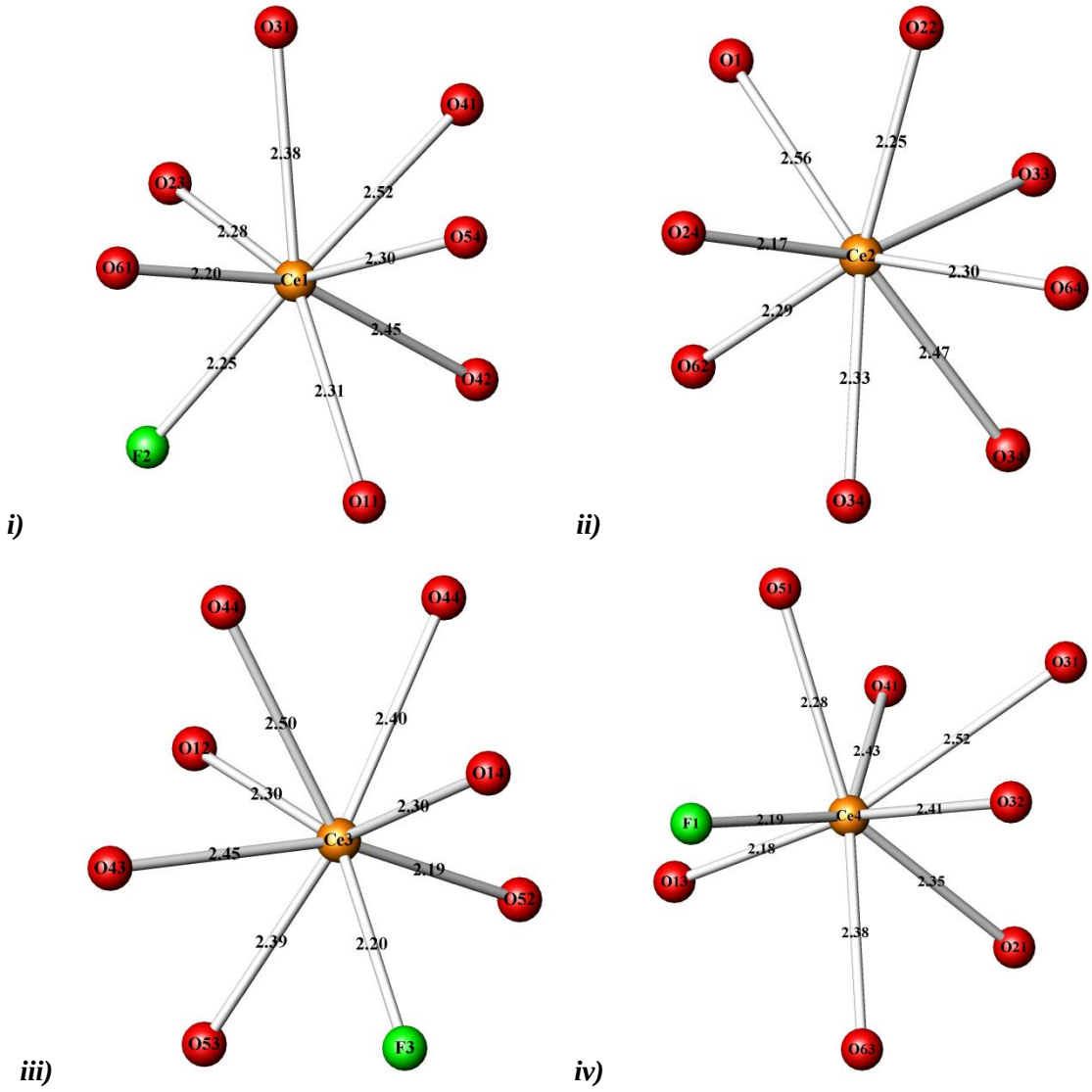

Figure 3.8: *Diagrams of* ***i)*** *Ce1,****ii)*** *Ce2,* ***iii)*** *Ce3 and* ***iv)*** *Ce4 bonding to oxygen and fluorine anions (lengths in Å)*

Hydrogen bonding is present within the channels between the NH_4^+ cations, H_2O molecules and the terminal fluoride ions. The average F---HN donor-acceptor distance is 2.76(3) Å, and F---HO 2.86(4) Å. These hydrogen bonding distances are assumed to exist along the vector associated with the F and N ions as the hydrogen ions could not be located in the SXD refinement.

Microscope IR analysis of a single crystal of **II** indicated high levels of NH_4^+ within the system (strong bands observed at 3211 and 1441 cm^{-1} associated with the NH_4^+ N-H stretches and deformations). Peaks associated with H_2O molecules were not clear as a consequence of the quantities of NH_4^+ that were evident from this method. The band at 3211 cm^{-1} is so large that neither the sharp peak associated with NH_4^+ cations, nor the broad peak of a H_2O molecule were obvious. It is likely that these water peaks are beneath this large peak. Unfortunately, thermal analysis, which could have supported the assumption, was not possible owing to the low product quantities and mixed nature of the reaction products.

3.3 Compound III: Fluorinated Cerium Arsenate - $Ce^{IV}(AsO_4)F$

3.3.1 Synthesis

$Ce^{IV}(AsO_4)F$ (**III**), and $Ce^{IV}(AsO_4)F(H_2O)$ (**IV**) were obtained from a single hydrothermal reaction; CeF_4 (0.1 g, 0.46 mmol, 99.9% Aldrich) and H_3AsO_4 (0.196 g, 1.38 mmol, 75% wt. BDP chemicals) were dissolved in H_2O (11 mL). RbOH solution (50 % in water, 0.235 g, 2.31 mmol, Aldrich) was added and the solution stirred for 30 minutes. The mixture was then transferred to a 23 mL Teflon-lined Parr autoclave and heated at 140 °C for 14 days. The autoclave was allowed to cool slowly to room temperature, and the solid product removed from the solution by filtration, washed with warm water and left to dry in air at 80 °C for 3 hours.

3.3.2 Results and Discussion

Compound **III** crystallises in the orthorhombic space group *Pnma* as rod shaped crystals (Fig. 3.9). The crystallographic details can be found in Table 3.8, and the atomic coordinates can be found in the Appendix, A.3.6.

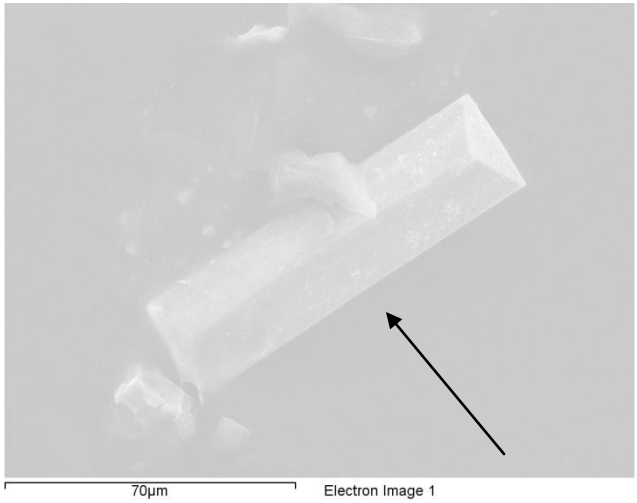

Figure 3.9: *SEM image of rod shaped $Ce^{IV}[AsO_4]F$ crystals (arrow denotes crystal)*

***Table 3.8**: Details of single crystal data collection for $Ce^{IV}[AsO_4]F$ (**IV**)*

Molecular Formula	**$Ce^{IV}[AsO_4]F$**
Formula Weight (g)	297.805
Crystal Appearance	Colourless rod
Crystal Size (mm)	0.2 x 0.2 x 0.2
Crystal System	Orthorhombic
Space Group	*Pnma*
Lattice Parameters	a = 8.6572(4) Å, α = 90°
	b = 7.0511(3) Å, β = 90°
	c = 6.5731(3) Å, γ = 90°
V (Å^3)	401.24(3)
Z	4
Temperature (K)	120
Theta range (°)	3.89-27.52
Calculated density (mg/m^3)	4.93
Wavelength (Å)	Mo *K*α (λ = 0.71073)
Number of Reflections Measured	Total – 5482, Unique - 504
R_1 [I>2σ (I)]^a	0.038
R1(all data)	0.045
wR_2	0.082
Goodness of fit indicator	1.157

Bond valence calculations[8,9] were completed on the structure of **III** after initial single crystal refinements, to isolate areas of low valence within the structure. Each anion site was calculated as both oxygen and fluoride anions, to aid the assignment of site occupancy. Table 3.9 depicts the BV values for the anions at each site, according to the sums obtained. BV calculations confirmed the F1 site lacked electron density (BV (O) = 0.98; BV (F) = 0.89), indicating the likely presence of an OH^-/F^- ion. The remaining sites

within compound **III** had BV values typical of a divalent anion (average BV = 1.98(4)), and thus these species were assumed to be oxygen ions.

Table 3.9 *Bond lengths and bond valence calculations for O/F anions within cerium and arsenate polyhedra for Ce[AsO$_4$]F*

Atoms	Ce-O/F bond	As-O bond	Ce-O/F bond length (Å)	As-O bond length (Å)	υ_{ij} Ce-O/F	υ_{ij} As-O	Total υ_{ij}
O1	Ce1-O1	As1-O1	2.26(7)	1.68(4)	0.53	1.27	2.02
	Ce1-O1		2.58(6)		0.22		
O2	Ce1-O2	As1-O2	2.23(9)	1.66(9)	0.58	1.34	1.92
O3	Ce1-O3	As1-O3	2.19(9)	1.66(9)	0.65	1.34	1.99
F1	Ce1-F1	n/a	2.24(7)	n/a	0.52	n/a	0.88
	Ce1-F1		2.35(7)		0.38		

EDX analysis showed the presence of cerium, arsenic, oxygen and fluorine within the single crystals equating roughly to a 1:1:1:4 Ce:As:F:4O ratio (Ce 22.2%; As 18.5%; F 12.4%; O 47.0%; Appendix A.3.8). The presence of fluorine within the EDX analysis indicated that the F1 site, which lacked electron density, was unlikely to house a hydroxide ion, and therefore a fluoride anion was assigned.

The structure of **III** is comprised of a three-dimensional framework containing distorted eight-coordinate, cerium-centred CeO_6F_2 polyhedra and arsenic-centred AsO_4 tetrahedra. Compound **III** is a relatively close-packed structure (Fig. 3.10) with no extra-framework species, channels or cavities. Corner-sharing bonding is observed parallel to the *b*-axis at the oxygen sites between AsO_4 tetrahedra and CeO_6F_2 polyhedra (Fig. 3.10.*ii*).

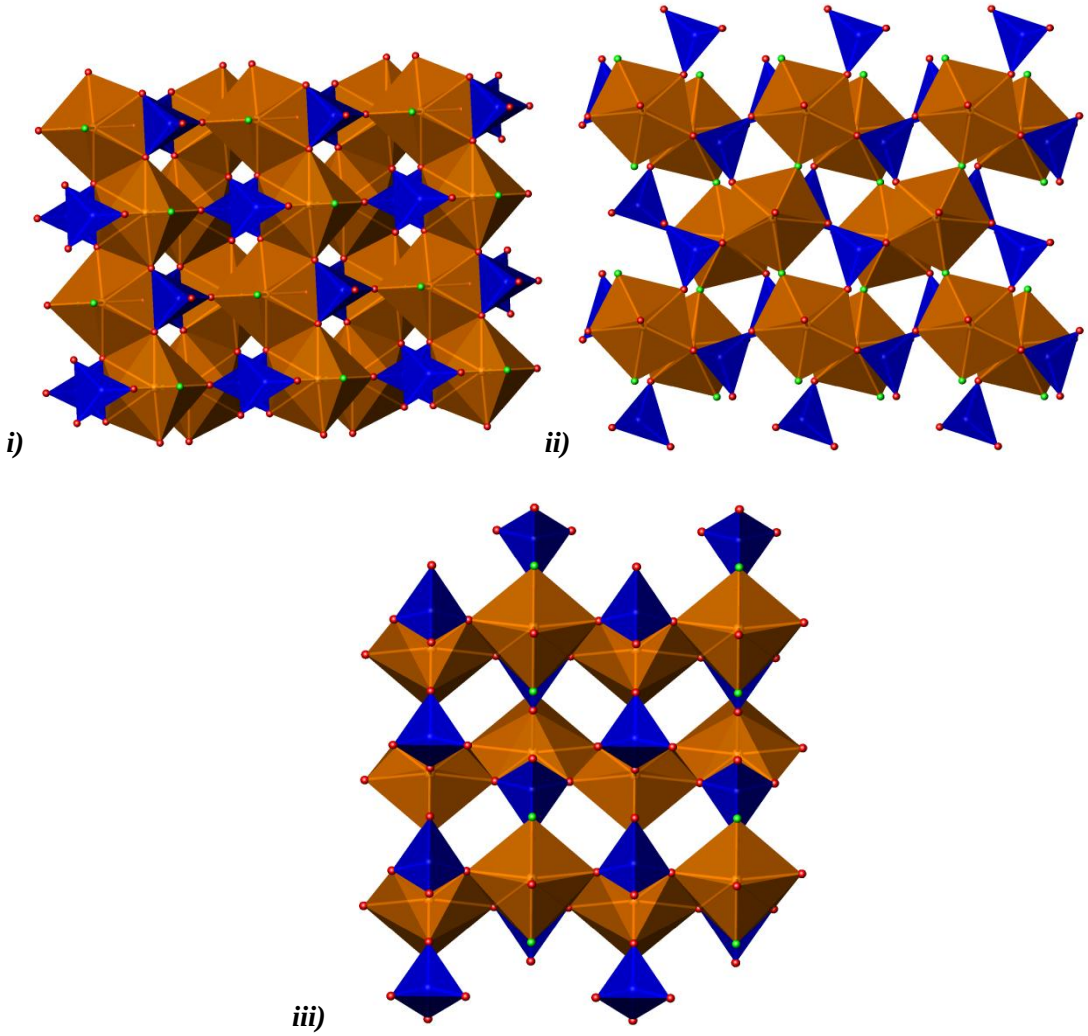

***Figure 3.10**: Structure of **III** viewed down the **i)** a, **ii)** b and **iii)** c-axis. [Key – orange polyhedra - CeO_6F_2, Blue tetrahedra – AsO_4, red sphere – O anions; green sphere – fluorine ions]*

The CeO_6F_2 polyhedra have no terminal anions and link to one another *via* ribbons of edge-sharing Ce-O-Ce bridging bonds (Fig. 3.10.*i/iii*) and corner-sharing Ce-F-Ce bonds (Fig. 3.10.*ii*). The arsenate tetrahedra are linked to the cerium framework through As-O-Ce corner-sharing bonds at all four oxygen sites (Fig. 3.10.*iii*). Figure 3.10.*ii* depicts the zigzag of the polyhedral and tetrahedral chains linked along the *b*-axis through corner sharing oxygen anions. The O1 site is triply bridging, twice to cerium (2.58 Å and 2.26 Å), and once to an arsenic cation (1.70 Å) (Fig 3.11). The remaining oxygen and fluorine atoms all bond to two ions within the crystal structure.

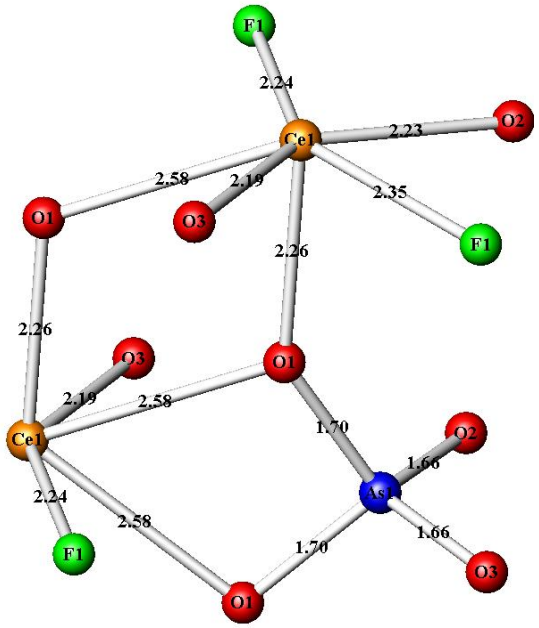

Figure 3.11: *Bonding of O1 atom (lengths in Å)*

Table 3.10: *Bond lengths and bond valence values for Ce within* ***III***

Atoms	Ce-O/F bond length (Å)	Ce-O/F Bond Valence
O1	2.26(7)	0.53
O1	2.26(7)	0.53
O1	2.58(6)	0.23
O1	2.58(6)	0.23
O2	2.23(9)	0.58
O3	2.19(9)	0.65
F1	2.24(7)	0.62
F1	2.35(7)	0.38
Total		**3.64**

Table 3.10 illustrates the bond valence values for the cerium within **III**. The BV for cerium is 3.64, larger than is found in structure **II**. This is anticipated to be a result of the lack of terminal

groups within **III**, therefore having an overall greater electrostatic charge and producing a value that is closer to the ideal of +4.

The cerium polyhedral unit can be observed in Figure 3.12. The presence of fluoride ions within the polyhedron distorted the bond angles and lengths as a result of the mixed mono and divalent anions within the eight-coordinate unit. The mixture of anions has resulted in longer Ce-O bond lengths than expected (maximum 2.58 Å), and some shorter lengths to balance this effect (minimum 2.19 Å). The average Ce-O bond length is 2.32(2) Å, compared to 2.30(6) Å for Ce-F.

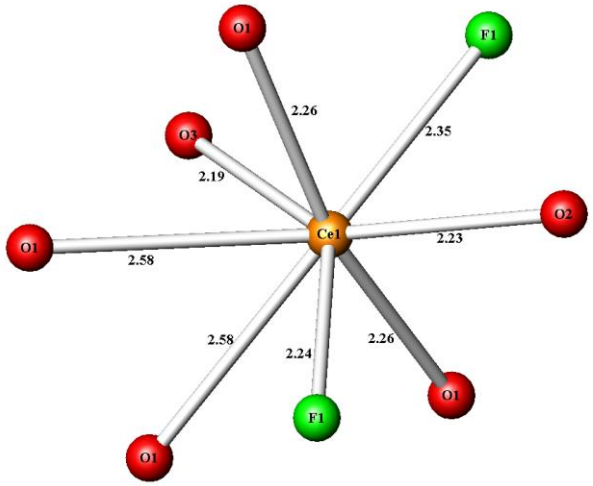

Figure 3.12: *CeO_6F_2 polyhedra (lengths in Å)*

Thermal and IR analysis of compound **III** was not possible due to the mixed nature and size of the crystals obtained. Reactions were repeated that altered the pH, temperature, ratios of starting materials and incubation periods in an attempt to fabricate a phase pure product, but single phase materials were not obtained.

3.4 Compound IV: Fluorinated Cerium Arsenate Hydrate - $Ce^{IV}(AsO_4)F(H_2O)$

3.4.1 Synthesis

Compound **IV** was synthesised in the same reaction vessel as **III,** refer to Section 3.3.1 for the synthetic conditions.

3.4.2 Results and Discussion

The crystallographic data for compound **IV** can be found in Table 3.11, and the atomic coordinates in the Appendix (section A.3.9). SEM images were collected for the diamond shaped crystals (Fig. 3.13).

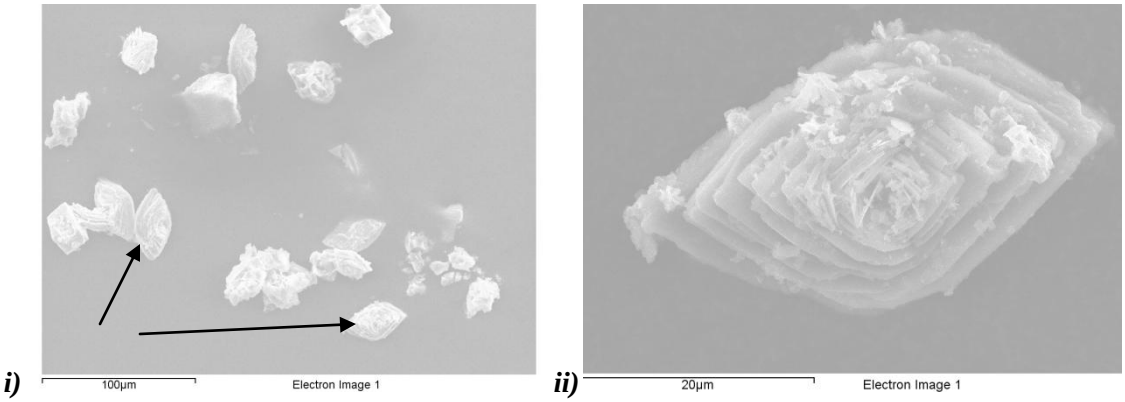

Figure 3.13: *SEM image of* ***i)*** *grouped and* ***ii)*** *single crystals (depicting inter-grown crystals) of* $Ce^{IV}[AsO_4][H_2O]F$

Compound **IV** crystallised in the monoclinic, $P2_1/n$ space group, with a diamond-shaped crystal morphology. Each 'single' crystal was in fact composed of many inter-grown crystals, which can be observed in the SEM image (Fig. 3.13.*ii*). The powder and crystal mix found on top of the crystals could not be removed to produce a truly single crystal, and this intergrowth was only observed under the more powerful SEM machine, resulting in a higher R_1 value than hoped for this material. In previous instances it was possible to crack the crystals in order to reduce the size or

remove solid powder from them in silicone oil to eradicate twinning problems. The crystals produced in this reaction were very small and the issues associated with their morphologies were only revealed after analysis under the SEM microscope. Alternative reaction conditions were attempted in the production of compounds **III** and **IV** to improve their crystal morphology, but these endeavours did not alter their physical forms and the problems associated with them.

Table 3.11: *Details of single crystal data collection for $Ce^{IV}[AsO_4][H_2O]F$ (**IV**)*

Molecular Formula	**$Ce^{IV}[AsO_4][H_2O]F$**
Formula Weight (g)	315.816
Crystal Appearance	Colourless diamond
Crystal Size (mm)	0.02 x 0.02 x 0.02
Crystal System	Monoclinic
Space Group	$P2_1/n$
Lattice Parameters	a = 5.0896(3) Å, α = 90°
	b = 7.5118(5) Å, β = 97.74(4)°
	c = 11.8183(8) Å, γ = 90°
V (Å^3)	447.72(3)
Z	4
Temperature (K)	120
Theta range (°)	3-27.5
Calculated density (mg/m^3)	4.69
Wavelength (Å)	Mo *K*α (λ = 0.71073)
Number of Reflections Measured	Total - 4520, Unique - 785
R_1 [I>2σ (I)]^a	0.071
***R*1(all data)**	0.091
wR_2	0.147
Goodness of fit indicator	1.210

The three-dimensional framework of **IV** contained distorted eight-coordinate cerium-centred polyhedra, within which there was one terminal atom, O1. Bond valence calculations illustrated a lack of electron density at the O1 site regardless of it being assigned as a fluoride or oxygen anion (BV (O) = 0.32, BV (F) = 0.30) (Table 3.12). The exceptionally low BV values are similar to those found for terminal H_2O molecules within structure **II** ((O26) BV – 0.24). The reduction in BV lessened the possibility that this site was populated with a fluoride or hydroxide anions. The Ce1-O1 length (2.46 Å) was longer than the average Ce1-O bond length within the polyhedra (2.34 Å). This accentuated the need for the O1 site to be further away from the centre of the polyhedron, as a result of its size. These factors indicated that O1 was likely to be a weakly bound terminal H_2O molecule rather than an F^- or OH^- anion.

Table 3.12: *Bond lengths and bond valence calculations for O/F anions within cerium and arsenate polyhedra for* ***IV***

Atoms	Ce-O/F bond	As-O bond	Ce-O/F bond length (Å)	As-O bond length (Å)	υ_{ij} Ce-O/F	υ_{ij} As-O	Total υ_{ij}
O1	Ce1-O1	n/a	2.44(6)	n/a	0.32	n/a	0.32
O2	Ce1-O1	As1-O1	2.29(4)	1.67(6)	0.49	1.30	1.79
O3	Ce1-O3	As1-O3	2.19(6)	1.66(6)	0.65	1.34	1.99
O4	Ce1-O4	As1-O4	2.24(5)	1.70(5)	0.56	1.20	1.76
O5	Ce1-O5	As1-O5	2.39(6)	1.69(6)	0.38	1.23	1.85
	Ce1-O5		2.55(6)		0.24		
F1	Ce1-F1	n/a	2.27(2)	n/a	0.48	n/a	0.83
	Ce1-F1		2.38(2)		0.35		

The F1 site had a lower bond valence (BV (O) = 0.90, BV (F) = 0.82) when compared with the other sites within the polyhedron, except the terminal O1 site, and is more typical of a monovalent ion such as fluoride or a hydroxide anion. EDX analysis established the presence of fluorine within the structure of **IV** (Appendix A.3.10). The percentage elemental content was 20.8% F, 19.2% Ce and 14.3% As O 45.7% within the

crystal analysed. This would indicate that there must be at least one anion within the crystal structure that is a fluorine ion (although this data is qualitative not quantitative), and the most likely place for it to exist would be at the F1 site.

Table 3.13: *Bond lengths and bond valence values for Ce within* ***IV***

Atoms	Ce-O/F bond length (Å)	Ce-O/F Bond Valence
O1	2.45(2)	0.32
O2	2.3(5)	0.48
O3	2.19(6)	0.65
O4	2.25(6)	0.55
O5	2.39(7)	0.38
O5	2.55(6)	0.24
F1	2.27(4)	0.48
F1	2.38(3)	0.35
Total		**3.45**

Table 3.13 illustrates the bond valence at the cerium cation. The BV is lower than anticipated (+4), but this could be a result of the weakly bound water molecule not contributing a large electrostatic contribution. The mixture of mono and divalent anions within the polyhedral unit will also have a large effect on this value, resulting in its deviation from its expected value.

The structure of **IV** consisted of distorted eight-coordinate cerium-centred $CeO_5F_2(OH_2)$ polyhedra and arsenic-centred AsO_4 tetrahedra. The $CeO_5F_2(OH_2)$ polyhedra demonstrated edge-sharing bonding, which resulted from the bridging bonds between Ce1-F1 and Ce1-O6 (Fig. 3.14). This is the only example of mixed fluorine and oxygen bridging bonds within the compounds described in this research project. A short literature review revealed examples of this type of bonding for metals such as vanadium[10] were known, but it is relatively uncommon. In the case of the vanadium examples, the polyhedral units alter from VO_5F and VO_4F rather than the identical $CeO_5F_2(OH_2)$ bridging

polyhedral units observed in structure **IV**. Structures **II** and **III** demonstrated Ce-O-Ce edge-sharing bridging bonds and also Ce-F-Ce in the case of **III**. Structures **I** and **V**, contain Ce-F-Ce edge-sharing bridging bonding. In compound **IV** the bridging bonds were stabilised *via* two elongated (Ce1-O5 – 2.55 Å and Ce1-F1 – 2.39 Å) and two shortened bonds (Ce-O5 = 2.38 Å and Ce-F1 = 2.27 Å). The mixture of fluoride and oxygen ions at these sites was expected to cause the varied bond lengths, which compensated for the varied charges associated with the two anions.

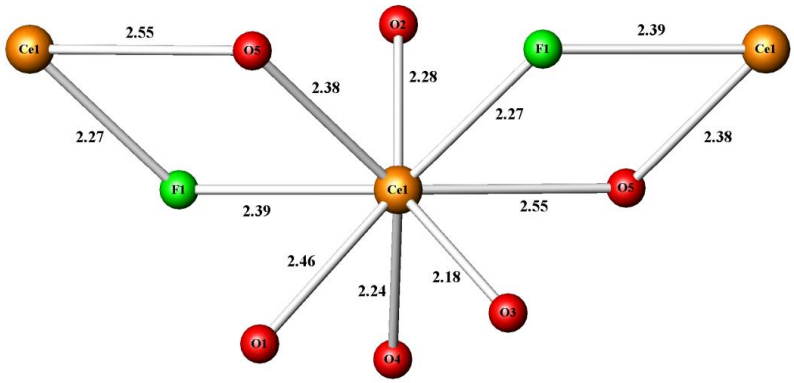

***Figure 3.14**: Bridging bonds between Ce1-F1 and Ce1-O6 (lengths in Å)*

The arsenate tetrahedra were linked to the cerium polyhedra through corner-sharing bonds with oxygen atoms O2, O3, O4, and O5; O5 is triply bridging twice to Ce1 and once to As1 (Fig. 3.15).

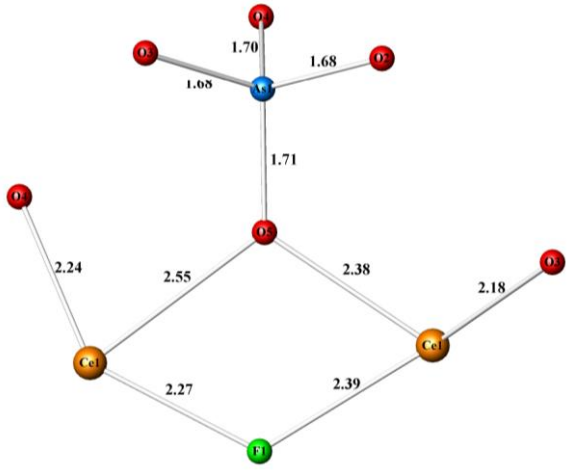

***Figure 3.15:** O6 atom exhibiting three bonds with As1 and Ce1 (twice) (lengths in Å)*

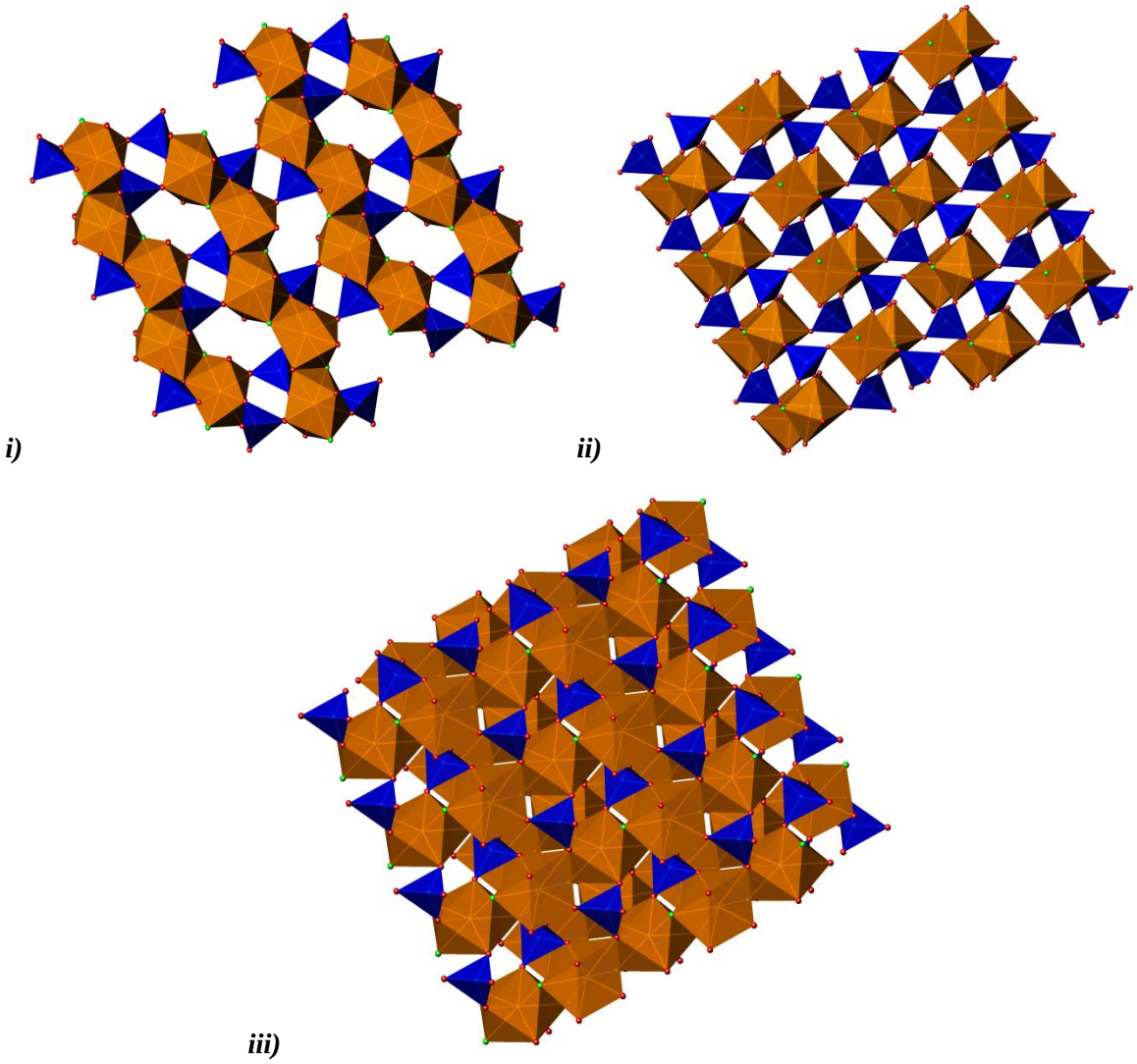

Figure 3.16: *Structure of* ***IV*** *viewed down the* ***i)*** *a-axis,* ***ii)*** *b-axis and* ***iii)*** *c-axis. [Key – orange polyhedra - CeO_6F_2, blue tetrahedra – AsO_4, red sphere – oxygen ion, green sphere – fluorine ion]*

Ribbons of cerium polyhedra were found when the structure was viewed through the *a*-axis, and the distinct layers of arsenate tetrahedra and cerium polyhedra were observed parallel to the *b*-axis (Fig. 3.16.*ii*). The structure of **IV** was found to be closely packed when viewed through the *c*-axis (Fig. 3.16.*iii*), a result of the edge-sharing of the cerium polyhedra. Structure **IV** has narrow channels, observed parallel to the *a*-axis (Fig. 3.16.*i*), into which the terminal H_2O molecules of the $CeO_5F_2(OH_2)$ polyhedra point. These channels (2.9 Å wide by 5.8 Å long) contained no uncoordinated cations or molecules. Weak O(1)---F donor-acceptor bonds (3.11 and 3.19 Å) were

observed in the framework (Fig. 3.17), a result of the terminal $O(1)H_2$ molecules (although hydrogen positions could not be determined *via* SXD) interacting with bridging fluoride anions.

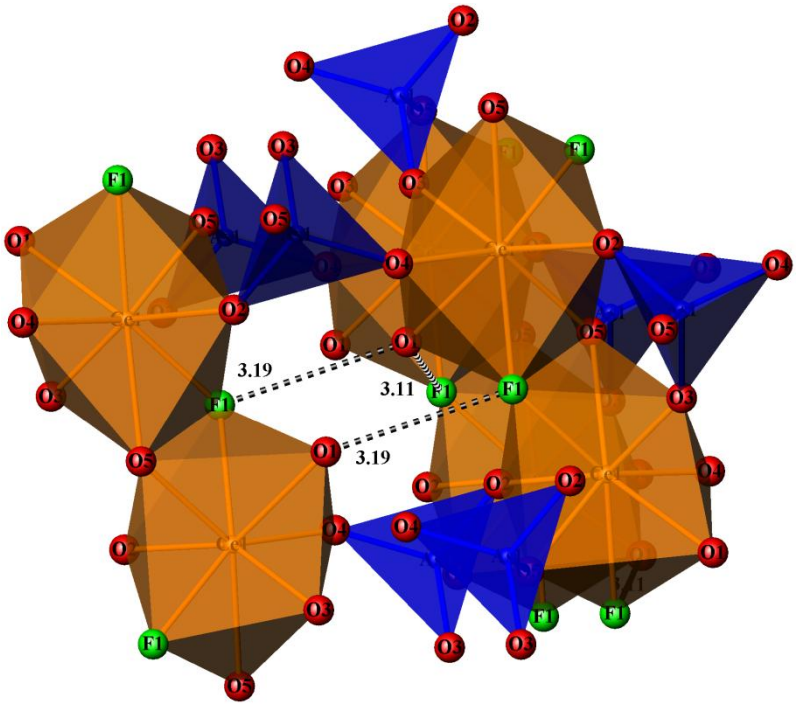

Figure 3.17: *Weak hydrogen bonding present within structure* ***IV*** *(hydrogen bonding - black dotted lines, lengths in Å)*

TGA and IR analyses were not performed on structures **III** and **IV** as they were synthesised as mixtures within the same reaction product. A substantial single phase sample for these analytical techniques was not obtainable despite attempts to alter the synthetic conditions.

3.5 Compound V: Ammonium Cerium Fluoride Arsenate - $[[NH_4]Ce^{IV}F_2[AsO_4]]$

3.5.1. Synthesis

Single crystals of compound **V**, $NH_4Ce^{IV}F_2(AsO_4)$, were obtained from the same hydrothermal synthesis as $[NH_4]_5[H_2O]_2[Ce^{IV}{}_4(AsO_4)_6(H_2O)F_3]$ (see Section 3.2.1 for specific conditions). The reason that this compound did not directly follow **II** within this thesis is that **V** is isostructural to a phosphate compound.

3.5.2 Results and Discussion

Compound **V** formed as large yellow hexagonal sheets crystallising in the monoclinic $P2_1/m$ space group (Fig. 3.18). The formation of **V** required the presence of NH_3 solution within the synthesis method. A single crystal was selected for SXD and details are given in Table 3.14. The atomic coordinates for compound **V** can be seen in the Appendix 3.11.

The crystals formed from this synthesis were exceptionally large. Initial analysis *via* SXD, produced a very large R_1 value even though the diffraction patterns contained what appeared to be perfect diffraction spots. The reason for the high R_1 factor was that the crystals were very large flat hexagonal plates where one axis was substantially smaller than the other two. To counteract this problem the crystal was cracked in half to reduce this difference in size, and as a result the analysis was greatly improved.

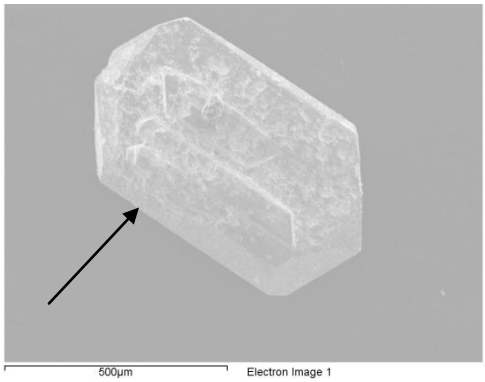

Figure 3.18: *SEM image of $[NH_4][Ce^{IV}F_2(AsO_4)]$ crystals*

Table 3.14: *Details of single crystal data collection for $[NH_4][Ce^{IV}F_2(AsO_4)]$ (**V**)*

Molecular Formula	$[NH_4][Ce^{IV}F_2(AsO_4)]$
Formula Weight (g)	335.08
Crystal Appearance	Yellow hexagonal sheet
Crystal Size (mm)	0.2 x 0.2 x 0.1
Crystal System	Monoclinic
Space Group	$P2_1/m$
Lattice Parameters	a = 6.7758(2) Å, α = 90°
	b = 6.0181(2) Å, β = 113.832(2)°
	c = 7.1315(2) Å, γ = 90°
V (Å^3)	266.009(14)
Z	2
Calculated density (mg/m^3)	4.18
Temperature (K)	120
Theta Range (°)	3.12-33.16
Wavelength (A)	Mo *K*α (λ = 0.71073)
Number of Reflections Measured	Total – 5124, Unique – 1096
R_1 **[*I*>2σ (*I*)]**[a]	0.028
***R*1(all data)**	0.028
wR_2	0.097
Goodness of fit indicator	1.339

Table 3.15: *Unit cell data for cerium fluoro-arsenates and phosphates*

Structure	**a (Å)**	**b (Å)**	**c (Å)**	**α (Å)**	**β (Å)**	**γ (Å)**	**Volume (Å^3)**
$[NH_4]Ce^{IV}F_2(PO_4)$[7]	6.635	5.898	7.071	90	114.149	90	252.47
$[NH_4]Ce^{IV}F_2(AsO_4)$	6.776(2)	6.018(2)	7.132(2)	90	113.832(16)	90	266.01(14)

The unit cell of **V** was found to be isostructural to that of $[NH_4][Ce^{IV}F_2(PO_4)]$ previously reported by Ranbo Yu *et al.*[11], and the crystal data for these two compounds can be seen in Table 3.15 for comparison. The cells are very similar and the novel arsenate compound had an enlarged unit cell, with most lattice lengths increasing in size by around 0.1 Å. The cell volume of the arsenate phosphate is enlarged and a smaller β angle was observed. These factors are all associated with the incorporation of the larger, although structurally similar, arsenic cation.

Table 3.16: *Bond lengths and bond valence calculations for O/F anions within cerium and arsenate polyhedra for* $[NH_4][Ce^{IV}F_2(AsO_4)]$

Atoms	Ce-O/F bond	As-O bond	Ce-O/F bond length (Å)	As-O bond length (Å)	υ_{ij} Ce-O/F	υ_{ij} As-O	Total υ_{ij}
O1	Ce1-O1	As1-O1	2.49(5)	1.69(5)	0.29	1.23	1.52
O2	Ce1-O2	As1-O2	2.17(3)	1.69(3)	0.68	1.23	1.92
O3	Ce1-O3	As1-O3	2.24(4)	1.67(4)	0.56	1.30	1.86
F1	Ce1-F1	n/a	2.33(2)	n/a	0.40	n/a	0.77
	Ce1-F1		2.36(2)		0.37		

The bond valence of compound **V** was calculated to specify the presence of mono and divalent ions within the structure. The results of BV sums (Table 3.16) implied that the proposed F1 site was consistent with a monovalent anion (OH/F) (BV (O) = 0.85, BV (F) = 0.77). The remaining oxygen anions within the structure were consistent with divalent ions, although the O1 site had a marginally lower BV than expected due to an enlarged bond length (2.49 Å) in comparison with other Ce-O bonds. This amplified distance was attributed to the O1 stabilising the structure, as a result of the fluoride ions bridging between the cerium centres. The lower bond valence at the F1 site when considered with EDX data, which emphasized the presence of fluorine within compound **V**, as well as Ce, As and O (Ce - 33.8 %; As – 19.6 %; F – 16.7 %; O – 29.8 %), suggests that the most likely position for the fluoride to reside was at the F1 site.

Table 3.17: *Bond lengths and bond valence values for Ce within* ***V***

Atoms	Ce-O/F bond length (Å)	Ce-O/F Bond Valence
O1	2.49(4)	0.29
O2	2.17(3)	0.68
O2	2.17(3)	0.68
O3	2.24(4)	0.56
F1	2.33(2)	0.40
F1	2.33(2)	0.40
F1	2.36(2)	0.37
F1	2.36(2)	0.37
Total		**3.77**

The calculated bond valence for cerium within the structure of **V** was found to be 3.8 (Table 3.17). This value is close to the anticipated +4 oxidation state of the starting material CeF_4. The presence of mono and divalent anions within the cerium polyhedral unit has resulted in a total BV value that is smaller than anticipated.

The structure of **V** consists of cerium-centred distorted eight-coordinate polyhedra (CeF_4O_4) and arsenic-centred AsO_4 tetrahedral units (Fig. 3.19). The cerium polyhedra are connected *via* edge-sharing bridging fluorine ions and corner-sharing AsO_4 tetrahedra. The arsenate tetrahedra are connected to the oxygen sites within the cerium polyhedra (Ce-O-As) and every oxygen within the AsO_4 unit is bonded to a cerium centre. The average Ce-F bond length is 2.35(2) Å, Ce-O is 2.27(13) Å and As-O is 1.68(9) Å.

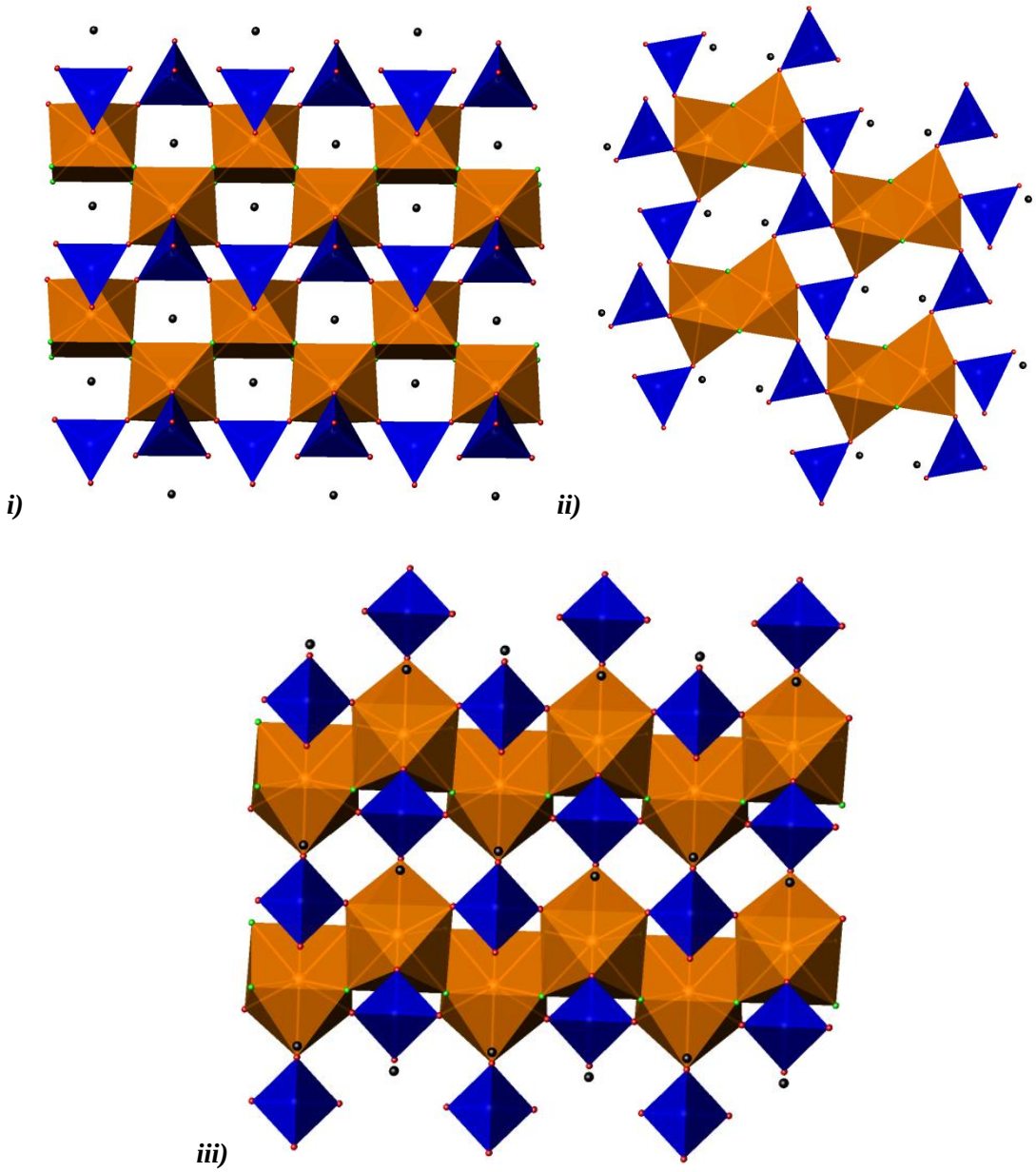

Figure 3.19: *Structure of* ***V*** *viewed down the* ***i)*** *a;* ***ii)*** *b and* ***iii)*** *c-axis. [Key: blue tetrahedra – AsO_4; orange polyhedra – CeO_4F_4, black sphere - NH_4^+ cation; red sphere – oxygen, green sphere - fluorine]*

NH_4^+ cations were located in the channels of **V**, which ran parallel to the *a*-axis (Fig. 3.19.*i*) and charge balance the $[Ce^{IV}F_2(AsO_4)]^-$ framework. Chains formed from the CeO_4F_4 units,

linked through *cis* fluoride ions, run parallel to the *b*-axis (Fig. 3.20). The zigzag of the cerium polyhedra was observed through the *a* and *c*-axes. Layers of AsO_4 tetrahedra were found to separate the edge-sharing $(CeO_4F_4)_2$ units when viewed through the *b*-axis.

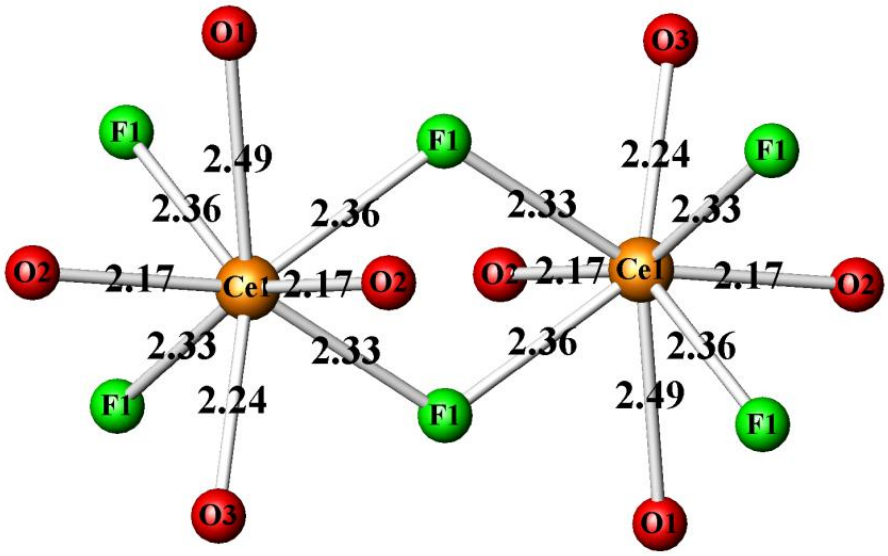

***Figure 3.20**: Bridging fluoride atoms in $[NH_4][Ce^{IV}F_2(AsO_4)]$(lengths in Å)*

TGA analysis (Fig. 3.21) showed that a mass equivalent to one mole of ammonia was lost on heating at above 400 °C, which agreed with the structural formula. This decomposition occurred at a similar temperature to that of the phosphate analogue, where a weight loss was noted between 350-500 °C[7]. This decomposition temperature is consistent with the loss of NH_4^+ rather than H_2O, which is more typically lost at between 150-350 °C from the channels of framework materials.

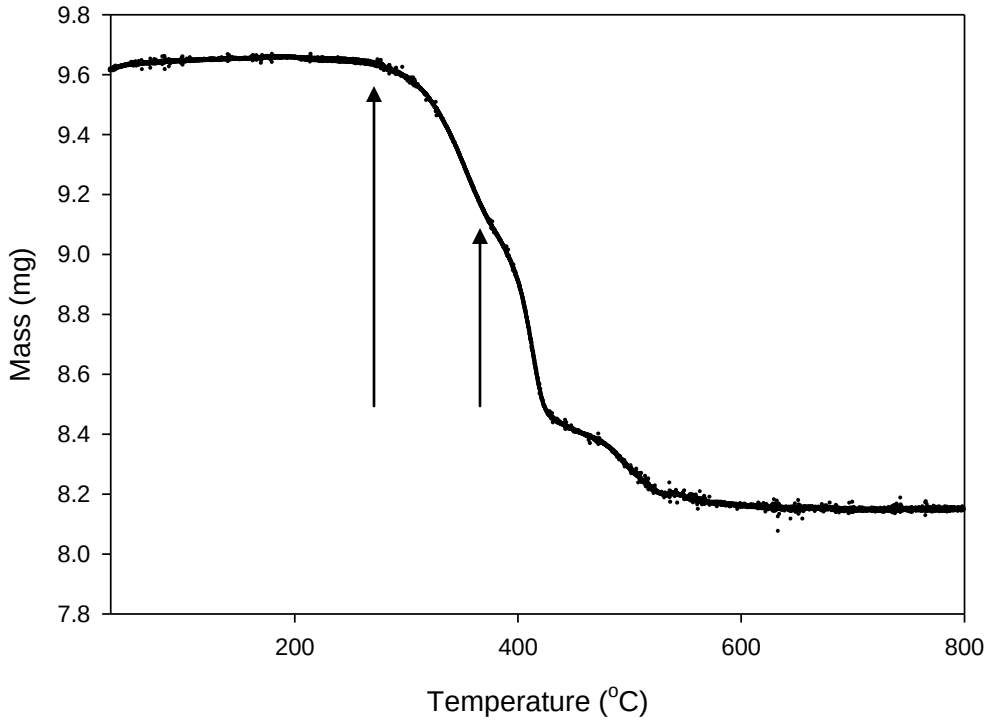

***Figure 3.21**: Mass loss vs. Temperature graph for $[NH_4][Ce^{IV}F_2(AsO_4)]$*

IR analysis confirmed the presence of NH_4^+ cations rather than alternative framework species, peaks were noted in the N-H stretching and deformation regions (3194 and 1416 cm^{-1}), which agreed with TGA analysis.

3.6 Experimental Summary

The production of the five novel cerium fluoride compounds resulted from a number of experimental efforts before suitable reaction conditions were obtained. Attempts are made within this section to discuss the reaction conditions and the reasoning behind the changes that were made at each stage. Table 3.1 in the Introduction houses the reaction and product information for a handful of experiments that were completed. Reactions within the Table are referred to *via* a reaction number (for example, (1)), which identifies conditions and the products obtained.

Solid state synthetic methods for cerium compounds have historically employed the use of starting materials such as CeO_2 and some cerium compounds have formed *via* this method, such as $Ce^{III}AsO_4$[12]. A number of framework structures that are constructed from metal or lanthanide polyhedra and oxotetrahedral units, are produced through solvothermal reactions when the use of a teflon-lined Parr autoclave is employed. This area has previously been fruitful in the production of zeolite and zeotypic structures, and in the search for cerium compounds of this type, which was the justification for the choice of this synthetic method.

Initial research into the chemistry of cerium and its ability to form three-dimensional and layered structures found that a large number of research groups used $Ce(SO_4)_2.xH_2O$ as a starting material. A short literature review into $Ce(SO_4)_2.xH_2O$ and its incorporation into a variety of solvothermal syntheses established that it produced materials that were of research interest such as YU-1 ($H_{25.5}(NH_4)_{10.5}Ce_9O_{27}F_{18}$)[13], $[Ce^{III}(SO_4)_{1.5}(HSO_4)_{0.5}].0.5H_3O$[14] and $NH_4Ce^{IV}F_2(PO_4)$[7]. Early research into the chemistry of cerium frameworks employed this starting material as well as NaF and H_3PO_4. Initial reactions were completed at a variety of temperatures (140, 175 and 200 °C) and these changes did not affect the products formed. Placing all of the reagents into a hydrothermal bomb in equal ratios (6) produced cerium ($Ce(PO_3)_4$) and sodium phosphates ($NaPO_3$). Increasing the fluorine source (NaF) (8) encouraged sodium cerium phosphates to form ($NaCe_2(PO_4)_5$) until a point when the sodium was in excess and $NaPO_3$ was the main product alongside the starting material $Ce(SO_4)_2.xH_2O$. As the amount of phosphate that was included enlarged (7) sodium phosphates formed and the cerium sulphate became unreactive. Increasing the quantity of $Ce(SO_4)_2.xH_2O$ (9), produced different forms of hydrated cerium sulphates and sodium phosphates. These reactions were relatively unsuccessful and so an alternative starting material was sought.

Hydrothermal reactions often employ fluorine in the solution such as HF[6], NaF[7] or NH_4F[15] to act as a mineraliser aiding the reaction mechanism and the formation of single crystals. HF is a dangerous reagent, and so an alternative route which incorporated $Ce^{III}F_3$ was developed to insert a large quantity of fluoride anions into the reaction mixture without the inclusion of other ions such as Na^+. This technique was not one which had been investigated in solvothermal systems and so reference material for reaction processes was unavailable. Initial reactions that involved CeF_3 were completed at 140, 175 and 200 °C using $H_3PO_4/NH_4H_2PO_4$ in water (10). The crystalline product was always the CeF_3 starting material. The solvent was altered to ethanol (11), NH_3 and HCl but CeF_3 was the only product obtained. The introduction of NaF (12) was also applied but CeF_3 was always the result. The unreactivity of CeF_3 was disappointing and so the oxidation state of the cerium was altered through the incorporation of $Ce^{IV}F_4$ to increase its reactivity. CeF_4 reactions produced a large number of yellow powders that often housed small single crystals. Analysis *via* SXD ascertained the powders to be phase pure examples of $(NH_4)CeF_2(PO_4)$[7].

The reactions that involved CeF_4 and a phosphate source only formed single crystals of $(NH_4)CeF_2(PO_4)$. If a powder was produced, known compounds and this stable crystal phase were the favoured reaction products. Varying the reaction solvent produced powders comprised of a variety of cerium and ammonium phosphates (13-16). Increasing the cerium content resulted in the basic $CePO_4$ (24), whereas larger quantities of phosphate resulted in alternative cerium phosphate phases (25). Group 1 and 2 hydroxides were added (20-23) to the solutions in an attempt to produce phases that had the potential for ion exchange by incorporating these cations. The phosphate reactions produced powders where cerium phosphates were found as well as the Group 1 and 2 phosphates. The introduction of arsenic into the same reaction formed the novel compound **I** for CsOH. The remaining reactions formed cerium phosphates and Group 1 and 2 arsenates.

Organic templates were employed (17-19) through a range of reaction temperatures, but powders were always obtained in both the phosphate and arsenate examples. The products included starting materials for the main part, and a few of the templates produced $CePO_4/CeAsO_4$ but their addition seemed to inhibit the reactions rather than producing novel phases.

Overall the arsenate materials were more reactive than the phosphates, as the cerium phosphates that formed were very stable and it was difficult to isolate alternative products through the use of CeF_4. $CePO_4$ powders formed at a rapid rate and often small amounts of precipitate were present before the solution had been placed into the autoclave. The arsenate reactions were solutions within the initial stages, but still some of the more basic $CeAsO_4$ products were the

predominant and stable phase. The addition of organic templates did not prove a successful pathway for the production of interesting single crystals or powders in either the phosphate or arsenate analogues, as starting materials and basic cerium phosphates or arsenates were produced. The inclusion of CeF_4 did not favour the use of organic templates in forming large frameworks. The addition of HF with $Ce(SO_4)$ and organic templates would be a beneficial comparison to observe whether it is the CeF_4 or the cerium systems that do not favour the inclusion of these ions. A number of templates were used; small molecules such as ethylenediamine, and the larger more bulky 1, 10 phenanthroline to observe the effect that size had on the products. The reactions were found to be very specific, and there was a very small window of opportunity to produce the desired phases. There are further opportunities in cerium framework chemistry, as the different synthetic conditions required to form these five cerium arsenate structures have shown. The introduction of CeF_4 has proved a productive pathway for the formation of interesting cerium frameworks.

3.7 Conclusions

Several new cerium fluoride structures have been synthesised and characterised *via* SXD. The hydrothermal method employed CeF_4 as the fluoride ion source, opposed to HF (to undertake the role of a mineraliser) and provided a number of novel frameworks. The volume of fluoride anions within the syntheses, led to its inclusion within the cerium frameworks. Moderating the amount of CeF_4 could produce similar compounds that exclude fluorine, if this was required. This research project was unsuccessful in producing cerium frameworks devoid of fluorine, but further alterations to the synthetic procedures could provide these results. Within this study isostructural compounds were produced ($[NH_4][Ce^{IV}F_2(AsO_4)]$), which implied that CeF_4 is equally capable of performing the same functions as reagents such as HF. These findings indicate that XF_4 could be an applicable alternative to HF in solvothermal synthesis, generating a safer synthetic route. The production of these compounds and other framework materials could become practical on an industrial scale, reducing the risk associated with the incorporation of HF.

The structures discovered have exhibited a variety of bonding motifs, specifically Ce-F-Ce (**I/V**), Ce-O-Ce (**II**) and mixed Ce-O-Ce, Ce-F-Ce (**III/IV**) bridging bonds have been observed. Fluoride ions adopt a variety of coordination geometries in these compounds, including terminal bonds (**II**), bridging bonds (**III**/**IV/V**) and a mixture of terminal and bridging bonds, with the

cerium (**I**) polyhedra. Research into the literature surrounding cerium structures illustrated that few cerium materials that also incorporated oxotetrahedral species existed[6,11], with even fewer that incorporated fluorine into the framework. An assortment of cerium polyhedra were found within the novel materials. Compound **I** was formed from CeF_8X (X = H_2O/F) units that have been previously noted in the oxide form (CeO_9)[16]. A further paper in 2004 detailed an analogous bonding sphere $CeO_8(OH_2)$, with the water molecule residing within the terminal position as found in **I**[17]. The cerium heteropolyoxotungstate discovered by Sousa[18], provided an example of a CeO_8 unit with an equivalent terminal ion that interacted with K^+ cations. This bonding was observed within the structure of **II** (CeO_7F and $CeO_7(OH_2)$). The framework of **III** had an identical cerium polyhedron to the materials YU-1 and $NaYFPO_4$ (CeO_6F_2), although the sodium phosphate possessed further similarities as the fluoride ions bridged between the lanthanide centres (*Ln*-F-*Ln*). Structure **IV** was similar to **III** being comprised of eight-coordinate building units, yet the terminal ion within **IV** generated voids within the framework. **IV** also displayed edge rather than corner sharing bonding. The polyhedra within **V** were formed of CeO_4F_4 units, isotypic to the known structure of $[NH_4][Ce^{IV}F_2(PO_4)]$[7]. Wang *et al.* have completed the most in depth studies of cerium framework materials, illustrating the varied bonding spheres can be exhibited[19]. However, although isotypic or structurally similar, the polyhedra CeF_8X (**I**), CeO_7X (**II**), and $CeO_5F_2(OH_2)$ (**IV**) are novel units.

As detailed in the Introduction of this Chapter, a variety of starting materials and synthetic conditions were included to increase the extent of reaction products. A number of these compounds were heavily dependent upon the incorporation of NH_4^+ cations within the framework. It was anticipated that templated frameworks would be generated when NH_4^+ cations were removed from the syntheses of materials, such as **II**. These reactions were completed through the introduction of starting materials such as H_3TO_4 and T_2O_5, reagent ratios and the organic templates employed. These alterations provided powdered products of known phases. The cerium compounds were heavily dependent upon the hydrogen bonding between the fluorine ions at terminal sites and the NH_4^+ cations within the channels that were heavily bound by the N---F-Ce donor-acceptor bonds. The NH_4^+ cations were assumed to possess very strong templating effects, so reactive that its presence inhibits alternative amines from replacing it within the frameworks[20].

Table 3.1 in the Introduction of this chapter highlights some of the reactions that produced single crystals and powder samples. Synthetic reactions that involved arsenic ions were more successful than those that utilised phosphorous. The majority of the arsenate materials were produced in very ratio, pH and temperature specific conditions. This was a frustrating aspect of the

research as alternative reaction routes and improved crystalline products were unobtainable as a consequence of their specific nature.

Cerium syntheses that involved phosphorous, regardless of the phosphate source, temperature, reaction length, pH, solvent, template or reaction ratio only produced crystals of $NH_4CeF_2PO_4$[11]. This phase was very stable and attempts to alter the products through the incorporation of HF and fluorophosphoric acid in order to compare their effects with CeF_4, were also completed, although these changes did not alter the outcome. This stability has contributed to the analysis of arsenate rather than phosphate materials within this research project. These results suggest that using CeF_4 is not the most appropriate starting material in the current experimental set-up. Alternative cerium sources with the more traditional HF/NaF/NH_4F mineraliser could prove more successful in the phosphate syntheses.

3.8 References:

(1) Lessing, P. A.; Erickson, A. W. *Journal of the European Ceramic Society* **2003**, *23*, 3049-3057.

(2) Hernandez, T.; Martin, P. *Journal of the European Ceramic Society* **2007**, *27*, 109-114.

(3) Assaaoudi, H.; Ennaciri, A.; Rulmont, A.; Harcharras, M. *Phase Transitions* **2000**, *72*, 1-13.

(4) Harley, G.; Yu, R.; De Jonghe, L. C. *Solid State Ionics* **2007**, *178*, 769-773.

(5) Dan Wang; Ranbo Yu; Yaohua Xu; Shouhua Feng; Ruren Xu; Nobuhiro Kumada; Nobukazu Kinomura; Yasuyuki Matsumura; Takano, M. *Chemistry Letters* **2002**, 1120-1121.

(6) Yu, R.; Wang, D.; Isiwata, S.; Saito, T.; Azuma, M.; Takano, M.; Chen, Y.; Li, J. *Chemistry Letters* **2004**, *33*, 458-459.

(7) Yu, R. B.; Wang, D.; Takei, T.; Kumada, N.; Koizumi, H.; Kinomura, N. *Journal of Solid State Chemistry* **2001**, *157*, 180-185.

(8) Brown, I. D.; Altermatt, D. *Acta Crystallographica Section B-Structural Science* **1985**, *41*, 244-247.

(9) Brese, N. E.; O'Keeffe, M. *Acta Crystallographica Section B-Structural Science* **1991**, *47*, 192-197.

(10) Riou, D.; Ferey, G. *Journal of Solid State Chemistry* **1994**, *111*, 422-426.

(11) Yu, R. B.; Wang, D.; Takei, T.; Koizumi, H.; Kumada, N.; Kinomura, N. *Journal of Solid State Chemistry* **2001**, *157*, 180-185.

(12) Brahim, A.; Mongi, F. M.; Amor, H. *Acta Crystallographica Section E-Structure Reports Online* **2002**, *58*, I98-I99.

(13) Yu, R. B.; Wang, D.; Kumada, N.; Kinomura, N. *Chemistry of Materials* **2000**, *12*, 3527-+.

(14) Yu, R.; Wang, D.; Chen, Y.; Xing, X.; Ishiwata, S.; Saito, T.; Takano, M. *Chemistry Letters* **2004**, *33*, 1186-1187.

(15) Wang, D.; Yu, R. B.; Kumada, N.; Kinomura, N.; Yanagisawa, K.; Matsumura, Y.; Yashima, T. *Chemistry Letters* **2002**, 804-805.

(16) Bagieubeucher, M.; Rzaigui, M. *Acta Crystallographica Section C-Crystal Structure Communications* **1991**, *47*, 1789-1791.

(17) Duan, L. M.; Xu, J. Q.; Xie, F. T.; Liu, Y. B.; Ding, H. *Inorganic Chemistry Communications* **2004**, *7*, 216-219.

(18) Sousa, F. L.; Paz, F. A. A.; Cavaleiro, A. M. V.; Klinowski, J.; Nogueira, H. I. S. *Chemical Communications* **2004**, 2656-2657.

(19) Wang, D.; Yu, R. B.; Wang, H.; Li, X. T.; Xing, X. R. *Microporous and Mesoporous Materials* **2007**, *101*, 66-72.

(20) Ferey, G. *Journal of Fluorine Chemistry* **1995**, *72*, 187-193.

CHAPTER FOUR

ZIRCONIUM ARSENATE STRUCTURES

4.0 Introduction

Within this scientific study zirconium phosphate and arsenate compounds have been investigated over a considerable period of time as they form similar three-dimensional structural archetypes to the zeolite frameworks. Increased industrial demand for functional solids led to the creation of a number of one, two, and three-dimensional zirconium frameworks. For example, the layered structures α-$Zr(HPO_4)_2.H_2O$ and γ-$ZrPO_4(H_2PO_4).2H_2O$ have been systematically examined[1] and have the potential for application in areas such as hydrogen storage[2], ion exchange[3] and catalysis[4]. Zirconium frameworks that incorporate AsO_4 tetrahedra are known and form similar or isotypic compounds to the phosphate analogues[5]. These materials have received less research interest, possibly as a result of their more hazardous nature. The differences in radii sizes of the arsenate (0.36 Å) and phosphate cations (0.17 Å)[6], creates potential for the discovery of entirely new structural families[7]. Reaction conditions for the arsenate compounds have been established to be less severe (lower temperatures, neutral pH, *etc.*) than their phosphate counterparts. Solvothermal methods have been employed in the search for novel zirconium frameworks as this route to formation is considered to be preferable to alternative techniques such as high pressure gold ampoule synthesis.

Scientific research into three-dimensional compounds that form from metal polyhedra and oxotetrahedral species has expanded, driven by the variety of reaction routes available to produce novel systems. Hydrothermal studies incorporating fluoride ions in the form of HF, can result in its incorporation into the structure[8]. These ions typically inhabit sites within the metal polyhedra, replacing the oxygen anions within the $MO_{x-y}F_y$ unit. The addition of fluoride anions can lead to improved crystallinity of the product by enhancing the growth media of the crystals. The integration of these ions within the polyhedra has produced novel structure types. Fluoride ions can form links to the polyhedral unit *via* terminal[9], bridging[10-12] and a mixture[13] of these two types of bonding. The type of bonding that the fluoride anions contribute to will affect the dimensionality of the structure, for example terminal fluorine groups tend to produce less three-dimensional structures, as their presence inhibits the continuation of the framework. ZrF_4 was used as the zirconium source throughout this research, which permitted the incorporation of large quantities of fluoride ions into the reactions. In lower concentrations, it has been noted that fluorine has mineralising properties improving the crystallinity within the reaction[14]. The introduction of excessive quantities of fluorine has been found to encourage its incorporation into the framework of the reaction product[15,16].

Zirconium phosphate and arsenate materials form from octahedral (ZrO_6) and oxotetrahedral (TO_4) units. The addition of fluoride anions into the reaction resulted in the oxygen within the octahedra being substituted by them, forming units such as, ZrO_4F_2 and ZrO_5F[17,18]. These fluorinated zirconium polyhedra exhibit terminal, bridging and a mixture of the two types of linkages, within their frameworks. A large number of materials that incorporate fluoride have also been found to include an organic template, which has led to its incorporation into the framework[9]. The fluoride anions exhibit an affinity to form hydrogen bonds (F---H-N) with the organic template, which provides extra stability in the framework. It has been noted that fluoride anions hydrogen bond preferentially to smaller template groups, which manipulates the dimensionality of the structures by inhibiting continuation of the lattice.

Table 4.1 summarises the types of reactions that were undertaken for this research thesis. Solvothermal reactions were carried out in 23 or 45 mL Teflon-lined Parr autoclaves. This research concentrates on the well-established solvothermal route[19], although it is acknowledged that alternative synthetic routes, such as sealed tube and flux reactions have also been successful.

A systematic programme of work was undertaken that involved alterations to reaction conditions. Changes were made to the ratios of starting materials (1:1, 1:3, 1:5, 1:7); temperature (140, 175, 190, 220 °C); pH (NH_3 solution), solvent (in general H_2O, but also HCl, NH_3, ethanol, methanol, isopropanol, NaOH); reaction length (3, 5, 7, 10, 14 and 21 days) and organic templating agents. The variety of synthetic conditions chosen was informed by a literature review of the different metal phosphate and arsenate structures. This knowledge increased the number of possible reaction routes and provided an overall understanding of the systems to be analysed.

Successful reactions that resulted in the production of novel single crystal are highlighted in Table 4.1 and described herein. The crystalline materials were primarily analysed *via* SXD and supporting techniques such as BV, IR, EDX, TGA and PXD were completed on the samples to clarify these results where possible. This study has involved both arsenate and phosphate starting materials, and this Chapter describes the successful zirconium arsenate frameworks.

Table 4.1: *Synthetic conditions for successful and similar zirconium structures (all Parr autoclaves 23 mL)*

Reaction No.	Reagents	Temp (°C)	Time (days)	Single Crystal	Product	Thesis	Same structure as Reaction No.
1	ZrF_4 (0.1 g); As_2O_5 (0.415 g); NH_3 (10 mL)	140	5	Elongated octahedra	$Zr^{IV}(HAsO_4)(AsO_4)(NH_4)$ (**VI**)	4.1	
2	ZrF_4 (0.1 g); $Ba(OH)_2$ (0.1 g); H_3AsO_4 (0.26g); H_2O (10 mL)	175	7	Trigonal prism	$Zr^{IV}(AsO_4)F(H_2O)$ (**VII**)	4.2	7,8,9,12
3	ZrF_4 (0.1 g); As_2O_5 (0.415 g); HCl (10 mL)	140	5	Rectangular cuboid	$Zr^{IV}(HAsO_4)_2$ (**VIII**)	4.3	
4	ZrF_4 (0.1 g); $NH_4H_2AsO_4$ (0.287 g); H_2O (10 mL); pH 9.5 (addition of NH_3)	175	5	Diamond	$Zr^{IV}_2(AsO_4)_3(NH_4)(H_2O)$ (**IX**)	4.4	10,11
5	ZrF_4 (0.1 g); H_3AsO_4 (0.257 g); CsOH (0.181 g); H_2O (11 mL)	140	14	3D block	$(Cs)Zr^{IV}_2(AsO_4)_3$ (**V**)	4.5	
6	ZrF_4 (0.1 g); H_3AsO_4 (0.121 g); DAT (0.06 g); H_2O (11 mL)	190	7	3D block	$(NH_4)Zr^{IV}_2(AsO_4)_3$ (**V**)	4.5	
7	ZrF_4 (0.1 g); H_3AsO_4 (0.257 g); TMAC (0.066 g); H_2O (10 mL)	140	7	Rods	$Zr^{IV}(AsO_4)F(H_2O)$ (**VII**)	4.2	2,7,8,9,12
8	ZrF_4 (0.1 g); H_3AsO_4 (0.257 g); TMAOH (0.055 g); H_2O (10 mL)	140	7	Rods	$Zr^{IV}(AsO_4)F(H_2O)$ (**VII**)	4.2	2,8,9,12
9	ZrF_4 (0.1 g); As_2O_5 (0.415 g); TMAC (0.066 g); H_2O (10 mL)	140	14	Rods	$Zr^{IV}(AsO_4)F(H_2O)$ (**VII**)	4.2	2,7,9,12
10	ZrF_4 (0.1 g); $Ba(OH)_2$ (0.1 g); H_3AsO_4 (0.257 g); H_2O (10 mL)	140	14	Rods	$Zr^{IV}(AsO_4)F(H_2O)$ (**VII**)	4.2	2,7,8,12
11	ZrF_4 (0.1 g); H_3AsO_4 (0.257 g); H_2O (10 mL); pH 9.5 (addition of NH_3)	175	5	Diamond	$Zr^{IV}_2(AsO_4)_3(NH_4)(H_2O)$ (**IX**)	4.4	4,11
12	ZrF_4 (0.1 g); As_2O_5 (0.415 g); H_2O (10 mL); pH 9.5 (addition of NH_3)	175	5	Diamond	$Zr^{IV}_2(AsO_4)_3(NH_4)(H_2O)$	4.4	4,10
13	ZrF_4 (0.1 g); H_3AsO_4 (0.257 g); H_2O (10 mL); TEAOH (0.031 g)	140	7	Rod	$Zr^{IV}(AsO_4)F(H_2O)$ (**VII**)	4.2	2,7,8,9
14	ZrF_4 (0.1 g); As_2O_5 (0.415 g); H_2O (10 mL); TEAOH (0.031 g)	140	7	Rod	$Zr^{IV}(AsO_4)F(H_2O)$ (**VII**)	4.2	
15	ZrF_4 (0.1 g); H_3AsO_4 (0.257 g); H_2O (10 mL); OAD (0.076 g)	140	7	Rod	$Zr^{IV}(AsO_4)F(H_2O)$ (**VII**)	4.2	

16	ZrF_4 (0.1 g); As_2O_5 (0.415 g); H_2O (10 mL); OAD (0.076 g)	140	7	Rod	$Zr^{IV}(AsO_4)F(H_2O)$ (**VII**)	4.2	
17	ZrF_4 (0.1 g); H_3AsO_4 (0.257 g); EDA (0.036 g); H_2O (10 mL)	140	7	Multi-phase powder	ZrF_4, As_2O_5	4.6	
18	ZrF_4 (0.1 g); H_3AsO_4 (0.257 g); PIP (0.052 g); H_2O (10 mL)	140	7	Multi-phase powder	ZrF_4, As_2O_5	4.6	
19	ZrF_4 (0.1 g); $FOP(OH)_2$ (0.24 g); DABCO (0.07 g) H_2O (10 mL)	140	7	Powder	$Zr(OH)(PO_4)$	4.6	
20	ZrF_4 (0.1 g); H_3AsO_4 (0.257 g); HCl (10 mL)	175	5	Multi-phase powder	α-$Zr^{IV}(HAsO_4)H_2O$	4.3	
21	ZrF_4 (0.1 g); $NH_4H_2AsO_4$ (0.287 g); NH_3 (10 mL)	175	5	Diamond	$Zr^{IV}_2(AsO_4)_3(NH_4)(H_2O)$ (**IX**)	4.4	
22	ZrF_4 (0.1 g); H_3PO_4 (0.204 g); NH_3 (10 mL)	175	5	Rod	$Zr^{IV}F_2(PO_4)(HPO_4)(NH_4)_3$	4.6	
23	ZrF_4 (0.1 g); $NH_4H_2PO_4$ (0.208 g); NH_3 (10 mL)	175	5	Rod	$Zr^{IV}F_2(PO_4)(HPO_4)(NH_4)_3$	4.6	
24	ZrF_4 (0.1 g); $FOP(OH)_2$ (0.24 g); HCl (10 mL)	140	7	Multi-phase powder	$Zr(HPO_4)_2.2H_2O$, β-$Zr(PO_4)(OH)$	4.6	
25	ZrF_4 (0.1 g); $NH_4H_2AsO_4$ (0.29 g); ethanol (10 mL)	175	5	Multi-phase powder	$Zr_3(AsO_4)_4$; $Zr_2(AsO_4)_3OH$	4.6	
26	ZrF_4 (0.1 g); H_3PO_4 (0.24 g); KOH (0.07 g); H_2O (10 mL)	175	5	Multi-phase powder	$KZr_2(PO_4)_3$, KH_2PO_4	4.6	
27	ZrF_4 (0.1 g); H_3PO_4 (0.24 g); RbOH (0.12 g); H_2O (10 mL)	175	5	Square block	$RbZr_2(PO_4)_3$	4.6	
28	ZrF_4 (0.1 g); H_3PO_4 (0.24 g); $Ba(OH)_2$ (0.1 g); H_2O (10 mL)	175	5	Multi-phase powder	$Zr(HPO_4)_2.H_2O$, $Ba_3P_4O_{13}$	4.6	
29	ZrF_4 (0.1 g); $NH_4H_2PO_4$ (0.21 g); $Ba(OH)_2$ (0.1 g); H_2O (10 mL)	175	5	Multi-phase powder	$Zr_2P_2O_7$, ZrF_4, $ZrPO_4$	4.6	

4.1 Compound VI: Ammonium Zirconium Arsenate - $Zr^{IV}(HAsO_4)(AsO_4)(NH_4)$

4.1.1 Synthesis

The synthesis of compound **VI** was undertaken using ZrF_4 (0.1 g, 0.60 mmol, 99.9%, Aldrich) and As_2O_5 (0.415 g, 1.81 mmol, 99%, Aldrich) in NH_3 solution (35%, 10 mL, Fisher). The reaction mixture was placed in a Teflon-lined Parr autoclave and heated at 140 °C for 5 days. The reaction was allowed to cool slowly to room temperature, and the solid product was removed from the solution by filtration and washed with warm water.

4.1.2 Results and Discussion

The reaction product, a mixture of powder and single crystals, contained elongated octahedral shaped crystals. Single crystals of **VI** were isolated and SEM images were obtained and can be seen in Figure 4.1. Crystallographic information and results of the data collection for compound **VI** can be found in Tables 4.2 and A.4.1 in the Appendix.

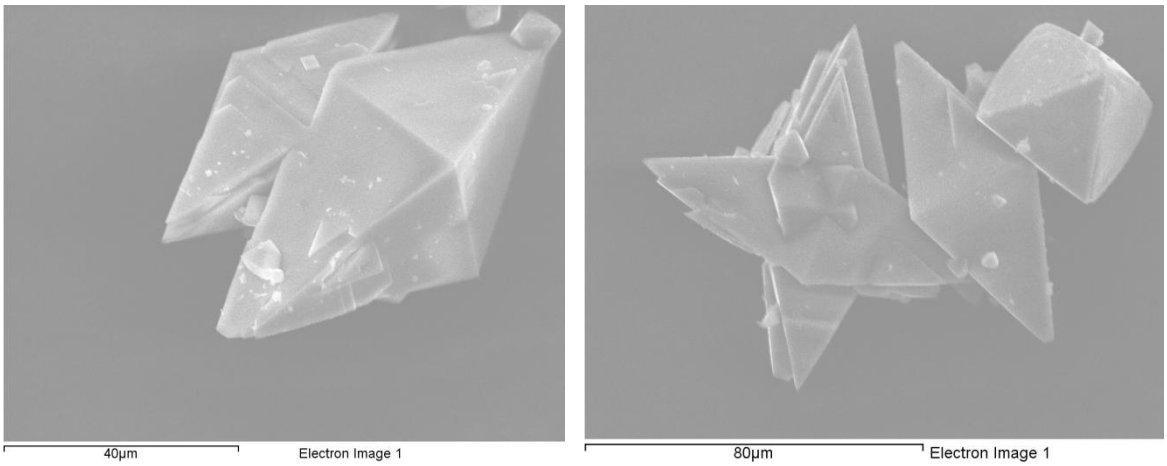

Figure 4.1: *SEM images of elongated octahedral shaped $Zr(HAsO_4)(AsO_4)(NH_4)$ crystals*

Table 4.2 *Details of single crystal data collection for $Zr(HAsO_4)(AsO_4)(NH_4)$* ***(VI)***

Molecular Formula	**$Zr^{IV}(HAsO_4)(AsO_4)(NH_4)$**
Formula Weight (g)	386.75
Crystal Appearance	Elongated octahedra
Crystal Size (mm)	0.1 x 0.1 x 0.2
Crystal System	Orthorhombic
Space Group	*Pnna*
Lattice Parameters	a = 13.6913(3) Å, α = 90°
	b = 17.7748(5) Å, β = 90°
	c = 6.8504(2) Å, γ = 90°
V (Å^3)	1667.11(1)
Z	11
Calculated density (mg/m^3)	2.88
Temperature (K)	120 K
Theta Range (°)	3-27.5
Wavelength (Å)	Mo *K*α (λ = 0.71073)
Number of Reflections Measured	Total – 12559, Unique – 1902
R_1 [$I>2\sigma(I)$]^a	0.044
***R*1(all data)**	0.073
wR_2	0.083
Goodness of fit indicator	1.079

Bond valence calculations[20,21] (Table 4.3) were completed for the oxygen anions within **VI**, showing a lower valence value at the O3 (1.27) and O6 (1.27) sites compared to the average BV for the remaining oxygen ions (1.96(5)), which are more typical of divalent anions. To charge balance the structure of **VI**, one AsO_4 and one $HAsO_4$ group was needed. It was deemed possible that the hydrogen attached to terminal oxygen ions could occupy both sites 50% of the time. SXD analysis showed the presence of electron density at the O6 site, which has been denoted a hydroxide group. O1, O2, O3 and O6 all interact with the NH_4^+ cations *via* donor-acceptor bonding. O3 and O6 are

terminal sites, whereas O1 and O2 are involved in bridging bonds between the arsenate and zirconium sites, as well as this hydrogen bonding interaction. The low bond valence at O3 and O6 is a result of the majority of the hydrogen bonding associated with the NH_4^+ cations being present at these sites. The NH_4^+ cation has a shorter hydrogen bonded length (O3 – 2.0 Å, O6 – 1.94 Å) than these terminal anions, indicating that they interact more strongly with the H-N groups.

Table 4.3: *Bond lengths and bond valence calculations for O anions within* ***VI***

Atoms	Zr-O bond length (Å)	As-O bond length (Å)	Bond Valence O-Zr	Bond Valence O-As	Total Bond Valence
O1	2.09(4)	As2 - 1.68(5)	0.65	1.26	1.91
O2	2.11(5)	As1 - 1.68(5)	0.61	1.27	1.88
O3	n/a	As2 - 1.68(5)	n/a	1.27	1.27
O4	2.06(6)	As1 - 1.67(6)	0.7	1.3	2
O5	2.06(5)	As2 - 1.67(5)	0.7	1.3	2
O6	n/a	As1 - 1.68(5)	n/a	1.27	1.27
O7	2.06(5)	As1 - 1.68(5)	0.7	1.27	1.97
O8	2.06(4)	As2 - 1.68(4)	0.7	1.27	1.97

Compound **VI** is constructed of zirconium-centred ZrO_6 octahedra, arsenic-centred AsO_4 or $HAsO_4$ tetrahedra and NH_4^+ cations (Fig. 4.2). Channels are observed when **VI** is viewed down the *a* and *c*-axis (Fig. 4.2.*i/iii*), which highlights the encapsulated NH_4^+ cations. The zirconium octahedra are fully connected to the arsenate tetrahedra through Zr-O-As linkages, producing a compact structure. The AsO_4 groups are bonded to three separate zirconium octahedra, which results in the zirconium units being bound to six separate tetrahedra. Corner-sharing bonding applies throughout the structure of **VI**.

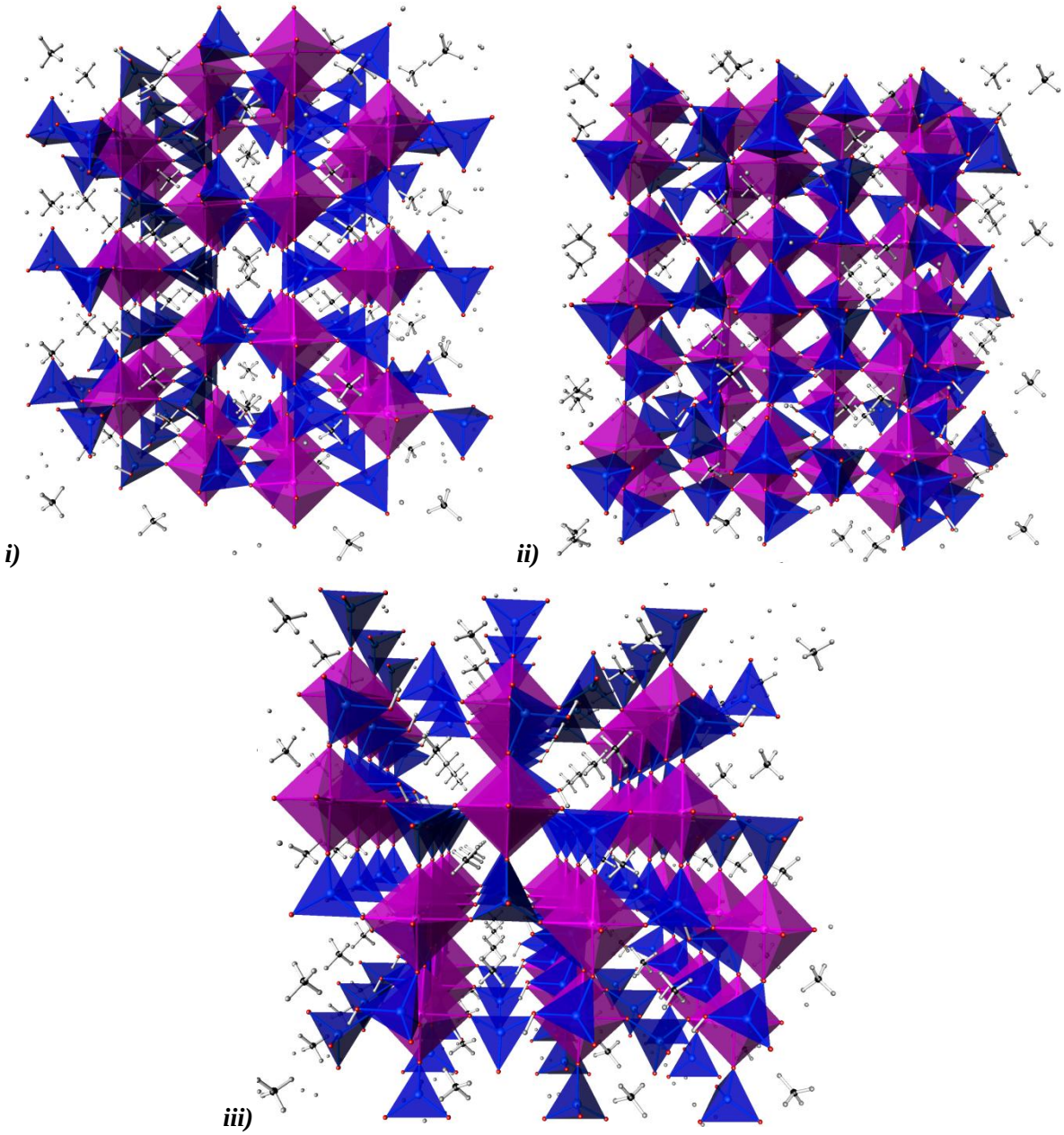

Figure 4.2: *Structure of* ***VI*** *viewed down the* ***i)*** *a;* ***ii)*** *b;* ***iii)*** *c-axis [Key: Blue tetrahedra – $HAsO_4/AsO_4$; Pink octahedra – ZrO_6; Black centred tetrahedra – NH_4^+ cations]*

Table 4.4**: Bond lengths and bond valence values for Zr within **VI

Atoms	Zr-O bond length (Å)	Zr-O bond valence
O1	2.09(4)	0.64
O2	2.11(5)	0.61
O4	2.06(6)	0.70
O5	2.06(5)	0.70
O7	2.06(5)	0.70
O8	2.06(4)	0.70
Total		**4.06**

Table 4.4 illustrates the bond valence for the zirconium cation. The zirconium bond valence is +4, as anticipated from the starting material Zr^{4+}. The NH_4^+ cations were isolated *via* SXD, and the hydrogen positions determined, as a consequence of the strong interactions between NH_4^+ cations and the $HAsO_4$ and AsO_4 tetrahedra. Figure 4.3 depicts the hydrogen bonding between the NH_4^+ cations and the oxygen ions. The hydrogen bonding lengths differ marginally for each NH_4^+ cation; N1 has an average hydrogen bond length of 2.03(9) Å, and N2, 2.05(5) Å.

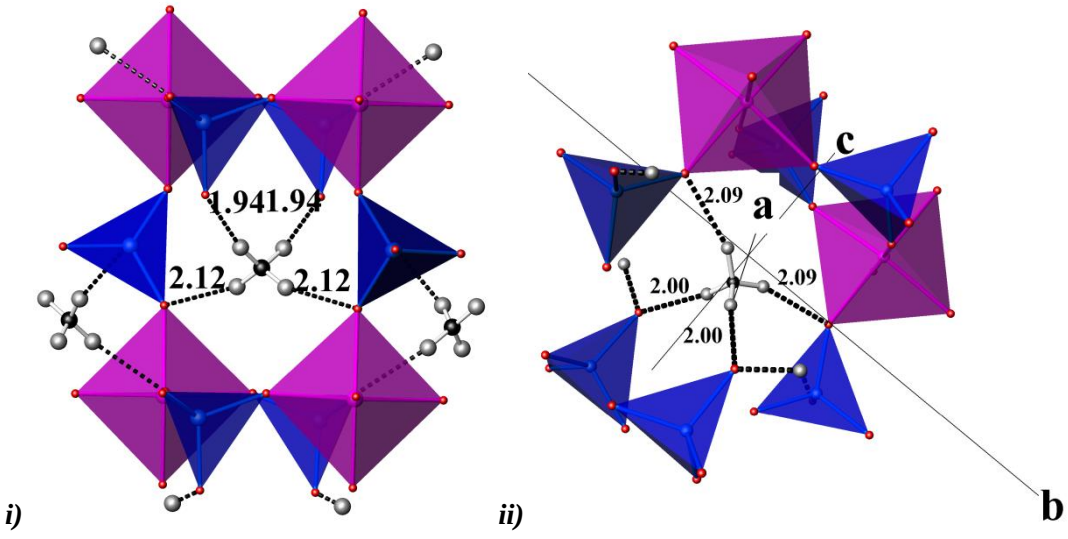

***Figure 4.3:** Hydrogen bonding lengths associated with N1 **i)** and N2 **ii)** sites within $Zr(HAsO_4)(AsO_4)(NH_4)$, depicted by black dotted lines (lengths in Å)*

EDX analysis (see Appendix A.4.2) was completed on compound **VI** to determine the elements present. This analysis showed an abundance of Zr (14%), As (24%), and O (62%) but no F (ratio from EDX Zr 1: As 1.71: O 4.4 compared to the structural formula Zr 1: As 2: O 8). The atomic percentages shown agreed roughly with the structural formula of **VI**, although this data is qualitative not quantitative.

IR analysis (see Appendix A.4.3) illustrated absorption in the NH_4^+ stretching regions (3194 and 1422 cm^{-1}), confirming that this cation was present within **VI**. TGA analysis of **VI** (Fig. 4.4) demonstrated mass loss (denoted by black arrows) starting at 175 °C, with a sharp change at 325 °C. A continuing reduction in mass was observed from 325 °C onwards until 625 °C where another sharp loss was noted. The initial mass loss was associated with the loss of ammonium cations from the channels of the structure. The elevated temperature at which the decline was recorded is more typical of NH_4^+ cations, than water molecules. The second loss in mass (Fig. 4.4 red arrows) is likely to be connected to the loss of OH groups from the AsO_4 tetrahedra. Analysis of the intermediate stages through analytical techniques such as variable temperature powder X-ray diffraction was not possible, in view of the small quantities of sample obtained. VT SXD is possible but unfortunately due to time constraints this was not possible.

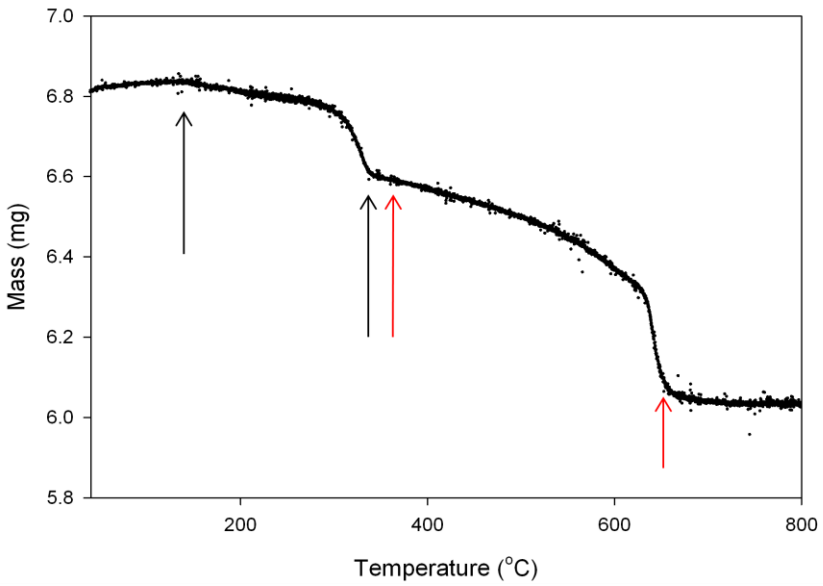

Figure 4.4: *Mass loss vs. temperature graph for $Zr(HAsO_4)(AsO_4)(NH_4)$ (black arrows – first mass loss; red arrows – second mass loss)*

4.2 Compound VII: Hydrated zirconium fluoro-arsenate – $Zr^{IV}(AsO_4)F(H_2O)$

4.2.1 Synthesis

ZrF_4 (0.1 g, 0.60 mmol, 99.9%, Aldrich), $Ba(OH)_2.xH_2O$ (0.104 g, 0.61 mmol, ≥ 98%, Aldrich) and H_3AsO_4 (0.257 g, 1.81 mmol, 75% wt., Aldrich) were dissolved in H_2O (11 mL) and stirred for thirty minutes. The reaction mixture was transferred into a 23 mL teflon-lined steel Parr autoclave, heated to 175 °C and held at that temperature for 7 days. The reaction was allowed to slowly cool to room temperature, filtered to collect the solid product, and finally washed with warm water. The reaction product, compound **VII**, $Zr(AsO_4)F(H_2O)$, was dried at 80 °C for 3 hours and analysed accordingly.

4.2.2 Results and Discussion

The reaction product was a mixture of powder and single crystals. A suitable single crystal was picked for SXD analysis (Fig. 4.5), and the results of the data collection can be seen in Tables 4.5 and A.4.4 in the Appendix.

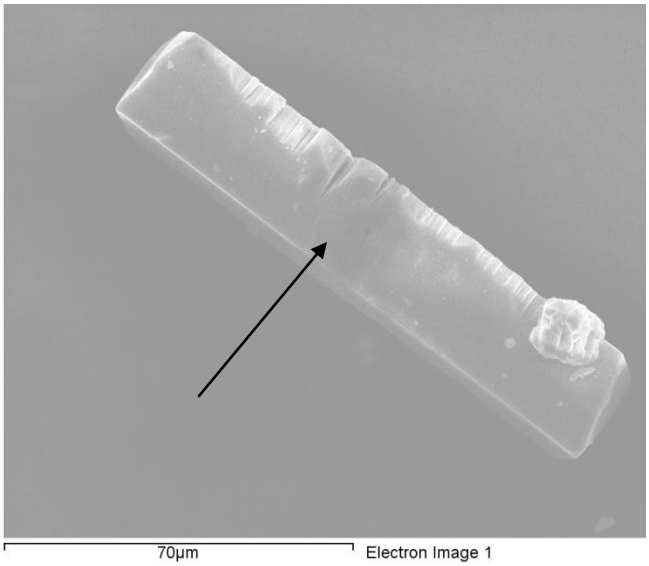

Figure 4.5 *SEM image of rod shaped $Zr(AsO_4)F(H_2O)$ crystals*

Table 4.5: *Details of single crystal data collection for $Zr(AsO_4)F(H_2O)$* ***(VII)***

Molecular Formula	**$Zr^{IV}(AsO_4)F(H_2O)$**
Formula Weight (g)	265.815
Crystal Appearance	Rod
Crystal Size (mm)	0.05 x 0.1 x 0.3
Crystal System	Monoclinic
Space Group	*C 2/m*
Lattice Parameters	a = 8.9074(5) Å, α = 90°
	b = 6.7703(3) Å, β = 100.738(3)°
	c = 7.9506(4) Å, γ = 90°
V (Å^3)	471.07(4)
Z	4
Calculated density (mg/m^3)	4.787
Temperature (K)	120 K
Theta Range (°)	3.81-27.49
Wavelength (Å)	Mo *K*α (λ = 0.71073)
Number of Reflections Measured	Total – 3292, Unique – 590
R_1 [I>2σ (I)]^a	0.051
***R*1(all data)**	0.062
wR_2	0.13
Goodness of fit indicator	1.13

Initial structural analysis *via* single crystal refinements, indicated that two of the ions attached to the zirconium polyhedra were likely to be fluoride and one a water molecule. The bond valence calculations[20,21] showed a lowered value than expected at the O4 site (Table 4.6 – BV (O4) = 0.44) compared with other oxygen ions within the polyhedra (average BV (O) = 1.93(9)), which highlighted the need for the extra two hydrogen ions associated with a water molecule. The longer bond length observed for the terminal oxygen ion (Zr1-O4) is 2.23(10) Å (Fig. 4.6), compared to the average Zr-O bond length of 2.14(6) Å, suggested the presence of a water molecule

that was weakly bound to the polyhedron. Hydrogen ions could not be placed through single crystal refinements and so these positions were assumed to exist at the O4 site through bond valence calculations and included in the model at a fixed position of 0.8 Å, with the torsial angle left free to refine. Bond valence calculations at the sites assumed to be fluoride anions displayed lower value (F1 – 1.00; F2 -1.12) compared to the average of the divalent ions (1.93(9)). These lowered values suggested the presence of monovalent ions such as OH/F. In order to support this assumption the presence of fluorine was identified in **VII** through EDX analysis (see Appendix A.4.5), which indicated that fluorine (~16%) was found within the crystal analysed. The amount of fluorine was roughly in a 1:1 ratio with zirconium and arsenic, in agreement with the structural formula (Zr-14.6 %; As-13.6 %; F-16.8 %; O-55.0 %, equating to a ratio of 1Zr:1As:1F:4O) of **VII**. These factors suggested the seven-coordinate polyhedral unit to be $ZrF_2O_4(H_2O)$.

Table 4.6: *Bond lengths and bond valence calculations for O/F anions within $Zr(AsO_4)F(H_2O)$ polyhedra*

Atoms	Zr-O/F bond length (Å)	As-O/F bond length (Å)	Bond Valence Zr-O/F	Bond Valence As-O/F	Total Bond Valence
O1	2.05(7)	1.68(6)	0.72	1.27	1.99
O1	2.05(7)	1.68(6)	0.72	1.27	1.99
O2	2.13(9)	1.65(8)	0.58	1.37	1.95
O3	2.15(9)	1.69(9)	0.55	1.23	1.78
O4	2.23(9)	n/a	0.44	n/a	0.44
F1	2.10(1)	n/a	0.50	n/a	1
	2.10(1)		0.50		
F2	2.06(1)	n/a	0.56	n/a	1.12
	2.06(1)		0.56		

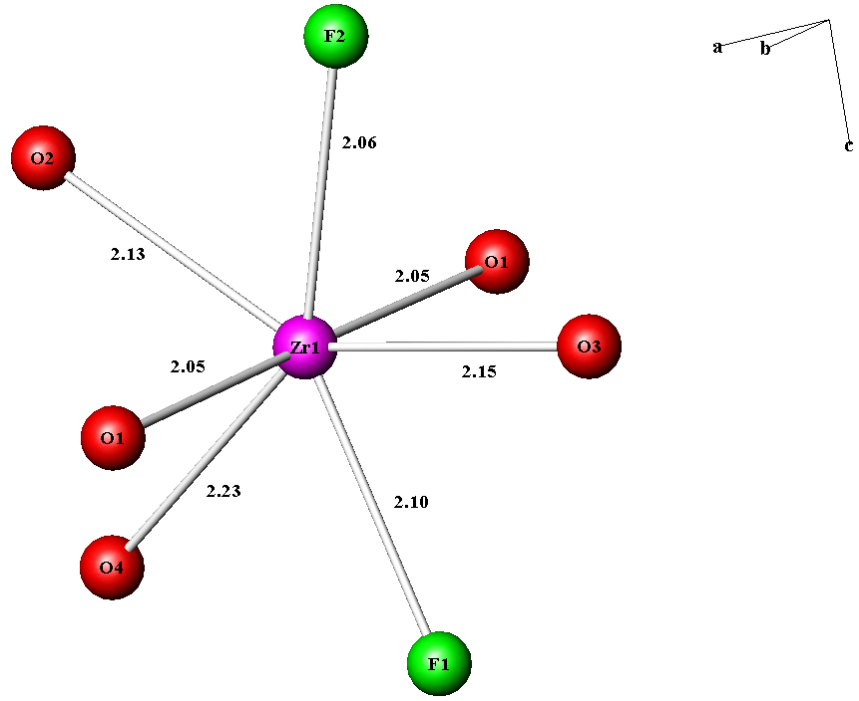

Figure 4.6: *Bond lengths in zirconium polyhedra observed in* ***VII*** *(lengths in Å)*

Table 4.7*: Bond lengths and bond valence values for Zr within* ***VII***

Atoms	Zr-O/F bond length (Å)	Zr-O/F bond valence
O1	2.05(6)	0.71
O1	2.05(6)	0.71
O2	2.13(9)	0.58
O3	2.15(8)	0.55
O4	2.22(9)	0.45
F1	2.1(1)	0.56
F2	2.06(1)	0.50
Total		**4.06**

The presence of fluoride anions within the zirconium octahedral unit created varied bond lengths. However, their presence did not alter the bond valence, which was calculated to be 4, as anticipated for Zr^{4+} (Table 4.7).

The structure of **VII** was composed of seven-coordinate, zirconium-centred, $ZrF_2O_4H_2O$ polyhedra (Fig. 4.6) and arsenic-centred AsO_4 tetrahedra. Distortion of the polyhedral units was observed, a consequence of mono and divalent anions linked to the zirconium centre. The zirconium polyhedra corner-share to one another through bridging Zr-F-Zr bonds forming a ribbon-like chain parallel to the *b*-axis (Fig. 4.7.*ii*). The arsenate tetrahedra exhibited corner-sharing bonding to four oxygen sites within the polyhedra, these being fully coordinated to the framework. The tetrahedra are connected to four different zirconium polyhedra, which highlights the corner-sharing nature of the bonds within the structure of **VII**. The O4 anion was found to be terminally bonded to the zirconium centre (Fig. 4.7.*iii*), pointing into the channels of **VII**. Additional space was required for the hydrogen cations associated with the O4 ion (assumed to be a weakly bound H_2O molecule), which formed these channels. Hydrogen ions could not be isolated *via* SXD, and so their presence has been assumed at the O4 site. This structure is isotypic to a hafnium arsenate ($Hf^{IV}(AsO_4)F(H_2O)$), previously synthesised by Redrup[22]. The bond valence at the terminal oxygen site was similar in the hafnium compound (0.48), to the zirconium (0.44). The hydrogen positions on the terminal sites were refined in the hafnium compound through joint SXD and NPD refinements, which demonstrated that is was a weakly bound water molecule. This analogous hafnium structure reinforces the assumption that the terminal oxygen ion is in fact a weakly bound water molecule.

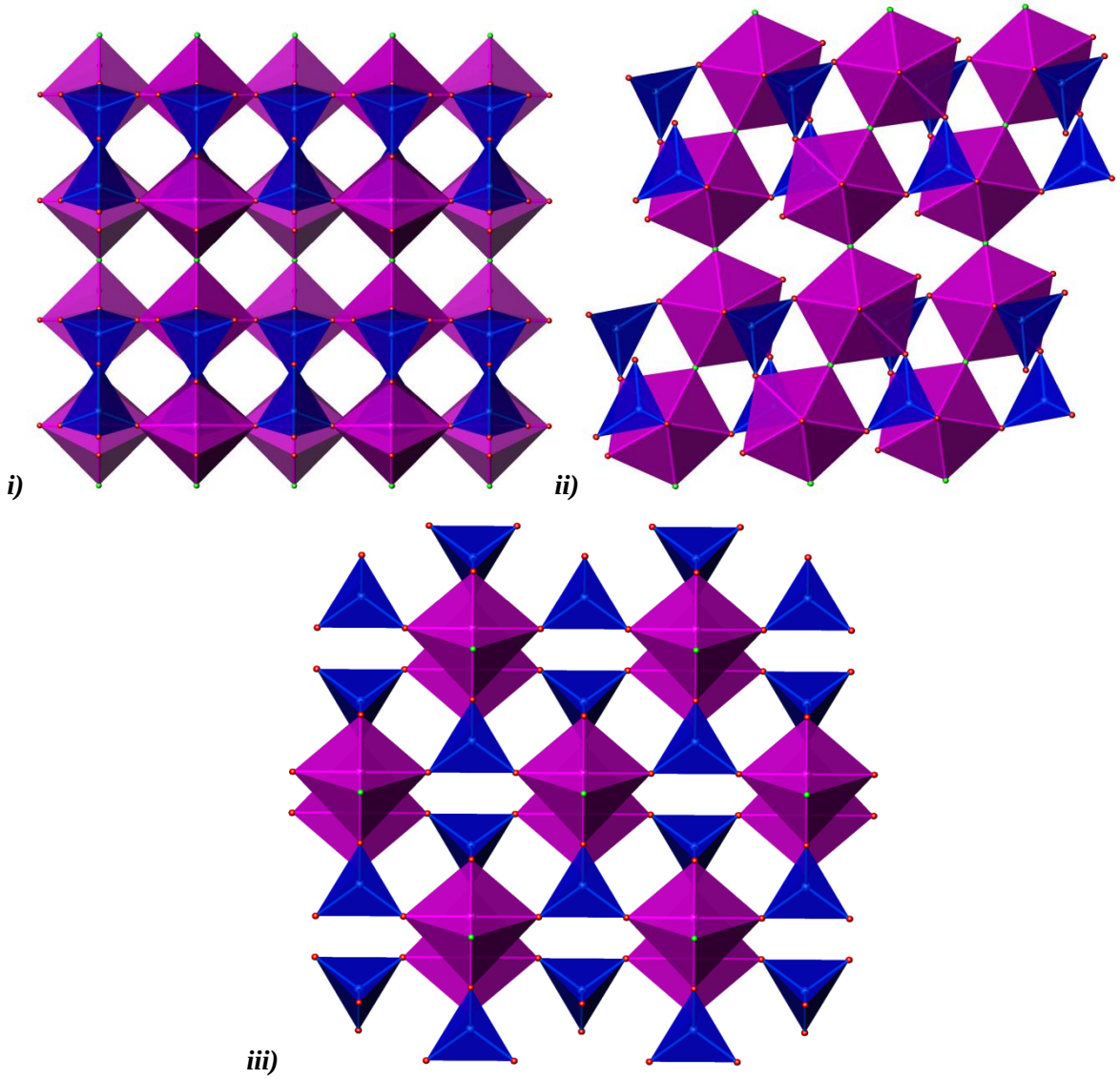

Figure 4.7: *Structure of* ***VII*** *observed down the* ***i)*** *a,* ***ii)*** *b,* ***iii)*** *and c-axis [Key: Blue tetrahedra - AsO_4, purple polyhedra – $ZrO_4F_2(H_2O)$ (hydrogen ions could not be isolated via SXD and thus are not included in diagrams)]*

The channels within **VII** are 4.95 by 4.88 Å in size at their largest points (Fig. 4.8). The distance between O3 and O4 (2.75 Å) is appropriate for a hydrogen bond, if it is assumed that the hydrogen atoms lie along the vector between O4 and O3 at a typical distance (0.97 Å).

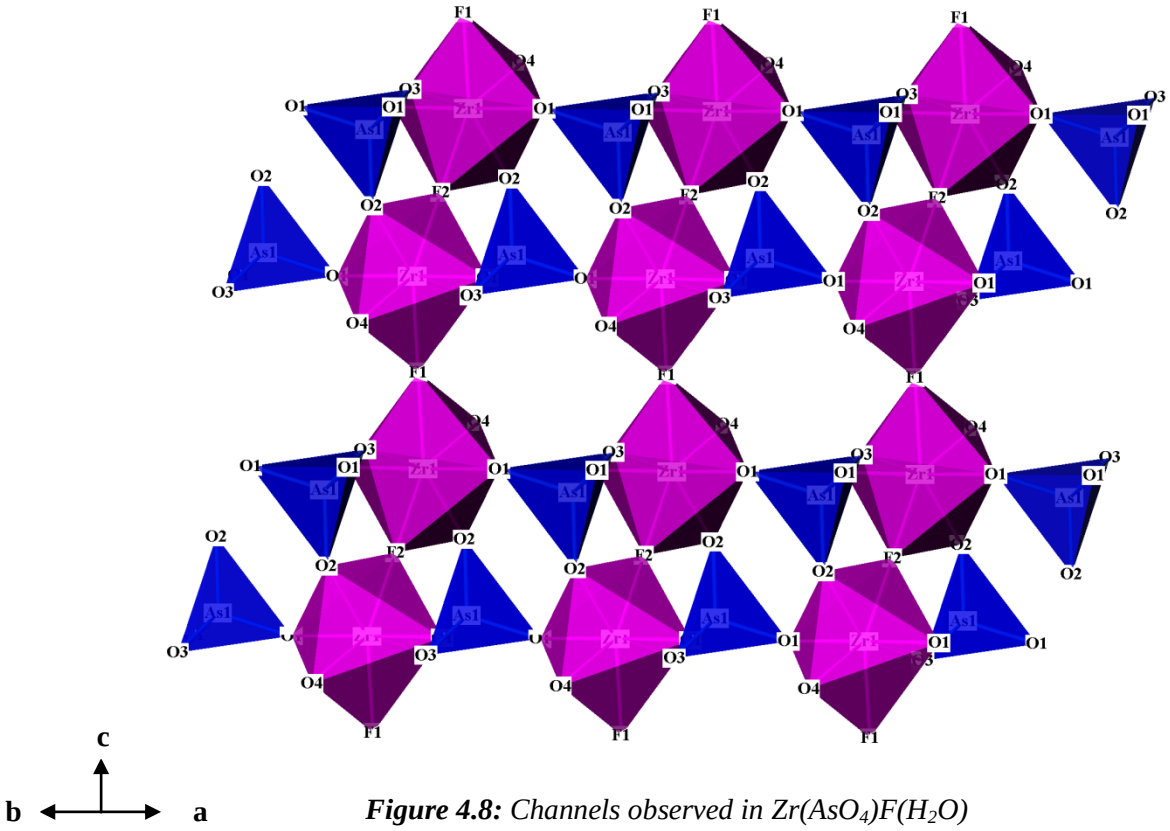

Figure 4.8: *Channels observed in $Zr(AsO_4)F(H_2O)$*

The presence of water in compound **VII** was isolated through IR analysis, which produced a broad peak at 3409.48 cm^{-1} (see Appendix A.4.6).

TGA analysis was undertaken (Fig. 4.9) to ascertain the temperature at which the water was lost from within **VII**. A mass loss was observed at 460 °C that continued until 800 °C, after which point the structure collapsed. The strength of the bonds between terminal O4 ion and the zirconium centre implied that the dehydration required a large quantity of energy. The removal of the terminal H_2O groups resulted in structural collapse, which occurred onwards from 800 °C.

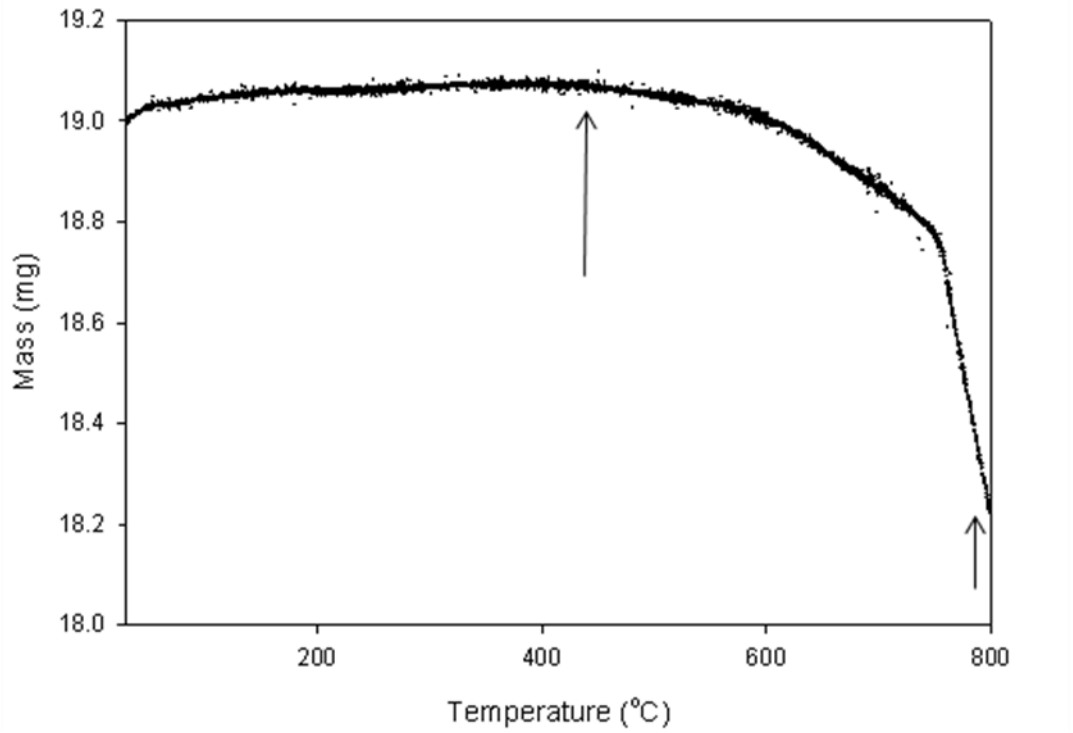

Figure 4.9: *Mass loss vs. temperature graph for $Zr(AsO_4)F(H_2O)$ (mass losses indicated by arrows)*

Compound **VII** is a hydrated zirconium fluoro arsenate with an isotypic structure to the hafnium compound, $Hf(AsO_4)F(H_2O)$, synthesised by Redrup[22]. In both reactions the starting materials MF_4 were used (M = Zr/Hf), As_2O_5 was employed in the hafnium and H_3AsO_4 in this zirconium synthesis. The experiments proceeded in acidic media (the hafnium reaction involved HCl and the zirconium synthesis was altered towards a lower pH through the inclusion of H_3AsO_4), which indicated that these synthetic conditions were suitable for the growth of $M(AsO_4)F(H_2O)$ compounds. The replication of these synthetic proceedings was attempted to create phosphate analogues. Modifications to the reaction pathway (starting material, temperature, solvent *etc.*) did not promote the formation of isotypic compounds. The design of $M(PO_4)F(H_2O)$ compounds may require synthetic routes that entail higher pressures and temperatures, which are beyond the capacity of our current Parr vessels.

4.3 Compound VIII: Zirconium hydrogen arsenate – $Zr^{IV}(HAsO_4)_2$

4.3.1 Synthesis

ZrF_4 (0.1 g, 0.60 mmol, 99.9%, Aldrich) and As_2O_5 (0.415 g, 1.81 mmol, 99%, Aldrich) were dissolved in concentrated HCl (36%, 11 mL, Fisher), and stirred for 30 minutes until dissolved. The reaction was placed in a 23 mL teflon-lined steel Parr autoclave and heated at 140 °C for 5 days. The autoclave was allowed to cool to room temperature slowly and the solid product was filtered and washed with warm water. The reaction product, compound **VIII**, $Zr(HAsO_4)_2$, was found to comprise of a crystalline sample.

4.3.2 Results and Discussion

Block shaped single crystals were the main product of the solvothermal reaction (Fig. 4.10). The sample was formed of crystals and powder, although the small size of the crystals made it difficult to isolate single examples of **VIII** appropriate for SXD analysis. Once a suitable crystal was found SXD was completed and results of the data collection are presented in Tables 4.8 and A.4.7 in the Appendix.

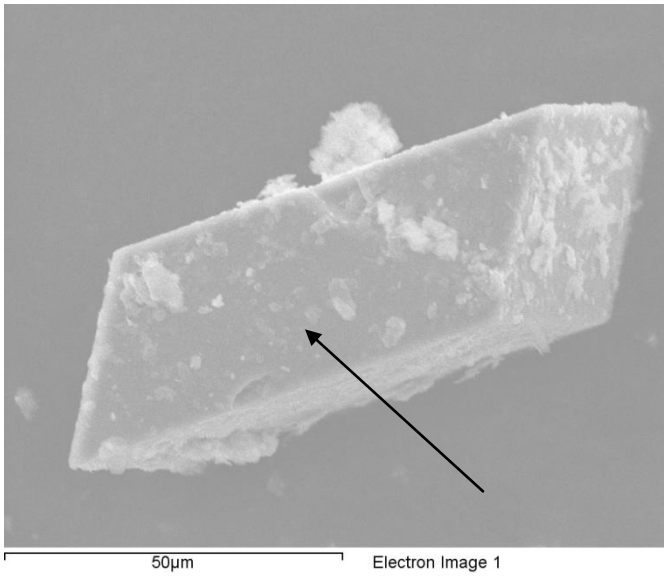

Figure 4.10 *SEM image of single $Zr(HAsO_4)_2$ crystal (crystal is covered with solid powder which was removed using silicone oil for SXD analysis)*

Table 4.8: *Details of single crystal data collection for $Zr(HAsO_4)_2$*

Molecular Formula	**$Zr^{IV}(HAsO_4)_2$**
Formula Weight (g)	367.71
Crystal Appearance	Rectangular cuboids
Crystal Size (mm)	0.05 x 0.1 x 0.3
Crystal System	Monoclinic
Space Group	*P* $2_1/n$
Lattice Parameters	a = 5.2831(2) Å, α = 90°
	b = 8.7006(4) Å, β = 103.715(2)°
	c = 7.5772(2) Å, γ = 90°
V (Å^3)	338.36(2)
Z	3
Calculated density (mg/m^3)	3.48
Temperature (K)	120 K
Theta Range (°)	3.6-27.5
Wavelength (Å)	Mo *K*α (λ = 0.71073)
Number of Reflections Measured	Total – 4466, Unique – 775
R_1 [I>2σ (I)]^a	0.044
***R*1(all data)**	0.049
wR_2	0.108
Goodness of fit indicator	1.141

Bond valence calculations[20,21] were undertaken on compound **VIII** (Table 4.9) after initial framework assignments had been made. O1, O2, and O4 bond to one arsenic anion and one zirconium centre, providing an average Zr-O bond valence of 2.12(5) typical for divalent oxygen ions. The terminal site O3 is bound to one arsenic atom, with a bond length of 1.68 Å. This value is larger than the average length of the fully connected oxygen anions, 1.64(9) Å, and more typical of P/As-OH bonds rather than P/As-O in primary and secondary phosphate and arsenates[23]. The O3 site had a bond valence of 1.27, typical of a monovalent hydroxide ion. The framework of **VIII** is

$Zr(AsO_4)_2^{2-}$ and must contain cations such as H^+ in order for it to charge balance. The findings from BV calculations indicated that the O3 site is an OH group, converting AsO_4 to $HAsO_4$ and charge balancing the structure of **VIII** to $Zr(HAsO_4)_2$. The hydrogen ion was included in the model for clarity, at a fixed distance of 0.8 Å, but its torsial angle was left free to refine.

Table 4.9: *Bond lengths and bond valence calculations for O anions within* $Zr(HAsO_4)_2$

Atoms	Zr-O bond length (Å)	As-O bond length (Å)	Bond Valence Zr-O	Bond Valence As-O	Total Bond Valence
O1	2.07(6)	1.65(5)	0.68	1.37	2.05
O2	2.05(6)	1.63(6)	0.72	1.45	2.17
O3	n/a	1.68(7)	n/a	1.27	1.27
O4	2.03(6)	1.65(7)	0.76	1.37	2.13

Table 4.10*: Bond lengths and bond valence values for Zr within* ***VIII***

Atoms	Zr-O bond length (Å)	Zr-O bond valence
O1	2.07(6)	0.63
O1	2.07(6)	0.63
O2	2.05(6)	0.73
O2	2.05(6)	0.73
O4	2.03(6)	0.76
O4	2.03(6)	0.76
Total		**4.31**

The calculated BV for zirconium was greater than the anticipated value of +4 (Table 4.10). The value was not close enough to 3/5 to suggest mixed valence on the metal site, but resulted from the varied bond lengths causing the structure to deviate from an ideal octahedral species.

EDX analysis (Appendix A.4.8) confirmed the presence of Zr (10.5%), As (18.9%) and O (70.6%) within the crystal sample, eliminating the possibility that fluorine ions rather than OH

groups were present at the terminal sites within the $HAsO_4$ tetrahedra. The ratio of the elements roughly agrees with the structural analysis, having 1Zr: ~ 2As: ~ 7-8 O within the bulk sample analysed, although this data is qualitative.

Compound **VIII** crystallises in the monoclinic, $P2_1/n$ space group, forming a three-dimensional zirconium hydrogen arsenate framework. The basic structure is composed of zirconium-centred ZrO_6 octahedra, and arsenic centred $HAsO_4$ tetrahedra (Fig. 4.11).

The zirconium octahedra are linked to the arsenate tetrahedra through corner sharing bonding of As-O-Zr. The structure of **VIII** displays layers of the zirconium octahedra and arsenate tetrahedra when viewed through the *b*-axis (Fig. 4.11.*ii*). The zirconium octahedra were found to be fully connected to the framework, through six separate $HAsO_4$ groups that surround it in a circular fashion, which can be observed through the *c*-axis (Fig. 4.11.*iii*). The arsenate tetrahedra are connected to three separate zirconium octahedra through corner-sharing bonding. Each tetrahedron has one terminal oxygen anion, O3, which houses an OH group. The presence of these OH groups has created channels, which can be viewed through the *a*-axis (Fig. 4.11.*i*). The channels are interrupted by the OH groups that sit opposite one another within the framework of **VIII**. Hydrogen bonding between neighbouring OH groups was detected, as the oxygen anions are 2.66 Å away from the hydroxide ions at the O3 site.

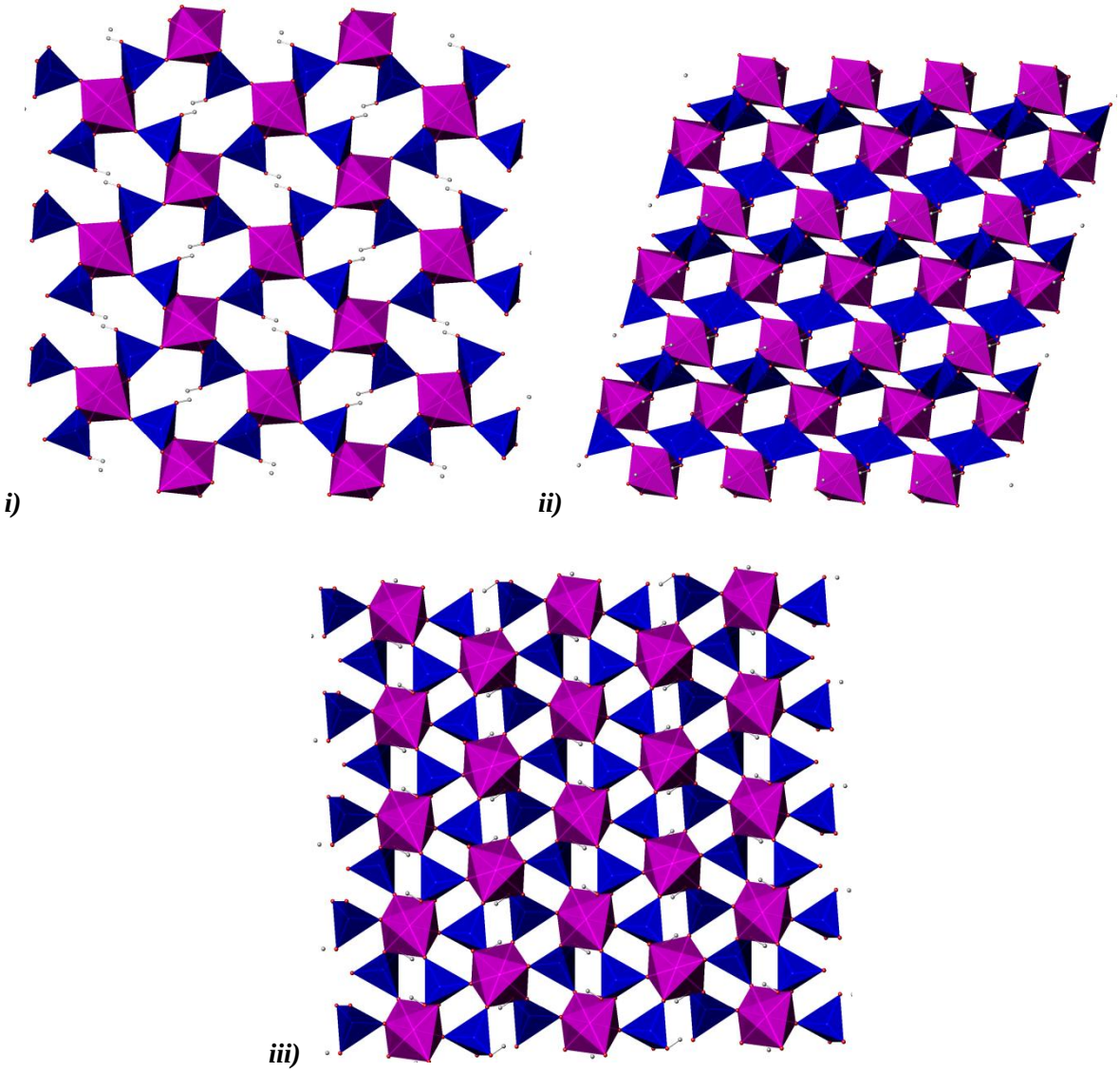

Figure 4.11: *The structure of* ***VIII*** *viewed down the* ***i)*** *a;* ***ii)*** *b and* ***iii)*** *c-axis [Key: Blue tetrahedra- $HAsO_4$; Pink octahedra – ZrO_6 octahedra]*

The hydrogen ions attached to the $HAsO_4$ unit were assumed to exhibit similar bonding to those found within τ-$Zr(HPO_4)_2$ previously synthesised by Anderson *et al.*[24]. In the phosphate version the OH groups displayed hydrogen bonds to the four adjacent HPO_4 groups, contributing and accepting one hydrogen bond, forming hydrogen-bonded spirals throughout the channels. In the arsenate example there were only two OH groups involved in hydrogen bonding within the channels, a consequence of the structural constraints of including the larger arsenate rather than phosphate ion at the centre of the tetrahedra. The synthetic conditions for the two materials are

similar in that they both form in HCl media. τ-$Zr(HPO_4)_2$ produced microcrystalline powders (with small single crystals), and the products were analysed through XRD in order to solve the structure. Further analyses, in the form of joint SXD and NPD were undertaken, to isolate the hydrogen positions of the zirconium phosphate. The lattice parameters of τ-$Zr(HPO_4)_2$ (a/b = 11.26 Å, c = 10.76 Å, α/β/γ = 90°, V=1364.4 $Å^3$) are different to those of the zirconium arsenate described here. There is a discussion in the Anderson paper, of some intermediate phases, which are produced when τ-$Zr(HPO_4)_2$ is heated above 225 °C. Intermediate I, $Zr(HPO_4)_2$, had lattice parameters (a = 8.1 Å, b = 7.6 Å, c = 10.7 Å, α/β/γ = 90°, V = 678.7 $Å^3$), which are different to the zirconium arsenate. The structure that seems to be most similar to the three-dimensional zirconium arsenate is the two-dimensional hemi-hydrate of α-$Zr(HPO_4)_2.0.5H_2O$[25] (a = 9.1 Å, b = 5.3 Å, c = 15.2 Å, β = 103.8°, V = 722.9 $Å^3$), which has a similar monoclinic symmetry. The inclusion of arsenate tetrahedral groups within the framework have an effect upon the structure, which is not isotypic to the phosphate τ-$Zr(HPO_4)_2$. There are intriguing similarities but also differences in all cases between the zirconium compounds discussed, thus **VIII** appears to be a novel three-dimensional zirconium arsenate.

In view of time constraints and the small amount of material obtained from the hydrothermal reactions NPD analysis was not attempted on the crystal sample of **VIII**. If more time had been available it would have been possible to replicate this reaction to provide sufficient products to complete a joint SXD and NPD refinement in order to locate the H^+ ions with certainty and produce a comparative study of the two three-dimensional materials, $Zr(HTO_4)_2$.

The IR spectra for **VIII** (see Appendix A.4.9) revealed an O-H stretch in the regions 3569.0, 3495.7 and 3163.79 cm^{-1} associated with the OH group at the O3 site. The multiple IR peaks could be due to the O-H groups being linked to different environments within the structure of **VIII.**

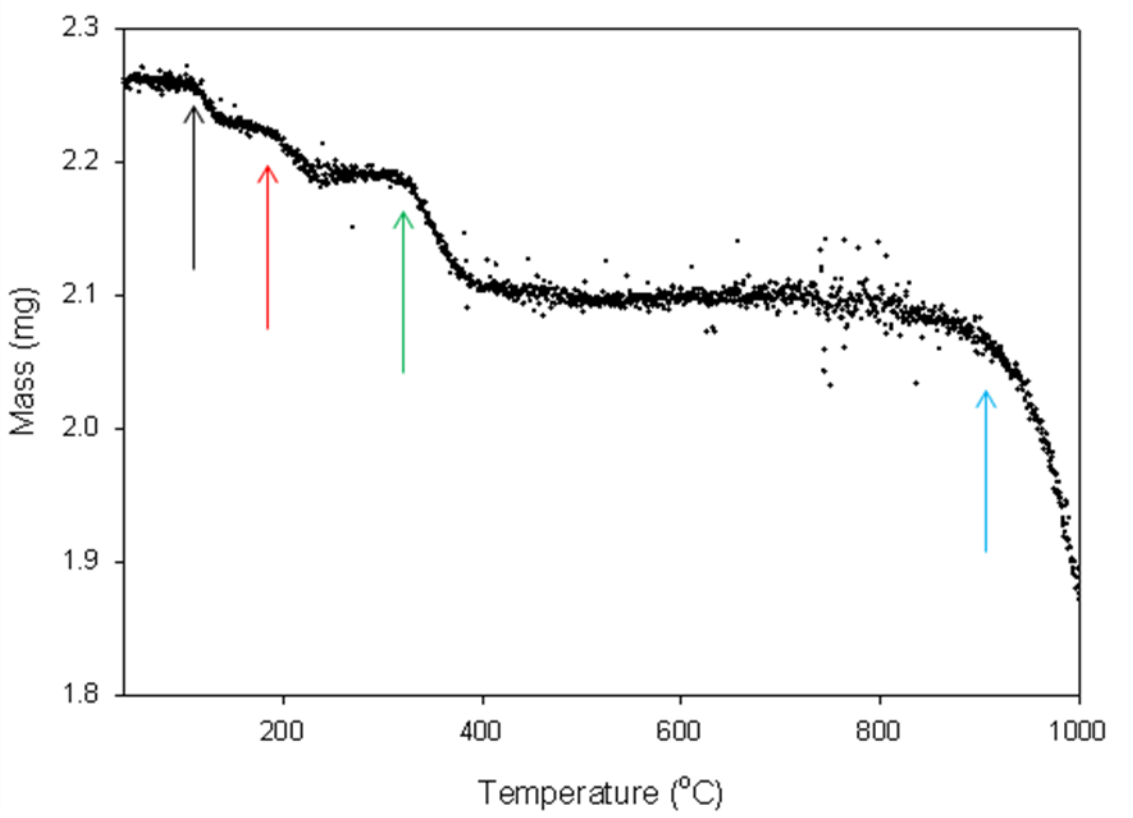

Figure 4.12: *Mass loss vs. temperature graph for $Zr(HAsO_4)_2$ (mass losses indicated by arrows)*

TGA analysis (Fig. 4.12) of the structure of **VIII** revealed three distinct losses in mass before the material was heated above 400 °C. The mass losses observed occurred at 130, 180 and 300 °C, all mutually contributing to the mass loss of one water molecule ($2HAsO_4^{2-} \rightarrow As_2O_7^{4-} + H_2O$). The staggered loss in mass suggested that the hydroxide groups in **VIII** were similar to crystal water or zeolitic water, being lost more readily, as opposed to τ-$Zr(HPO_4)_2$ where the mass loss was detected as one loss that began at 400 °C. The thermal analysis highlighted the difference in the way that the hydroxide ions are bonded within the two structures **VIII** and τ-$Zr(HPO_4)_2$. A further loss in mass is observed from 800 °C onwards, attributed to the ongoing decomposition of **VIII**. τ-$Zr(HPO_4)_2$ appeared to be stable up to 1000 °C, although two intermediate phases were noted, forming intermediate I ($Zr(HPO_4)_2$), intermediate II (ZrP_2O_7) and finally ZrP_2O_7. It can therefore be concluded that the structure of **VIII** is different to that of τ-$Zr(HPO_4)_2$, and thus a novel three-dimensional zirconium arsenate was formed as a result of hydrothermal synthesis. The presence of the larger arsenate ion formed a structurally similar material to the phosphate compound but it is not isotypic.

4.4 Compound IX: Hydrated ammonium zirconium arsenate – $Zr^{IV}_2(AsO_4)_3(NH_4)(H_2O)$

4.4.1 Synthesis

Compound **IX**, $Zr_2(AsO_4)_3(NH_4)(H_2O)$, was synthesised under hydrothermal conditions. ZrF_4 (0.1 g, 0.60 mmol, 99.9%, Aldrich) and $NH_4H_2AsO_4$ (0.287 g, 1.81 mmol, 99%, Aldrich) were dissolved in distilled water (11 mL) and the pH was altered using NH_3 solution to 9.5. The reaction was transferred to a 23 mL teflon-lined steel Parr autoclave and this vessel was heated at 175 °C for 5 days. The experiment was allowed to cool to room temperature, the solid product recovered by filtration, washed with warm water and allowed to cool in air.

4.4.2 Results and Discussion

The product of this reaction was composed entirely of octahedral shaped crystals that were picked for SXD analysis (Fig. 4.13). The reaction was ratio and pH specific to encourage the crystals to form. The results of the data collection are found in Tables 4.11 and A.4.10 in the Appendix section.

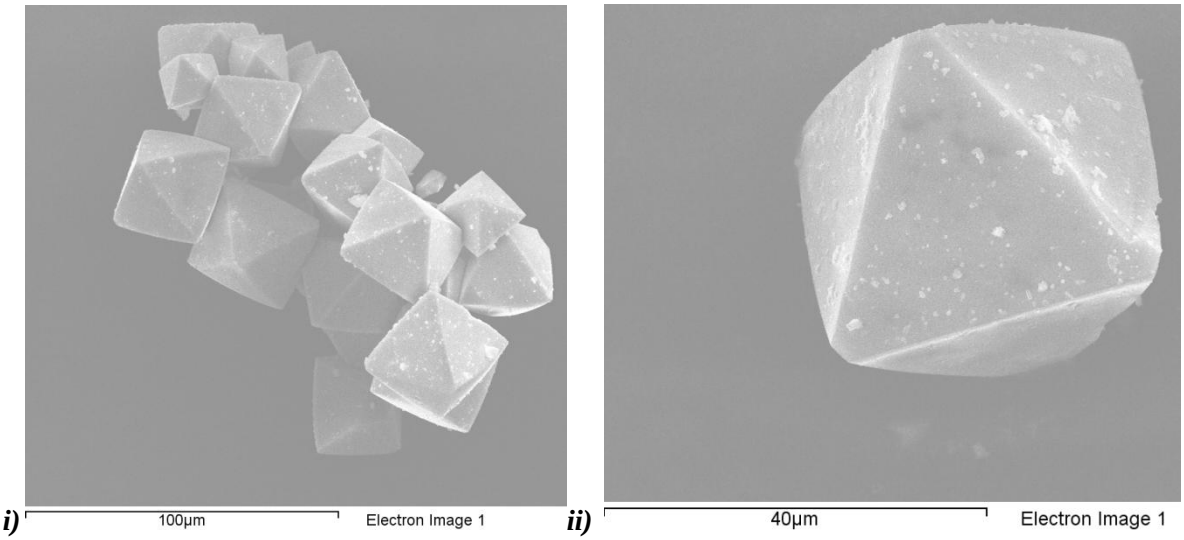

Figure 4.13: *SEM images of* ***i)*** *multiple and* ***ii)*** *single octahedral shaped $Zr_2(AsO_4)_3(NH_4)(H_2O)$ crystals*

Table 4.11: *Details of single crystal data collection for $Zr_2(AsO_4)_3(NH_4)(H_2O)$*

Molecular Formula	$\mathbf{Zr_2^{IV}(AsO_4)_3(NH_4)(H_2O)}$
Formula Weight (g)	632.558
Crystal Appearance	Diamond
Crystal Size (mm)	0.1 x 0.1 x 0.1
Crystal System	Cubic
Space Group	$P2_13$
Lattice Parameters	a = 10.5324(10) Å, α = 90°
	b = 10.5324(10) Å, β = 90°
	c = 10.5324(10) Å, γ = 90°
V (Å^3)	1168.374(19)
Z	11
Calculated density (mg/m^3)	3.379
Temperature (K)	120 K
Theta Range (°)	3.35-27.48
Wavelength (Å)	Mo *K*α (λ = 0.71073)
Number of Reflections Measured	Total – 5852, Unique – 888
$\boldsymbol{R_1}$ **[*I*>2σ (*I*)]**^{a}	0.0262
***R*1(all data)**	0.0276
$\boldsymbol{wR_2}$	0.0644
Goodness of fit indicator	0.555

The three-dimensional structure of compound **IX** was composed of zirconium-centred ZrO_6 octahedra and arsenic-centred AsO_4 tetrahedra. The zirconium units exhibited corner-sharing bonds with the arsenate tetrahedra, which caused the zirconium centre to be connected to six different arsenate tetrahedra. The oxygen ions within both types of building units exhibited bridging bonds; there were no terminal ions within the structure of **IX**. This cubic compound was also found to contain H_2O molecules and NH_4^+ cations, which occupy the small spaces between the polyhedral and tetrahedral units. The hydrogen atoms could not be placed through SXD analysis and so

assumptions have been made that they reside on the non-framework species sites. In order for the $Zr_2(AsO_4)_3^-$ unit to charge balance one NH_4^+ cation and one H_2O molecule were required, and the temperature factors associated with these ions within the SXD refinement were more suited to this assignment of atoms. Bond valence calculations[20,21] (Table 4.12) showed that the oxygen anions within the structure have typical values for divalent ions (average bond valence 1.99(6)). It was therefore assumed that there were no hydroxide or water molecules attached to the zirconium polyhedra or arsenate tetrahedra.

Table 4.12: *Bond lengths and bond valence calculations for O anions within* $Zr_2(AsO_4)_3(NH_4)(H_2O)$

Atoms	Zr-O bond length (Å)	As-O bond length (Å)	Bond Valence Zr-O	Bond Valence As-O	Total Bond Valence
O1	2.11(4)	1.67(4)	0.61	1.30	1.91
O2	2.07(4)	1.66(4)	0.68	1.34	2.02
O3	2.07(4)	1.67(4)	0.68	1.30	1.98
O4	2.03(4)	1.67(4)	0.76	1.30	2.06

The structure of **IX** is tightly-packed with no channels or cavities present. Figure 4.14 depicts the view along the *a*, *b*, and *c*-axis of **IX**. The average bond length for Zr-O is 2.07(1) Å and As-O 1.67(5) Å, typical for these types of bonding.

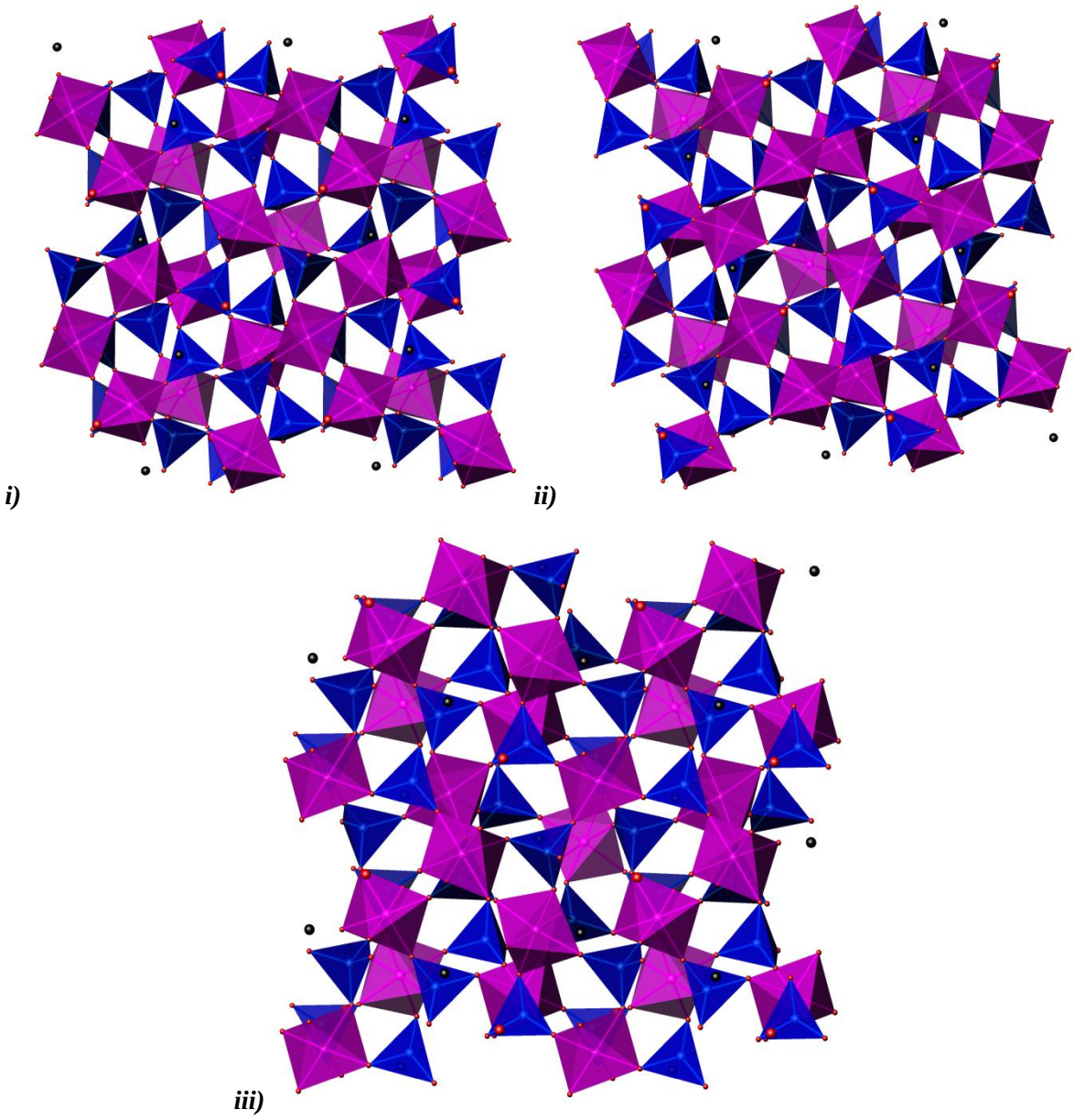

***Figure 4.14**: Structure of **IX** viewed down the **i)** a, **ii)** b, **iii)** c-axis for $Zr_2(AsO_4)_3(NH_4)(H_2O)$ [Key: blue tetrahedra - AsO_4, purple octahedra – ZrO_6, red sphere- O associated with H_2O molecules and black sphere – N associated with NH_4^+ cations both enlarged for clarity]*

The bond valence of the zirconium cations was anticipated to be +4 and BV calculations identified that this assumption was correct (Table 4.13).

Table 4.13**: Bond lengths and bond valence values for Zr within **IX

Zr cation	Atoms	Zr-O bond length (Å)	Zr-O Bond Valence
Zr1	O1	2.11(4)	0.62
Zr1	O1	2.11(4)	0.62
Zr1	O1	2.11(4)	0.62
Zr1	O4	2.03(4)	0.77
Zr1	O4	2.03(4)	0.77
Zr1	O4	2.03(4)	0.77
Total			**Zr1 - 4.16**
Zr2	O2	2.07(4)	0.68
Zr2	O2	2.07(4)	0.68
Zr2	O2	2.07(4)	0.68
Zr2	O3	2.06(4)	0.69
Zr2	O3	2.06(4)	0.69
Zr2	O3	2.06(4)	0.69
Total			**Zr2 - 4.13**

The two zirconium octahedra have bond angles that average, O-Zr1-O = 90.19° and O-Zr2-O = 92.01°, which exhibit mild distortion from their expected shape (Fig. 4.15). The AsO_4 units have an average bond angle of 109.96(5) °, as expected for tetrahedral units.

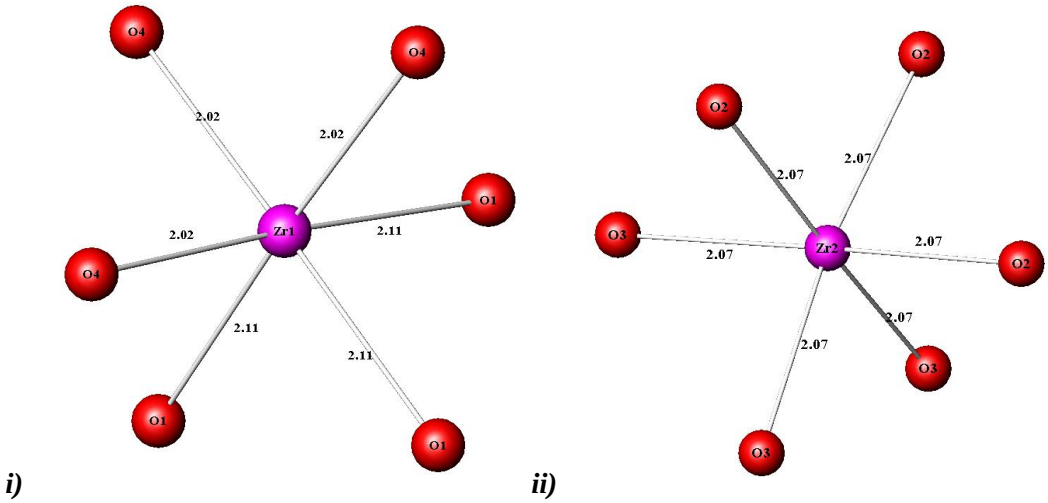

***Figure 4.15**: Zirconium octahedra ZrO_6 for **i)** Zr1 and **ii)** Zr2 (lengths in Å)*

Fluorine was contained within the starting material in this reaction (ZrF_4), but it was not incorporated into the structure. It has been assumed that it played a vital role in improving the crystallinity of **IX**. Compound **IX** was also found to form with a variety of alternative starting materials such as As_2O_5, $NH_4H_2AsO_4$ or H_3AsO_4, and through alterations to the pH of solution (as long as the reaction was alkaline and contained NH_4^+). A solution of exclusively NH_3 was used to replace the water in the reaction this did not produce the same structure, so it is clear that the incorporation of water was key to the synthesis of this material.

EDX analysis of the octahedral shaped crystals (see Appendix A.4.11) confirmed the presence of zirconium, arsenic and oxygen, which was the expected result. The atomic weight percentages given illustrate that there was more arsenic than zirconium within the sample (2:3 ratio of Zr:As), and a ratio of almost four oxygen for one arsenic atom, which agreed with the structural formula relatively well (13.7%Zr:18.5%As:67.8%O. This suggests a ratio of 2O:3As:10O), although this data is qualitative.

TGA analysis (Fig. 4.16) demonstrated a mass loss of 2% of the overall molecular weight at 150 °C, which corresponded to the loss of a formula unit of H_2O from the framework. From 150 °C onwards a further loss of 2 % was observed associated with the loss of NH_4^+ cations. At 480 °C all of the H_2O and NH_4^+ had been lost from the structure of **IX**. The final mass loss began at 650 °C where a loss of 14% was displayed, contributing to the decomposition of the framework. Variable

temperature PXD would be beneficial here to observe the changes within the structure as a result of increased temperature. Unfortunately, time constraints meant that this was not possible.

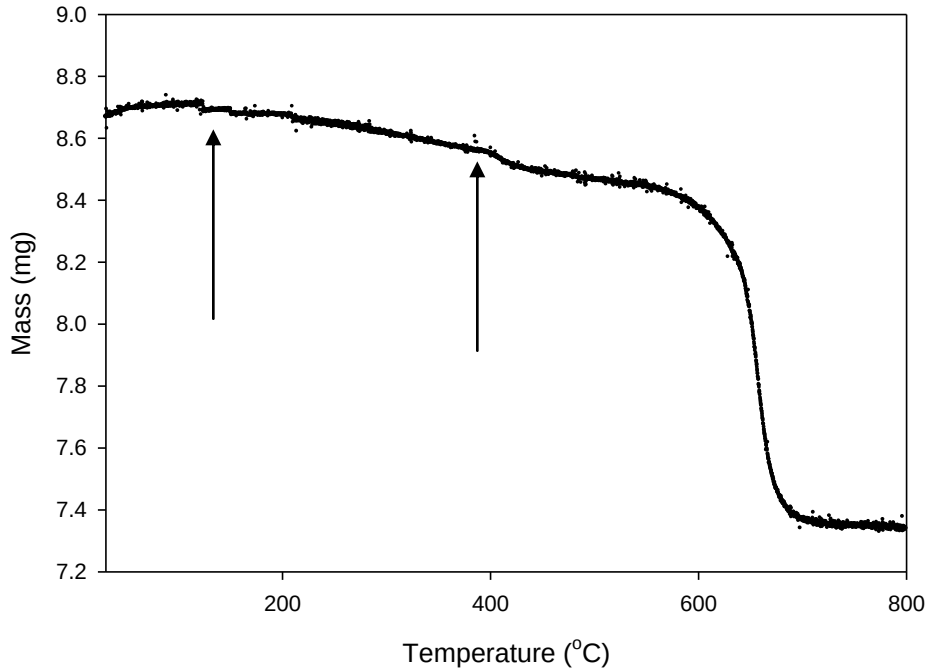

Figure 4.16: *Mass vs. temperature graph for **IX** (mass losses indicated by arrows)*

IR analysis (see Appendix A.4.12) confirmed the presence of NH_4^+ cations through absorption in the N-H stretching region (3181 and 1421.7 cm^{-1}), and H_2O was noted in the stretching region 3478.44 cm^{-1}. PXD analysis produced a pattern indicating that the sample of **IX** was phase pure. The defined crystal morphology of **IX**, improved the PXD powder pattern obtained.

Compound **IX** is isostructural to the mineral Langbeinite, $K_2Mn_2(SO_4)_3$, crystallising in the cubic $P2_13$ space group. The Langbeinite family is a cubic structural modification of the Nasicon (sodium super ion conductor) structure type ($XM_2(TO_4)_3$) discussed later in this Chapter (section 4.6, **X**). The sulphate mineral Langbeinite, can form a variety of isostructural compounds composed of the general formula $M^I{}_2M^{II}{}_2(SO_4)_3$ (where M^I=K, Rb, Cs, Tl, NH_4 and M^{II}=Ca, Mg, Co, Ni, Zn, Cd, or Fe). The sulphate group can be substituted for phosphorous and arsenic TO_4 as for example in the case of $K_2FeZr(PO_4)_3$[26] and in the structure of **IX**. The compound

$(NH_4)(H_3O)Ti_2(PO_4)_3$, is a structure that contains mixed valence (III/IV) titanium and includes M^I ions similar to that of **IX**[27]. The characteristic feature present within the Langbeinite and Nasicon structures is the presence of charge balancing cations within the framework. The difference between the two compounds is that the former contains two interstitial holes, whereas the latter generally has four. The Langbeinite family require all of these framework holes to be filled whereas the Nasicon material can exist when some areas are not packed with cations. These attributes affect the potential applications of the two materials. Langbeinite materials are capable of containing toxic cations (radioactive waste), as these ions remain within the holes and cannot migrate throughout the structure. This family of materials have further potential in applications such as plasma display panel (PDP) phosphors for use in wall mounted flat screen televisions. Research has shown that by doping lanthanide elements into this structure type it can act as the host in the preparation of PDPs[28].

4.5 Compound X – Ammonium Zirconium Arsenate $Zr^{IV}_2(AsO_4)_3(A)$ ($A = NH_4^+/Cs^+$)

4.5.1 Synthesis

Compound **X** with $A = NH_4^+$, was produced from a reaction involving ZrF_4 (0.1g, 0.60mmol, 99.9% Aldrich), H_3AsO_4 (0.121 g, 0.85 mmol, 75% wt., Aldrich) and 3, 5, diamino-1, 2, 4, triazole (DAT) (0.06 g, 0.61 mmol, 99% Aldrich), which were weighed and dissolved in water (11 mL) and left to stir for 30 minutes. The reagents were then transferred into a 23 mL teflon-lined steel Parr autoclave, heated to 190 °C and held at this temperature for 7 days. The reaction was allowed to cool slowly to room temperature, the solid product filtered, washed with warm water, and dried at 80 °C for 3 hours.

Compound **X** with $A = Cs^+$, was isolated from a reaction of ZrF_4 (0.1g, 0.60mmol, 99.9% Aldrich), H_3AsO_4 (0.257g, 1.81mmol, 75% wt. Aldrich) and CsOH (0.181g, 1.21mmol, 99% Aldrich), that were weighed and dissolved in water (11 mL) and left to stir for 30 minutes. The solution was transferred into a 23 mL teflon-lined steel Parr autoclave, heated at 140 °C and held for 14 days. The steel autoclave was allowed to cool slowly to room temperature, the solid reaction product was then filtered, washed with warm water, and dried at 80 °C for 3 hours.

4.5.2 Results and Discussion

Single crystals of compound **X** were obtained through hydrothermal reactions. The formation of both compounds involved the arsenic source H_3AsO_4, but alternative reagents added to the systems resulted in the incorporation of different cations within the material (NH_4^+/Cs^+). The structures were chemically similar, thus the framework discussion assumes that it would be possible for several cationic species to reside within the channels.

Suitably sized single crystals were isolated from the two samples and analysed *via* SXD analyses. The crystals were viewed under an SEM microscope and images are depicted below (Fig. 4.17). The images show that the two types of crystals have a similar morphology regardless of the *A* cation present. There appears to be a growth defect, as the crystals were found to have empty spaces and chunks missing from their faces. The crystals obtained were all slightly different, rather than uniform in their shape and size. These defects caused the SXD analyses to have enlarged R_1

values. The results from the SXD can be observed in Table 4.14 and in the Appendix section A.4.13 and A.4.16.

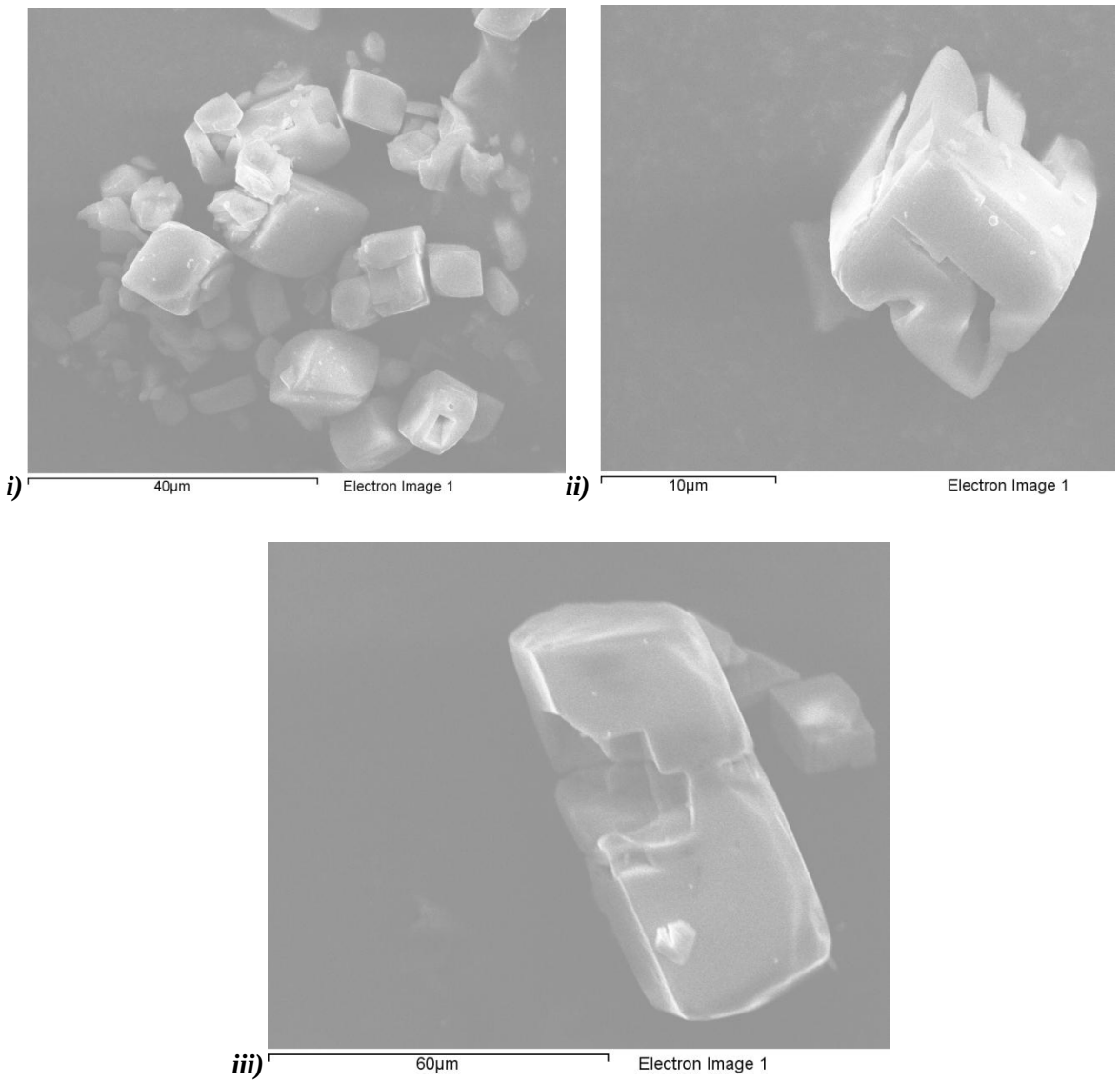

Figure 4.16: *SEM images of* ***i)*** *the bulk and* ***ii)*** *single rectangular crystals of* $(NH_4)Zr_2(AsO_4)_3$ *and* ***iii)*** $CsZr_2(AsO_4)_3$

Table 4.14: *Details of single crystal data collection for (A)$Zr_2(AsO_4)_3$*

Empirical Formula	**$(NH_4)Zr^{IV}_2(AsO_4)_3$**	**$(Cs)Zr^{IV}_2(AsO_4)_3$**
Formula Weight (g)	614.547	729.418
Crystal Appearance	Rectangular blocks	Rectangular blocks
Crystal Size (mm)	0.05 x 0.05 x 0.08	0.1 x 0.1 x 0.3
Crystal System	Trigonal	Trigonal
Space Group	$R\bar{3}c$	$R\bar{3}c$
Lattice Parameters	a = 9.0245(7) Å, α = 90°	a = 8.8919(4) Å, α = 90°
	b = 9.0245(7) Å, β = 90°	b = 8.8919(4) Å, β = 90°
	c = 24.7799(16) Å, γ = 120°	c = 25.727(2) Å, γ = 120°
V (Å^3)	1747.7(2)	1761.63(2)
Z	10	3
Calculated density (mg/m^3)	3.496	2.07
Temperature (K)	120	120
Theta Range (°)	4.2-27.71	3.08-27.48
Wavelength (Å)	Mo *K*α (λ = 0.71073)	Mo *K*α (λ = 0.71073)
Number of Reflections Measured	Total – 3460, Unique – 458	Total – 4188 , Unique – 457
R_1 [I>2σ (I)]^a	0.0518	0.049
***R*1(all data)**	0.0802	0.071
wR_2	0.0869	0.098
Goodness of fit indicator	1.106	1.122

Single crystals of **X** were analysed *via* SXD and bond valence calculations[20,21] were completed to assess the presence of mono and divalent anions within the compound (Table 4.15). Regardless of the assumption that sites O1 and O2 were oxygen or fluoride ions the average bond valence obtained was that of divalent anions assumed to be oxygen (A = NH_4, BV(O) = 2.02, A = Cs^+, BV(O) = 1.97(2)).

Table 4.15: *Bond lengths and bond valence calculations for O anions within* $(A)Zr_2(AsO_4)_3$

Atoms	Zr-O bond length (Å)	As-O bond length (Å)	Bond Valence Zr-O	Bond Valence As-O	Total Bond Valence
[A=NH_4^+] O1	2.07(6)	1.66(6)	0.68	1.34	2.02
[A=NH_4^+] O2	2.05(7)	1.67(5)	0.72	1.30	2.02
[A=Cs^+] O1	2.07(7)	1.68(7)	0.68	1.27	1.95
[A=Cs^+] O2	2.05(7)	1.68(6)	0.72	1.27	1.99

The calculated BV for zirconium cations indentified that the metal was in a +4 oxidation state (Table 4.16).

Table 4.16: *Bond lengths and bond valence values for Zr within* ***X***

Atoms	Zr-O bond length (Å)	Bond Valence Zr-O
[A=NH_4^+] O1	2.07(6)	0.68
[A=NH_4^+] O1	2.07(6)	0.68
[A=NH_4^+] O1	2.07(6)	0.68
[A=NH_4^+] O2	2.05(7)	0.72
[A=NH_4^+] O2	2.05(7)	0.72
[A=NH_4^+] O2	2.05(7)	0.72
Total		**4.2**
[A=Cs^+] O1	2.07(7)	0.67
[A=Cs^+] O1	2.07(7)	0.67
[A=Cs^+] O1	2.07(7)	0.67
[A=Cs^+] O2	2.05(7)	0.71
[A=Cs^+] O2	2.05(7)	0.71
[A=Cs^+] O2	2.05(7)	0.71
Total		**4.16**

The three-dimensional structure of **X** is composed of zirconium-centred ZrO_6 octahedra and arsenic-centred AsO_4 tetrahedra. The Zr-O-As groups are connected through corner-sharing bonds between the tetrahedral and polyhedral units. The oxygen anions within these two building units are fully connected by means of Zr-O-As bonding, presenting a closely-packed structure with no terminal groups. The zirconium polyhedra are surrounded by six different arsenate tetrahedra, forming a circular unit, which can be seen in Figure 4.18.*ii*. Channels that formed within compound **X** are filled with cations, observed when the structure is viewed down the *a/b*-axis (Fig. 4.18.*i*). The presence of the ammonium/caesium cations charge balances the $Zr_2(AsO_4)_3^-$ framework. Further voids exist when the structure is viewed through the *c*-axis (Fig. 4.18.*iii*), that did not include any ions, lying empty.

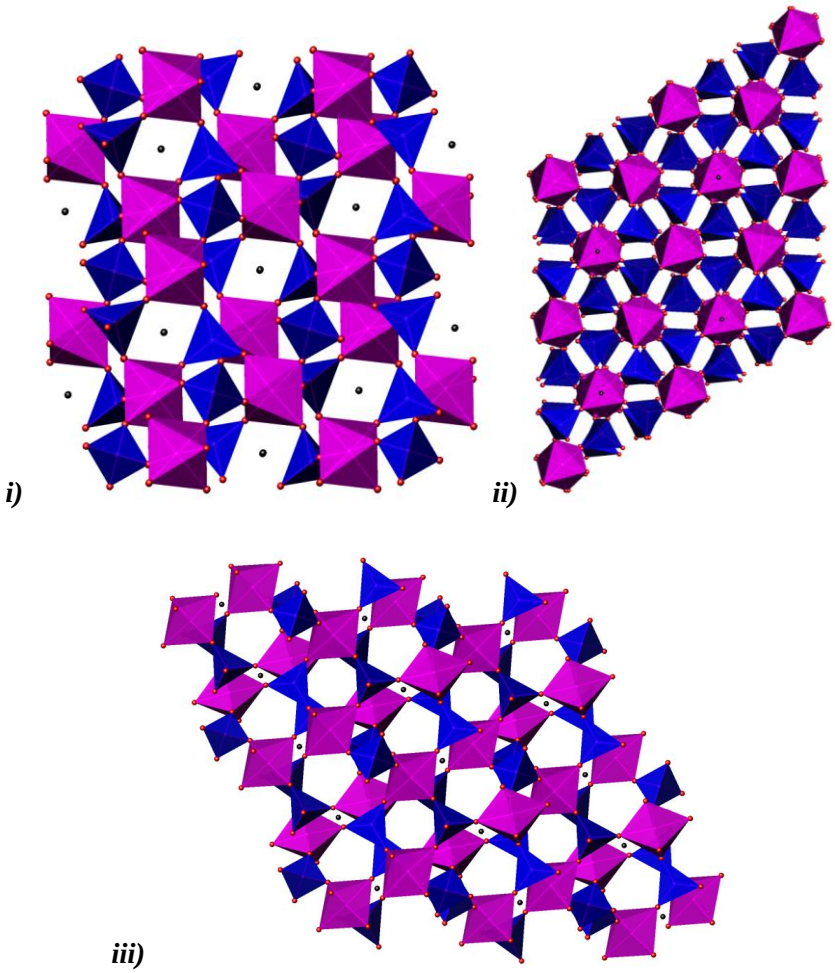

Figure 4.18: *Structure of **X** viewed down the **i)** a (b-axis identical) and **ii)** c-axis; and **iii)** the empty channels within structure of **X** [Key: purple octahedra – ZrO_6, Blue tetrahedra – AsO_4; Black spheres - NH_4^+/Cs^+ cations]*

EDX analysis was completed to clarify the elements present within **X** and Zr, As, and O were confirmed in both samples, as well as Cs^+ when $A = Cs^+$ ($A = NH_4^+$; Zr-16.8%, As-19.9%, O-63.4% leading to ~2Zr:2.4As:7.5O; $A = Cs^+$; Cs-23.4%, Zr-21.3%, As-22.8%, O-32.5% leading to ~ 1Cs:1Zr:1As:3O). Tables A.4.14 and A.4.17 in the Appendix section illustrated that in both structures the quantities of zirconium were marginally lower than that of arsenic, in agreement with the structural formula. The largest atomic percentage was attributed to the oxygen anions, although this data is qualitative.

IR analysis was completed through the use of KBr disks in order to detect whether NH_4^+/Cs^+ cations were present within the channels of **X**. When $A = NH_4^+$, peaks at 3240.9 and 1419.9 cm^{-1} associated with the N-H stretching region of NH_4^+ cations were isolated (Appendix 4.15). In the crystal sample when $A = Cs^+$, the only peak observed was the As-O stretching region at 854.16 cm^{-1} which highlighted that the other cations such as NH_4^+ were not present within the framework channels (Appendix 4.18).

TGA analysis was completed on **X** when $A = NH_4^+$ and indicated a mass loss typical of an NH_4^+ cation was lost between 480-685 °C (Fig. 4.19). This is higher than the expected loss of water within framework materials (100-300 °C), again amplifying the presence of NH_4^+, rather than water within the structure of **X**. The ammonium cation was very tightly bound in **X,** illustrated by the elevated temperature at which it was lost. **X** was stable up to 800 °C when the material began to exhibit a mass loss associated with structural decomposition. TGA analysis was completed on a sample of **X** when $A = Cs^+$, but the mixed nature of the product (single crystals within a powder of starting materials and zirconium arsenates) inhibited the technique from showing the loss of the caesium cation from the structure. The similarities in the two samples of **X** would suggest that the caesium cation would be lost at a comparable temperature to the NH_4^+ (lost at ~ 500 °C), although this assumption could not be tested.

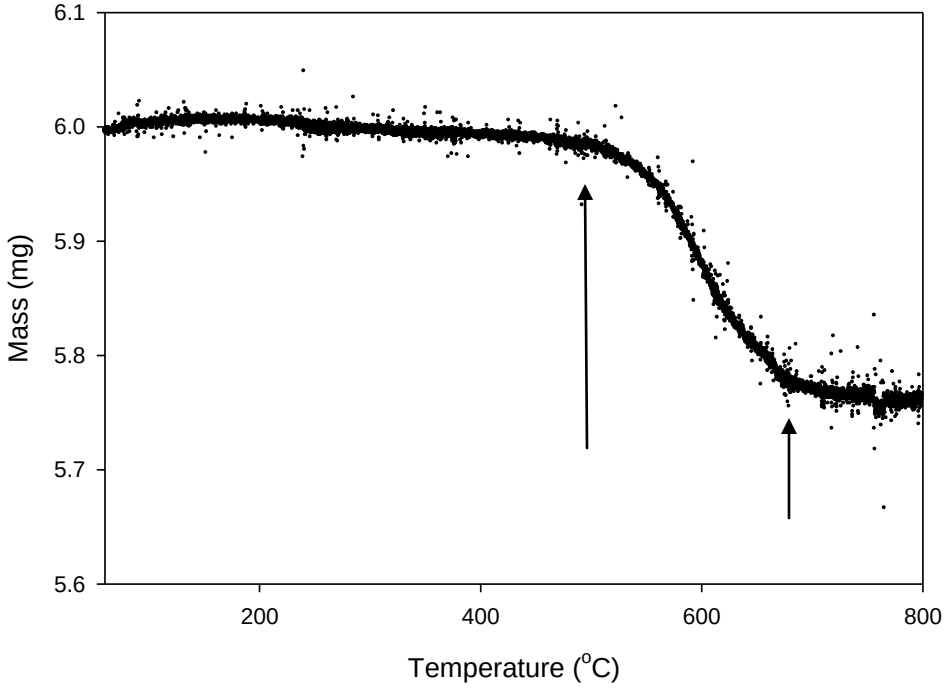

Figure 4.19: *Mass vs. Temperature graph for compound **X**, A = NH_4^+ (mass loss indicated by arrows)*

Compound **X** where *A* = Cs^+, has previously been synthesised in powder form by Chernoruukov *et al.*[29]. It is detailed within this thesis as a thorough literature review revealed that SXD analysis had not been performed. These materials belong to the Nasicon family $AZr_2(PO_4)$, where monovalent cations charge balance the negatively charged framework; *A* = Li^+ [30], Na^+, K^+, Rb^+, Cs^+, $Ca^+_{0.5}$, $Sr^+_{0.5}$, $Ba^+_{0.5}$ etc. The arsenate materials have received less interest, but are known for *A* = Li^+, K^+, Na^+, Rb^+, Cs^+ [31]; and in the form $AZr_4(AsO_4)_6$ for *A* = Ca^{2+}, Sr^{2+}, Ba^{2+}, Mn^{2+}, Co^{2+}, Cu^{2+} and Zn^{2+} [29]. The flexibility within the structures provides a pathway for multiple element substitution, which has led to a vast number of analogous materials. Structural modifications exist as highlighted within Section 4.4.2 for the Langbeinite frameworks that contain two less interstitial holes in comparison with the Nasicon materials. The importance of the phosphate compounds as a family of alkali-ion conductors (with the lithium[30] and sodium[32] phases being the most investigated) has been established. The Nasicon materials have also received significant attention as a result of their applications in areas such as low thermal expansion[33], nuclear waste storage[34] and thermal shock resistance[35] applications.

4.6 Experimental Summary

The research presented in this chapter describes a range of powder and crystal products of known as well as novel structure types.

Previous research into cerium phosphate and arsenate materials provided insight into the reactivity of $CeF_{3/4}$ and for this reason ZrF_4 was employed in all reactions detailed within this research. This starting material was very reactive, producing the most crystalline samples of all the elements studied. A large number of zirconium reactions produced the same structure by employing alternative synthetic routes and the morphology of the crystalline materials was very specific in all cases. The defined shapes aided rapid analysis of the crystal products and if further investigations into this system were to be undertaken this should inform future work. The reactions referred to in this section can be found in Table 4.1 in the introduction to this chapter.

The use of solvents to replace water as the reaction media was relatively successful for zirconium syntheses. Structure **VI** was the product of a synthesis in NH_3 solution, and **VIII** in HCl. Similar reactions were undertaken with phosphate starting material, regardless of the reagents involved, $Zr^{IV}F_2(PO_4, HPO_4)(NH_4, H_2O)_3$ (previously synthesised by Redrup[22]) was the major product in NH_3 solution, whilst reactions proceeding in HCl created basic zirconium phosphates, such as $Zr(HPO_4)_2.H_2O$[36]. There was only one example of a zirconium arsenate that housed fluoride anions within its structure. Varying the ratio of ZrF_4 could present further materials that fulfil these criteria, since the introduction of more ZrF_4 will provide greater volumes of fluoride. Future research efforts in this area could provide interesting results. The pH of the solution had a large effect on the formation of crystals. Acidic and neutral pH (altered by the addition of HCl/NH_3 solutions) reactions formed powder phases such as $ZrAsO_4$, whereas alkaline media produced compound **VI**. Reactions using phosphate starting materials formed $Zr^{IV}F_2(PO_4, HPO_4)(NH_4, H_2O)_3$ in the alkaline pH range, and layered phosphates in more acidic conditions.

The addition of organic templates to these reactions was successful in producing compounds that housed these ions (detailed later in Chapter 6). In the vast majority of cases their presence aided the formation of compound **VII**. The templating agents TMAC, TEAOH, TMAOH, and OAD always produced a phase pure crystalline product of **VII** in the arsenate reactions. Varying the organic template to EDA or PIP generated powder starting materials for both the phosphate and arsenate reactions. The use of DABCO produced $Zr(OH)(PO_4)$ as the major product

in phosphate syntheses and a mixture of zirconium arsenates when arsenic starting materials were used. The temperature of the reaction also played an important role within these reactions. Crystalline products were obtained in both high and low temperature forms. In the case of structure **VIII** replication of the reaction at higher temperatures produced the alternative α-zirconium arsenate ($Zr(HAsO_4)_2.H_2O$).

The synthetic reactions employed the use of ZrF_4, which formed well-known phases of simple zirconium phosphates. Synthetic pathways involving phosphate reagents were less reactive than arsenic compounds, as was the case for reactions involving CeF_4. These results suggest that this reaction route does not favour the formation of crystal reaction products when MF_4 and phosphate starting materials are combined.

4.7 Conclusions

Six novel (or previously not synthesised or analysed as single crystals) three-dimensional zirconium arsenate frameworks have been created through the introduction of ZrF_4 into the reaction system. The majority of the zirconium materials did not incorporate fluoride ions into their frameworks, unlike the cerium structures previously discussed in Chapter 4, which produced three-dimensional frameworks. The only exception to this rule was compound **VII**, which has fluoride present as bridging bonds between zirconium centres (Zr-F-Zr). The structure of **VII** does not include NH_4^+, which would promote terminal fluorine anions within the zirconium polyhedra through the introduction of F----HNH_3 hydrogen bonds. This bonding can lead to less complex structures as the terminal fluoride ions inhibit the replication of the structure in one or two dimensions. If the NH_4^+ cations are removed from the synthetic proceedings the fluoride is likely to form bridging links between metal centres. The presence of ammonium cations has also been found to create smaller channels within the structure (due to the size of the cations) as they are so strongly bonded, which can reduce the potential applications of the material.

The lack of fluorine within the zirconium arsenate materials indicates that these fluoride ions have a mineralising effect within these reactions. The inclusion of organic templates produced compound **VII**. This suggests that the templates employed provide a pathway for the formation of the fluorinated structure of **VII**. The synthetic research completed for this thesis has included the templates: EDA, TMEDA, DETA, DAT, AEP, PHEN, PIP, OAD, TMAC, TMAOH and TEAOH.

These reagents have been tested at various temperatures (140-200 °C) and reaction lengths (3-14 days) and only crystals of **VII** and **XVI** (discussed in Chapter 6) were observed of varying quality (longer reaction times promoted growth of good quality crystals until the reactions lasted more than 7 days when the products exhibited twinning). The majority of reactions that included an organic template produced crystals of compound **VII**, $Zr(AsO_4)F(H_2O)$ and their substitution had no effect on the creation of **VII**. The reaction required the presence of these templates as their removal resulted in powdered samples.

When H_2O and NH_4^+ were present within the starting materials, the reaction product was always $Zr^{IV}_2(AsO_4)_3(NH_4)(H_2O)$, **IX**, regardless of the arsenic starting material. These reactions were all alkaline. This indicated the stability of the compound in alkaline media. In ammonium solution the phosphate analogue of **IX** (previously synthesised by Redrup[22]) was also the product regardless of the phosphate starting material. Variations to the reaction (temperature, duration *etc.*) resulted in **IX,** which demonstrated the ease with which it formed.

Zirconium phosphate frameworks have typically incorporated HF or NH_4F into the reaction synthesis rather than ZrF_4[37]. In this work the introduction of ZrF_4, establishing a large amount of fluoride anions in the reaction mixture, produced an alternative reaction pathway that led to the production of novel three-dimensional frameworks.

4.8 References

(1) Vivani, R.; Alberti, G.; Costantino, F.; Nocchetti, M. *Microporous and Mesoporous Materials* **2008**, *107*, 58-70.

(2) Brunet, E.; Alhendawi, H. M. H.; Cerro, C.; de la Mata, M. J.; Juanes, O.; Rodriguez-Ubis, J. C. *Angewandte Chemie-International Edition* **2006**, *45*, 6918-6920.

(3) Geng, L. N.; Li, N.; Dai, N.; Wen, X. F.; Zhao, F. L.; Li, K. A. *Colloids and Surfaces B: Biointerfaces* **2003**, *29*, 81-88.

(4) Alberti, G.; Cavalaglio, S.; Marmottini, F.; Matusek, K.; Megyeri, J.; Szirtes, L. *Applied Catalysis A: General* **2001**, *218*, 219-228.

(5) Bortun, A. I.; Clearfield, A.; Suárez, M.; Llavona, R.; Rodríguez, J. *Materials Chemistry and Physics* **1998**, *55*, 152-154.

(6) Shannon, R. D. *Acta Crystallographica Section A* **1976**, *32*, 751-767.

(7) Chakrabarti, S.; Pati, S. K.; Green, M. A.; Natarajan, S. *European Journal of Inorganic Chemistry* **2003**, 3820-3825.

(8) Beitone, L.; Marrot, J.; Lorentz, C.; Taulelle, F.; Loiseau, T.; Ferey, G. *Solid State Sciences* **2001**, *3*, 641-647.

(9) Lakiss, L.; Simon-Masseron, A.; Gramlich, V.; Chaplais, G.; Patarin, J. *Microporous and Mesoporous Materials* **2008**, *114*, 82-92.

(10) Loiseau, T.; Ferey, G. *Journal of the Chemical Society-Chemical Communications* **1992**, 1197-1198.

(11) Yin, X. T.; Nazar, L. F. *Journal of the Chemical Society-Chemical Communications* **1994**, 2349-2350.

(12) Serpaggi, F.; Loiseau, T.; Taulelle, F.; Ferey, G. *Microporous and Mesoporous Materials* **1998**, *20*, 197-206.

(13) Loiseau, T.; Ferey, G. *Acta Crystallographica Section C-Crystal Structure Communications* **2005**, *61*, M315-M317.

(14) Sung, H. H. Y.; Yu, J. H.; Williams, I. D. *Journal of Solid State Chemistry* **1998**, *140*, 46-55.

(15) Poojary, D. M.; Zhang, B. L.; Clearfield, A. *Journal of the Chemical Society-Dalton Transactions* **1994**, 2453-2456.

(16) Kemnitz, E.; Wloka, M.; Trojanov, S.; Stiewe, A. *Angewandte Chemie-International Edition in English* **1996**, *35*, 2677-2678.

(17) Wloka, M.; Troyanov, S. I.; Kemnitz, E. *Journal of Solid State Chemistry* **1998**, *135*, 293-301.

(18) Wloka, M.; Troyanov, S. I.; Kemnitz, E. *Journal of Solid State Chemistry* **2000**, *149*, 21-27.

(19) Dong, J. X.; Liu, L.; Li, J. P.; Li, Y.; Baerlocher, C.; McCusker, L. B. *Microporous and Mesoporous Materials* **2007**, *104*, 185-191.

(20) Brown, I. D.; Altermatt, D. *Acta Crystallographica Section B-Structural Science* **1985**, *41*, 244-247.

(21) Brese, N. E.; O'Keeffe, M. *Acta Crystallographica Section B-Structural Science* **1991**, *47*, 192-197.

(22) Redrup, K. V., *Synthesis and Characterisation of new Framework Materials,* PhD, University of Southampton, **2009**.

(23) Curry, N. A.; Jones, D. W. *Journal of the Chemical Society a -Inorganic Physical Theoretical* **1971**, 3725-&.

(24) Andersen, A. M. K.; Norby, P.; Hanson, J. C.; Vogt, T. *Inorganic Chemistry* **1998**, *37*, 876-881.

(25) Alberti, G.; Costantino, U.; Millini, R.; Perego, G.; Vivani, R. *Journal of Solid State Chemistry* **1994**, *113*, 289-295.

(26) Orlova, A. I.; Trubach, I. G.; Kurazhkovskaya, V. S.; Pertierra, P.; Salvadó, M. A.; García-Granda, S.; Khainakov, S. A.; García, J. R. *Journal of Solid State Chemistry* **2003**, *173*, 314-318.

(27) Fu, Y. L.; Xu, Z. W.; Ren, J. L.; Ng, S. W. *Acta Crystallographica Section E-Structure Reports Online* **2005**, *61*, I158-I159.

(28) Zhang, Z.-J.; Yuan, J.-L.; Chen, H.-H.; Yang, X.-X.; Zhao, J.-T.; Zhang, G.-B.; Shi, C.-S. *Solid State Sciences* **2009**, *11*, 549-555.

(29) Chernorukov, N. G.; Korshunov, I. A.; Prokofyeva, T. V. *Kristallografiya* **1978**, *23*, 844-845.

(30) Catti, M.; Comotti, A.; Di Blas, S. *Chemistry of Materials* **2003**, *15*, 1628-1632.

(31) Chakir, M.; Jazouli, A. E.; Waal, D. d. *Materials Research Bulletin* **2003**, *38*, 1773-1779.

(32) Losilla, E. R.; Aranda, M. A. G.; Bruque, S.; Sanz, J.; Paris, M. A.; Campo, J.; West, A. R. *Chemistry of Materials* **2000**, *12*, 2134-2142.

(33) Woodcock, D. A.; Lightfoot, P.; Ritter, C. *Chemical Communications* **1998**, 107-108.

(34) Bois, L.; Guittet, M. J.; Carrot, F.; Trocellier, P.; Gautier-Soyer, M. *Journal of Nuclear Materials* **2001**, *297*, 129-137.

(35) Yoon, C. S.; Kim, J. H.; Kim, C. K.; Hong, K. S. *Materials Science and Engineering B-Solid State Materials for Advanced Technology* **2001**, *79*, 6-10.

(36) Smith, G. D.; Clearfield, A. *Inorganic Chemistry* **1969**, *8*, 431-436.

(37) Wang, D.; Yu, R. B.; Kumada, N.; Kinomura, N. *Chemistry of Materials* **2000**, *12*, 956-960.

CHAPTER FIVE

HAFNIUM PHOSPHATE AND ARSENATE MATERIALS

5.0 Introduction

The investigations detailed within this chapter concentrate on the use of hafnium (HfF_4) as the starting material in the production of novel hafnium phosphate and arsenate materials. When alternative oxidation states were tested within research described elsewhere in this study (CeF_3 and CeF_4 with cerium), the +4 oxidation state was found to be the most successful starting reagent. This finding was used to inform the choice of HfF_4 as the reagent to be used within the synthetic reactions.

The Group four elements hafnium and zirconium are chemically similar and commonly lead to isotypic structures. The layered compounds α-$Hf(HPO_4)_2.H_2O$[1] and γ-$Hf(PO_4)(H_2PO_4).2H_2O$[2] are analogous to the zirconium materials described within chapter 4, and have received scientific research interest in view of their abilities to exchange protons for cations (leading to lithium ion conductors[3]), and intercalate polar molecules between their layers. Further hafnium and zirconium phosphates have demonstrated high levels of chemical and thermal stability[4], for example the barium hafnium phosphates have the ability to form solid solutions with actinide phosphates revealing them to be suitable nuclear waste storage media[5,6].

Recent scientific research has focussed upon doping hafnium into compounds to improve their potential applications and through reactions that involve zirconium materials have been produced that emit UV radiation. Potential applications for these materials include the replacement of X-ray by UV images in radiographic processes[7]. Hafnium doped β-$Zn_3(PO_4)_2$ shows long-lasting phosphorescence (LLP) with practical applications such as emergency lighting and road signs[8].

Reactions that incorporated hafnium, utilised synthetic conditions that covered the same range of temperature, ratio, pH, reaction length and solvent as undertaken for the zirconium and cerium materials. SXD was the primary means of analysis of the crystals produced, although other methods already discussed in relation to zirconium (such as EDX, IR, TGA, *etc.*), contributed to the analyses and assumptions made for these new materials.

Syntheses involving hafnium typically involved HfF_4 and a phosphate or arsenate source (H_3TO_4/$NH_4H_2TO_4$/T_2O_5) mixed in a solvent (~10 mL) for thirty minutes to ensure optimum reagent mixing, before placing the reaction into a Teflon-lined Parr autoclave. The mixture was then heated in an oven to the desired temperatures, left to react, typically for 5 days, allowed to cool, and the

solid product separated *via* filtration and analysed. A large number of single crystal and powder products were found, and a comprehensive summary is detailed in Table 5.1 to provide an understanding of the system. The novel materials synthesised within this chapter have formed both one and three-dimensional crystal systems, demonstrating the structural diversity of these hafnium materials.

Table 5.1: *Synthetic conditions for successful and similar hafnium structures (all Parr autoclaves used 23 mL)*

Reaction No.	Synthesis	Temperature (°C)	Reaction time (days)	Single Crystal/ Powder	Product	Thesis	Same structure as Reaction No.
1	HfF_4 (0.1 g); P_2O_5 (0.17 g); NH_3 (10 mL);	140	5	Rod	$Hf^{IV}F_2(PO_4,HPO_4,H_2PO_4)_2(NH_4, H_2O)_3$ (**XI**)	5.1	2, 3
2	HfF_4 (0.1 g); P_2O_5 (0.17 g); NH_3 (10 mL);	175	5	Rod	$Hf^{IV}F_2(PO_4,HPO_4,H_2PO_4)_2(NH_4, H_2O)_3$ (**XI**)	5.1	1, 3
3	HfF_4 (0.1 g); H_3PO_4 (0.11 g); NH_3 (10 mL);	140	5	Rod	$Hf^{IV}F_2(PO_4,HPO_4,H_2PO_4)_2(NH_4, H_2O)_3$ (**XI**)	5.1	1, 2
4	HfF_4 (0.1 g); $NH_4H_2PO_4$ (0.14 g); NH_3 (10 mL);	175	6	Colourless block	$Hf_2F_2(H(PO_4)_2)(NH_4)_2$ (**R1**)	5.3	
5	HfF_4 (0.1 g); As_2O_5 (0.27 g); NH_3 (10 mL);	140	7	Cube	$Hf_2(AsO_4)_3(NH_4)$ (**XII**)	5.2	7, 12 (phosphate analogue)
6	HfF_4 (0.1 g); As_2O_5 (0.27 g); NH_3 (10 mL);	180	6	Colourless plate	$HfF(AsO_4)_2(NH_4)_3$ (**R2**)	5.3	
7	HfF_4 (0.1 g); $NH_4H_2AsO_4$ (0.19 g); HCl (10 mL)	140	7	Cube	$Hf_2(AsO_4)_3(NH_4)$ (**XII**)	5.2	5, 12 (phosphate analogue)
8	HfF_4 (0.1 g); As_2O_5 (0.27 g); HCl (10 mL)	180	5	Colourless sheet	$Hf(AsO_4)F(H_2O)$ (**R3**)	5.3	
9	HfF_4 (0.1 g); As_2O_5 (0.27 g); HCl (10 mL)	140	7	Polycrystalline powder	β-$Hf(HAsO_4)_2$, τ-$Hf(HPO_4)_2$, HfP_2O_7, $HfOCl_2.6H_2O$	5.3	
10	HfF_4 (0.1 g); $NH_4H_2AsO_4$ (0.19 g); ethanol (10 mL)	180	6	Colourless block	$Hf_2F_9(AsO_4H)_3(NH_4)_3(H_2O)$ (**R4**)	5.3	
11	HfF_4 (0.1 g); H_3AsO_4 (0.11 g); ethanol (10 mL);	140	7	Amorphous powder	Amorphous powder	5.3	
12	HfF_4 (0.1 g); $NH_4H_2PO_4$ (0.19 g); H_2O (10 mL)	175	6	Colourless block	$Hf_2(PO_4)_3(NH_4)$ (**R5**)	5.3	5, 7 (arsenate analogues)
13	HfF_4 (0.1 g); H_3PO_4 (0.11 g); RbOH (g); H_2O (10 mL)	140	10	Amorphous powder	Amorphous powder	5.3	
14	HfF_4 (0.1 g); H_3AsO_4 (0.17g); RbOH (0.08g); H_2O (10 mL)	175	5	Polycrystalline powder	Rubidium arsenates (such as Rb_3AsO_4) and hafnium arsenates	5.3	
15	HfF_4 (0.1 g); H_3AsO_4 (0.06 g); CsOH (0.12 g); H_2O (10 mL)	140	10	Polycrystalline powder	$CsH_5(PO_4)_2$, $Hf(HPO_4)_2.H_2O$	5.3	
16	HfF_4 (0.1 g); As_2O_5 (0.27 g); CsOH (0.12 g); H_2O (10 mL)	175	7	Polycrystalline powder	$Hf(PO_3)_4$, Cs_2ZrO_3, CsOH	5.3	
17	HfF_4 (0.1 g); H_3AsO_4 (0.17 g); $Ba(OH)_2.xH_2O$ (0.07 g); H_2O (10 mL)	175	5	Polycrystalline powder	$Hf(PO_3)_4$, $Ba(H_2PO_4)_2$, $Ba(OH)_2.8H_2O$	5.3	

5.1 Compound XI – Hafnium fluoro-phosphate - $Hf^{IV}F_2(PO_4,HPO_4, H_2PO_4)_2(NH_4, H_2O)_3$

5.1.1 Synthesis

Compound **XI**, $Hf^{IV}F_2(PO_4,HPO_4,H_2PO_4)_2(NH_4, H_2O)_3$, was synthesised under solvothermal conditions. HfF_4 (0.1 g, 0.391 mmol, Aldrich 99 %) and P_2O_5 (0.17 g, 1.198 mmol, Aldrich 99.99 %) were dissolved in NH_3 solution (35%, 10 mL, Fisher). The reagents were stirred for 30 minutes, placed in a 23 mL teflon–lined Parr autoclave, heated to 140 °C and held at this temperature for 5 days. The reaction was allowed to cool to room temperature, the product filtered, washed with warm distilled water, and allowed to dry in air. A suitable rod shaped single crystal was then chosen for SXD analysis.

5.1.2 Results and Discussion

The products of this reaction were formed entirely of rod shaped crystals (Fig. 5.1). The results of the SXD data collection on one such crystal can be found in Tables 5.2 and A.5.1 in the Appendix.

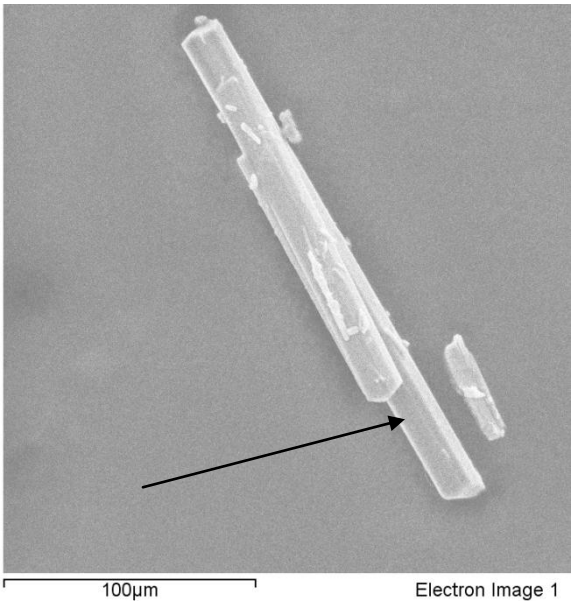

***Figure 5.1**: SEM image of rod shaped $Hf^{IV}F_2(PO_4,HPO_4,H_2PO_4)_2(NH_4, H_2O)_3$ crystals*

Table 5.2: *Details of single crystal data collection for $Hf^{IV}F_2(PO_4,HPO_4,H_2PO_4)_2(NH_4, H_2O)_3$*

Molecular Formula	$\mathbf{Hf^{IV}F_2(PO_4,HPO_4,H_2PO_4)_2(NH_4, H_2O)_3}$
Formula Weight (g)	461.88-464.51
Crystal Appearance	Rod
Crystal Size (mm)	0.3 x 0.1 x 0.1
Crystal System	Triclinic
Space Group	$P\bar{1}$
Lattice Parameters	a = 5.2216(3) Å, α = 74.231(3)°
	b = 8.1225(4) Å, β = 88.296(3)°
	c = 12.6140(6) Å, γ = 87.834(1)°
V (Å^3)	514.57(5)
Z	2
Calculated density (mg/m^3)	2.97
Temperature (K)	120 K
Theta Range (°)	3.4-27.7
Wavelength (Å)	Mo $K\alpha$ (λ = 0.71073)
Number of Reflections Measured	Total – 8081, Unique – 2356
$\boldsymbol{R_1}$ **[I>2σ (I)]**[a]	0.047
$\boldsymbol{R}$**1(all data)**	0.057
$\boldsymbol{wR_2}$	0.096
Goodness of fit indicator	1.118

The basic framework of the structure of **XI** was obtained through SXD analysis**.** Further investigation utilised bond valence calculations[9,10] (Table 5.3) found lower BV values at the terminal sites within the hafnium octahedra. The bond valence was significantly below unity when the sites were assumed to be oxygen or fluoride ions. These values suggested that monovalent anions (F^-/HO^-) were bonded at the terminal sites of the hafnium octahedra. EDX analysis established the presence of fluorine within the single crystal sample (F- 19.5%; P- 22.0% and Hf- 10.8%, Appendix A.5.2), which demonstrated a ratio of Hf:2F:2P (this data should not be

interpreted as quantitative). The Hf-F bond lengths are 1.97 (F1) and 2.00 Å (F2) respectively, slightly shorter than the average Hf-O bond lengths within the polyhedra (2.09(3) Å), more typical of fluoride ions.

Table 5.3: *Bond length and valence calculations for O/F ions within* ***XI***

Atoms	Bond	Hf-O/As-O bond length (Å)	υ_{ij}	Total υ_{ij}
O(1)	O(1)-P(3)	1.536(6)	1.244	1.857
	O(1)-Hf(1)	2.104(6)	0.613	
O(3)	O(3)-P(4)	1.537(6)	1.241	1.895
	O(3)-Hf(1)	2.080(6)	0.654	
O(5)	O(5)-P(4)	1.534(7)	1.251	2.012
	O(5)-Hf(1)	2.024(7)	0.761	
O(6)	O(6)-P(3)	1.536(6)	1.244	1.857
	O(6)-Hf(1)	2.104(6)	0.613	
O(7)	O(7)-P(4)	1.5348(6)	1.248	1.248
O(8)	O(8)-P(4)	1.5198(7)	1.300	1.300
O(9)	O(9)-P(3)	1.5401(7)	1.231	1.231
O(10)	O(10)-P(3)	1.5119(7)	1.328	1.328
F(1)	F(1)-Hf(1)	1.9731(6)	0.717	n/a
	O(1)-Hf(1)	1.9731(6)	0.873	
F(2)	F(2)-Hf(1)	2.0030(5)	0.661	n/a
	O(2)-Hf(1)	2.0030(5)	0.806	

The lack of bond valence at the O7, O8, O9 and O10 sites offered alternative sites for the fluoride anions to connect to. The average bond valence at the four oxygen sites (1.28(4) Å) was greater than the bond valence of the terminal sites on the hafnium polyhedra (average BV if O-0.84 (3)/F-0.69 (3)), which suggested that the fluoride ions would reside in the terminal positions.

The oxygen ions that exhibit a lower bond valence values (O7, O8, O9 and O10), form part of the phosphate centred tetrahedral units. It was deduced that these sites were likely to be hydroxide ions rather than oxide through SXD refinements, although this did not result in the assignment of hydrogen to specific oxygen anions. It is possible for all of these lower valence sites to be OH groups, and without the fixed hydrogen positions this aspect of the molecular formula must be assumed. The hydroxide groups tend to inhabit areas within the tetrahedra where there is minimum steric hindrance (further away from the hafnium polyhedra). All four sites (O7, O8, O9 and O10) are capable of containing OH groups as they sit on the terminal positions. The presence of NH_4^+ was confirmed through IR analysis. The IR spectrum for **XI** was measured, which showed **s**harp peaks at 3219.8 and 1400.2 cm^{-1}. This confirmed the presence of NH_4^+ cations (A.5.1) through the respective bending and stretching regions observed. The region of the spectrum where the O-H band was expected (as a result of HPO_4) was masked by the strong N-H peak (in region of 3200 cm^{-1}) that resulted from the NH_4 within **XI**. This broad peak also disguised possible bands associated with free water molecules within the layers of **XI**, which could be present.

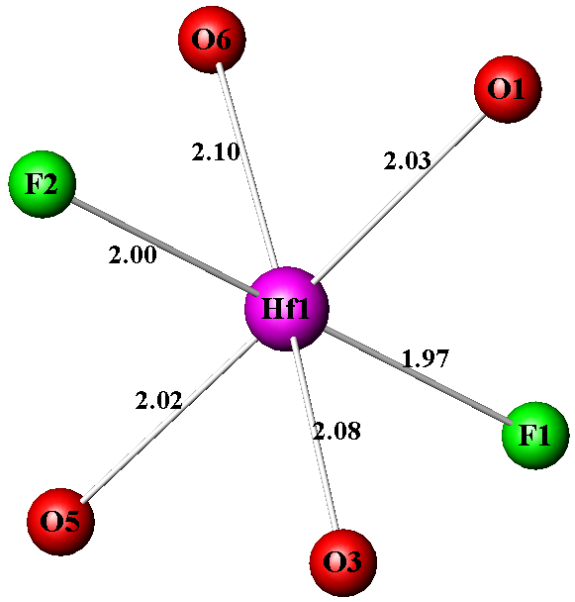

Figure 5.2: *Hafnium polyhedra in **XI** (lengths in Å)*

The hafnium polyhedra (Fig. 5.2) are slightly distorted with O/F-Hf-O bond angles ranging from 86-91°, with an average angle of 89.24°. Bond valence calculations were completed (Table

5.4), which concluded that the oxidation state of the hafnium was +4. The fluoride anions caused mild distortion to the polyhedra, which is reflected in the mildly enlarged hafnium BV value (4.15).

Table 5.4: *Bond lengths and bond valence values for Hf within* ***XI***

Atoms	Hf-O/F bond length (Å)	Hf-O/F Bond Valence
O1	2.03(6)	0.74
O3	2.08(6)	0.66
O5	2.02(7)	0.76
O6	2.10(6)	0.61
F1	1.97(6)	0.72
F2	2.00(5)	0.66
Total		**4.15**

These factors support the assumption that the atoms on the two terminal sites were fluoride rather than oxygen ions. The incorporation of mixed mono and divalent anions within the polyhedral unit caused deviations from the expected bond angles (90°) and lengths, which compensated for the difference in charges. These findings indicate that the hafnium octahedra are composed of HfO_4F_2 octahedral units.

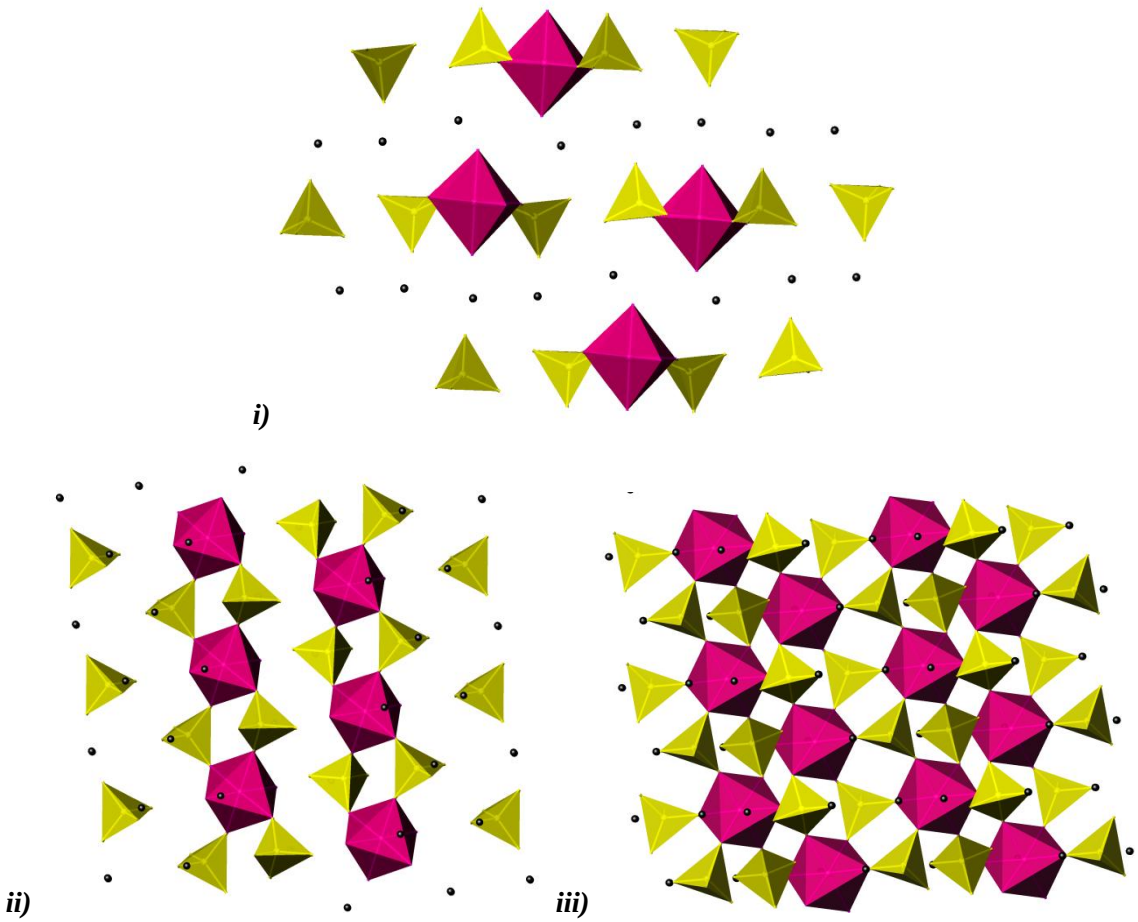

***Figure 5.3**: Structure of **XI** viewed down the **i)** a, **ii)** b, **iii)** c-axis [Key: Yellow tetrahedra – $PO_4/HPO_4/H_2PO_4$, Magenta polyhedra – HfO_4F_2, black sphere – NH_4^+ cation/H_2O molecules]*

Compound **XI** crystallises in the triclinic *P-1* space group, forming a chain-like structure (Fig. 5.3) when viewed through the *a/b*-axis (5.3.*i/ii)*. The structure of **XI** is composed of hafnium-centred octahedra (HfO_4F_2) and phosphorous-centred tetrahedral units (PO_4, HPO_4 or H_2PO_4). As a result of bridging bonds (Hf-O-P), the hafnium octahedra exhibit corner-sharing bonding with neighbouring phosphate tetrahedra. The hafnium octahedra are connected to four separate tetrahedra, and this layered material demonstrates a lack of continuation of the structure as a result of the incorporation of terminal hydroxide (H_2PO_4/HPO_4) and fluoride anions (Fig. 5.3.*i*) into these units. The close packed nature of the bonding within the layers of **XI** can be observed when the structure is viewed down the *c*-axis (Fig. 5.3.*iii*).

Three non-framework species were isolated within the SXD refinement, assigned as oxygen and nitrogen ions. The hydrogen ions could not be isolated using this analysis method, which is

why these sites are not defined within the molecular formula ($(NH_4, H_2O)_3$). The NH_4^+ cations and H_2O molecules are located between the layers of hafnium polyhedra and phosphorous tetrahedra of **XI** (Fig. 5.4). It was assumed that donor-acceptor bonding existed between the NH_4^+ cations or water molecules and the terminal fluoride ions on the hafnium polyhedra if it is assumed that the hydrogen ions lie along the vector between nitrogen and fluorine at a typical length (*i.e.* ~ 1 Å). The distance between the nitrogen or oxide and fluoride anions is appropriate for a hydrogen bond between H---F (average bond length 2.87 Å).

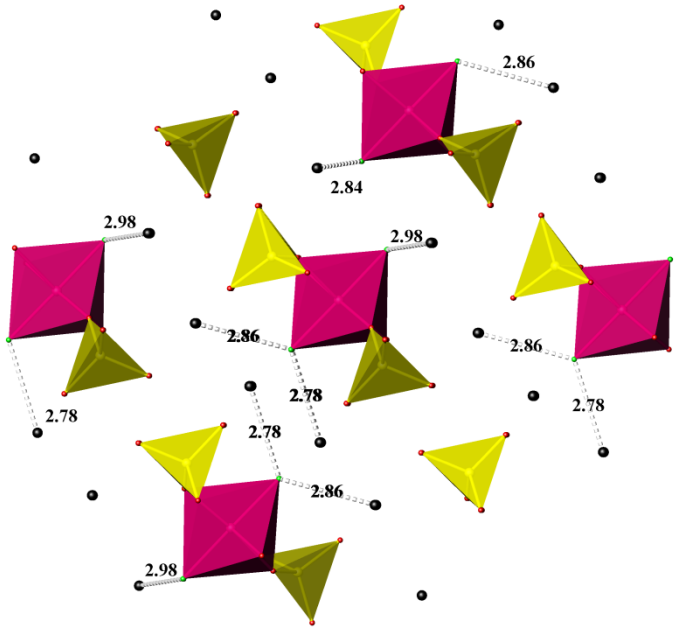

Figure 5.4: *Donor-acceptor bonding in **XI** between F and NH_4^+ ions/H_2O molecules, shown as dotted lines (lengths in Å)*

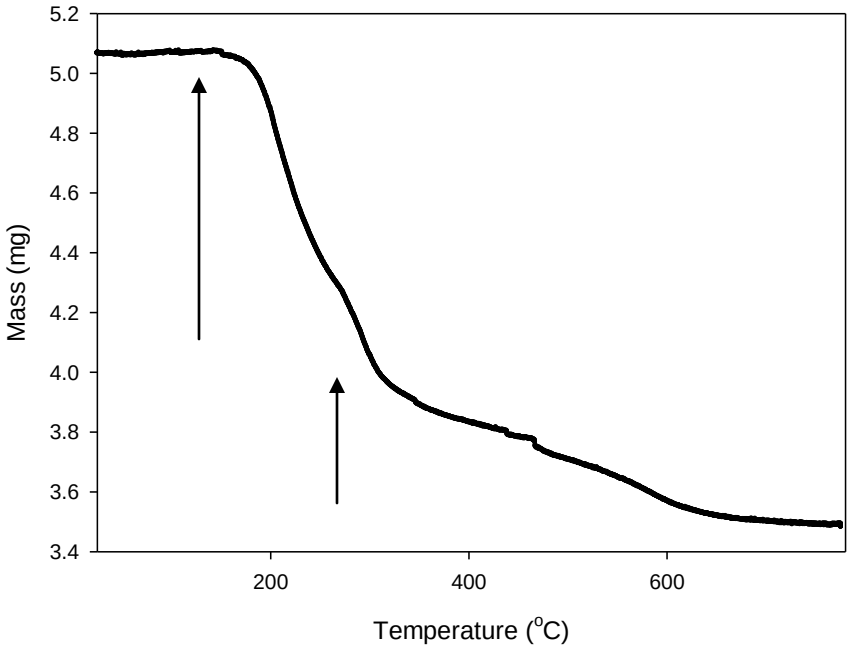

Figure 5.5: *Mass loss vs. Temperature graph for* ***XI*** *(black line - mass loss)*

TGA analysis (Fig. 5.5) exhibited an initial mass loss which began at 174 °C and continued until 333 °C. A further reduction in mass was noted from 333-427 °C. The structure continued to lose mass to 775 °C. The initial mass loss at 174 °C was assumed to be a result of the loss of NH_4^+ cations or H_2O molecules from between the layers of the structure. The second mass loss was believed to be the result of the loss of hydroxide groups, followed finally by the breakdown of phosphate groups within the HPO_4 and PO_4 tetrahedra.

XI is isostructural with the fluorophosphates of the zirconium and titanium compounds, ($Zr^{IV}F_2(PO_4, HPO_4, H_2PO_4)_2(NH_4, H_2O)_3$ and $Ti^{IV}F_2(PO_4, HPO_4, H_2PO_4)_2(NH_4, H_2O)_3$) previously synthesised by Redrup[11]. The synthetic procedures differ greatly depending on the metal ions used. The reactions proceeded in alkaline media for the hafnium (NH_3 solution) and zirconium (large quantities of DABCO, pH 9) materials, whereas the titanium syntheses proceeded in a more neutral solution (ethanol). The hafnium and zirconium structures formed at lower temperatures (140 °C) in comparison to the titanium reaction (175 °C). The variations in the synthetic proceedings necessary to form these structures highlights the effect that substitution of the metal cation has on the reaction conditions and also the ease with which these materials form analogous compounds.

The molecular formula of **XI** was assumed as the hydrogen positions could not be placed through SXD analysis. The research undertaken within this thesis has enabled the most likely structure that **XI** will form to be deduced. The oxidation state of the material was calculated when the phosphate source was H_2PO_4, HPO_4 and PO_4. It was established that NH_4^+ cations are present within the layers of **XI** through IR analysis, and therefore, structures that contain three H_2O molecules are not possible. The possible formulae of **XI** that charge balance are listed below:

a) $HfF_2(H_2PO_4)(PO_4)(NH_4)_2(H_2O)$
b) $HfF_2(H_2PO_4)(HPO_4)(NH_4)(H_2O)_2$
c) $HfF_2(HPO_4)_2(NH_4)_2(H_2O)$
d) $HfF_2(HPO_4)(PO_4)(NH_4)_3$

The presence of hydroxide anions attached to the phosphate tetrahedra were highlighted through bond valence calculations and four of the oxide ions exhibit low bond valence (O7, O8, O9 and O10). The structure will contain OH or OH_2 groups to counteract these lower valence values, and the hydrogen ions are expected to be shared between terminal oxide anions on the tetrahedra. The large and sharp peaks (observed within the IR spectra) associated with NH_4^+ cations indicated this to be the major interlayer species within **XI**. It is therefore unlikely that compound 'b' would be the preferred formula. The low bond valence over four oxygen sites indicates that the hydrogen ions will be shared with neighbouring phosphate tetrahedra, and therefore a structure that contains hydrogen groups on both tetrahedral units would be preferred. It has therefore been deduced that compound 'c' is the most likely form of **XI**.

5.2 Compound XII – Ammonium hafnium arsenate – $Hf^{IV}_2(AsO_4)_3(NH_4)$

5.2.1 Synthesis

Compound **XII**, $Hf^{IV}_2(AsO_4)_3(NH_4)$, was synthesised under solvothermal conditions. HfF_4 (0.1 g, 0.39 mmol, 99 %, Aldrich) and $NH_4H_2AsO_4$ (0.19 g, 1.20 mmol, 99 %, Aldrich) were mixed for 30 minutes in HCl (36%, 10 mL, Fisher). The solution was transferred to a 23 mL teflon-lined Parr autoclave and heated at 140 °C for 7 days. The reaction mixture was allowed to cool slowly to room temperature, the solid product separated *via* filtration, washed with distilled water and dried in air.

5.2.2 Results and Discussion

Compound **XII** is analogous to structure **X** described in Chapter 4. In view if this and to avoid repetition discussion here concerns EDX, SXD, BV, IR, and TGA analyses highlighting the similarities and comparing the effects of different metal cations within the same structure.

A suitable crystal was selected for SXD analysis and the results are shown in Tables 5.5 and A.5.4 in the Appendix. SEM images were collected for **XII**, which revealed their block-like morphology (Fig. 5.6). **XII** was more uniform in shape and size when compared to the crystals produced in the synthesis of **X** (Fig. 4.16).

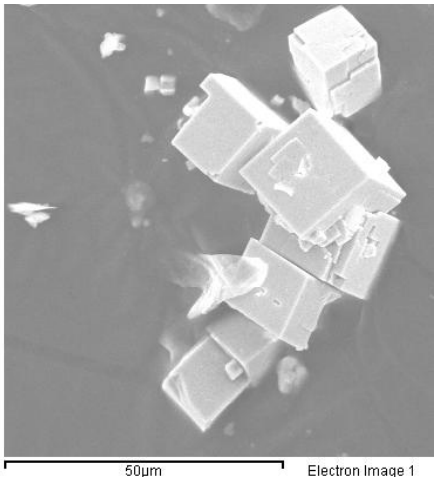

***Figure 5.6**: SEM image of cuboid shaped $Hf_2(AsO_4)_3(NH_4)$ crystals*

Table 5.5: *Details of single crystal data collection for $Hf_2(AsO_4)_3(NH_4)$*

Molecular Formula	**$Hf^{IV}_2(AsO_4)_3(NH_4)$**
Formula Weight (g)	794.63
Crystal Appearance	Cuboid
Crystal Size (mm)	0.2 x 0.2 x 0.05
Crystal System	Trigonal
Space Group	$R\bar{3}c$
Lattice Parameters	a = 9.0056(9) Å, α = 90°
	b = 9.0056(9) Å, β = 90°
	c = 24.7438(31) Å, γ = 120°
V (Å^3)	1737.89(3)
Z	5
Calculated density (mg/m^3)	4.52
Temperature (K)	120 K
Theta Range (°)	3.4-27.7
Wavelength (Å)	Mo *K*α (λ = 0.71073)
Number of Reflections Measured	Total – 1897
	Unique – 422
R_1 [I>2σ (I)]^a	0.066
***R*1(all data)**	0.095
wR_2	0.157
Goodness of fit indicator	1.137

Compound **XII** is a three-dimensional framework comprised of hafnium-centred octahedra (HfO_6) and arsenate-centred tetrahedra (AsO_4) with NH_4^+ cations within the channels of the structure.

Table 5.6: *Bond length and valence calculations for O ions within* ***XII***

Atoms	Bond	Hf-O/As-O bond length (Å)	υ_{ij}	Total υ_{ij}
O(1)	O(1)-As(1)	1.647(15)	1.383	2.035
	O(1)-Hf(1)	2.081(16)	0.652	
O(2)	O(2)-As(1)	1.670(17)	1.299	1.991
	O(2)-Hf(1)	2.059(16)	0.692	

Bond valence calculations[9,10] (Table 5.6) completed on the O1 and O2 sites produced expected sums for divalent ions (~2), agreeing with the structural assumptions of oxygen anion at these sites. EDX analysis indicated that the elements, Hf, As and O (Appendix A.5.5) were present within the crystalline sample, contributing to the assumption that oxygen, and not fluoride, is present within **XII**.

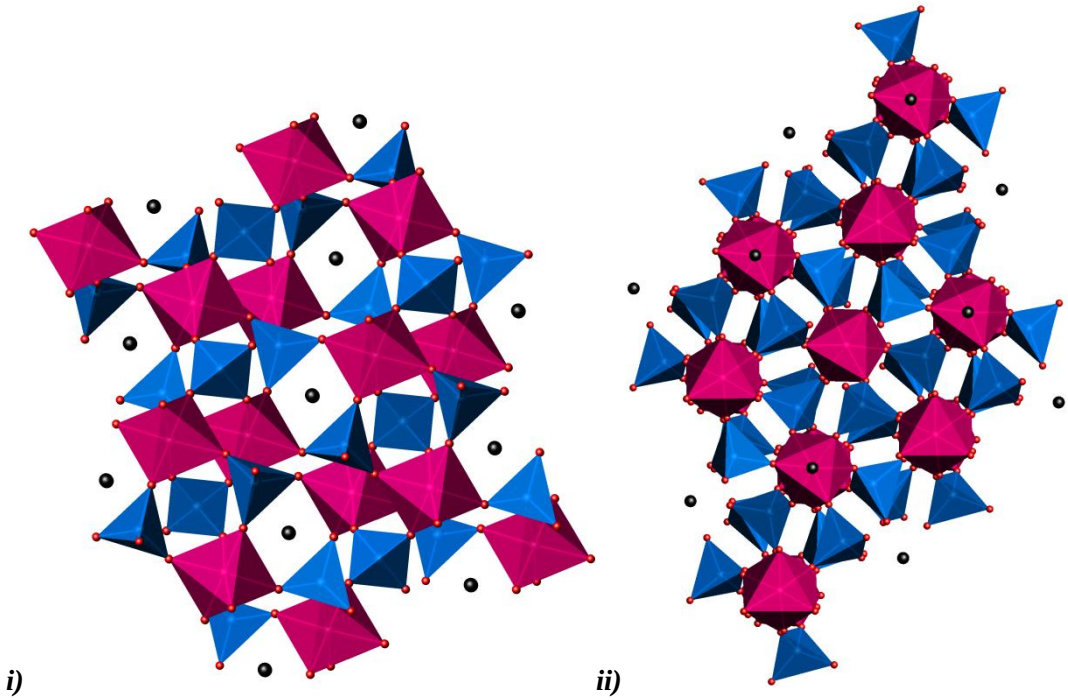

i) ***ii)***

Figure 5.7: *Structure of* ***XII*** *viewed down the* ***i)*** *a-axis;* ***ii)*** *c-axis [Key: Blue tetrahedra – AsO_4; Magenta octahedra – HfO_6; Black sphere –NH_4^+ cations; Red sphere – oxygen ions]*

Table 5.7: *Bond lengths and bond valence values for Hf within* ***XII***

Atoms	Hf-O bond length (Å)	Hf-O Bond Valence
O1	2.08(2)	0.66
O1	2.08(2)	0.66
O1	2.08(2)	0.66
O2	2.06(2)	0.69
O2	2.06(2)	0.69
O2	2.06(2)	0.69
Total		**4.05**

Bond valence calculations were undertaken for the hafnium cation to identify whether the oxidation state deviates from the expected +4 value. The calculations (Table 5.7) indicated that the hafnium was in a +4 oxidation state.

IR analysis combined with the SXD provided information about the content of the channels within **XII**. Two large peaks associated with the N-H stretching regions in the NH_4^+ cations (1417.3 and 3441.3 cm^{-1}) were found, which eliminated the possibility of alternative molecules, such as water, residing within the channels of **XII**.

TGA analysis on compound **XII** (Fig. 5.8) provided a mass loss that was similar to that found within **X**. The structure containing hafnium exhibited a loss at an elevated temperature when compared with the zirconium analogue (~ 500 °C), which indicates that the NH_4^+ is more strongly bound to the hafnium framework.

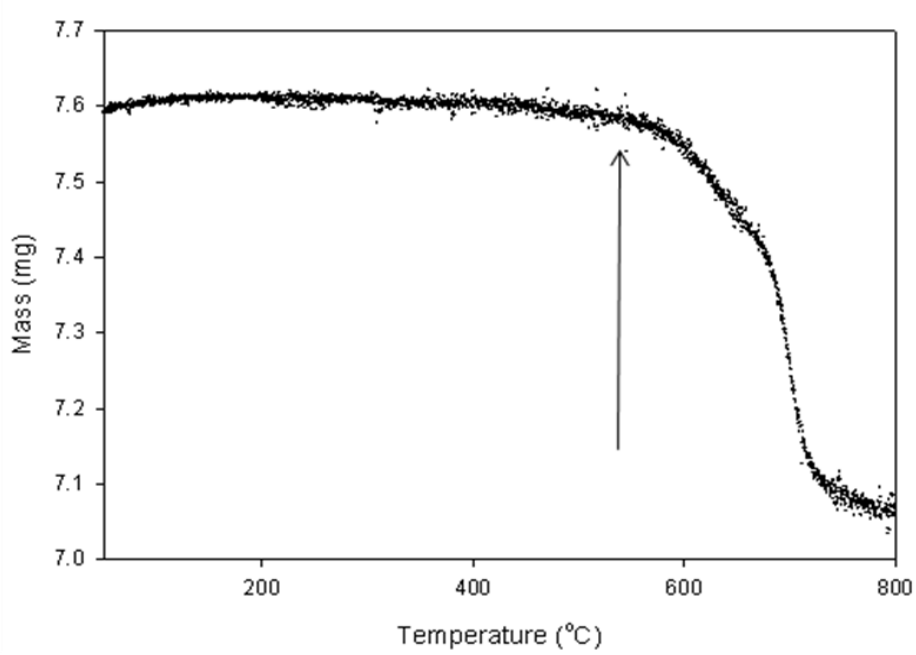

Figure 5.8: *Mass loss vs. Temperature graph for compound **XII** (mass loss indicated by arrows)*

Compound **XII** is isostructural to the hafnium phosphate $Hf_2(PO_4)_3(NH_4)$ previously synthesised by Redrup[11]. Although these structures are analogous, their synthetic conditions varied greatly. The hafnium phosphate was produced at high temperatures (200 °C) from $NH_4H_2PO_4$ in H_2O, whereas **XII** was formed in an acidic medium (HCl) at lower temperatures (140 °C). These differences indicate that the presence of alternative oxotetrahedral species can require greatly dissimilar synthetic conditions. Within this research project the use of the solvothermal route, MF_4 and a phosphate source rarely produced new frameworks. It is possible that the presence of phosphates requires greater extremes in the reaction conditions in the search for new materials.

5.3 Experimental Summary

Research undertaken by Redrup[11], applying solvothermal methods to hafnium phosphate and arsenate materials has informed and made a significant contribution to the findings in this chapter. The contribution is acknowledged by including the structures formed by Redrup in Table 5.1 (referred to as 4-R1, 6-R2, 8-R3 *etc.*) as part of a comprehensive summary of the synthetic conditions for successful and similar hafnium structures. It is important to clarify that these compounds were not synthesised within this research, but similarly employed HfF_4 as starting materials.

The synthetic reactions described highlighted the versatility of hafnium in the formation of new frameworks and analogous materials. In this and other research studies the production of crystals has been observed across a wide pH range. The hafnium arsenate compounds exhibit diversity in their preferred pH, with crystalline products forming readily in alkaline (NH_3: 5, 6-R2) acidic (HCl: 7, 8-R3) and neutral (ethanol: 10-R4) solutions. The range of pH and reaction media indicates that there is great potential for additional arsenate products to form, given the correct synthetic conditions. The phosphate materials did not exhibit a similar range of pH and reaction solvent, forming crystals in alkaline (NH_3: 1, 2, 3, 4-R1) and neutral (H_2O: 12-R5) conditions.

The production of hafnium compounds appears to be heavily dependent upon the presence of ammonium cations within the reaction syntheses, as a result of the ammonium based starting materials and the reaction solvent (NH_3). In general, the inclusion of ammonium caused oxygen ions within the polyhedra to be substituted by fluoride. The presence of strong donor-acceptor bonds (F---H-NH_3) encouraged these structural arrangements. The exception to this rule was the stable Nasicon structure (**XII**) that formed readily without the presence of fluoride in the hafnium octahedra (although NH_4^+ cations were present). The two compounds that formed without fluoride anions attached to their polyhedra, did so in an acidic HCl medium, which suggested that more three-dimensional frameworks could form in acidic conditions, by inhibiting the formation of F---HN bonds.

Research into hafnium framework synthesis could develop further by investigating the relative pH of solutions. Where fluorinated materials are of interest, neutral or alkaline media should be chosen, alternative starting materials such as As_2O_5 and H_3AsO_4 create opportunities to produce frameworks (in acidic media), that do not contain ammonium cations. When ammonium

cations are not present or they are removed, more three-dimensional structures can form. The fluorinated hafnium arsenate (5-R1) is an example of this type of three-dimensional structure, which exhibits bridging fluorine bonding, as observed for $Zr(AsO_4)F(H_2O)$ in Chapter 4.

Variations to the reaction temperatures produce different synthetic results. Identical reaction conditions involving HfF_4, As_2O_5 and NH_3 solution were completed and two entirely different results were obtained (140 °C: 5 - $Hf_2(AsO_4)_3(NH_4)$; 180 °C: 6-R2 - $HfF(AsO_4)_2(NH_4)_3$). When the reaction solvent was altered to HCl, polycrystalline powders were acquired at 140 °C (9), whereas a crystalline sample was achieved at 180 °C (8-R3 - $Hf(AsO_4)F(H_2O)$). Conversely, syntheses that involved P_2O_5 did not provide alternative reaction products ($HfF_2(PO_4, HPO_4)(NH_4, H_2O)_3$) at either 140 °C (1) or 175 °C (2), however, substitution of the phosphate source to H_3PO_4 generated this product at 140 °C (3); and $NH_4H_2PO_4$ provided a novel framework (4-R1 - $Hf_2F_2(H(PO_4)_2)(NH_4)_2$). The different structures obtained at low and high temperatures indicate how important it is to investigate a range of temperatures in order to understand the systems more comprehensively.

The majority of the hafnium products were single phases formed entirely of crystals. If powdered samples were obtained then PXD was performed to identify these materials. The limited research into hafnium compounds resulted in fewer powder patterns being available in current databases. The similarities in the chemistry of zirconium and hafnium materials enabled thorough searches to be performed, by substituting zirconium for hafnium (using the EVA[12] software package).

The inclusion of Group 1 and 2 hydroxides in hydrothermal reactions has been found to increase the solubility of the reagents. In this research project the cations within the starting materials entered the framework of the reaction product (**I**), producing interesting structures that may have the potential for application within areas such as ionic exchange. The experimental work involving hafnium did not produce single crystal phases when these hydroxides were introduced into the reactions. Within the hafnium syntheses their presence (Table 5.1) generated polycrystalline powders containing Group 1 or 2 phosphate or arsenates and hafnium phosphates. Therefore, to date the addition of Group 1 or 2 hydroxides to the hydrothermal reactions has not been shown to produce novel hafnium frameworks.

5.4 Conclusions

Two novel examples of analogous hafnium compounds have been synthesised through solvothermal techniques and characterised *via* SXD as the primary method of analysis. The first of these, **XI**, forms a one-dimensional chain structure, and the second, **XII**, exhibits a three-dimensional framework. These two hafnium examples have exhibited HfO_4F_2 and HfO_6 octahedra respectively and TO_4 tetrahedra in both cases.

The hafnium compounds produced formed structures incorporating fluoride and ammonium ions simultaneously as well as one example, which lacked fluoride although NH_4^+ is incorporated. It has been noted that the frameworks formed can be heavily dependent upon the presence of fluorine, which is stabilised through the introduction of ammonium cations. These examples highlight that compounds such as the Nasicon hafnium analogue (**XII**) can form, without stabilisation through F---HN hydrogen bonds. These non-fluorinated compounds that also contain ammonium cations formed in acidic media (HCl). It is possible that further three-dimensional frameworks could be formed in these conditions, as the fluoride ions do not tend to connect to the hafnium polyhedra. HfF_4 is a versatile starting material, dependent upon the quantities of reagents, reaction media, *etc.* hence a range of modifications can be made that would encourage the formation of one, two and three-dimensional hafnium compounds.

By developing previous research into the formation of hafnium phosphate and arsenate materials[11] it has been possible to produce greater understanding of the hafnium reaction pathway. Many identical products were obtained using alternative synthetic conditions, highlighting the versatility of this method.

5.5 References

(1) Suarez, M.; Barcina, L. M.; Llavona, R.; Rodriguez, J. *Journal of Molecular Structure* **1998**, *470*, 105-119.

(2) Suarez, M.; Barcina, L. M.; Llavona, R.; Rodriguez, J.; Salvado, M. A.; Pertierra, P.; Garcia-Granda, S. *Journal of the Chemical Society-Dalton Transactions* **1998**, 99-102.

(3) Sugantha, M.; Varadaraju, U. V. *Solid State Ionics* **1997**, *95*, 201-205.

(4) Wallez, G.; Souron, J. P.; Quarton, M. *Solid State Sciences* **2006**, *8*, 1061-1066.

(5) Popa, K.; Konings, R. J. M.; Benes, O.; Geisler, T.; Popa, A. F. *Thermochimica Acta* **2006**, *451*, 1-4.

(6) Popa, K.; Bregiroux, D.; Konings, R. J. M.; Gouder, T.; Popa, A. F.; Geisler, T.; Raison, P. E. *Journal of Solid State Chemistry* **2007**, *180*, 2346-2355.

(7) Torardi, C. C.; Miao, C. R.; Li, J. *Journal of Solid State Chemistry* **2003**, *170*, 289-293.

(8) Peng, Z. F.; Xu, Z.; Luo, C. Q.; Yu, J. B.; Zhang, G. B. *Luminescence* **2008**, *23*, 14-16.

(9) Brown, I. D.; Altermatt, D. *Acta Crystallographica Section B-Structural Science* **1985**, *41*, 244-247.

(10) Brese, N. E.; O'Keeffe, M. *Acta Crystallographica Section B-Structural Science* **1991**, *47*, 192-197.

(11) Redrup, K. V. *Synthesis and Characterisation of new Framework Materials, University of Southampton* **2009**.

(12) Kijkowska, R. *Journal of Materials Science* **2004**, *39*, 2017-2022.

CHAPTER SIX

TEMPLATES MATERIALS

6.0 Introduction

Organic templating agents have been used in hydrothermal reactions for a considerable period of time. Originally they were limited to aluminosilicate zeolites[1], although they went on to be used in reactions that formed other compounds, such as the aluminophosphates[2]. Variations to the starting materials, temperatures and templates present within reactions produce a large number of alternative structure types[3]. In consequence, alternative organic materials have been applied to successful reactions in order to encourage the formation of a variety of three-dimensional and layered materials. The presence of the organic component can affect the reaction in a number of ways. It can act in a structure directing fashion, forming novel materials as a result of its presence within the solution[4]. The incorporation of these organic materials in solvothermal syntheses can be instrumental in the production of phase pure samples. It can also affect the morphology, creating sites for the material to grow around[5]. These factors impact upon the size and shape of the pores, channels and layers within the inorganic framework. As science in this field has matured and the number of materials synthesised in this way increased, there are a growing variety of structures that incorporate these organic materials within their framework channels[6] and layers[7]. The success of the aluminophosphate and gallophosphate materials has produced greater understanding of reaction conditions and solvents necessary to produce metal and lanthanide frameworks, and more recently the metal-organic framework (MOF) structures. The latter consist of metal units connected to organic linkers forming three-dimensional materials[8]. These structures have the ability to be targeted towards specific applications by altering the synthetic proceedings to produce defined shapes. The MOF compounds are perceived to exhibit significant potential for future applications, such as the storage of gases[9]. The initial interest in framework materials containing large pores has developed as a result of the potential to meet a variety of industrial needs in applications such as ion exchange, adsorption and catalysis[10]. The introduction of MOFs creates opportunities to synthesise structures with the potential for a more rational design of materials specific to industrial needs.

The formation of the aluminosilicate zeolite structures tends to be dependent upon the specific template that is added to the synthesis. These alkylammonium cations produce a site around which the aluminosilicate can grow. When the aim is to form large or small pores, channels and layers the specific size or shape of the template ions is very important. A compound can be described as microporous when pore size is less than 2 nm, mesoporous if greater than 2 and less

than 50 nm, and macroporous when the diameter is larger than 50 nm[11]. The size of the pores is a crucial factor in any assessment of the material's properties within industrial applications.

The organic template ions can be removed from the structure at a temperature of between 300-400 °C, dependent upon the interaction of the organic template with the framework. The organic compounds within the pores are released from the materials in the form of CO_2, NO_x and H_2O leaving the empty porous inorganic framework. The pores that remain are specific to the template that was originally incorporated. The removal of the organic templates can cause a structural collapse if the compound is heavily dependent upon charge balancing cations to stabilise the structure. Advances in materials science have led researchers to investigate supercritical carbon dioxide drying processes that provide access to the pores without this framework collapse highlighting the importance of investigating known structures when looking at inorganic porous frameworks[12].

The synthesis of templated Group 4 structures is widely understood for titanium[13] and zirconium[14] frameworks. Initial investigations led to the formation of a large number of two-dimensional structures[15]. More recently three-dimensional frameworks have been produced using the fluoride route, incorporating HF within the reaction medium to produce novel titanium[16] and zirconium structures[17,18].

Within this project organic template ions were included in a large number of hydrothermal syntheses with the aim of producing novel framework structures capable of a variety of practical applications. Table 6.1 provides a comprehensive summary of a selection of reaction products synthesised in both powder and single crystal form and at a variety of temperatures, pH, solvents, reaction lengths and starting material ratios. The details of Table 6.1 will be discussed further in the experimental summary within this chapter. This discussion begins with a structural description and characterisation of the novel single crystal products that were formed.

***Table 6.1**: Synthetic conditions for novel and known organically template reactions (all Parr autoclaves 23 mL)*

Reaction No.	Synthesis	Temp (°C)	Time (days)	Single Crystal/ Powder	Product	Thesis	Same structure as Reaction No.
1	HfF_4 (0.1 g); H_3AsO_4 (0.14 g); EDA (0.02 g); H_2O (11 mL)	190	5	Rectangular plate	$Hf^{IV}_2F(HAsO_4)(AsO_4)_2[(C_2H_8N_2)\text{-}H_2]_{1/2}(H_2O)_{1.5}$	6.1	2
2	HfF_4 (0.1 g); H_3AsO_4 (0.17 g); DETA (0.04 g); H_2O (11 mL)	190	5	Rods	$Hf^{IV}_2F(HAsO_4)(AsO_4)_2[(C_4H_{16}N_3)\text{-}H_3]_{1/3}(H_2O)_{1.5}$	6.1	1
3	HfF_4 (0.1 g); H_3PO_4 (0.21 g); PHEN (0.11 g); H_2O (10 mL)	175	5	Powder	α-$Hf(HPO_4)_2.H_2O$	6.0	
4	HfF_4 (0.1 g); H_3AsO_4 (0.07 g); PHEN (0.11 g); H_2O (10 mL)	190	7	Multi-phase powder	$Hf(HAsO_4)_2.H_2O$,	6.0	
5	HfF_4 (0.1 g); H_3AsO_4 (0.07 g); EDA (0.02 g); H_2O (10 mL)	190	7	Multi-phase powder	$HfAs_2O_7$, $Hf_2O(AsO_4)_2$	6.0	
6	HfF_4 (0.1 g); DABCO-P (0.25 g); H_2O (10 mL)	140	6	Multi-phase powder	γ-$Hf(HPO_4)_2.2H_2O$, $Hf_2H(PO_4)_3$, β-$HfPO_4(OH)$	6.0	
7	HfF_4 (0.1 g); $NH_4H_2PO_4$ (0.14 g); TMAC (0.04 g); H_2O (10 mL)	140	9	Amorphous powder	n/a	6.0	
8	HfF_4 (0.1 g); $NH_4H_2PO_4$ (0.14 g); TMAOH (0.11 g); H_2O (10 mL)	140	9	Amorphous powder	n/a	6.0	
9	HfF_4 (0.1 g); $NH_4H_2PO_4$ (0.14 g); DABCO (0.04 g); H_2O (10 mL)	140	9	Multi-phase powder	$Hf_2(H_3O)(PO_4)_3$, $Hf(PO_4)_3$, $Hf_4P_6O_{23}$	6.0	
10	ZrF_4 (0.1 g); H_3AsO_4 (0.14 g); EDA (0.02 g); H_2O (11 mL)	190	5	Square plate	$Zr^{IV}_2(AsO_4)_2F_4(H_2O)_2[(C_2H_8N_2)\text{-}H_2]$	6.2	
11	ZrF_4 (0.1 g); H_3AsO_4 (0.257 g); TMAC (0.066 g); H_2O (10 mL)	140	7	Rods	$Zr^{IV}(AsO_4)F(H_2O)$	4.2	8-13
12	ZrF_4 (0.1 g); H_3AsO_4 (0.257 g); TMAOH (0.055 g); H_2O (10 mL)	140	7	Rods	$Zr^{IV}(AsO_4)F(H_2O)$	4.2	7, 9-13
13	ZrF_4 (0.1 g); As_2O_5 (0.415 g); TMAC (0.066 g); H_2O (10 mL)	140	14	Rods	$Zr^{IV}(AsO_4)F(H_2O)$	4.2	7, 8, 10-13
14	ZrF_4 (0.1 g); H_3AsO_4 (0.257 g); H_2O (10 mL); TEAOH (0.031 g)	140	7	Rod	$Zr^{IV}(AsO_4)F(H_2O)$	4.2	7-9, 11-13

15	ZrF_4 (0.1 g); As_2O_5 (0.415 g); H_2O (10 mL); TEAOH (0.031 g)	140	7	Rod	$Zr^{IV}(AsO_4)F(H_2O)$	4.2	7-10, 12, 13
16	ZrF_4 (0.1 g); H_3AsO_4 (0.257 g); H_2O (10 mL); OAD (0.076 g)	140	7	Rod	$Zr^{IV}(AsO_4)F(H_2O)$	4.2	7-11, 13
17	ZrF_4 (0.1 g); As_2O_5 (0.415 g); H_2O (10 mL); OAD (0.076 g)	140	7	Rod	$Zr^{IV}(AsO_4)F(H_2O)$	4.2	7-12
18	ZrF_4 (0.1 g); H_3AsO_4 (0.257 g); EDA (0.036 g); H_2O (10 mL)	140	7	Multi-phase powder	ZrF_4, As_2O_5	4.6	
19	ZrF_4 (0.1 g); H_3AsO_4 (0.257 g); PIP (0.052 g); H_2O (10 mL)	140	7	Multi-phase powder	ZrF_4, As_2O_5	4.6	
20	ZrF_4 (0.1 g); $FOP(OH)_2$ (0.24 g); DABCO (0.07 g) H_2O (10 mL)	140	7	Powder	$Zr(OH)(PO_4)$	4.6	
21	CeF_4 (0.2 g); $NH_4H_2PO_4$ (0.3 g); DABCO (0.1 g); H_2O (11 mL)	140	7	Multi-phase powder	CeF_3, $CePO_4.H_2O$, organic phases	3.6	
22	CeF_4 (0.2 g); H_3AsO_4 (0.13 g); TEA (0.12 g); H_2O (11 mL)	140	7	Multi-phase powder	CeF_3, $CeAsO_4$	3.6	
23	CeF_4 (0.2 g); H_3AsO_4 (0.13 g); PYR (0.05 g); H_2O (11 mL)	140	7	Multi-phase powder	As_2O_5, $CeAsO_4$	3.6	

6.1 Compound XIII: Templated hafnium fluoro arsenates –

$Hf^{IV}_2F(HAsO_4)(AsO_4)_2[Temp\text{-}H_n]_{1/n}(H_2O)_{1.5}$

6.1.1 Synthesis

Two templated hafnium fluoro arsenates were formed from similar hydrothermal reactions and so both syntheses will be described here for *n* = 2 (**XIII(2)**); Temp = ethylenediamine (EDA) and what is assumed to be *n* = 3 (**XIII(3)**); Temp = diethylenetriamine (DETA).

The hydrothermal synthesis of compound **XIII(2)** was completed using HfF_4 (0.1 g, 0.391 mmol, 99 % Aldrich), H_3AsO_4 (0.14 g, 0.986 mmol, 75 % wt. BDH chemicals) and EDA (0.02 g,0.333 mmol, 99 % Aldrich), which were added together in water (11 mL) and stirred for thirty minutes. The solution was transferred to a 23 mL teflon-lined steel Parr autoclave and heated at 190 °C for 5 days. The reaction was allowed to cool to room temperature, the solid product separated *via* filtration, and washed with warm water.

Compound **XIII(3)** was synthesised hydrothermally using HfF_4 (0.1 g, 0.391 mmol, Aldrich 99 %), H_3AsO_4 (0.17 g, 1.198mmol, 75 % wt. BDH chemicals) and DETA (0.04 g, 0.388 mmol, 99 % Aldrich). The reagents were mixed in water (11 mL) and stirred for thirty minutes. The mixture was transferred to a 23 mL teflon-lined steel Parr autoclave and heated at 190 °C for 7 days. The reaction was slowly cooled to room temperature, the solid product separated *via* filtration, and washed with warm distilled water.

Single crystals of both compounds were obtained from dry samples and analysed accordingly.

6.1.2 Results and Discussion

The SEM images of the single crystals of compounds **XIII(2)** and **XIII(3)** are shown in Figure 6.1. The reaction conditions were very similar for both materials although different organic templating agents were used, and the reaction that involved DETA was longer (seven days). The frameworks of the two compounds are similar, but the presence of the organic template alters the lattice parameters slightly and thus the morphology of the crystals.

Suitable single crystals of the two types of compound **XIII(2)** and **XIII(3)** were obtained and analysed through SXD. The single crystal formed for this hafnium framework can be seen in Figure 6.1, which provides an indication of the template effect on crystal morphologies. The use of EDA within the reaction resulted in rectangular plate-like crystals being synthesised, whereas the incorporation of DETA produced crystals with a more rod-like shape.

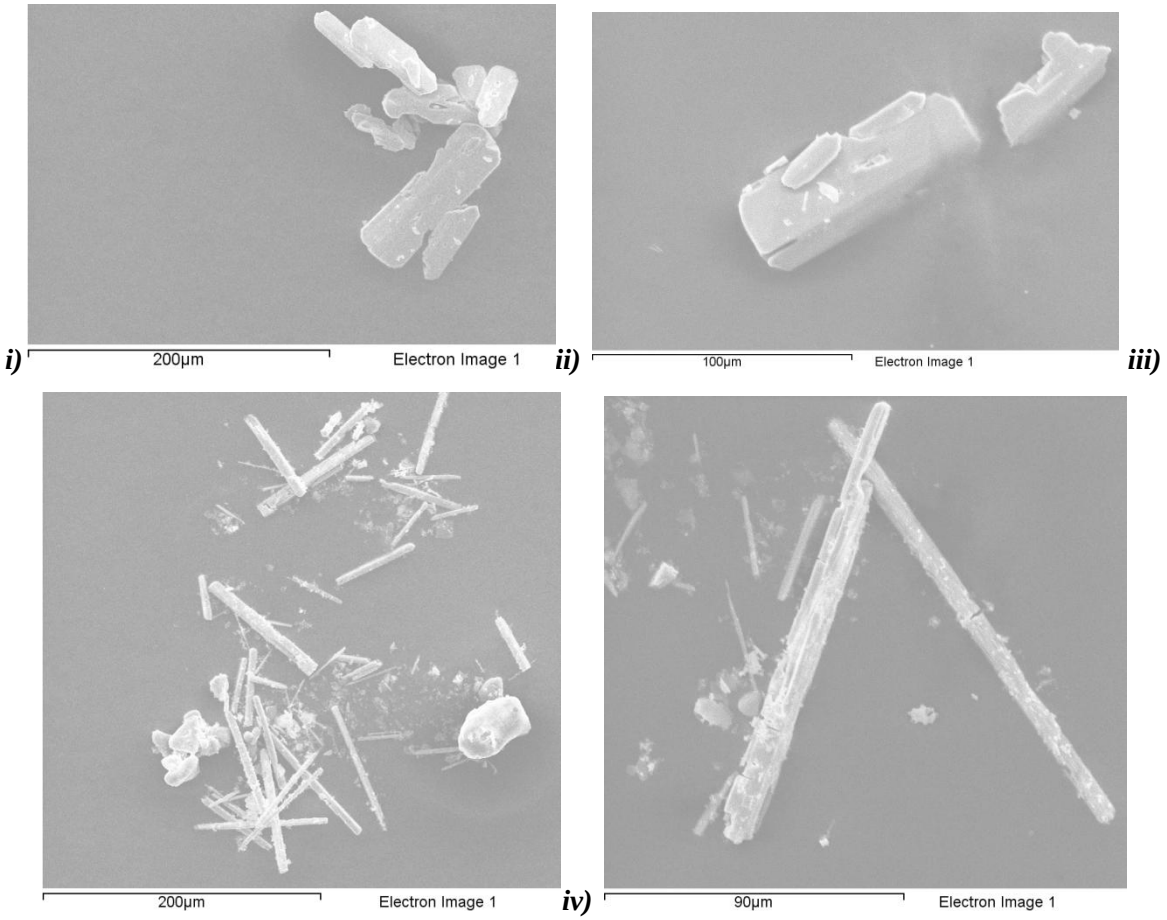

Figure 6.1: *SEM images of* ***i)*** *multiple and* ***ii)*** *single* $Hf^{IV}_2F(HAsO_4)(AsO_4)_2[(C_2H_8N_2)\text{-}H_2]_{1/2}(H_2O)_{1.5}$ *crystals; and* ***iii)*** *multiple and* ***iv)*** *single crystals of* $Hf^{IV}_2F(HAsO_4)(AsO_4)_2[(C_4H_{16}N_3)\text{-}H_3]_{1/3}(H_2O)_{1.5}$

The incorporation of the organic templates affected the lattice parameters and the cell volume of the two materials within compound **XIII**. The incorporation of DETA altered the β angle as well as the *c*-axis, as can be observed in Table 6.2 and Table A.6.1 and A.6.4 in the Appendix.

Table 6.2 *Details of single crystal data collection*

Molecular Formula	$Hf^{IV}_2F(HAsO_4)(AsO_4)_2[(C_2H_8N_2)\text{-}H_2]_{1/2}(H_2O)_{1.5}$	$Hf^{IV}_2F(HAsO_4)(AsO_4)_2[(C_4H_{16}N_3)\text{-}H_3]_{1/3}(H_2O)_{1.5}$
Formula Weight (g)	889.88	930.31
Crystal Appearance	Rectangular plates	Thin rods
Crystal Size (mm)	0.1 x 0.1 x 0.05	0.1 x 0.01 x 0.01
Crystal System	Monoclinic	Monoclinic
Space Group	*C2/c*	*C2/c*
Lattice Parameters	*a* = 17.7600(4) Å, α = 90°	*a* = 28.455(5) Å, α = 90°
	b = 6.7813(2) Å, β = 93.799(2)°	*b* = 6.773(5) Å, β= 123.861°
	c = 23.7325(8) Å, γ = 90°	*c* = 17.686(5) Å, γ = 90°
V(Å^3)	2851.96(4)	2830.43(3)
Z	4	8
Calculated Density (mg/m^3)	3.95	4.07
Temperature (K)	120	120
Theta Range (°)	3-25	3.5-27.6
Wavelength (Å)	Mo *K*α (λ = 0.71073)	Mo *K*α (λ = 0.71073)
Number of Reflections Measured	Total – 12037, Unique –2508	Total – 19368, Unique – 3237
R[*I*>2σ(*I*)][a]	0.049	0.063
***R*1(all data)**	0.071	0.09
***wR*$_2$**	0.090	0.144
Goodness of fit	1.138	1.103

The two hafnium structures were solved using the WinGX software package[19]. The structure of **XIII(3)** exhibited disorder within the channels of the framework and as a result the

template ions and water molecules exhibited disorder and could not be isolated. It was possible to isolate the basic framework of **XIII** $[Hf_2F(AsO_4)_2(HAsO_4)]^{-1}$, although some of the arsenate and hafnium polyhedra were disordered. Thermal analysis indicated that an organic template was present within the material. Thus, the specific nature of the template ion within **XIII(3)** is unclear, but further analysis provided some indication if certain assumptions were made.

Compound **XIII** was analysed using SXD and the basic lattice parameters were obtained. The presence of fluorine was isolated within the structure, when n = 2 or 3, through bond valence calculations[20,21] (Table 6.3 and Table A.6.5 in the Appendix). The majority of the sites (**XIII(2)**; O1-O11; and **XIII(3)**; O1-O8, O10-O12) displayed bond valences typical of divalent anions (average BV: **XIII(2)** BV=2.01(5); **XIII(3)** BV=1.96(8)). In **XIII(2)** the sites O12 and F1, and in **XIII(3)**, O9 and F1, provided alternative bond valences. O12 (1.13) and O9 (1.27) had bond valences more typical of a hydroxide or fluoride anion. These ions were both linked to an AsO_4 group. Within this research study fluoride ions have not been found to bond with the arsenate groups. This finding together with the larger bond valence suggests that these atoms were most likely to be an OH group and this has been assumed. The O12 site also exhibited an increase in the As-O bond length (1.72 Å), compared to the average lengths exhibited by As-O within the structure (average As-O length when **XIII(2)** = 1.66(10) Å, **XIII(3) =** 1.68(5) Å), which is typical of a weakly bound OH group. These are terminal sites within the arsenate tetrahedra (O12 and O9) and were therefore assumed to be hydroxide anions.

Further bond valence calculations indicated that the F sites were substantially under-bonded (compared to the O12 and O9 sites), regardless of whether they were classed as oxygen or fluoride anions (**XIII(2)**: BV O-0.81, F-0.67, **XIII(3)**: BV O-0.90, F-0.74). The bond lengths observed for Hf-F in both structures (**XIII(2)**: Hf-F = 2.0 Å, **XIII(3)**: Hf-F = 1.96 Å), were lower than expected for an Hf-O bond (~ 2.2 Å), and less than the average bond lengths for Hf-O within **XIII** (**XIII(2)/ XIII(3)**: Hf-O = 2.06(2) Å). This indicated that the anion on the F1 sites within both structures was monovalent and likely to be a fluoride ion. EDX analysis completed on the single crystals, demonstrated the presence of fluoride ions within **XIII** ((**XIII(2)**: F = 4.5%; **XIII(3)**: F = 5.23%); Appendix A.6.2, A.6.6), alongside hafnium, arsenic and oxygen. The F1 site houses a monovalent anion within **XIII**, and the presence of fluorine within the EDX analysis indicates that it is a fluoride anion bonded at this site.

Table 6.3: *Bond lengths and bond valence calculations for O anions within* ***XIII(2)***

Atoms	F/O-Hf bond length (Å)	O-As bond length (Å)	Bond Valence F/O-Hf	Bond Valence O-As	Bond Valence Sum
O1	Hf2-2.04(10)	As2-1.66(10)	0.73	1.34	2.07
O2	Hf2-2.11(11)	As1-1.66(10)	0.61	1.32	1.93
O3	Hf2-2.04(11)	As1-1.68(10)	0.73	1.25	1.98
O4	Hf2-2.04(10)	As1-1.67(10)	0.73	1.31	2.04
O5	Hf2-2.08(9)	As3-1.66(9)	0.65	1.34	1.99
O6	Hf2-2.07(10)	As3-1.64(10)	0.68	1.40	2.08
O7	Hf1-2.03(10)	As1-1.66(9)	0.74	1.35	2.09
O8	Hf1-2.07(10)	As2-1.67(10)	0.68	1.31	1.99
O9	Hf1-2.07(10)	As2-1.66(10)	0.67	1.33	2
O10	Hf1-2.08(10)	As3-1.66(9)	0.65	1.34	1.99
O11	Hf1-2.09(10)	As2-1.67(9)	0.64	1.30	1.94
O12	n/a	As3-1.72(11)	n/a	1.13	1.13
F1	1.9993	n/a	0.67	n/a	0.67

The bond valence of the hafnium cations was calculated for **XIII(2)** (Table 6.4) and **XIII(3)** (Appendix A.6.6). In both instances the values expected for hafnium (+4) were observed and any small deviations were anticipated to be a result of the mixture of mono and divalent anions within the hafnium polyhedral unit.

Table 6.4: *Bond lengths and bond valence values for Hf within* ***XIII(2)***

Atoms	Hf-O bond length (Å)	Hf-O Bond Valence
Hf1 – O7	2.03(10)	0.75
Hf1 – O8	2.07(10)	0.67
Hf1 – O9	2.07(10)	0.67
Hf1 – O10	2.08(9)	0.65
Hf1 – O11	2.09(10)	0.64
Hf1 – F1	2.0(8)	0.67
Total		**4.05**
Hf2 – O1	2.04(10)	0.73
Hf2 – O2	2.11(11)	0.6
Hf2 – O3	2.04(9)	0.73
Hf2 – O4	2.04(11)	0.73
Hf2 – O5	2.08(9)	0.65
Hf2 – O6	2.07(10)	0.67
Total		**4.11**

The same building units were obtained in both **XIII(2)** and **XIII(3)**. The materials differed in relation to the presence of alternative organic template ions within the channels. Despite the disorder found within **XIII(3)**, the material formed a structure that was isotypic to **XIII(2)**. For this reason the framework of **XIII(2)** is discussed herein. The templates have been removed from the images in Figure 6.2 for clarity as the framework is stable, but the organic compound exhibits disorder within the channels and is different for **XIII(2)** and **XIII(3)**.

The structure of **XIII** is composed of hafnium-centred octahedra (HfO_6 and HfO_5F) and arsenic-centred tetrahedra (AsO_4 and $HAsO_4$).

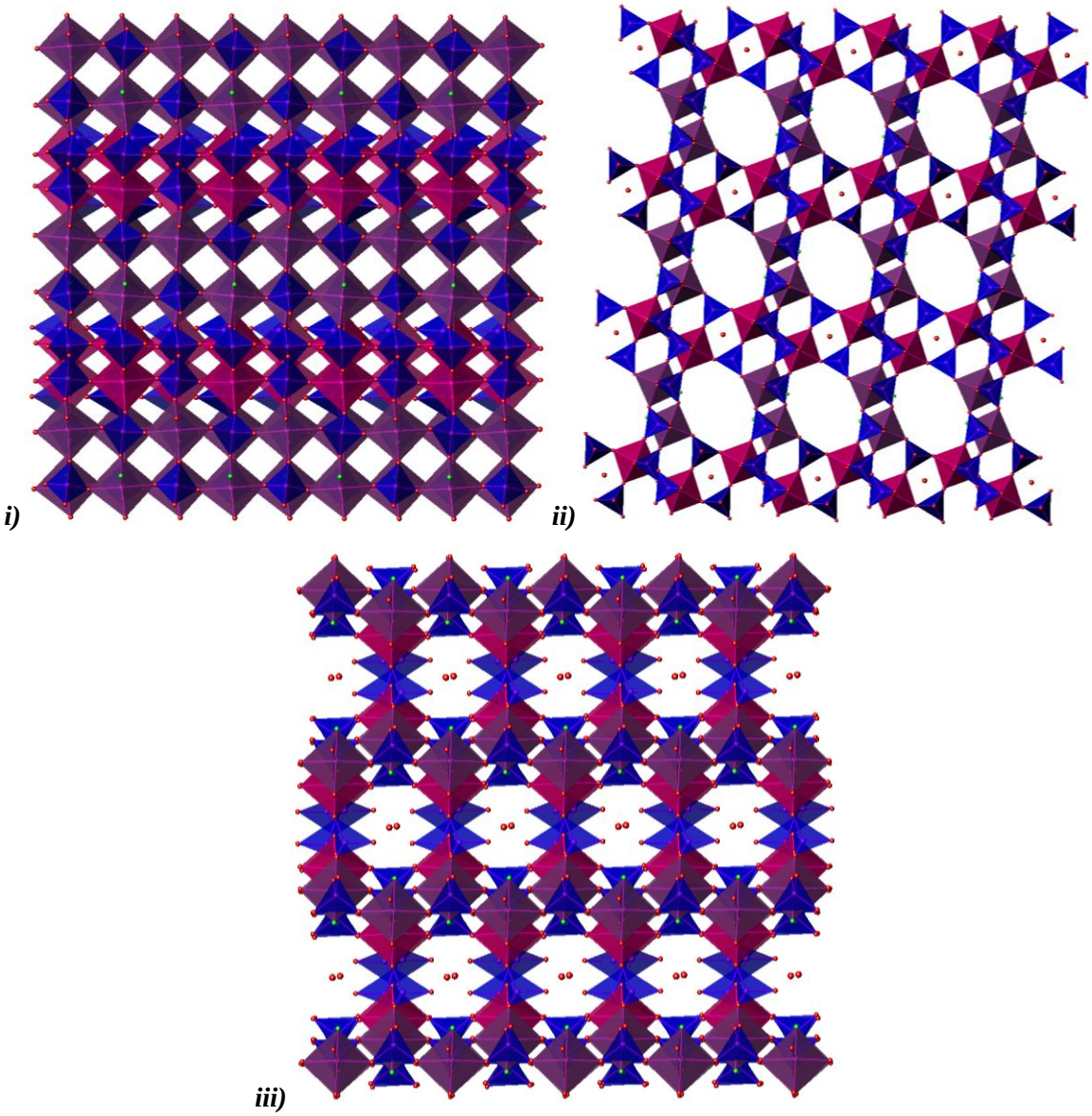

Figure 6.2: *Framework of* ***XIII*** *with the organic template removed, viewed down the* ***i)*** *a* ***ii)*** *b and* ***iii)*** *c-axis [Key: Magenta octahedra – HfO_6, purple octahedra – HfO_5F, Blue tetrahedra – AsO_4; red spheres in channels – H_2O molecules, green sphere in octahedra – F^-, red sphere in octahedra - O^{2-}]*

The hafnium octahedra are fully coordinated within the framework when they exist as HfO_6, and bond to six different arsenate tetrahedra. They exhibit corner-sharing bonding through Hf-O-As links. The HfO_5F octahedra are connected through corner-sharing bonding to five arsenate groups (Hf-O-As) and the final terminal fluoride ion points into the channels that are

viewed through the *b*-axis of the framework (Fig. 6.2.*ii*). The structure of **XIII** contains two distinct channels, one houses the disordered organic template cations and water molecules (large pore within Fig. 6.2 left empty for clarity) and the other is smaller housing further water molecules (Fig.6.2*ii*), included within the diagrams as red spheres. The channels that house the organic templates are roughly 8.11 by 5.71 Å, and the ones which contain water molecules are 4.38 by 3.48 Å. There is one further channel, which lies empty, and is found next to the channels that house the water and this is 5.39 by 3.15 Å. Viewing **XIII** through the *c*-axis (Fig. 6.2.*iii*) highlights the terminal OH groups attached to the $HAsO_4$ tetrahedral units. Hydrogen bonding is assumed to exist between the terminal OH groups and the free water molecules within this channel, (Fig. 6.3; OH (O12) groups have been drawn in yellow for clarity). The assumed hydrogen bonds (hydrogen ions could not be placed through SXD on the terminal O12 or O3W sites) have a length along the O12 and O3W vector of 2.67 Å, which is as expected for hydrogen bonded donor-acceptor distances.

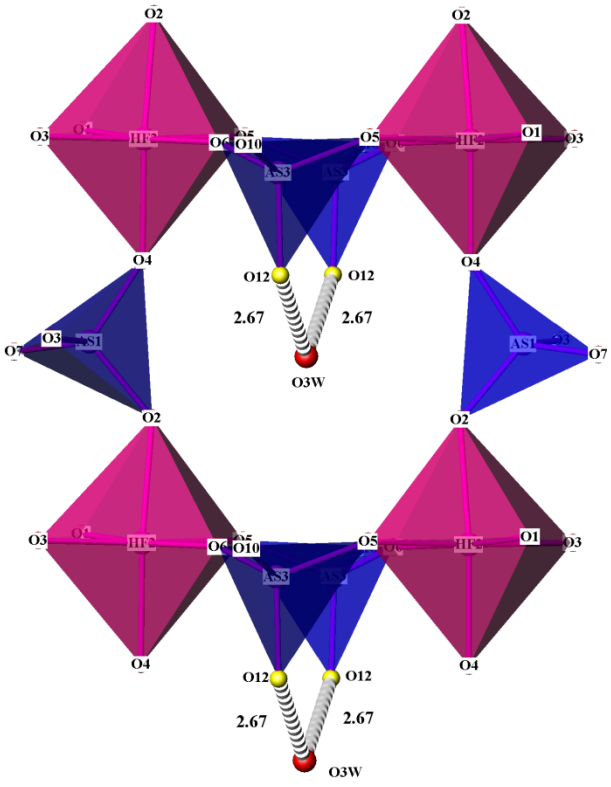

***Figure 6.3**: Hydrogen bonding between terminal hydroxide groups and free water within channels (lengths in Å, OH groups (O12) are coloured yellow for clarity)*

The template ions within the structure of **XIII** were isolated when n = 2 (**XIII(2)**) and are assumed to be fully protonated ($(C_2H_8N_2)$-H_2). The framework was refined but there was disorder within the channels. With the assistance of Dr Mark Light, the disorder of the EDA and water molecules was solved. The electron density within the large pores of the hafnium framework gave rise to bond lengths that were consistent with C-C and C-N distances. Every atom within the EDA unit was found to be half occupied, which formed a cyclic structure. Where the NH_4 atoms overlap there are two half occupied sites, thus becoming one fully occupied N atom (Fig. 6.4). The ions in one colour (red or blue) are present at any one time within the channels, implying that the water molecules hydrogen bond to the hafnium framework on one side, and the protonated EDA molecules on the other. This produces a structure that contains $[(C_2H_8N_2)\text{-}H_2]_{0.5}$ as described in the structural formula.

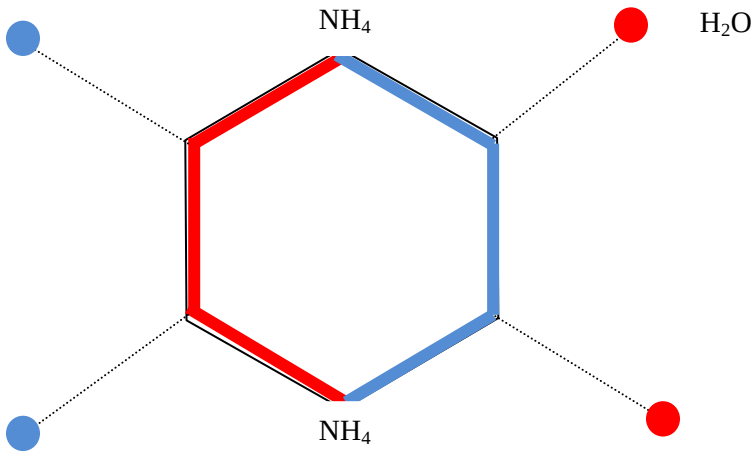

Figure 6.4: *Disorder within the channels of* ***XIII*** *when n=2 and T=EDA*

Figure 6.5 depicts the orientation of the disordered EDA cation within the cavity of the hafnium framework. This image illustrates the entire template unit described in Fig. 6.4, whereas in reality only half of this EDA molecule would exist at any one time within the channels. There is hydrogen bonding between the protons attached to the nitrogen of the EDA unit and the terminal fluoride anions within the hafnium polyhedra (F---HN = 1.87 Å). This interaction aids the stabilisation of the cation, and requires a higher temperature to observe the loss of the template.

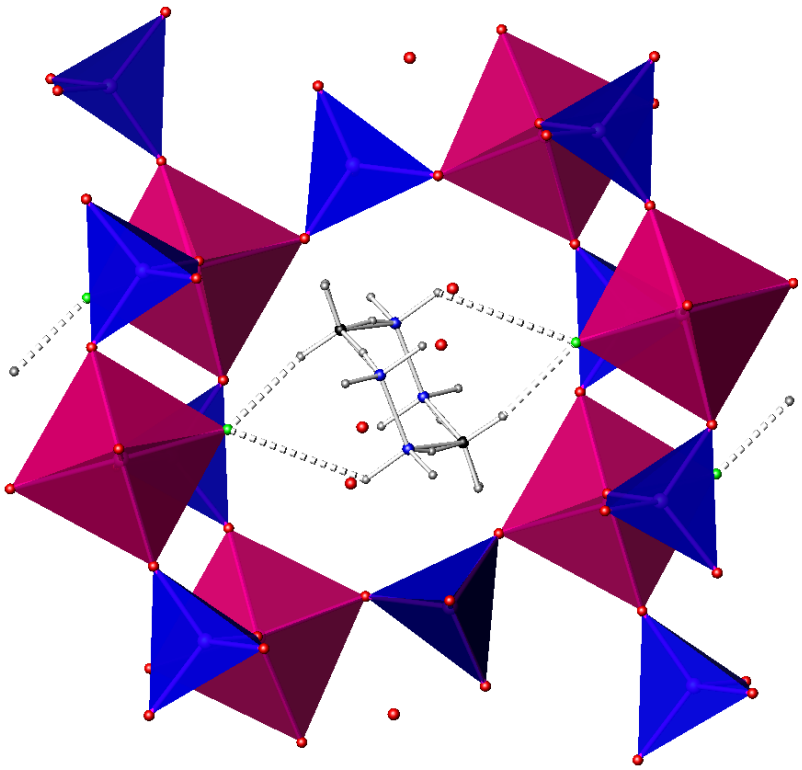

***Figure 6.5**: Channels within **XIII** when n=2, housing disordered protonated EDA*

The IR spectra for compound **XIII(2)** and **XIII(3)** can be found in the Appendix (A.6.3 and A.6.7). The spectra are very similar as a result of their shared framework. The peaks associated with ethylenediamine and diethylenetriamine (3440, 3260, 1585, 1090 cm^{-1}) are found within both spectra, as well as peaks associated with the presence of free water molecules (3600-3200 and 1600 cm^{-1}).

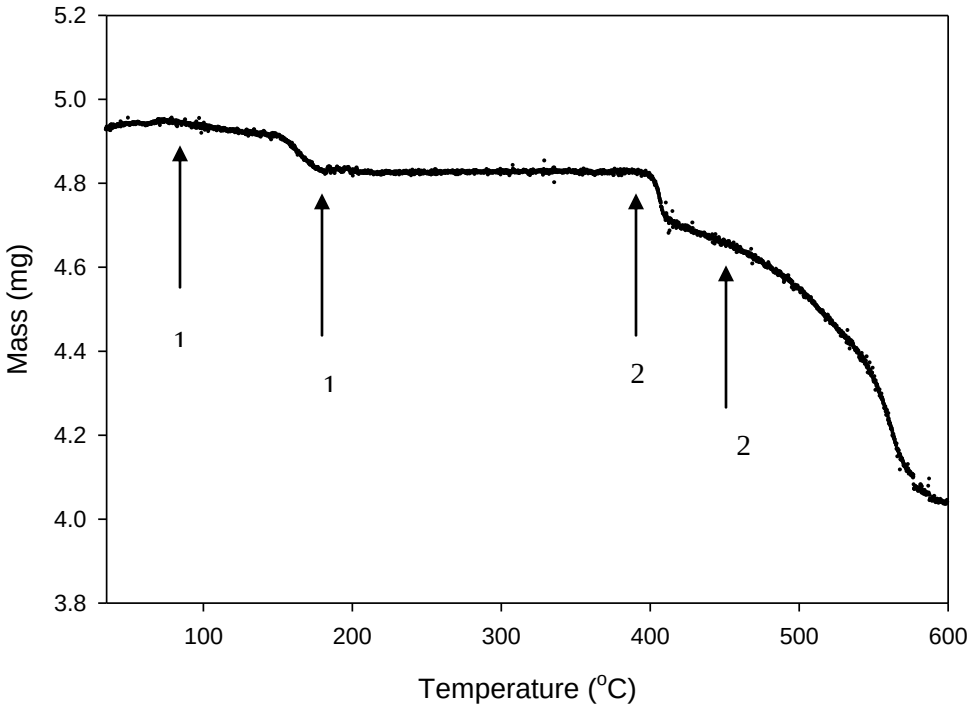

Fig. 6.6: *Mass loss vs. Temperature graph for compound* ***XIII(2)***

Figure 6.6 illustrates the data obtained through thermal analysis for **XIII(2)**. An initial weight loss (1-1) was observed from 82-181 °C, which corresponded to the loss of water within the channels. The low temperature value for the initial loss of mass (1) is associated with H_2O and demonstrates its presence (rather than the higher temperatures required to release ammonia from frameworks). A second mass loss began at 384 and ended at 450 °C (2-2). This relates to the loss of $((C_2H_8N_2)\text{-}H_2)_{0.5}$ within the framework channels. After this point the framework continually lost mass, which was attributed to the collapse of the framework. Overall a mass loss close to 17 % was observed, resulting from the loss of water and organic template.

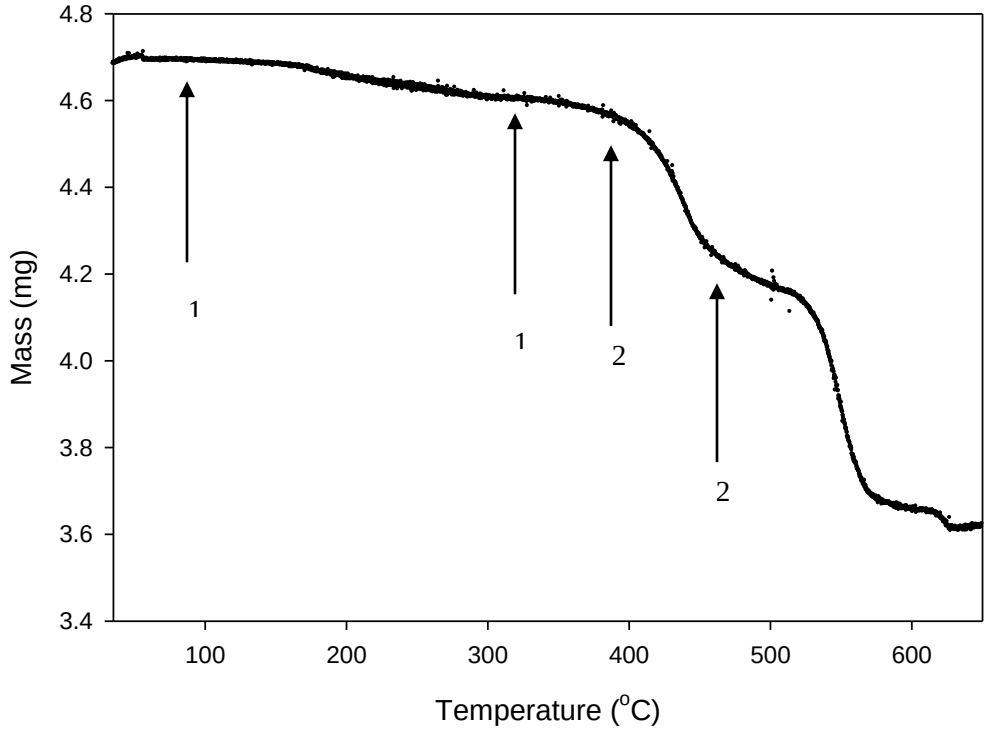

Fig. 6.7: *Mass vs. Temperature graph for compound* ***XIII(3)***

Figure 6.7 illustrates the mass loss for compound **XIII(3)** in air. The initial loss occurs between 94-319 °C. This loss represents the removal of water from within the channels of the framework. The reduction in mass in the form of water requires more energy than for **XIII(2)**, indicating that it is more strongly bound to this structure. The second mass loss begins at 400 and ends at 450 °C. This loss is associated with the removal of $[(C_4H_{13}N_3)\text{-}H_3]_{0.33}$ from the framework channels. The mass loss is similar to that of **XIII(2)**, denoting the connection between these two structures and their similar affinity to these organic templates. Overall a mass loss of 21 % is observed, attributed to the loss of water and organic template. The structure collapses when heated above 550 °C where a continued loss in mass was observed. Although the DETA template could not be placed through SXD analysis there is sufficient information to assume that this exists within the structure of **XIII(3)**.

Throughout this discussion the materials have been referred to as **XIII(2)** and **XIII(3)**. The reason for this is that these hafnium structures are analogous to zirconium fluoro phosphate structures previously synthesised by Wloka *et al*[18]. The structures that involve hafnium have almost

identical unit cell parameters and cell volumes. The only noticeable difference is the presence of an additional half a molecule of water within the channels of the hafnium material. The zirconium frameworks revealed that the template ions exhibited a strong tendency to be disordered within the framework channels. The structure containing zirconium and DETA cations exhibited disorder of the phosphate groups, as is observed within these arsenate analogues. The zirconium materials incorporated a variety of alternative templates such as *N*-methylethylenediamine, 1,3-diaminopropane, *N,N,N',N'*-tetramethylethylenediamine, and in a later paper *trans*-1,4-diaminocyclohexane and 2,2-dimethyl-1,3-diaminopropane[22]. The ease with which the hafnium materials formed these fluorinated templated frameworks suggests that efforts to form these additional compounds would proceed with relative ease. As a result of time constraints, further studies into templated hafnium arsenates and phosphates were not possible within this research project.

6.2 Compound XIV – Layered zirconium arsenate housing EDA and H_2O

$Zr^{IV}_2(AsO_4)_2F_4(H_2O)_2[(C_2H_8N_2)\text{-}H_2]$

6.2.1 Synthesis

The hydrothermal synthesis of compound **XIV** was completed using ZrF_4 (0.1 g, 0.391 mmol, Aldrich 99 %), H_3AsO_4 (0.14 g, 0.986 mmol, 75 % wt. BDH chemicals), and ethylenediamine (EDA) (0.02 g, 0.333 mmol, 99% Aldrich), mixed in water (11 mL) and stirred for thirty minutes. The solution was transferred to a 23 mL teflon-lined steel Parr autoclave and heated at 190 °C for 5 days. The reaction was allowed to cool to room temperature, the solid product separated *via* filtration and washed with warm water.

6.2.2 Results and Discussion

Single crystals of compound **XIV** were isolated from the solid product. The SEM image of the square plates can be seen in Figure 6.8. Results from the SXD data collection can be found in Tables 6.5 and A.6.8 in the Appendix.

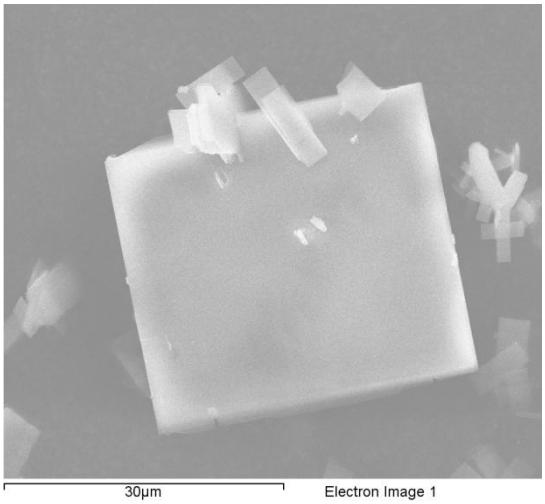

Figure 6.8: *SEM image of $Zr^{IV}_2(AsO_4)_2F_4(H_2O)_2[(C_2H_8N_2)\text{-}H_2]$ crystals*

Table 6.5: *Details of single crystal data collection for* $Zr^{IV}_2(AsO_4)_2F_4(H_2O)_2[(C_2H_8N_2)\text{-}H_2]$

Molecular Formula	$\mathbf{Zr^{IV}_2(AsO_4)_2F_4(H_2O)_2[(C_2H_8N_2)\text{-}H_2]}$
Formula Weight (g)	634.42
Crystal Appearance	Square plate
Crystal Size (mm)	0.05 x 0.05 x 0.02
Crystal System	Triclinic
Space Group	$P\bar{1}$
Lattice Parameters	a = 6.7464(5) Å, α = 87.009(5)°
	b = 6.7872(5) Å, β = 71.274(5)°
	c = 8.5887(7) Å, γ = 89.815(6)°
V (Å^3)	371.91(7)
Z	2
Calculated density (mg/m^3)	2.81
Temperature (K)	120 K
Theta Range (°)	3.0-27.8
Wavelength (Å)	Mo $K\alpha$ (λ = 0.71073)
Number of Reflections Measured	Total – 6999, Unique – 1713
$\boldsymbol{R_1}$ **[I>2σ (I)]**[a]	0.074
$\boldsymbol{R}$**1(all data)**	0.118
$\boldsymbol{wR_2}$	0.147
Goodness of fit indicator	1.15

The basic structure of **XIV** was isolated through the SXD refinement. Bond valence calculations[20,21] (highlighted in Table 6.6), were completed on the suspected mono and divalent anions attached to the framework. Regardless of the assumptions made as to whether these sites were fluoride or oxide, the F1 and F2 sites had bond valences typical of monovalent ions. The remaining sites within **XIV** (O1, O2, O3, and O4) had valences of divalent anions. The presence of fluoride was confirmed within the single crystals of **XIV** through EDX analysis (Appendix A.6.9). The amount of fluorine present (20.1 %) was greater than the quantities of zirconium and

arsenic, which agreed with the structural formula. Within this research project the fluoride anions typically bond to terminal sites within the polyhedra but also exhibit bridging bonds between the metal centres.

Table 6.6: *Bond length and valence calculations for O/F ions within* ***XIV***

Atoms	Bond	Zr-O/As-O bond length (Å)	Bond Valence Zr-O/F and As-O	Bond valence sum
O(1)	O(1)-As(1)	1.6777(7)	1.273	1.969
	O(1)-Zr(1)	2.0621(7)	0.696	
O(2)	O(2)-As(1)	1.6751(8)	1.282	1.929
	O(2)-Zr(1)	2.0891(7)	0.647	
O(3)	O(3)-As(1)	1.6863(7)	1.244	1.887
	O(3)-Zr(1)	2.0915(8)	0.643	
O(4)	O(4)-As(1)	1.6620(7)	1.328	2.009
	O(4)-Zr(1)	2.0700(8)	0.681	
F(1)	F(1)-Zr(1)	2.0099(6)	0.642	0.642
F(2)	F(2)-Zr(1)	1.9850(6)	0.687	0.687

The bond valence of the zirconium within the octahedral unit was +4 (Table 6.7) as anticipated from the starting material (ZrF_4) the presence of fluoride anions within has caused very mild distortions to the octahedra, but these have not affected the electrostatic interactions, and thus the bond valence.

Table 6.7: *Bond lengths and bond valence values for Zr within* ***XIV***

Atoms	Zr-O bond length (Å)	Zr-O Bond Valence
O1	2.06(7)	0.70
O2	2.09(7)	0.65
O3	2.09(8)	0.65
O4	2.07(7)	0.68
F1	2.01(6)	0.64
F2	1.99(6)	0.68
Total		**3.99**

The framework of **XIV** consists of zirconium-centred octahedra (ZrO_4F_2) and arsenic-centred tetrahedra (AsO_4). Each zirconium octahedron is connected to four separate tetrahedra through Zr-O-As corner-sharing bonds on the equatorial sites. The arsenate tetrahedra are fully connected to the layered structure of **XIV**. Fluoride ions reside at the apical sites within the octahedra, which are terminally bonded to the zirconium. The layers within **XIV** can be observed through the *a/b*-axis (Fig. 6.9.*i/ii*), which depicts the zigzag of the zirconium octahedra (Fig. 6.9.*i*). The layers of zirconium and arsenate polyhedra house protonated ethylenediamine ($C_2H_{10}N_2^{2+}$ (EDA)) and water molecules. The hydrogen ions could not be isolated through refinement and so have been placed in fixed positions of 0.8 Å from the ions to which they are connected.

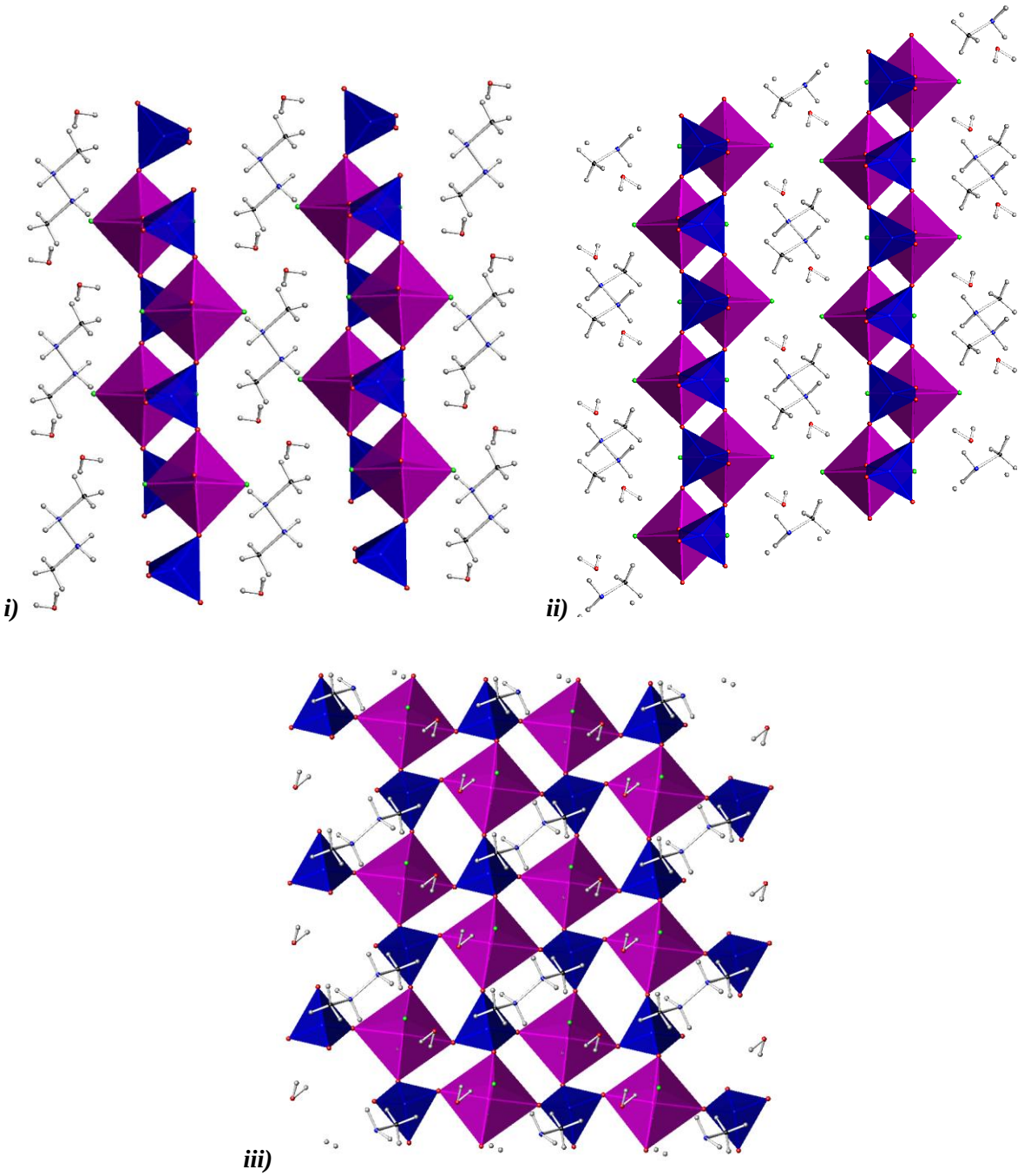

***Figure 6.9**: Structure of **XIV** viewed down the **i)** a **ii)** b and **iii)** c-axis with water molecules and protonated EDA ($C_2H_{10}N_2$) between the layers [Key: Purple octahedra – ZrO_4F_2, blue tetrahedra – AsO_4/$HAsO_4$]*

The framework of **XIV** ($[Zr^{IV}_2(AsO_4)_2F_4]^{-2}$) is charge balanced through protonated EDA molecules within the layers. In a number of inorganic solids that house organic amines, the template molecules exist as cations that charge-balance the structure and also donate electron density to the closest framework O/F anions[23]. The presence of the two extra hydrogen ions within the EDA molecules charge balances the framework, with the H^+ being H-donors to the terminal fluoride anions. Hydrogen bonding is assumed to exist between the terminal fluoride anions and the hydrogen ions attached to the EDA and H_2O molecules. There are F---HOH bonds (2.1 Å) and F---HNH_2 bonds (1.91 Å, Fig. 6.10), although the bond lengths have not been included in the diagrams to aid clarity. The fluoride anions appear to interact with one hydrogen ion from the H_2O molecule (Fig. 6.10.*ii*) and two from the protonated EDA. The lengths of the hydrogen bonds indicate that the materials within the layers are strongly bound, inhibiting easy collapse of the structure of **XIV**.

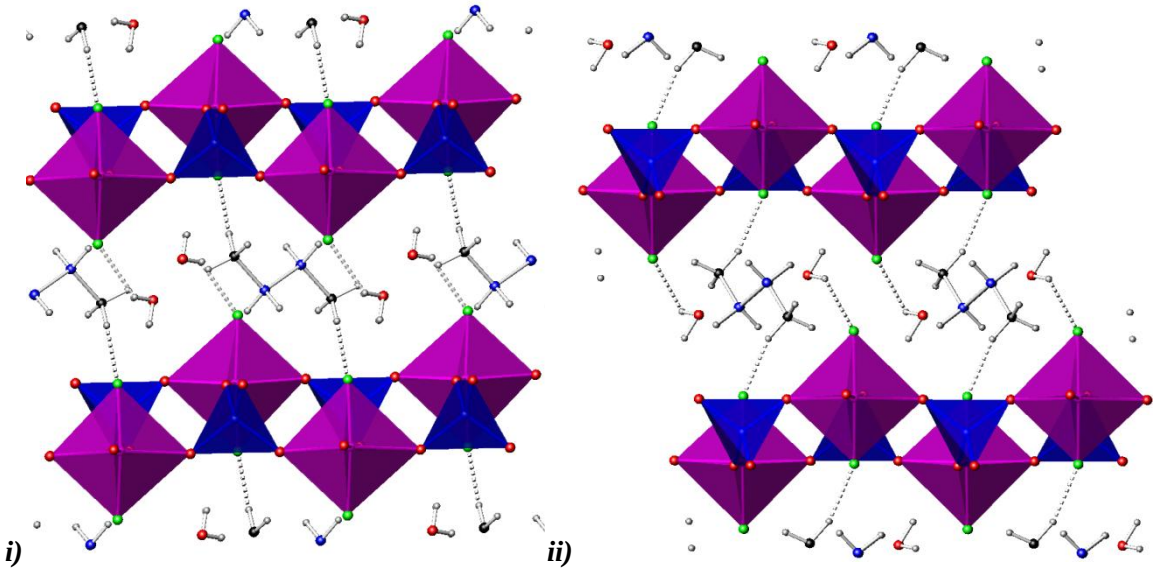

Figure 6.10: *Hydrogen bonding associated with terminal fluoride anions and protonated EDA and H_2O molecules*

Infra-red analysis was completed on a sample of **XIV** in a KBr medium (Appendix A.6.10). Typically, ethylenediamine exhibits asymmetric and symmetric N-H stretching regions as well as N-H bending and C-N stretching[24]. The expected values and the peaks observed are found in Table 6.8. Interactions between the template ions and the framework will affect the values of the

wavenumbers observed (shifting them marginally), as these frequencies are found for free EDA molecules, which accounts for the small shifts within the spectra.

Table 6.8**: Infrared frequencies for ethylenediamine and compound **XIV

Assignment	Wavenumber (EDA)	Wavenumber (XIV)
Asymmetric stretch (N-H)	3440, 3350	3548, 3441
Symmetric stretch (N-H)	3260	3110
N-H bending	1585	1538
C-N stretching	1090, 1040	1119, 1028

Peaks associated with the presence of water within the lattice would be expected between 3600-3200 and 1630-1600 cm^{-1}. The IR spectrum had peaks at 3197 and 1620 cm^{-1}, which accounted for the presence of water within the layers of **XIV**.

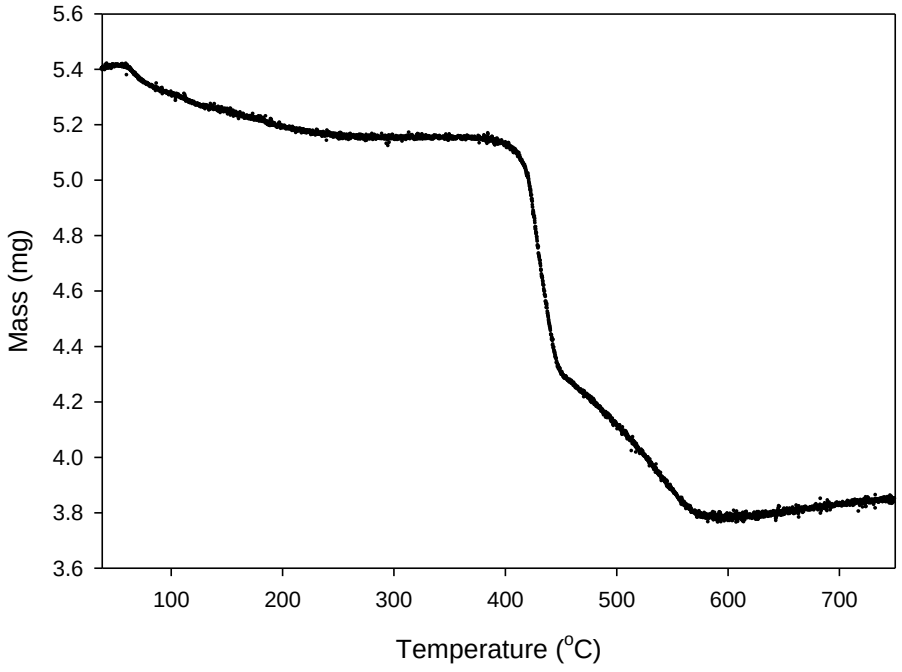

Fig.6.11:** Mass vs. Temperature graph for compound **XIV

Figure 6.11 illustrates the mass loss upon heating in air for compound **XIV**. The initial loss between 94-220 °C, represents the removal of water from within the layers. The loss of water is a slow process requiring a lot of energy that results from its affinity to the terminal fluoride anions attached to the zirconium polyhedra. The second mass loss begins at 420 and ends at 445 °C. This loss is associated with the removal of $[(C_2H_8N_2)\text{-}H_2]$ from between the layers of **XIV**. This value is typical for the removal of EDA, and has been observed for other layered and framework phosphates and arsenates[25]. The removal of template ions produces CO_2, NO_x and H_2O. A further loss can be observed after 445 °C associated with the breakdown of the structure. The collapse of compounds once the organic templates are removed is commonly noted and results from charge misbalances within the structure[26]. Overall a total mass loss of 29 % is observed, which can be attributed to the loss of water and organic template ions.

The structure of **XIV** is not analogous to any known zirconium phosphates or arsenates and has been characterised primarily through SXD analysis. The synthesis of **XIV** was similar to those conducted by Wloka[18] when forming the three-dimensional zirconium fluoride structures. The reaction temperature and concentrations are identical but the presence of ZrF_4 rather than $ZrOCl_2$ and HF is different. This is an example demonstrating that the introduction of ZrF_4 as opposed to $ZrOCl_2$ and HF (as carried out by Wloka using standard fluoride methods), has formed a new zirconium structure.

6.3. Experimental Summary

Despite strenuous efforts, the research described in this chapter has produced just three crystalline structures incorporating organic template ions. Cerium reactions did not produce any successful structures and in addition products such as powdered starting materials (Chapter 3) or basic cerium phosphates and arsenates were obtained. A number of reactions were undertaken with metal starting materials that incorporate these alkylammonium ions and the majority were unsuccessful. The lack of research into hafnium chemistry has led to fewer powder patterns available on the databases, and so similar metal phosphate and arsenate materials were used (zirconium) to identify the results (Table 6.1).

Zirconium reactions that incorporated organic templates produced one new phase (**XIV**) at high temperatures (190 °C). The remaining syntheses (incorporating TMAC, TEAOH, TMAOH and OAD) formed a phase pure crystalline product of **VII**. At lower temperatures the inclusion of EDA or piperazine prevented the reaction from proceeding and consequentially starting materials were obtained in powder form. The increased temperature (190 °C) produced structure **XIV**. Further investigation into alternative templated starting reagents could be applied at these elevated temperature levels, if suitable organic reagents were chosen that would not denature.

Hafnium compounds produced two synthetic analogues to the previously investigated zirconium materials discovered by Wloka[18]. The similarities between the two metal cations (zirconium and hafnium) have been demonstrated by the ease of their formation. The difference between the two structures is minimal, except for the substitution of alternative organic template groups within the channels. A number of further organic templates were encapsulated in the framework highlighted in a later zirconium paper[22]. Similar reactions have been completed for hafnium starting reagents, and defined powder phases were obtained. These powders may contain alternative materials within the channels of the framework, but the lack of single crystal products has thus far hindered analysis of these phases. Repetition of the syntheses with a range of reaction conditions could prove valuable in the production of single crystal forms of these potentially analogous compounds. Similarly, investigation of further hafnium reactions containing alternative organic template ions beyond those investigated within this thesis would also be valuable. The inclusion of different starting materials combined with HF, would be a useful comparison to make with the reactions described in this thesis to observe whether there is enhanced ease of single crystal formation through either technique. The powdered products that did not include crystals or

unknown phases formed a variety of documented hafnium phosphate and arsenate structures. These framework and layer structures appear to form readily (starting materials were not detected) within the powdered reaction product.

This chapter has highlighted not only the difficulty in inserting organic templates into the MF_4 system, but also the lack of phosphate analogues. The phosphate reactions have tended not to form crystalline phases producing powder samples of $M(HTO_4).xH_2O$. Phosphate analogues have formed when alternative starting materials were employed, such as the zirconium fluoro phosphates described above[18,22] when $ZrOCl_2.8H_2O$ was used. Further research into the +4 metals and lanthanides would benefit from re-investigation of alternative starting materials that do not incorporate fluoride (such as $ZrOCl_2$ and HF) to provide comparisons with the reactivity of the materials investigated here.

6.4. Conclusions

Two novel three-dimensional hafnium (**XIII**) and one two-dimensional zirconium (**XIV**) fluorinated templated structures have been synthesised as a result of hydrothermal reactions. The fluoride was obtained from the MF_4 (M = Zr/Hf) starting materials as opposed to the typical $HF/NH_4F/NaF$ reagents. The elevated reaction temperatures (190 °C) were successful in comparison to previous attempts to produce framework materials that proceeded at 140 and 175 °C. Organic templates including and similar to EDA (DETA), favoured these systems. A number of powder patterns were obtained that produced unknown phases. Further research would be valuable into alterations of the reaction conditions in order to provide pathways to crystal formation of these potentially analogous hafnium materials.

The aim of this chapter has been to form structures that house organic template groups. The majority of the syntheses were unsuccessful regardless of the size or shape of the template included or the temperature at which the reaction proceeded. Novel compounds were obtained that did not contain these template ions, and in other cases the presence of the template increased solubility within the solution which enabled new phases to form. In some cases, such as for cerium reactions, it was assumed that the CeF_4 altered the reaction in a way that did not facilitate incorporation of the template, thereby inhibiting it from reacting (Chapter 3).

6.5 References

(1) Sang, S. Y.; Chang, F. X.; Liu, Z. M.; He, C. Q.; He, Y. L.; Xu, L. In *3rd Asia-Pacific Congress on Catalysis*; Elsevier Science Bv: Dalian, PEOPLES R CHINA, 2003, p 729-734.

(2) Cheng, S. F.; Tzeng, J. N.; Hsu, B. Y. *Chemistry of Materials* **1997**, *9*, 1788-1796.

(3) Gier, T. E.; Bu, X. H.; Feng, P. Y.; Stucky, G. D. *Nature* **1998**, *395*, 154-157.

(4) Chatelain, T.; Patarin, J.; Fousson, E.; Soulard, M.; Guth, J. L.; Schulz, P. *Microporous Materials* **1995**, *4*, 231-238.

(5) Loiseau, T.; Simon, N.; Marrot, J.; Ferey, G. *Solid State Sciences* **2006**, *8*, 1361-1367.

(6) Kongshaug, K. O.; Fjellvag, H.; Lillerud, K. P. *Chemistry of Materials* **2000**, *12*, 1095-1099.

(7) Chippindale, A. M.; Gaslain, F. O. M.; Cowley, A. R.; Powell, A. V. *Journal of Materials Chemistry* **2001**, *11*, 3172-3179.

(8) Cheon, Y. E.; Park, J.; Suh, M. P. *Chem Commun (Camb)* **2009**, 5436-8.

(9) Hong, S.; Oh, M.; Park, M.; Yoon, J. W.; Chang, J.-S.; Lah, M. S. *Chem Commun (Camb)* **2009**, 5397-9.

(10) Nouar, F.; Eckert, J.; Eubank, J. F.; Forster, P.; Eddaoudi, M. *Journal of the American Chemical Society* **2009**, *131*, 2864-2870.

(11) Kickelbick, G. *Hybrid materials: synthesis, characterization, and applications* John Wiley, 2007.

(12) Andrew I. Cooper; Rosseinsky, M. J. *Nature Chemistry* **2009**, *1*, 26-27.

(13) Ekambaram, S.; Serre, C.; Ferey, G.; Sevov, S. C. *Chemistry of Materials* **2000**, *12*, 444-449.

(14) Dong, J. X.; Liu, L.; Li, J. P.; Li, Y.; Baerlocher, C.; McCusker, L. B. *Microporous and Mesoporous Materials* **2007**, *104*, 185-191.

(15) Wang, D.; Yu, R. B.; Kumada, N.; Kinomura, N. *Chemistry of Materials* **2000**, *12*, 956-960.

(16) Serre, C.; Guillou, N.; Ferey, G. *Journal of Materials Chemistry* **1999**, *9*, 1185-1189.

(17) Kemnitz, E.; Wloka, M.; Trojanov, S.; Stiewe, A. *Angewandte Chemie-International Edition in English* **1996**, *35*, 2677-2678.

(18) Wloka, M.; Troyanov, S. I.; Kemnitz, E. *Journal of Solid State Chemistry* **1998**, *135*, 293-301.

(19) Farrugia, L. J. *Journal of Applied Crystallography* **1999**, *32*, 837-838.

(20) Brown, I. D.; Altermatt, D. *Acta Crystallographica Section B-Structural Science* **1985**, *41*, 244-247.

(21) Brese, N. E.; O'Keeffe, M. *Acta Crystallographica Section B-Structural Science* **1991**, *47*, 192-197.

(22) Wloka, M.; Troyanov, S. I.; Kemnitz, E. *Journal of Solid State Chemistry* **2000**, *149*, 21-27.

(23) Zhao, Y. N.; Zhu, G. S.; Jiao, X. L.; Liu, W.; Pang, W. Q. *Journal of Materials Chemistry* **2000**, *10*, 463-467.

(24) Stuart, B. H. *Infrared spectroscopy: fundamentals and applications*; John Wiley, 2004.

(25) Escobal, J.; Pizarro, J. L.; Mesa, J. L.; Lezama, L.; Olazcuaga, R.; Arriortua, M. I.; Rojo, T. *Chemistry of Materials* **2000**, *12*, 376-382.

(26) Xu, L.; Sun, Y. Q.; Wang, E. B.; Shen, E. H.; Liu, Z. R.; Hu, C. W. *Journal of Solid State Chemistry* **1999**, *146*, 533-537.

CHAPTER SEVEN

HEXAGONAL LANTHANIDE PHOSPHATES

7.0 Introduction

Lanthanide orthophosphates are known to form five structural classes. Monazite-type $LnPO_4$ (Ln = La-Gd)[1], xenotime $LnPO_4$ (Ln = Tb-Lu)[2], mineral Rhabdophane-type $LnPO_4.nH_2O$ (Ln = La-Dy, n = 0.25-2.5)[3], weinschenkite-type $LnPO_4.2H_2O$ (Ln = Gd-Yb)[4] and orthorhombic $DyPO_4.1.5H_2O$[5]. The hydrated lanthanide phosphates investigated in this research thesis are of the Rhabdophane type.

Hydrated lanthanide phosphates were first isolated by Mooney *et al.*[6,7], in the late 1940s. Since that time extensive studies have been carried out on these materials and there have been a significant number of research papers outlining their characteristics and wide range of practical uses. These applications include nuclear waste management[8] (in view of their high chemical and thermal stability and low solubility in water[9]) optical and optoelectronic applications such as lasers[10], fuel cells[11], sensors, and the labelling of cells[12].

Water is typically present within these structures, and a number of studies have included thermal analysis (TGA) of these materials[9, 13-15]. It is thought that the Rhabdophane mineral structure contains interstitial water within the channels[16], whereas within the weinschenkite material the water is structurally bonded, requiring more energy and therefore higher temperatures to remove it from the framework. There is an ongoing debate as to the level of hydration within these Rhabdophane compounds. Alternative preparative methods are reported in the literature, which include hydrothermal techniques, high temperature solid state, precipitation, and sol-gels reactions. The resultant structures have differing values of water, ranging between 0.5 - 2.5 per Ln^{3+} ion[17,18]. It is proposed that this is a consequence of the differing synthetic routes employed, which affects the structure formation, and hence the degree of hydration.

There are no reported examples of single crystals of the Rhabdophane phase in the literature as the formation of these lanthanide products is rapid, hence the powders or crystals precipitated tend to be too small for analysis[19]. There has been no research to date that defines the exact placement of the water molecules within these crystal structures, how they are bonded, and how this affects the lattice of these hydrated lanthanide phosphates.

Initial research efforts within this part of the study focussed on producing new lanthanide phosphate structures. The overall aim was to synthesise interesting new frameworks that incorporated organic template ions such as small DABCO and the larger PHEN. It was believed

that any new materials produced would exhibit similar structural archetypes to the aluminosilicate zeolites, and that the presence of the lanthanide ions would support potential applications in areas such as sensors and storage.

Using the techniques of thermal analysis (TGA), variable temperature powder X-ray diffraction (VT-PXD) and fluorescence spectroscopy, this chapter examines the degree of hydration within neodymium and terbium phosphates, two lanthanide orthophosphate compounds with a Rhabdophane structure. The aim was to observe the level of hydration within these materials and how the presence of water (or lack of it) affected the structure.

7.1 Synthesis

The resulting powder samples were prepared *via* hydrothermal methods. $Ln(NO_3)_3.xH_2O$ (0.1 g, Nd - 0.0003 mmol, Tb – 0.0002 mmol, Aldrich, 99.99%) was dissolved in distilled water (6 mL). H_3PO_4 (Nd – 0.15 g, 0.0015 mmol; Tb – 0.11 g, 0.0011 mmol, Aldrich, 99.99%) was dissolved separately in distilled water (5 mL). The two solutions were slowly mixed together, and allowed to stir for ten minutes. The reaction mixture was placed in a 23 mL Teflon-lined Parr autoclave and sealed. The hydrothermal bomb was placed in an oven, heated to 140 °C and held at this temperature for 5 days. The reaction was allowed to cool to room temperature slowly. The resulting solids (Nd – purple; Tb – white) were filtered, washed with hot distilled water, and dried at 95 °C for 2 hours to remove surface water.

7.2 Results and Discussion

It was not possible to obtain crystals suitable for single crystal X-ray diffraction analysis *via* the hydrothermal methods employed. The product precipitated immediately into solution when the starting materials were mixed, hence resulting in polycrystalline powders. Varying reaction parameters such as pH, reaction time and temperature did not encourage single crystal growth. The powders from the hydrothermal reactions were analysed through X-ray diffraction, which confirmed they were phase pure $LnPO_4.nH_2O$ (*Ln* = Nd, Tb).

The Rhabdophane lanthanide orthophosphate system $LnPO_4.nH_2O$ (*Ln* = La-Tb) has a hexagonal structure with channels that are observed when viewed down the *c*-axis[6]. The lanthanide polyhedra are eight-coordinate, and are linked to the phosphate tetrahedra at all oxygen sites. The framework is fully connected, and exhibits edge-sharing of the lanthanide polyhedra to one another and the phosphate groups. Figure 7.1 depicts the structure of the orthophosphate and the channels present. The water molecules have been removed from the structure to aid clarity, and they are assumed to reside within the channels.

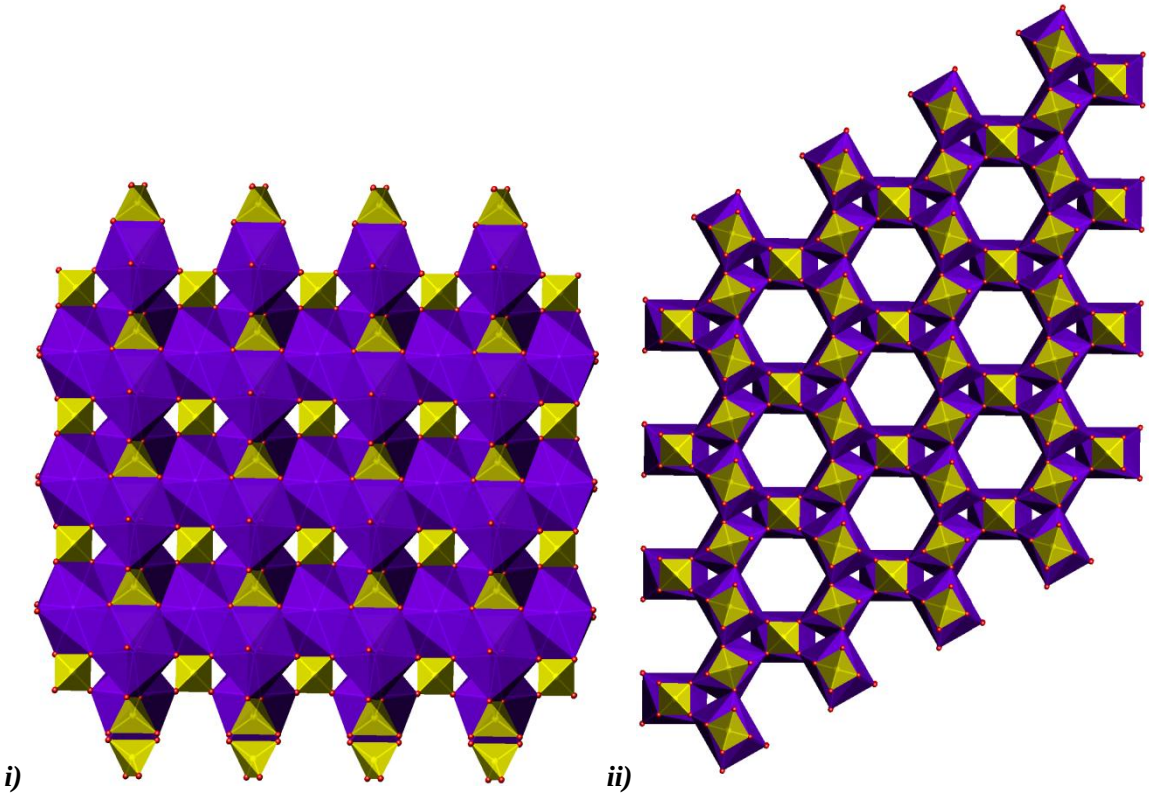

***Figure 7.1**: The structure of hexagonal $LnPO_4.nH_2O$ (water has been removed for clarity) viewed down the **i)** a, and **ii)** c-axis [Key: Yellow tetrahedra – PO_4, purple polyhedra – LnO_8 (Ln = Nd/Tb)]*

EDX analysis was performed on the bulk sample. The results highlighted that both the terbium and neodymium phosphate samples were entirely composed of Tb/Nb, P and O. Both samples were found to consist of lanthanide, phosphate and oxygen atoms. Small single crystallites were not found within the SEM images and so analyses through PXD techniques were applied.

The powder products were characterised using PXD, which confirmed that they were phase pure hydrated hexagonal phases of neodymium and terbium phosphates. The samples were dried at 350 °C; a temperature that ensured the complete loss of water without the possibility of a phase change. PXD patterns of the dehydrated samples were recorded in an air sensitive sample holder, and then the samples were left in air for 24 hours before re-collecting PXD patterns. The patterns exhibited a lattice shift to the right when dehydrated (Fig. 7.2), indicating that the unit cell had increased in size. PXD also demonstrated that leaving the dehydrated samples in air for 24 hours was sufficient to rehydrate them, resulting in a reversion to their original form. When the water was removed from the structures a small colour alteration was observed. The neodymium sample

changed from lilac in the hydrated form to a greyer shade of lilac when anhydrous. The terbium sample was white when hydrated, and off-white when dehydrated. The colour change was not permanent, and when left in air to rehydrate the materials reverted to their original forms.

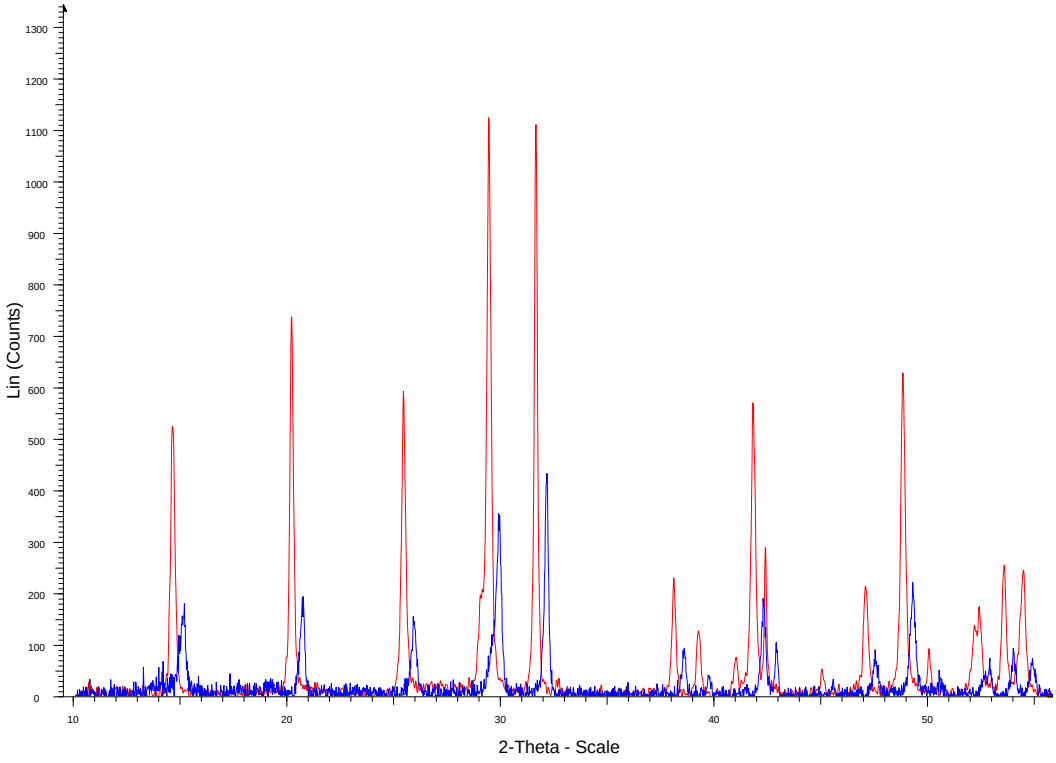

Figure 7.2: *XRD patterns for hydrated $NdPO_4.nH_2O$ (orange) and dehydrated $NdPO_4$ (red)*

Thermal analyses of the powder samples were performed to determine the water content of the two materials. The results of the TGA analysis for both neodymium and terbium phosphates are shown in Figure 7.3. A small mass loss is observed in both cases below 100 °C, which is attributed to the loss of surface water that was not removed in the drying process. The change that occurs between at 140-240 °C is associated with the loss of water from within the channels of the structures. The temperatures at which the mass losses occur indicate that water is weakly bound (if it was more strongly bound the water loss would occur at higher temperatures). These factors indicate that zeolitic rather than chemically bound H_2O units are present. The temperature at which the water loss is complete (full dehydration), varies depending on the Ln^{+3}, for example, this occurs at 250 °C for neodymium compared to 215 °C for terbium. The reduction in the size of the

effective ionic radii (Nd: 1.109, Tb: 1.040[20] Å) increases the ease with which water is lost from the framework. The strength of the attraction between the lanthanide ion and the water molecules lessen with the reduction in ionic radii. The decrease in effective lanthanide size allows the atoms within the structure to cluster together, reducing the size of the unit cell. Making the assumption that the mass loss is due solely to water calculations from the TGA analyses produces a mass loss of 0.59 H_2O molecules for both structures, implying that $n = 0.59$. This is in line with recent work undertaken by Lucas[17], where the Rhabdophane phases produced contained 0.6 water molecules.

The second exothermic process which occurs between 750-850 °C is due to a structural change, whereby the crystal system undergoes a change from the hexagonal to monoclinic monazite type ($LnPO_4$) that is not related to any mass loss. This phase change has been documented by other research groups[15]. The monazite phase is stable to high temperatures, and PXD analysis of the residual powder after thermal investigations demonstrated this to be the resulting product for both neodymium and terbium phosphates.

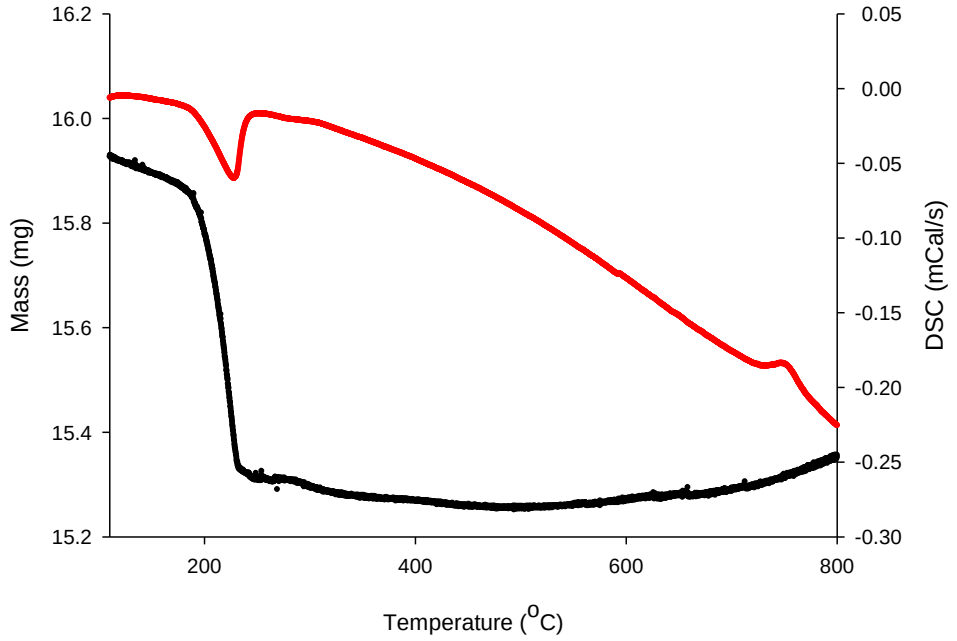

i)

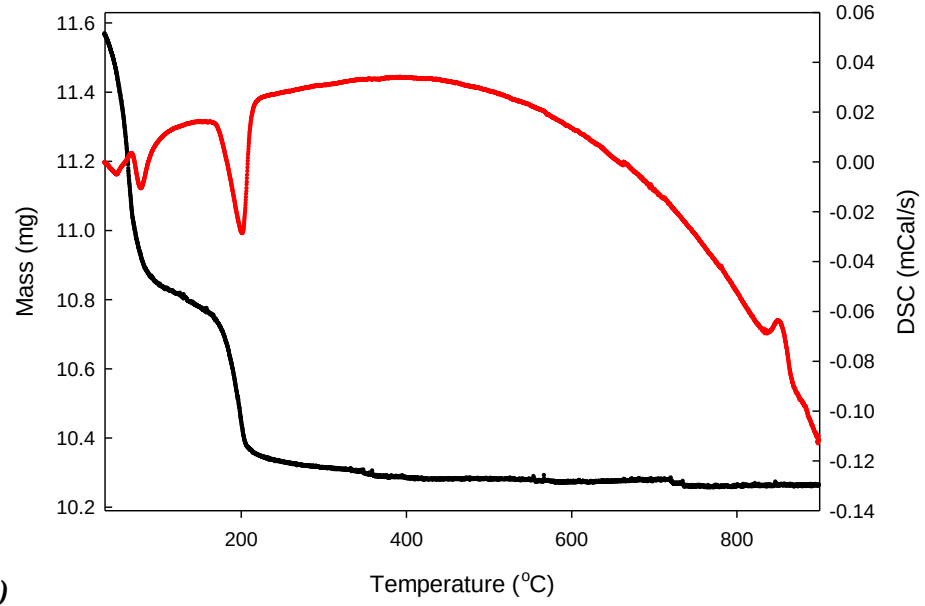

ii)

Figure 7.3: *Mass vs. Temperature graph for* ***i)*** *$NdPO_4.nH_2O$ and* ***ii)*** *$TbPO_4.nH_2O$ [Key: TGA curve – black; DSC curve – red]*

Variable temperature powder X-ray diffraction (VT-PXD) studies were performed on the two materials to investigate the link between the level of hydration and the lanthanide ion. Powder

patterns were recorded across the temperature range 30-350 °C, specifically at the following steps: 30, 100, 140, 180, 200, 230 and 350 °C. This series showed the complete transformation from hydrated to anhydrous (140-180°C). The dehydration processes occurred more rapidly in the VT-PXD studies than in the TGA analyses. It is proposed here that this is a result of the samples remaining at each temperature step for 24 hours to allow for data collection (in the VT-PXD studies), whereas the TGA was collected using a continuous heating rate of 1 °C per minute. The refinement programme GSAS[21] was used to calculate the unit cell parameters for both $NdPO_4$ and $TbPO_4$ at each temperature step, Figure 7.4 illustrates how the *a* and *c* parameters vary as a function of temperature. The Rietveld fits can be seen in the appendix (A.7.1, A.7.2, A.7.3 and A.7.4). The hexagonal anhydrous $NdPO_4$[7] and $TbPO_4$[16] structures were used as a starting model in the refinement. The Rietveld plots provided information regarding the changes to the unit cell lengths as a function of temperature for neodymium and terbium phosphates (Fig. 7.4).

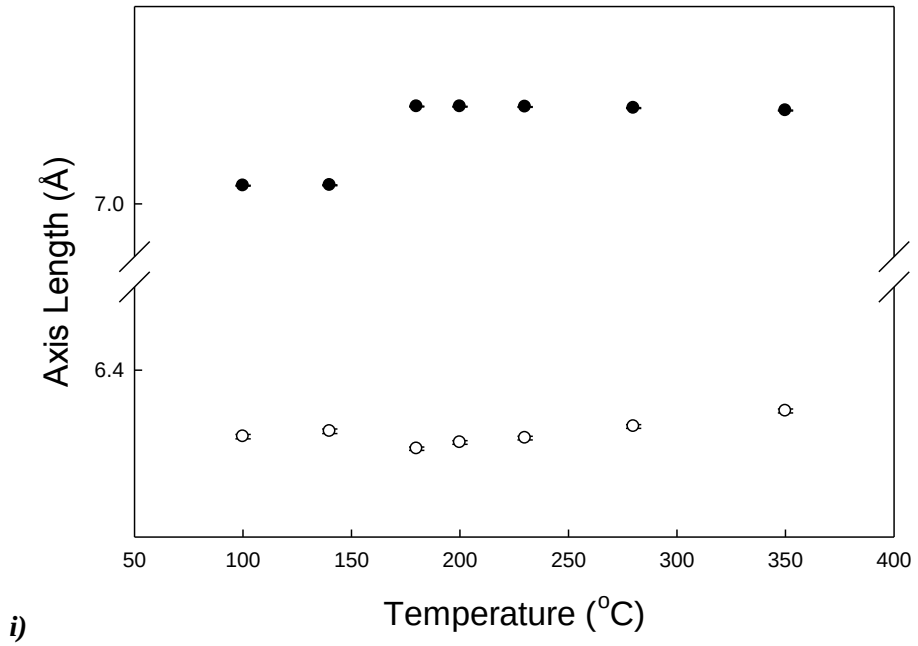

i)

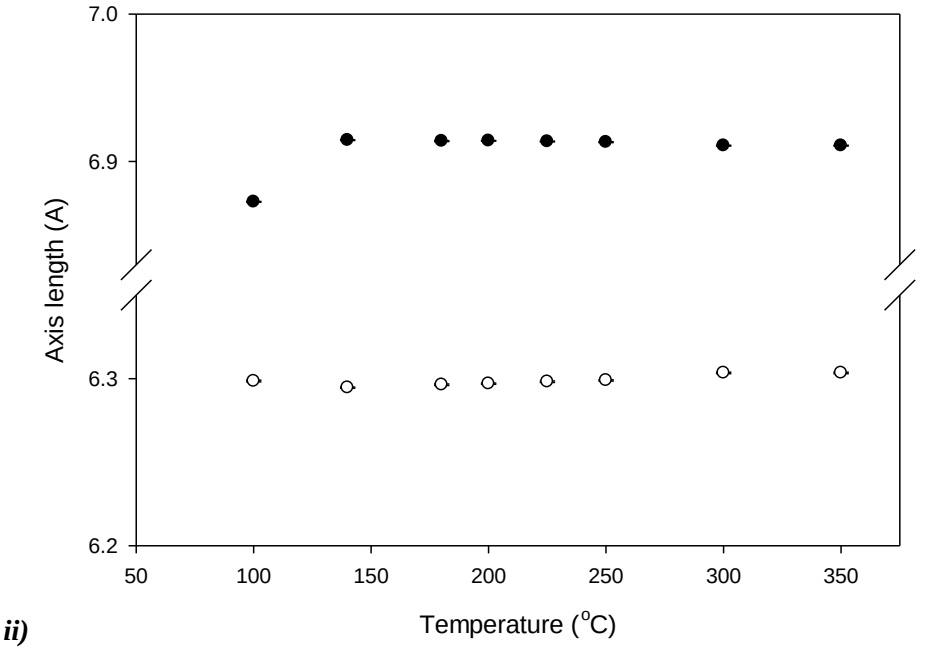

ii)

Figure 7.4: *Graph to show the changes in lattice (a-axis (black) c-axis (white)) vs. temperature with error bars included for* ***i)*** *$NdPO_4.nH_2O$ and* ***ii)*** *$TbPO_4.nH_2O$*

The data illustrated that the lattice expands through the *a*-axis once heated for both materials. The water is bound more weakly in the terbium material as an increase in the *a*-axis is observed at 140 °C, whereas in the case of neodymium this requires more energy and is noted at 180 °C. This indicates that the incorporated water creates a lattice shift that decreases the size of the unit cell when hydrated at room temperature. The resultant void of the water molecules (when the materials are dehydrated) causes the lattice to expand. Using these results it is proposed that the lanthanide ions interact with the water molecules within the channels causing a 'shrinking' effect. The dehydration of the structure means that the lanthanide atoms are no longer attracted to the water molecules, causing the change to lattice size. The shift in the *a*-axis for terbium is 6.87 to 6.91 Å (an increase of 0.04 Å) between 100 and 140 °C. Neodymium exhibits a larger alteration from 7.01 to 7.07 Å (an increase of 0.06 Å) between 140 and 180 °C in the *a*-axis, which is assumed to be a result of the variation in lanthanide ion sizes. Thus, both materials exhibit small, but noticeable differences in their lattice parameters. The contraction when water is present and expansion when water is lost is a movement observed through the *a*-axis; the width of the channels within the structure, expands when the water is removed. Figure 7.5 shows the TGA curve versus the temperature and cell volume for $NdPO_4.nH_2O$. The change in unit cell volume is directly related to the water that is lost from the structure.

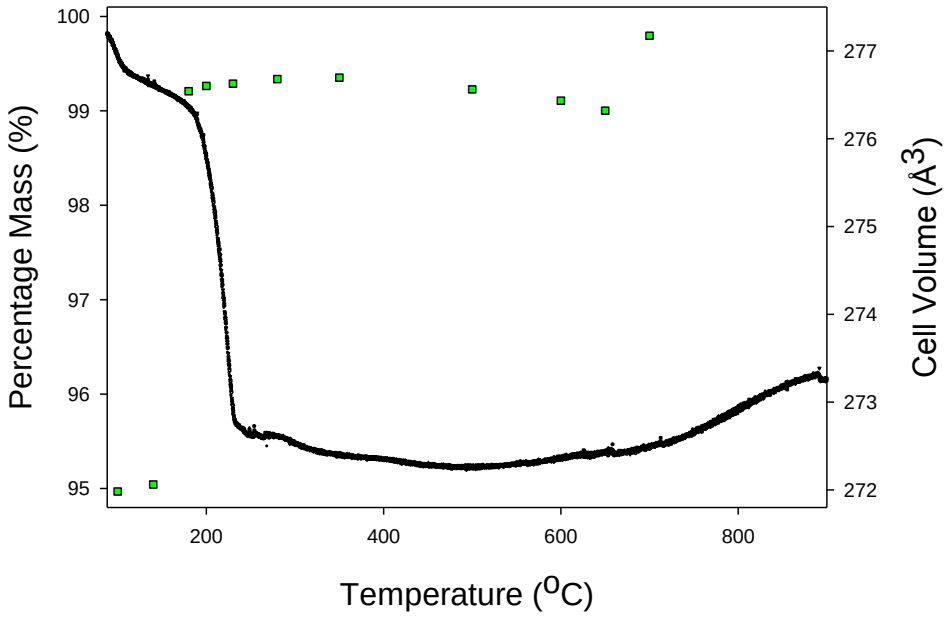

Figure 7.5: *Graph to show the TGA curve (black) and unit cell volume (green) vs. the temperature*

The cell volume also increases in size upon heating, and there is a resultant loss of water for both the terbium and neodymium phosphate structures (Fig. 7.6). The change in the volume occurs at a lower temperature in the terbium sample than for neodymium.

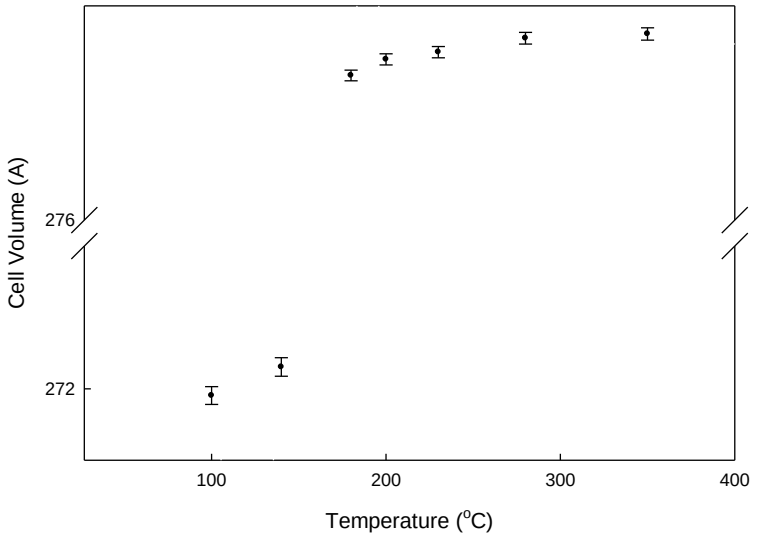

i)

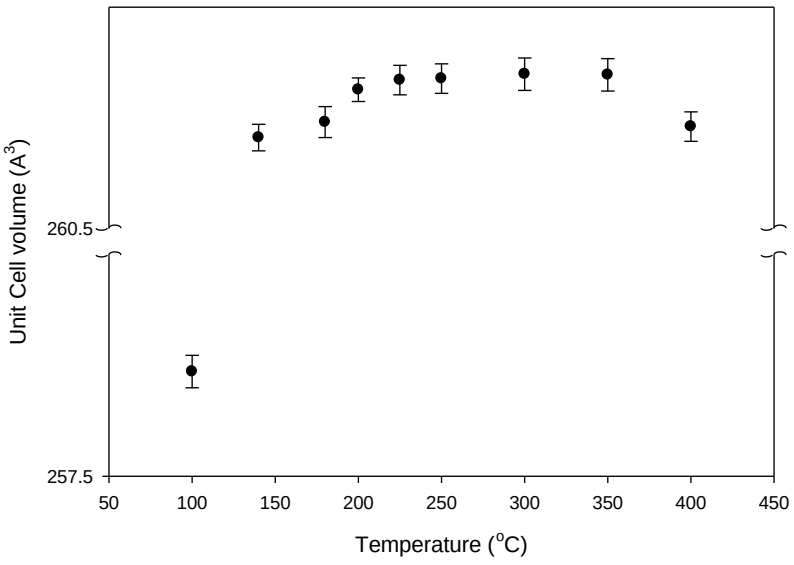

ii)

Figure 7.6: *Change in unit cell volume (Å^3) vs. temperature (°C) for* ***i)*** *$NdPO_4.nH_2O$ and* ***ii)*** *$TbPO_4.nH_2O$*

The cell volume of terbium increases from 257.6 to 260.6 Å ^{3} (an increase of 3 Å) and neodymium from 272 to 276.6 Å^3 (an increase of 4.6 Å) between 100 and 140 °C. The water loss causes a change of between 3-4 Å^3 in the respective volumes of the unit cell, and an increase in the *a*-axis, although there is no change to the hexagonal structure. These results contradict previous research in 2004, where the lanthanide orthophosphates (cerium) were described as shrinking upon heating[15]. The findings provided here suggest that these factors may have been misinterpreted in the earlier research, and that the interaction of the lanthanide ion with the interstitial water molecules is fundamental to the unit cell parameters.

Lanthanide elements are fluorescent materials that produce emissions as a result of the excitation of electrons in the 4*f* orbitals[22]. The transitions are spin-forbidden since they are movements from states of different multiplicities, and so the process is relatively slow. The fluorescence of neodymium is generally less than that of terbium[23], as a result of Tb^{3+} (and Er^{3+}) having excited levels that require less energy than other lanthanide elements in order to emit fluorescence.

The fluorescence spectra for neodymium and terbium were recorded on both hydrous and anhydrous samples of the powdered materials. The results indicated that there were no major differences in the two neodymium spectra. The terbium sample exhibited small changes, which can be observed in Figure 7.7. The sample was dried in an oven overnight at 350 °C and placed in an air sensitive sample holder and the fluorescence spectrum recorded. The sample was then left in air for 24 hours in order for the material to fully rehydrate, and a second spectrum documented.

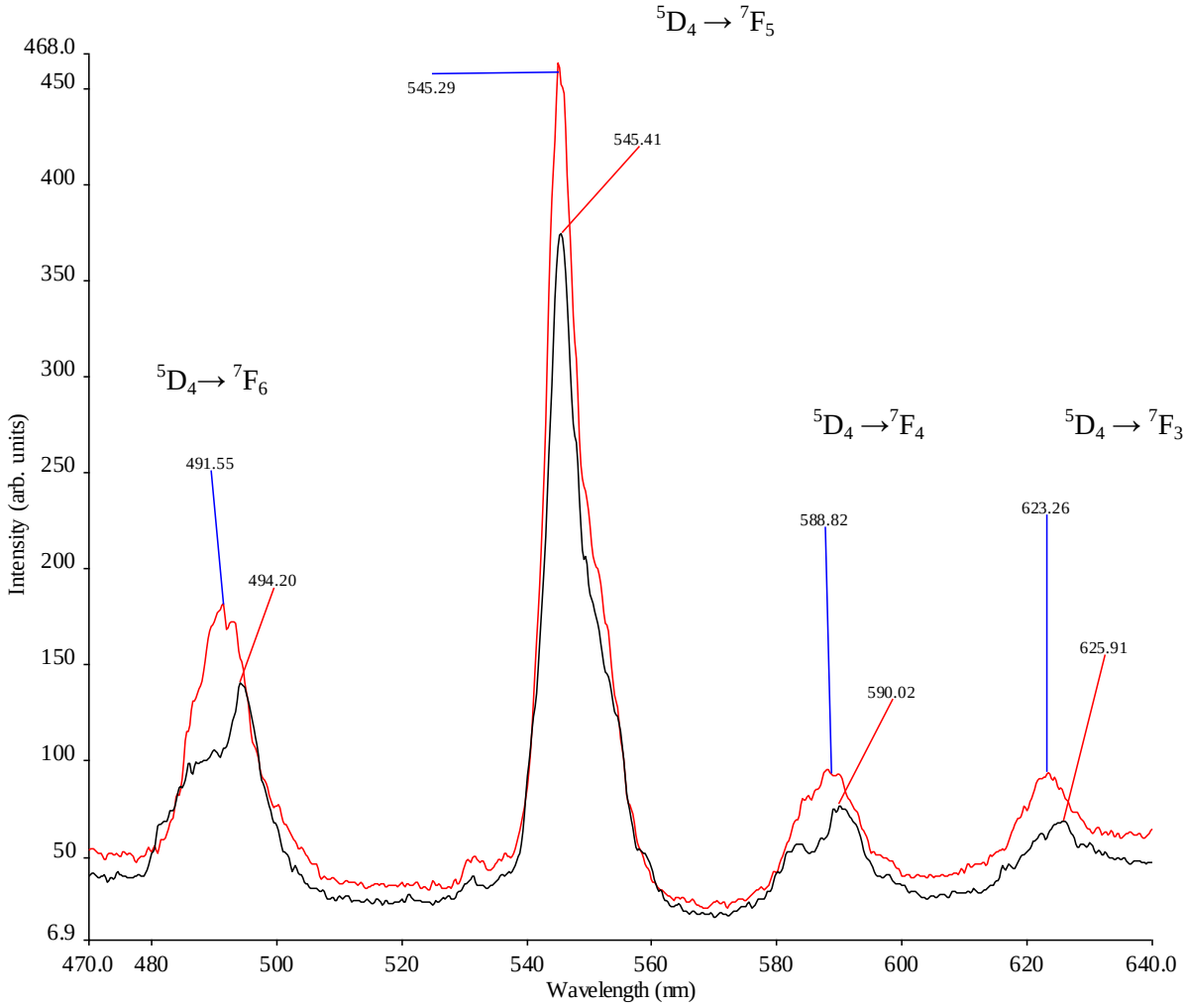

Figure 7.7: *Emission spectra for $TbPO_4.nH_2O$ excited at 255 nm (red lines depict hydrates sample, black lines are a dehydrated sample heated to 350 °C and placed in an airtight sample holder)*

Figure 7.7 represents the transition bands for the terbium phosphate fluorescence emissions. The spectrum for $TbPO_4.nH_2O$ does not show any peak splitting, and a broad and more intense pattern is observed. The $TbPO_4$ spectrum differs to a small extent as a result of the loss of water from the structure. The peaks are marginally shifted (494, 590 and 625 nm) compared to the original hydrated sample. The anhydrous sample exhibits splitting, two peaks are found when there was previously only one (494 nm). The terbium ion within $TbPO_4$ is surrounded solely by phosphate groups. The hydrated sample has terbium atoms in the same coordination environment as $TbPO_4$, and some that are also coordinated to the water molecules within the channels. This affects the coordination geometry and the crystal-field splitting within the sample. The mixed bonding at the terbium sites results in broad band's within the spectrum, and an increased intensity of the

observed pattern. The difference observed between the two samples reveals the interaction of the lanthanide ion and the water molecules within the channels.

These hydrated phosphate materials have great potential for use as sensors. If a sensor was produced that was active at 490 nm, it would be possible to observe a splitting of the peak when it was dehydrated, and a broad peak when it was hydrated. Further analysis on the intensity of these peaks could also offer insight into the degree of hydration within the material at any stage of the process.

7.3 Conclusions

The neodymium and terbium hydrated orthophosphates have been synthesised under mild hydrothermal conditions. Unfortunately, although varying reaction parameters were investigated, it was not possible to produce single crystals suitable for SXD analyses.

Thermal analysis indicated that 0.6 water molecules were present per formula unit within the hydrated neodymium and terbium phosphate structure, which was contrary to previous conclusion of between 0.5-2.5 per unit cell. This could be a result of the hydrothermal preparation process encouraging this level of hydration. The removal of the water molecules caused an expansion of the lattice in the *a*-axis, and as a result an increase to the overall cell volume. The removal of water was reversible in air and thus concluded to be zeolitic rather than lattice water.

The interaction of the lanthanide cation with the water molecules has been highlighted through fluorescence spectroscopy. There are small but distinct differences within the wet and dry spectra that indicate a change to the bonding of the lanthanide. These materials could be engineered to become sensors that monitor dry and wet areas. The sensor would be very versatile, as the reversible process of dehydration is easy and cheap to regenerate.

Further analysis by joint Rietveld PXD and NPD would be beneficial as it could provide useful information regarding the precise placement of water molecules within these lanthanide structures. Time constraints meant that this analysis was not possible but it would be beneficial to complete if the work was continued.

7.4 References

(1) Pepin, J. G.; Vance, E. C. *Journal of Inorganic Nuclear Chemistry* **1981**, *43*, 2807-2809.

(2) Carron, M. K.; Mrose, M. E.; K.J.Murata *The American Mineralogist* **1958**, *43*, 985-989.

(3) Min, W.; Daimon, K.; Ota, T.; Matsubara, T.; Hikichi, Y. *Materials Research Bulletin* **2000**, *35*, 2199-2205.

(4) Hikichi, Y.; Sasaki, T.; Murayama, K.; Nomura, T.; Miyamoto, M. *Journal of the American Ceramic Society* **1989**, *72*, 1073-1076.

(5) Donaldson, J. D.; Hezel, A.; Ross, S. D. *Journal of Inorganic and Nuclear Chemistry* **1967**, *29*, 1239-1242.

(6) Mooney, R. C. L. *Journal of Chemical Physics* **1948**, *16*, 1003.

(7) Mooney, R. C. L. *Acta Crystallographica* **1950**, *3*, 337.

(8) Lessing, P. A.; Erickson, A. W. *Journal of the European Ceramic Society* **2003**, *23*, 3049-3057.

(9) Hernandez, T.; Martin, P. *Journal of the European Ceramic Society* **2007**, *27*, 109-114.

(10) Assaaoudi, H.; Ennaciri, A.; Rulmont, A.; Harcharras, M. *Phase Transitions* **2000**, *72*, 1-13.

(11) Harley, G.; Yu, R.; De Jonghe, L. C. *Solid State Ionics* **2007**, *178*, 769-773.

(12) Huo, Z. Y.; Chen, C.; Chu, D.; Li, H. H.; Li, Y. D. *Chemistry-a European Journal* **2007**, *13*, 7708-7714.

(13) Assaoudi, H.; Ennaciri, A. *Spectrochimica Acta Part A* **1997**, *53*, 895 - 902.

(14) Kijkowska, R. *Thermochimica Acta* **2003**, *404*, 81-88.

(15) Lucas, S.; Champion, E.; Bernache-Assollant, D.; Leroy, G. *Journal of Solid State Chemistry* **2004**, *177*, 1312-1320.

(16) Hezel, A.; Ross, S. D. *Journal of Inorganic Nuclear Chemistry* **1967**, *29*, 2085-2089.

(17) Lucas, S.; Champion, E.; Bregiroux, D.; Bernache-Assollant, D.; Audubert, F. *Journal of Solid State Chemistry* **2004**, *177*, 1302-1311.

(18) Kijkowska, R. *Journal of Materials Science* **2003**, *38*, 229-233.

(19) Yan, Z.-G.; Zhang, Y.-W.; You, L.-P.; Si, R.; Yan, C.-H. *Journal of Crystal Growth* **2004**, *262*, 408-414.

(20) Shannon, R. D. *Acta Crystallographica Section A* **1976**, *32*, 751-767.

(21) Larson, A. C.; Von Dreele, R. B., *General Structure Analysis System GSAS, Los Alamos National Laboratory Report LAUR 86-748*, **2000**

(22) Lakowicz, J. R. *Principles of Fluorescence Spectrometry Third Edition*; Springer, **2006**.

(23) Kaltsoyannis, N.; Scott, P. *The f elements*; Oxford University Press, **1999**.

CHAPTER EIGHT

CONCLUSIONS

8.0 Conclusions

The aim of this project was to synthesise novel open framework materials with potentially useful properties through solvothermal methods. The research presented within this thesis centred on using lanthanide and Group 4 or 5, XF_4 (X = Ce, Zr, Hf) reagents combined with phosphate or arsenate and in some cases an organic template species. A systematic study into these materials was undertaken with a view to forming and structurally characterising new framework structures.

The research produced five cerium, seven zirconium and four hafnium compounds that were previously unreported (or previously not synthesised in single crystal form). By removing the need for HF the reaction pathway that included XF_4 has provided a safer synthetic route, to the formation of new frameworks that contain fluoride.

The hydrothermal formation of the Rhabdophane mineral form of the lanthanide phosphate ($LnPO_4.nH_2O$) led to investigations of its structure. Neodymium and terbium based samples were also subjected to an in-depth analysis, and findings from variable temperature X-ray diffraction studies highlighted unusual changes to the lattice dimensions, specifically along the *a*-axis. The lanthanide ions were found to form weak interactions with water molecules when present within the channels of the framework, and as a result the lattice exhibited shrinkage when hydrated and expansion when dehydrated. These materials offer potential applications as sensors.

When a new framework type was obtained from a reaction, the synthesis was reproduced substituting the XF_4 species, altering temperatures, templating agents and solvents in order to attempt to produce further novel structures. In the majority of cases alterations to the reaction conditions resulted in the formation of previously reported powder phases that incorporated arsenate or phosphate groups (XTO_4). This research highlighted the specific nature of these reactions. The new crystal structures obtained from these specific solvothermal reaction conditions were commonly the minor product. In the cerium reactions, there tended to be a mixture of two types of crystals within the product. This finding was also documented by Yu *et al.* in the production of similar cerium materials (YU-1[1] and $NH_4CeF_2PO_4$[2]). This result created problems in analysing the single crystals through techniques; such as TGA, since the procedures could not be completed upon mixed phase samples. As a consequence research efforts were focussed upon distinguishing individual phases through further alterations to the reaction conditions. These efforts proved to be unsuccessful in all cases. In some circumstances separation of individual crystals from the sample

was undertaken in order to acquire chemical information through techniques such as microscope IR (**II** and **IV**). However, isolating a sample large enough to analyse was often not possible.

Investigation into the structures produced within this research, has enabled discussions regarding the variety of bonding motifs that the fluoride species can display. In the case of metal frameworks (*M* = Zr/Hf), we have observed two distinct types of bonding. The first example is the substitution of fluoride into the metal polyhedral unit as a terminal anion (as found for **XI,** $Hf^{IV}F_2(PO_4,HPO_4)_2(NH_4, H_2O)_3$). Examples of both one, and two, terminally bonded fluoride ions in a single polyhedral unit have been noted (**XIII** – HfO_5F; **XI** – HfO_4F_2).

The fluoride ions frequently bond to the terminal positions of the polyhedra that would typically house oxygen ions. The bond lengths between *M* and F were found to be shorter than their *M*-O counterparts. When fluoride ions occupy terminal positions, the compounds often contain cations within the channels (such as NH_4^+), forming donor-acceptor bonds *M*-F---H-NH_3. The presence of these hydrogen bonds provides additional stability within the structures, and the removal of these ions from the synthesis procedure will typically inhibit their formation. These reaction syntheses contained NH_4^+ added in the form of $NH_4H_2TO_4$ (*T* = P/As) or through the replacement of H_2O by NH_3 solution as the reaction solvent. If NH_4^+ cations were removed from previously successful syntheses *via* the addition of H_3TO_4 or T_2O_5 or the removal of amine templates, generally powdered products were formed. These reaction products were composed of starting materials or single crystals of alternative structures, hinting at dependence on these cations for formation.

The second type of bonding that fluoride exhibited was bridging between two metal centres (*M*-F-*M*) of the polyhedral units. This form of bonding was found in materials such as $Zr(AsO_4)F(H_2O)$ (corner sharing Zr-F-Zr). The presence of the fluoride ions linking polyhedra typically produced higher dimensionality frameworks. The $Zr(AsO_4)F(H_2O)$ structure contains H_2O molecules connected to the polyhedra as terminal species. Extra framework ammonium cations were generally not incorporated within this structure type, as fluoride ions act as linkers and are not available for the formation of hydrogen bonds to the NH_4^+ cations.

The hydrothermal chemistry of lanthanides is relatively under researched in comparison to that of transition metal phosphate and arsenates. Analysis of the cerium 4+ crystal systems produced in this study has also provided information on the types of bonding that fluoride can possess within lanthanide frameworks. Terminal and bridging fluoride anions were observed within the cerium based structures, similar to those found for zirconium and hafnium materials (terminal:

$[(NH_4)_5(H_2O)_2][Ce^{IV}{}_4(AsO_4)_6(H_2O)F_3]$ and bridging: $Ce[AsO_4]F$, $Ce[AsO_4]F(H_2O)$). When *M* = Ce, a mixture of the two types of bonding involving fluorine is observed within the same structure. Mixed terminal and bridging bonding of the fluoride ions was observed within the structure of $Cs[Ce_2^{IV}F_8[F.H_2O]$. This unusual connectivity has not been witnessed within any other metal or lanthanide structure synthesised in this research project. It is however, the only framework not to include the TO_4 oxotetrahedral species. The lanthanide cation's ability to form polyhedral units with larger coordination numbers, because of its larger ionic radius, and alternative bonding types than the other transition metal cations investigated in this work leads to very different structure types.

Contrary to previously reported metal framework examples, $[NH_4][Ce^{IV}F_2(AsO_4)]$ exhibited bridging bonds between the cerium polyhedra and incorporated NH_4^+ cations within the structure. This structure type is not found when *M* = Hf/Zr, indicating the larger coordination numbers of the lanthanide. The reaction that produced $[(NH_4)_5(H_2O)_2][Ce^{IV}{}_4(AsO_4)_6(H_2O)F_3]$, was an example of a framework that relied upon the incorporation of NH_4^+ within the solvothermal reaction in order for it to form. When the synthesis was attempted without NH_4^+ within the starting materials, to produce an identical structure with empty channels, powdered examples of known cerium phosphates were the product. This highlighted the underlying dependence on template species for the formation of these structures.

This research project has not revealed examples of fluoride ions that are directly linked to the tetrahedral *T* atom. Previous discussions have highlighted that fluoride forms terminal or bridging bonds to the metal and lanthanide polyhedral units. It is unusual to observe fluorine substituted for an oxygen ion in a TO_4 group but it is known, for example, in the case of $Ni(H_2O)_6(NH_4)_2(PO_3F)_2$[3] where strong hydrogen bonding is observed from the water molecules connected to the Ni and the fluorine from the fluorophosphate (PO_3F) groups. The central cation within the tetrahedral units (As^{5+}/P^{5+}) is more highly positively charged than the metal or lanthanide ions (M^{4+}/Ce^{4+}). As a result of these differences in charge, the oxotetrahedral species will tend to form with more negatively charged species surrounding the central cation. Therefore, anions with a -2 (O) rather than -1 (F) charge will be favoured. The presence of hydroxide groups on TO_4 units, *i.e.* $T(O_3OH)$, effectively lower the charge of the oxygen to that of a monovalent anion, and many compounds are known that contain this species *e.g.* $Zr(HAsO_4)_2$ (**VIII**) and $(NH_4)Zn_2(PO_4)(HPO_4)$[4]. These factors imply that the metal polyhedral unit is more likely to contain the fluorine anions as a result of this preferential bonding. An increased oxidation state in the metal centre may also reduce the inclination for the fluorine to bond to the metal (*e.g.* Mo^{6+}) due to its weak charge balancing

effect. When these materials are octahedrally coordinated, the metal centre requires greater negative charge to be associated with the positive metal, compared to the phosphate or arsenate groups, thus oxygen may preferentially bond at this site, and fluorine will attach to the oxotetrahedral species. Hence effectively the 4+ oxidation state and 6/7 coordinate polyhedral species seem to be the optimum conditions for MO_nF_y polyhedra.

The polyhedra species found in the compounds characterised within this research have varied as a result of the addition of XF_4 reagents to the reaction mixture. This method incorporated large quantities of fluoride ions into the synthesis, which often led to the species being incorporated in the polyhedral units. The cerium units exhibit the following coordination spheres; CeF_8(F, H_2O), CeO_7F, $CeO_7(OH_2)$, CeO_6F_2, $CeO_5F_2(OH_2)$, CeO_4F_4; whereas the transition metal species have formed fewer examples; ZrO_6, $ZrO_4F_2(OH)_2$, ZrO_4F_2, HfO_6, HfO_5F and HfO_4F_2. The transition metal compounds all form from octahedral building units, whereas the lanthanide materials exhibit both eight and nine-coordinate polyhedral units. The introduction of fluoride into the polyhedral species also formally reduces the local symmetry of the metal as a result of the mixed nature of the anions present. Controlled addition of the fluorinated starting materials could provide a rational pathway to design one, two and three-dimensional framework structures through variation of the XF_4 ratios. The family of materials A_2MPO_4F (A = Li/Na and M = Fe, Mn, Co, Ni) have been the subject of recent research interest as possible new battery materials[5]. These compounds exhibit di-octahedral species ($Fe_2O_7F_2$) comprised of face-sharing octahedra (FeO_4F_2). The fluoride anions are found in bridging positions between the iron centres, as documented in relation to some of the structures described in this thesis. The materials produced within this research project have been shown to exhibit similar bonding to the battery materials. Reactions that employ XF_n could provide synthetic routes to this important class of compounds.

The incorporation of organic template ions within the pores of the frameworks of the reaction products was relatively uncommon. The addition of certain reagents ($NH_4H_2TO_4/NH_3$ solution) to the solution resulted in structures that house NH_4^+ within their channels and layers. It was noted by Ferey *et al.* that the NH_4^+ cations exhibit a templating effect that has a stronger affinity to other organic species when added to the reaction mixture[6]. Therefore, substitution of these cations by alternative organic compounds is unlikely to be successful unless the ammonium based phosphate and arsenate reagents are also replaced. However, within this study, it was commonly noted that substitution of these phosphate and arsenate materials within a reaction synthesis did not lead to the formation of alternative compounds (producing simple metal and lanthanide phosphate or arsenate structures). This indicates that these structures are dependent upon

the presence of these cations to form. The ULM frameworks synthesised by Ferey *et al.* also exhibited terminal fluoride anions with strong hydrogen-bonding to the NH_4^+ cations within the structure[7]. These characteristics indicate that for frameworks to form, with channels housing larger template ions, the addition of alternative reagents (H_3TO_4 and T_2O_5) to the reaction is necessary.

This research has revealed that phosphate frameworks do not form as commonly as the arsenate materials when XF_4 was incorporated into the reaction synthesis. The structures documented within this thesis include only one example of a new phosphate compound, the chain-like structure of $HfF_2(PO_4, HPO_4)_2(NH_4, H_2O)_3$ (**XI**). This material forms part of the novel family $MF_2(PO_4, HPO_4)_2(NH_4, H_2O)_3$ first isolated by Redrup[8] (Table 5.1). Arsenate analogues of these compounds have not formed for any transition metal or lanthanide cation. Despite the efforts that were made to produce arsenate and phosphate analogues of all the structures described within this thesis, only one example was found for the cerium arsenate material (**V**), which is analogous to the phosphate described previously by Yu *et al*[9].

Solvothermal reactions offer a route to formation of crystal structures that increase the reagent solubility and reactivity. This has been highlighted within the cerium arsenate materials, where a larger number of novel structures formed over a wider reaction range than their phosphate counterparts. It is possible that the pK_a within the solutions had an effect on this reduction in formation. The pK_a of the triprotic arsenic acid[10] is slightly different to that of the phosphate (pK_a of H_3PO_4: 2.15, 7.2, 12.35; pK_a of H_3AsO_4: 2.2, 7, 11.5). The values observed are lower at each stage for the point at which the protons are lost (except in acidic conditions), implying that arsenic acid is a weaker acid than its phosphate counterpart. It is possible that the pH of the successful reactions was more favourable for the arsenate starting materials than the phosphate, which resulted in much greater success in crystal formation (especially in alkaline media, where the biggest difference between phosphoric and arsenic acid was noted). This is likely to be one of the main reasons that the arsenate materials formed most readily within these solvothermal conditions.

In general within acidic hydrothermal media, fluoride is not incorporated into the structures that form. If the reaction includes HCl then the fluoride ions are not as strongly solvated by water and therefore prefer to remain within solution. When the HCl is removed and the solution is maintained as acidic through the incorporation of reagents such as H_3TO_4, the solid products again do not incorporate fluoride anions. The acidic conditions promote the formation of protonated oxygen species. The exception to this observation has been the $Zr(AsO_4)F(H_2O)$ structure that forms Zr-F-Zr corner-sharing bonds within acidic conditions. The presence of $Ba(OH)_2.xH_2O$ and

in other cases organic templates (TMAC, TMAOH, OAD *etc*.) aids the formation of this fluorinated structure in acidic media. The barium and organic templating reagents increased the reaction pH to a more appropriate level for crystal formation or possibly acted in a structure directing fashion that enabled the incorporation of fluoride within the zirconium structure. The result of their incorporation provides the unusual situation whereby a structure formed in an 'acidic' medium also includes fluorine anions bonded to the metal centre. Acidic conditions should therefore not be discarded as unsuitable for further investigations, as the inclusion of these types of reagents could lead to many novel structures.

The research in this thesis could be developed by undertaking further experimental work to reproduce the reactions described, using a wider variety of starting materials than used thus far (Ti, Zr, Hf, Nb, Ta, Sn and Pb fluorides). Successful reactions, in terms of producing fluoride containing frameworks, have been undertaken with Zr, Hf, Ti and Nb thus far. Crystals were formed within the titanium syntheses but their size inhibited conclusive analysis. A range of alternative reaction conditions were undertaken with this starting material (although unsuccessful), but further research into this area could produce new fluorinated titanium arsenate and phosphate materials.

It would be valuable to extend research efforts into the practical applications of this family of frameworks. Recent studies into potential battery materials have shown that the inclusion of fluorine in the framework is beneficial, for example in A_2FePO_4F (A = Li/Na)[11]. Therefore, there would be scientific merit in testing the potential (for industrial applications) of these materials in ion exchange, small molecule storage and as actinide hosts. Similarly, repeating a range of reactions that previously involved the use of HF and replacing this with metal or lanthanide fluoride sources could provide a profitable area to study, in order to investigate the versatility of these reagents, and whether identical or alternative products are formed.

8.1 References

(1) Yu, R. B.; Wang, D.; Kumada, N.; Kinomura, N. *Chemistry of Materials* **2000**, *12*, 3527-+.

(2) Yu, R. B.; Wang, D.; Takei, T.; Koizumi, H.; Kumada, N.; Kinomura, N. *Journal of Solid State Chemistry* **2001**, *157*, 180-185.

(3) Berraho, M.; R'Kha, C.; Vegas, A.; Rafiq, M. *Acta Crystallographica Section C* **1992**, *C48*, 1350-1352.

(4) Bircsak, Z.; Harrison, W. T. A. *Acta Crystallographica Section C* **1998**, *C54*, 1383-1385.

(5) Ramzan, M.; Lebegue, S.; Larsson, P.; Ahuja, R. *Journal of Applied Physics* **2009**, *106*.

(6) Ferey, G. *Journal of Fluorine Chemistry* **1995**, *72*, 187-193.

(7) Loiseau, T.; Ferey, G. *Journal of Fluorine Chemistry* **2007**, *128*, 413-422.

(8) Redrup, K. V., *Synthesis and Characterisation of new Framework Materials*, PhD, University of Southampton, **2009**.

(9) Yu, R. B.; Wang, D.; Takei, T.; Kumada, N.; Koizumi, H.; Kinomura, N. *Journal of Solid State Chemistry* **2001**, *157*, 180-185.

(10) Black, B.; Perry, S.; Chinn, T. D.; Chowdhury, Z. K.; Awwa; U.S.E.P.A *Implementation of Arsenic Treatment Systems Part 2: Design Considerations, Operation, and Maintainance* **2002**.

(11) Ellis, B. L.; Makahnouk, W. R. M.; Makimura, Y.; Toghill, K.; Nazar, L. F. *Nat Mater* **2007**, *6*, 749-753.

APPENDICES

Appendices

Chapter 3:

***A.3.1**: Atomic coordinates and U(eq) for [$CsCe_2^{IV}F_8[H_2O,F]$]*

Atom	x	y	z	U(eq)
Ce(1)	0.2137(1)	1.0967(1)	0.2945(1)	0.006(1)
Cs(1)	0.5000	1.1048(1)	0.2500	0.012(1)
F(1)	0.3397(3)	0.8954(6)	0.3631(6)	0.008(1)
F(2)	0.3306(3)	1.2809(6)	0.2760(6)	0.009(1)
F(3)	0.3343(3)	1.1807(6)	0.5688(5)	0.010(1)
F(4)	0.1851(3)	1.0489(7)	0.0131(5)	0.011(1)
F(5)	0.0465(5)	1.0894(8)	0.1517(8)	0.017(1)
O(1)	0.0465(5)	1.0894(8)	0.1517(8)	0.017(1)

***A.3.2**: Atomic weight percentages for [$CsCe_2^{IV}F_8[H_2O,F]$] from EDX analysis*

Element	Atomic %	Calculated ratio of elements	Expected ratio of elements
O	5.78	1	1
F	70.63	12.2	8
Cs	7.65	1.3	1
Ce	15.93	2.8	2
Totals	100	17.3	12

***A.3.3**: IR spectrum for [$CsCe_2^{IV}F_8[H_2O,F]$]*

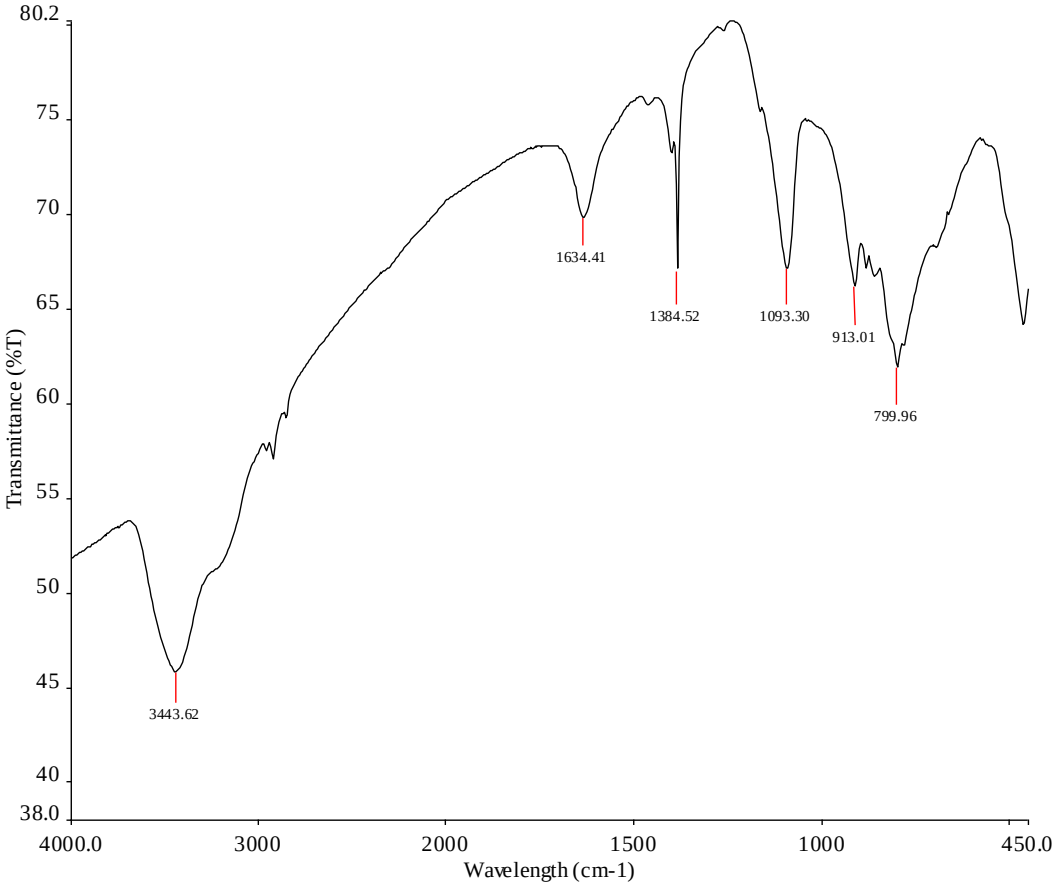

A.3.4: *Atomic coordinates and U(eq) for* $[(NH_4)_5(H_2O)_2][Ce^{IV}_4(AsO_4)_6(H_2O)F_3]$

Atom	x	y	z	U(eq)
Ce(1)	0.2631(1)	0.8295(1)	0.2754(1)	0.006(1)
Ce(2)	-0.0365(1)	0.2859(1)	0.0330(1)	0.005(1)
Ce(3)	0.0437(1)	1.2261(1)	0.4740(1)	0.006(1)
Ce(4)	-0.2454(1)	0.6953(1)	0.2225(1)	0.005(1)
As(1)	0.6760(1)	0.8758(1)	0.3811(1)	0.006(1)
As(2)	0.0409(1)	0.9736(1)	0.1298(1)	0.006(1)
As(3)	-0.1071(1)	0.5186(1)	0.1304(1)	0.006(1)
As(4)	0.1290(1)	1.0062(1)	0.3734(1)	0.006(1)
As(5)	-0.0097(1)	0.5462(1)	0.3678(1)	0.006(1)
As(6)	0.3403(1)	0.6464(1)	0.1126(1)	0.005(1)
F(1)	-0.4696(5)	0.5136(6)	0.2367(2)	0.024(1)
F(2)	0.4925(5)	1.0165(5)	0.2596(2)	0.017(1)
F(3)	0.2421(5)	1.4588(5)	0.4827(2)	0.022(1)
O(11)	0.4743(5)	0.8174(5)	0.3660(2)	0.009(1)
O(12)	0.7765(5)	1.0682(5)	0.4129(2)	0.009(1)
O(13)	0.7183(6)	0.8455(6)	0.2998(2)	0.013(1)
O(14)	0.7255(6)	0.7645(5)	0.4434(2)	0.011(1)
O(21)	-0.1352(5)	0.8991(5)	0.1546(2)	0.010(1)
O(22)	0.0696(5)	1.1544(5)	0.1107(2)	0.008(1)
O(23)	0.2064(5)	0.9925(5)	0.1968(2)	0.009(1)
O(24)	0.0167(6)	0.8628(5)	0.0508(3)	0.014(1)
O(31)	-0.0030(5)	0.6762(5)	0.1956(2)	0.008(1)
O(32)	-0.2954(5)	0.5059(5)	0.1196(2)	0.011(1)
O(33)	-0.0883(6)	0.3537(5)	0.1483(2)	0.010(1)
O(34)	-0.0410(6)	0.5409(5)	0.0524(2)	0.010(1)
O(41)	0.0257(5)	0.8625(5)	0.3008(2)	0.010(1)
O(42)	0.3162(5)	1.0125(5)	0.3848(3)	0.011(1)
O(43)	0.1230(6)	1.1793(5)	0.3622(2)	0.010(1)
O(44)	0.0503(6)	0.9703(5)	0.4474(2)	0.009(1)
O(51)	-0.1743(6)	0.5444(6)	0.3042(3)	0.013(1)
O(52)	0.0316(6)	0.6623(5)	0.4477(2)	0.011(1)
O(53)	-0.0596(6)	0.3599(5)	0.3834(2)	0.010(1)
O(54)	0.1559(5)	0.6172(5)	0.3348(2)	0.011(1)
O(61)	0.3019(6)	0.6905(5)	0.1924(2)	0.010(1)
O(62)	0.2810(5)	0.7447(5)	0.0448(2)	0.009(1)
O(63)	0.5407(5)	0.7026(5)	0.1253(2)	0.007(1)
O(64)	0.2330(5)	0.4514(5)	0.0861(2)	0.008(1)
O(1)	-0.2730(5)	0.0519(5)	0.0576(2)	0.011(1)
OW1	0.4637(6)	0.0581(5)	0.1049(3)	0.015(1)
OW2	0.4077(7)	0.2982(7)	0.0292(3)	0.030(1)
N(1)	-0.1954(7)	1.1504(7)	0.2486(3)	0.014(1)
N(2)	0.6079(7)	0.2154(7)	0.4943(3)	0.018(1)

N(3)	0.2292(8)	0.3768(9)	0.2545(4)	0.030(2)
N(4)	0.4600(8)	0.4621(9)	0.4071(3)	0.037(2)
N(5)	0.5624(9)	0.2970(8)	0.3310(4)	0.034(2)

A.3.5*: Atomic weight percentages for* $[(NH_4)_5(H_2O)_2][Ce^{IV}{}_4(AsO_4)_6(H_2O)F_3]$ *from EDX analysis*

Element	Atomic %	Calculated ratio of elements	Expected ratio of elements
O	41.55	7.41	27
F	16.78	3	3
As	20.23	3.63	6
Ce	21.44	3.81	4
Totals	100	17.85	40

A.3.6: *IR spectrum for* $[(NH_4)_5(H_2O)_2][Ce^{IV}{}_4(AsO_4)_6(H_2O)F_3]$

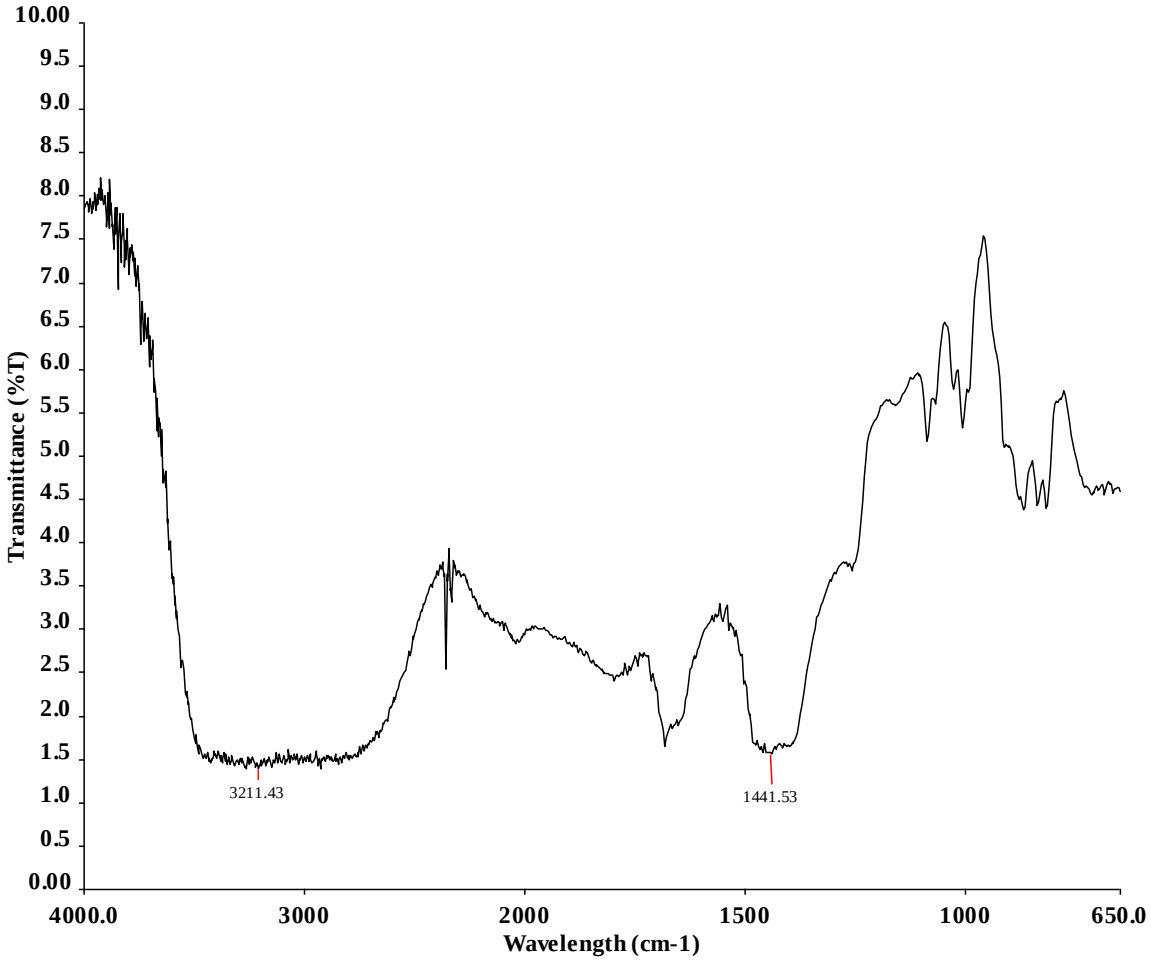

***A.3.7**: Atomic coordinates and U(eq) for $[Ce^{IV}[AsO_4]F]$*

Atom	x	y	z	U(eq)
Ce(1)	0.4572(1)	0.7500	0.1448(1)	0.007(1)
As(1)	0.1039(2)	0.7500	-0.1757(2)	0.008(1)
F(1)	0.7122(8)	0.7500	0.1997(11)	0.011(2)
O(1)	0.0708(7)	0.5678(9)	-0.3384(9)	0.010(1)
O(2)	-0.0199(10)	0.7500	0.0172(14)	0.010(1)
O(3)	0.2873(10)	0.7500	-0.1025(13)	0.010(1)

***A.3.8**: Atomic weight percentages for $[Ce^{IV}[AsO_4]F]$ from EDX spectrum*

Element	Atomic %	Calculated ratio of elements	Expected ratio of elements
O	47.53	4.30	4
F	11.05	1	1
As	18.87	1.71	1
Ce	22.55	2.04	1
Totals	100	9.05	7

***A.3.9**: Atomic coordinates and U(eq) for $[Ce^{IV}[AsO_4]F[H_2O]]$*

Atom	x	y	z	U(eq)
Ce(1)	0.2165(3)	0.7057(2)	0.1889(1)	0.008(1)
As(1)	0.7900(5)	0.8621(3)	0.3868(2)	0.009(1)
F(1)	0.1330(20)	0.5038(17)	0.3230(11)	0.009(1)
O(1)	-0.1230(30)	0.8880(20)	0.0779(13)	0.009(1)
O(2)	0.6120(30)	0.7100(20)	0.3067(13)	0.009(1)
O(3)	0.6170(30)	1.0490(20)	0.3940(13)	0.009(1)
O(4)	0.8770(30)	0.7820(20)	0.5211(13)	0.009(1)
O(5)	1.0690(30)	0.9010(20)	0.3272(13)	0.009(1)

***A.3.10:** Atomic weight percentages for $[Ce^{IV}[AsO_4]F[H_2O]]$ from EDX analysis*

Element	Atomic %	Calculated ratio of elements	Expected ratio of elements
O	45.65	3.19	5
F	20.83	1.46	1
As	14.28	1	1
Ce	19.24	1.35	1
Totals	100	7	8

***A.3.11**: Atomic coordinates and U(eq) for $[NH_4][Ce^{IV}F_2(AsO_4)]$*

Atom	x	y	z	U(eq)
Ce(1)	0.3820(1)	0.25	0.3032(1)	0.002(1)
As(1)	-0.2281(1)	0.25	0.0413(1)	0.002(1)
F(1)	0.6606(4)	-0.0039(4)	0.4574(3)	0.007(1)
O(1)	-0.0010(7)	0.25	0.2596(6)	0.006(1)
O(2)	0.2280(5)	-0.0259(4)	0.1019(4)	0.008(1)
O(3)	0.5507(7)	0.25	0.0903(6)	0.007(1)
N(1)	1.0544(8)	0.25	0.6799(7)	0.007(1)

***A.3.12:** Atomic weight percentages for $[NH_4][Ce^{IV}F_2(AsO_4)]$ from EDX analysis*

Element	Atomic %	Calculated ratio of elements	Expected ratio of elements
O	29.82	1.78	4
F	16.72	1	2
As	19.64	1.17	1
Ce	33.82	2.02	1
Totals	100	5.97	8

***A.3.13**: IR spectrum of $[NH_4][Ce^{IV}F_2(AsO_4)]$*

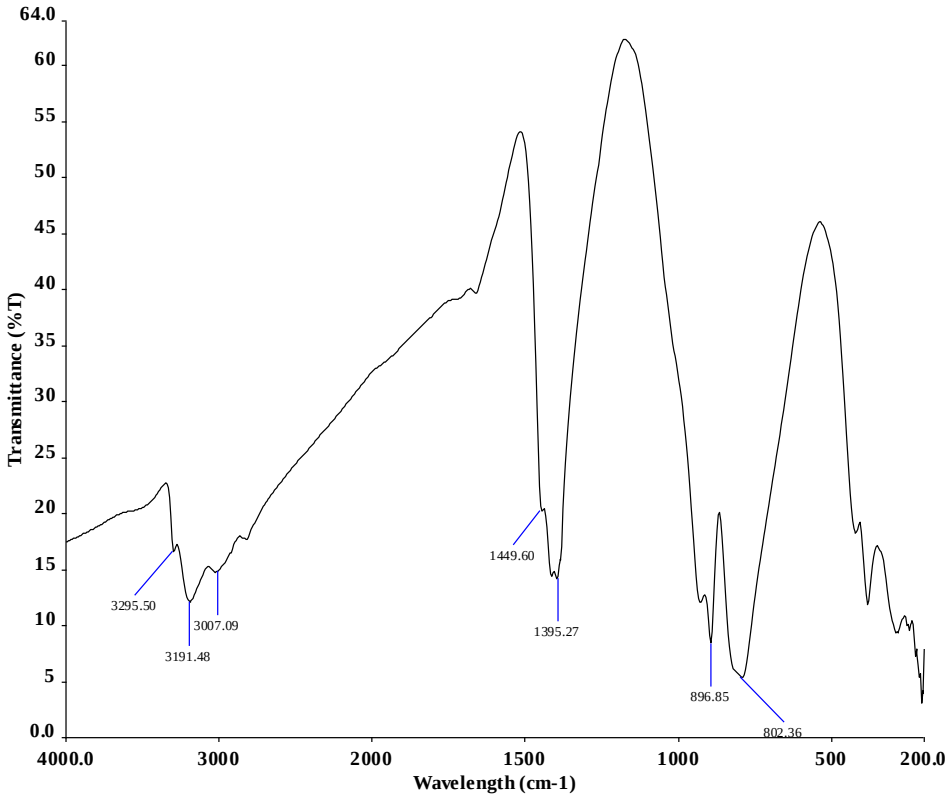

Chapter 4:

***A.4.1**: Atomic Coordinates and U(eq) for $Zr(HAsO_4)(AsO_4)(NH_4)$*

Atom	x	y	z	U(eq)
Zr(1)	0.8747(1)	0.3748(1)	1.0096(1)	0.005(1)
As(1)	0.9115(1)	0.1713(1)	0.9953(1)	0.006(1)
As(2)	0.6226(1)	0.4217(1)	1.0742(1)	0.007(1)
O(1)	0.7221(3)	0.3762(3)	0.9926(7)	0.011(1)
O(2)	0.8684(3)	0.3735(3)	0.7021(7)	0.007(1)
O(3)	0.6208(3)	0.4242(3)	1.3194(7)	0.012(1)
O(4)	0.8681(3)	0.2590(3)	1.0023(7)	0.012(1)
O(5)	0.6258(3)	0.5096(3)	0.9873(7)	0.010(1)
O(6)	0.5338(3)	0.3252(3)	1.4910(8)	0.012(1)
O(7)	0.8709(3)	0.3763(3)	1.3100(7)	0.010(1)
O(8)	0.5249(3)	0.3743(3)	0.9907(7)	0.007(1)
N(1)	0.6558(7)	0.2500	0.7500	0.014(2)
N(2)	0.7500	0.5000	0.5672(13)	0.012(2)

***A.4.2:** Atomic weight percentages for $Zr(HAsO_4)(AsO_4)(NH_4)$*

Element	Atomic %	Calculated ratio of elements	Expected ratio of elements
O	62.97	4.54	8
As	23.15	1.67	2
Zr	13.88	1	1
Totals	100	5.97	11

A.4.3: *IR spectrum for $Zr(HAsO_4)(AsO_4)(NH_4)$*

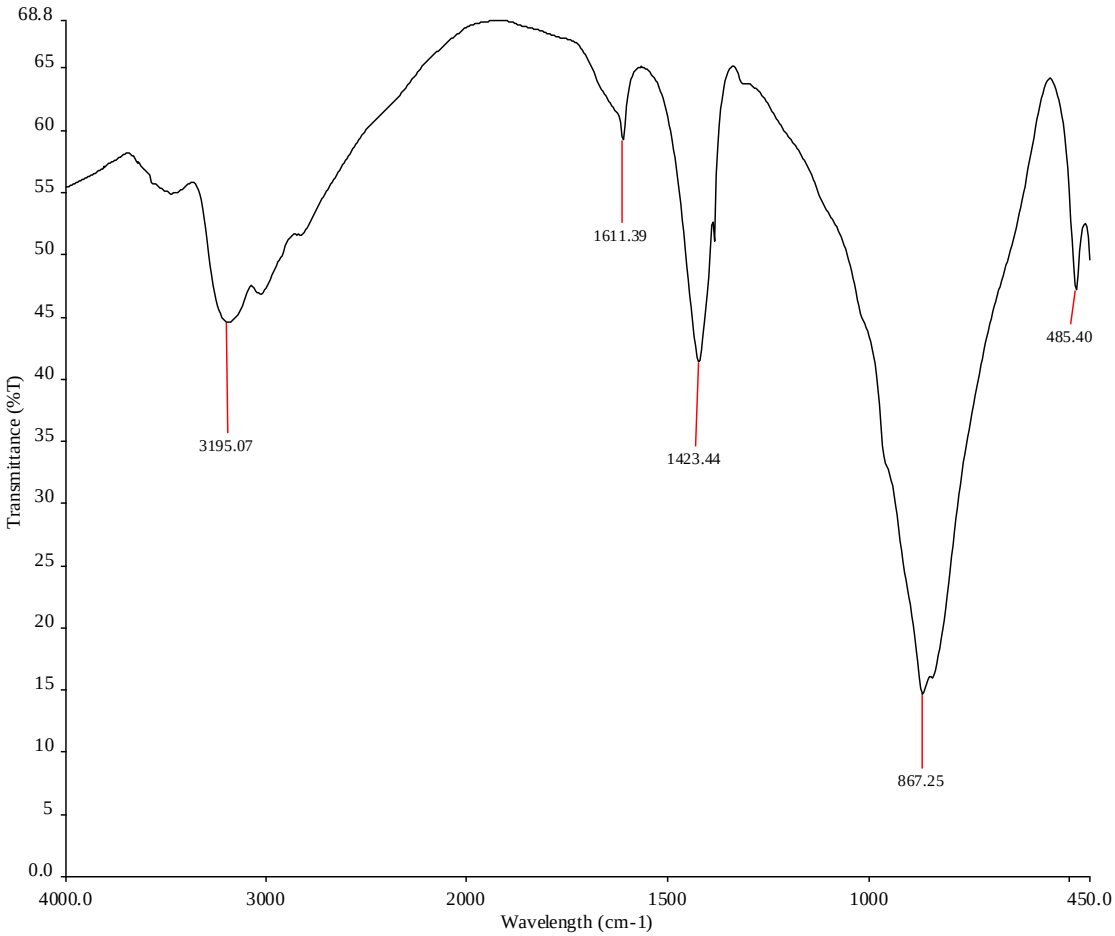

A.4.4*: Atomic Coordinates and U(eq) for $Zr(AsO_4)F(H_2O)$*

Atom	x	y	z	U(eq)
Zr(1)	0.0711(1)	0	0.2675(1)	0.005(1)
As(1)	0.1822(1)	0.5	0.3281(1)	0.006(1)
O(1)	0.0712(7)	0.3033(10)	0.2655(8)	0.013(1)
O(2)	0.2712(11)	0	0.4607(11)	0.017(2)
O(3)	-0.1750(10)	0	0.2156(11)	0.014(2)
O(4)	0.2698(11)	0	0.1341(12)	0.019(2)
F(1)	0	0	0	0.017(2)
F(2)	0	0	0.5	0.035(4)

A.4.5: *Atomic weight percentages for $Zr(AsO_4)F(H_2O)$*

Element	Atomic %	Calculated ratio of elements	Expected ratio of elements
O	54.97	4.04	5
F	16.79	1.24	1
As	13.59	1	1
Zr	14.66	1.08	1
Totals	100	7.36	8

A.4.6: *IR spectrum for $Zr(AsO_4)F(H_2O)$*

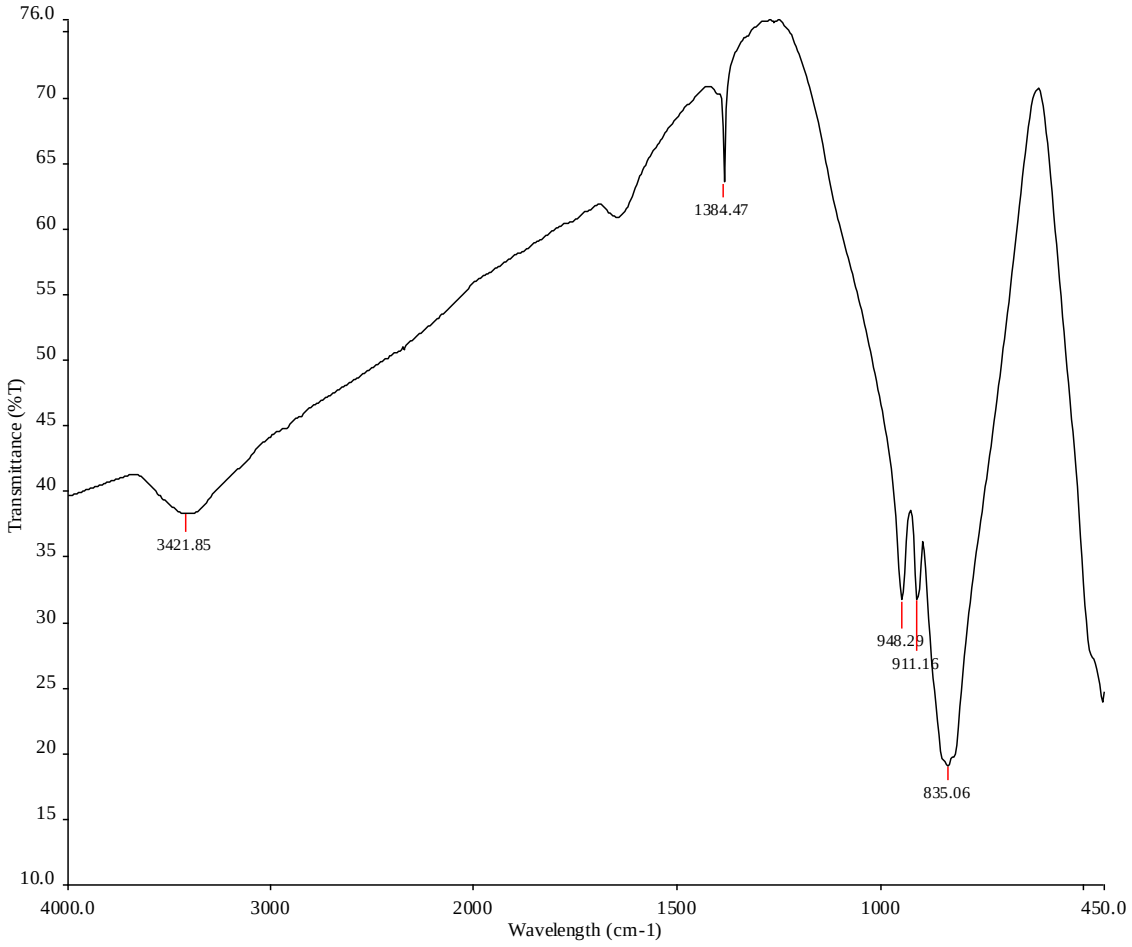

***A.4.7**: Atomic Coordinates and U(eq) for $Zr(HAsO_4)_2$*

Atom	x	y	z	U(eq)
Zr(1)	0.5	0.5	0.5	0.011(1)
As(1)	0.0942(1)	0.3423(1)	0.7607(1)	0.012(1)
O(1)	0.2608(12)	0.3526(7)	0.6019(8)	0.026(1)
O(2)	-0.1931(12)	0.4218(13)	0.6980(10)	0.062(3)
O(3)	0.2616(19)	0.4335(12)	0.9470(9)	0.066(3)
O(4)	0.0730(20)	0.1638(8)	0.8275(12)	0.055(2)

***A.4.8:** Atomic weight percentages for $Zr(HAsO_4)_2$*

Element	Atomic %	Calculated ratio of elements	Expected ratio of elements
O	60.8	4.11	8
As	24.42	1.65	2
Zr	14.79	1	1
Totals	100	6.76	11

***A.4.9**: IR spectrum for $Zr(HAsO_4)_2$*

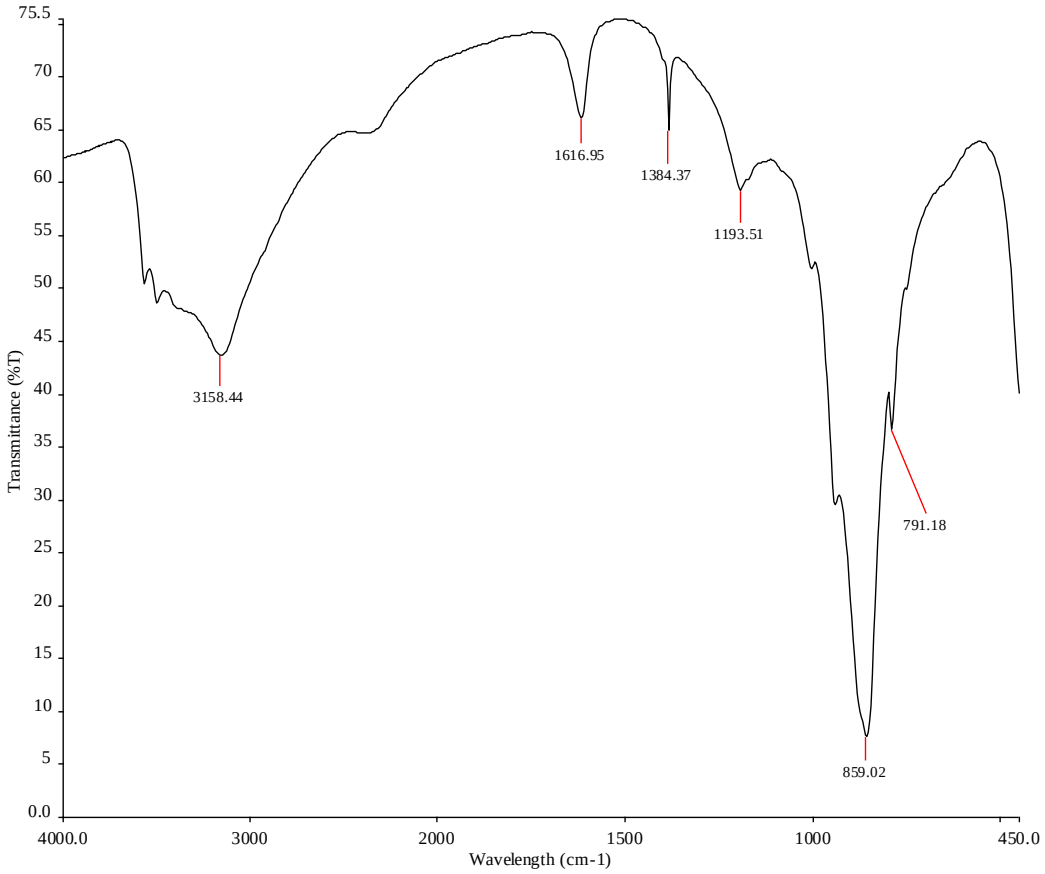

***A.4.10**: Atomic Coordinates and U(eq) for $Zr_2(AsO_4)_3(NH_4)(H_2O)$*

Atom	x	y	z	U(eq)
Zr(1)	0.1379(1)	0.6379(1)	0.8621(1)	0.007(1)
Zr(2)	0.4139(1)	0.9139(1)	0.5861(1)	0.007(1)
As(1)	0.1274(1)	0.9540(1)	0.7713(1)	0.007(1)
O(1)	0.0811(5)	0.8023(4)	0.7631(5)	0.019(1)
O(2)	0.2633(5)	0.9775(5)	0.6946(5)	0.019(1)
O(3)	0.1470(5)	0.9977(4)	0.9218(4)	0.016(1)
O(4)	-0.0175(4)	0.5446(5)	0.7981(5)	0.015(1)
OW(1)	-0.2164(10)	0.7836(10)	0.7836(10)	0.065(4)
N(1)	0.4221(16)	1.0779(16)	0.9221(16)	0.100(8)

***A.4.11:** Atomic weight percentages for $Zr_2(AsO_4)_3(NH_4)(H_2O)$*

Element	Atomic %	Calculated ratio of elements	Expected ratio of elements
O	67.8	4.96	13
As	18.53	1.35	3
Zr	13.67	1	2
Totals	100	7.31	18

A.4.12: *IR spectrum for $Zr_2(AsO_4)_3(NH_4)(H_2O)$*

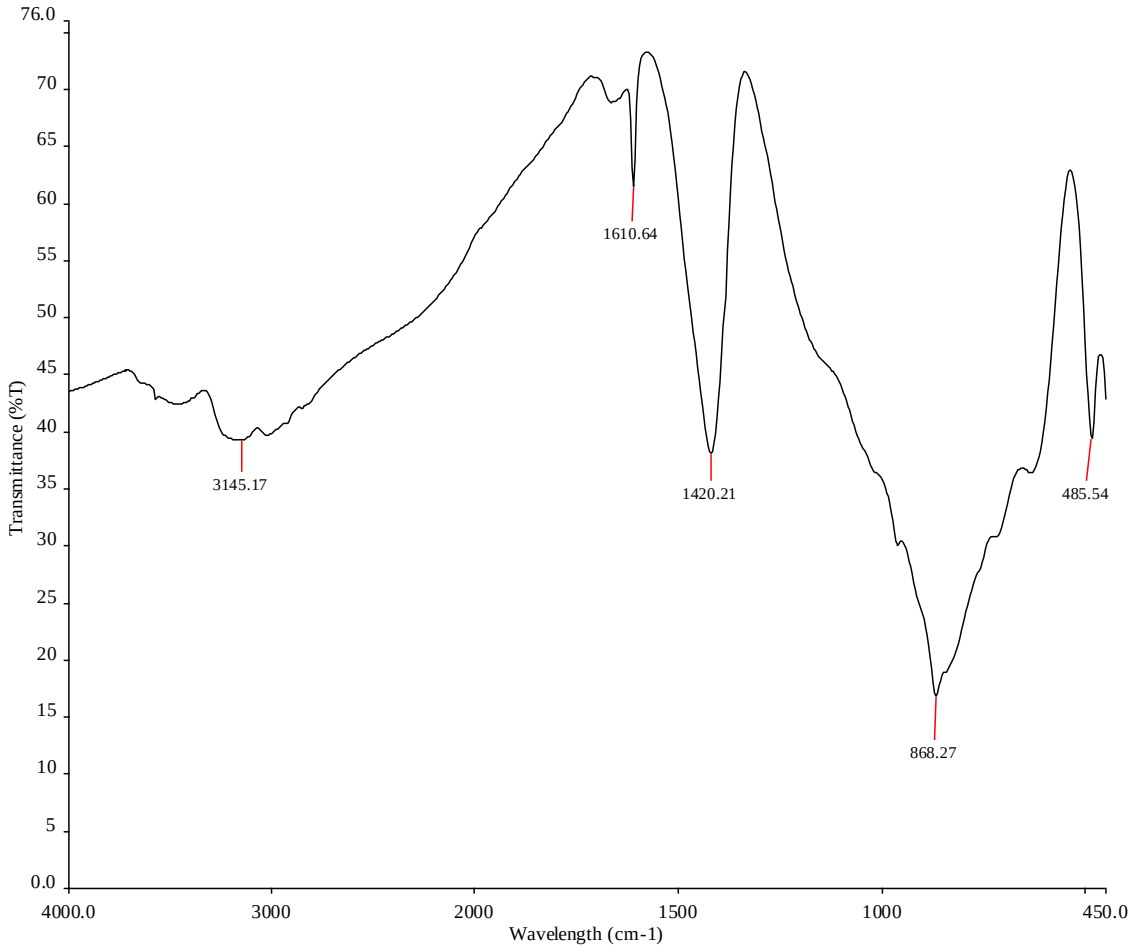

A.4.13*: Atomic Coordinates and U(eq) for $(NH_4)Zr_2(AsO_4)_3$*

Atom	x	y	z	U(eq)
Zr(1)	0.3333	0.6667	0.0181(1)	0.007(1)
As(1)	0.6667	0.6158(1)	0.0833	0.008(1)
O(1)	0.4978(8)	0.6370(9)	0.0695(2)	0.016(2)
O(2)	0.7176(9)	0.5386(8)	0.0297(2)	0.016(2)
N(1)	0.3333	0.6667	0.1667	0.019(4)

A.4.14: *Atomic weight percentages for $(NH_4)Zr_2(AsO_4)_3$*

Element	Atomic %	Calculated ratio of elements	Expected ratio of elements
O	63.36	4.96	12
As	19.86	1.18	3
Zr	16.78	3.78	2
Totals	100	9.92	17

A.4.15: *IR spectra for $(NH_4)Zr_2(AsO_4)_3$*

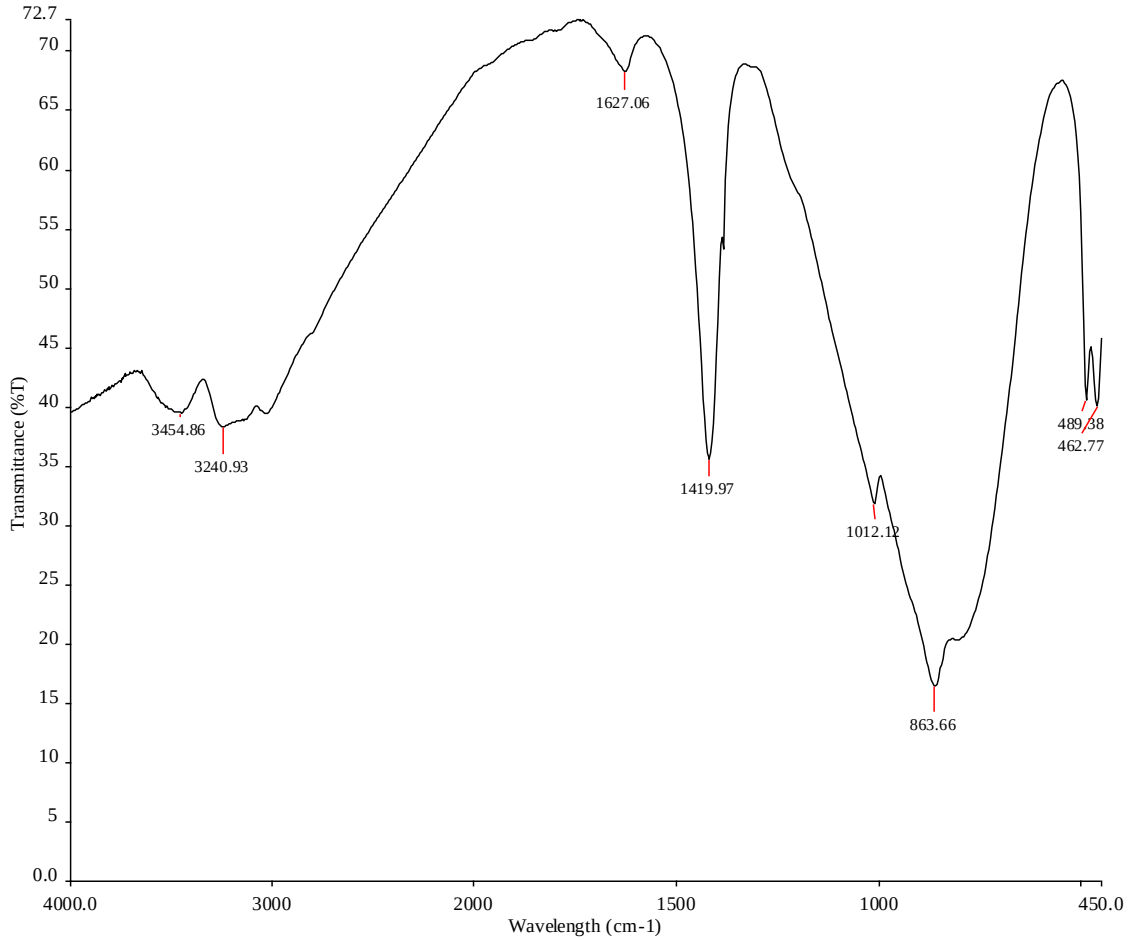

***A.4.16**: Atomic Coordinates and U(eq) for $CsZr_2(AsO_4)_3$*

Atom	x	y	z	U(eq)
Cs(3)	0.3333	-0.3333	0.0155(1)	0.008(1)
Zr(1)	0	0	0	0.022(1)
As(1)	-0.0558(2)	0.3333	0.0833	0.008(1)
O(1)	-0.1934(9)	0.2612(9)	0.0328(2)	0.011(2)
O(2)	0.1346(9)	0.4999(9)	0.0633(3)	0.012(2)

***A.4.17:** Atomic weight percentages for $CsZr_2(AsO_4)_3$*

Element	Atomic %	Calculated ratio of elements	Expected ratio of elements
O	32.52	1.53	12
As	22.82	1.07	3
Zr	21.26	1	2
Cs	23.41	1.1	1
Totals	100	4.7	18

***A.4.18:** IR spectra for $CsZr_2(AsO_4)_3$*

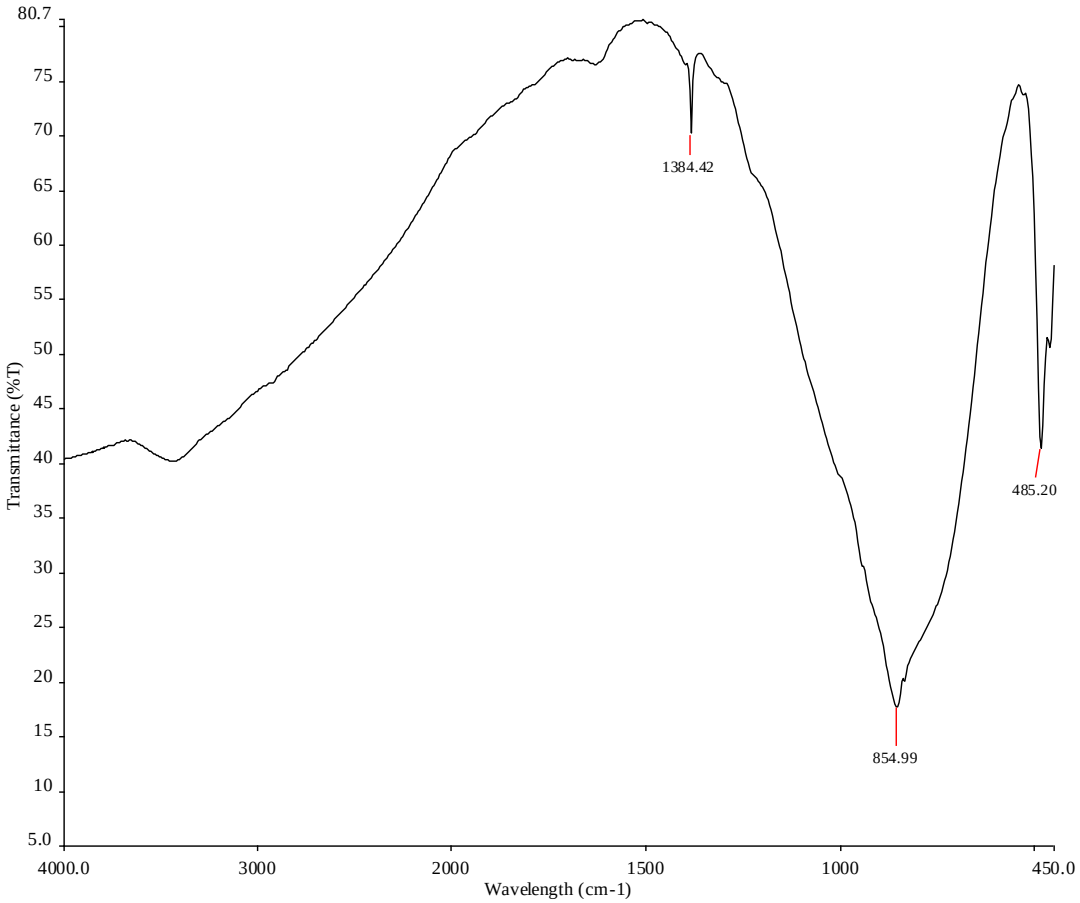

Chapter 5:

A.5.1: *Atomic Coordinates and U(eq) for $Hf^{IV}F_2(PO_4,HPO_4, H_2PO_4)_2(NH_4, H_2O)_3$*

Atom	x	y	z	U(eq)
Hf(1)	0.2614(1)	0.7079(1)	0.7732(1)	0.008(1)
P(3)	0.7608(4)	0.6075(3)	0.6237(2)	0.008(1)
P(4)	-0.2435(4)	0.9066(3)	0.8716(2)	0.010(1)
O(1)	-0.0394(11)	0.6157(8)	0.7108(5)	0.011(1)
O(3)	0.0229(12)	0.8198(8)	0.8707(5)	0.010(1)
O(5)	0.5652(13)	0.7942(10)	0.8360(6)	0.020(2)
O(6)	0.5000(11)	0.5763(8)	0.6841(5)	0.009(1)
O(7)	-0.3075(13)	0.9136(8)	0.9899(5)	0.013(1)
O(8)	-0.2495(15)	1.0853(9)	0.7930(6)	0.021(2)
O(9)	0.8372(13)	0.4527(8)	0.5799(6)	0.014(1)
O(10)	0.7568(12)	0.7700(8)	0.5303(5)	0.013(1)
F(1)	0.02461(11)	0.9219(7)	0.6530(5)	0.018(1)
F(2)	0.2611(11)	0.4925(7)	0.8968(4)	0.016(1)
N(1)	0.2508(14)	0.8999(10)	0.4364(6)	0.011(2)
N(2)	-0.2445(15)	1.3286(10)	0.9165(7)	0.013(2)
N(3)	0.2513(17)	1.2410(11)	0.7071(7)	0.020(2)

A.5.2: *IR spectrum for $Hf^{IV}F_2(PO_4,HPO_4, H_2PO_4)_2(NH_4, H_2O)_3$*

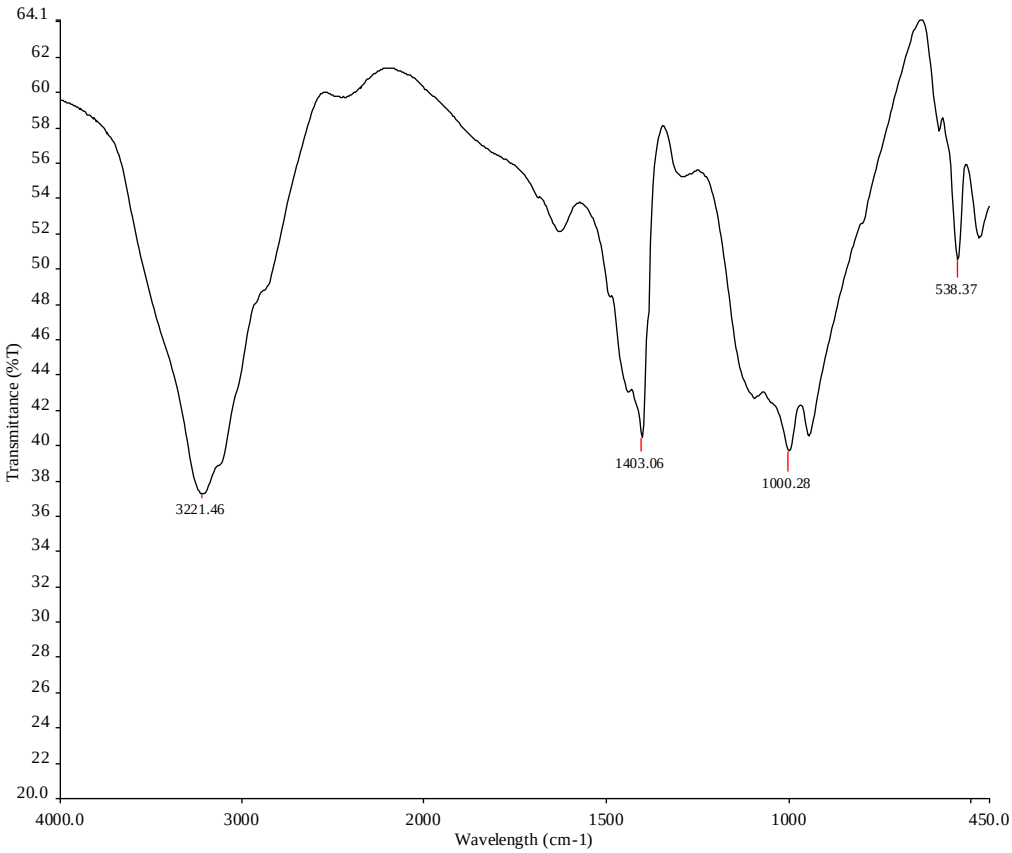

A.5.3: *Atomic weight percentages for $Hf^{IV}F_2(PO_4,HPO_4, H_2PO_4)_2(NH_4, H_2O)_3$*

Element	Atomic %	Calculated ratio of elements	Expected ratio of elements
O	47.79	4.44	8-11
F	19.49	1.81	2
P	21.96	2.04	2
Hf	10.76	1	1
Totals	100	9.29	13-16

A.5.4*: Atomic Coordinates and U(eq) for $Hf_2(AsO_4)_3(NH_4)$*

Atom	x	y	z	U(eq)
Hf(1)	0.3333	0.3844(4)	1.0178(1)	0.011(1)
As(1)	0.3333	0.3844(4)	0.9167	0.010(1)
O(1)	0.2780(20)	0.4550(20)	0.9710(6)	0.017(4)
O(2)	0.5040(20)	0.3650(30)	0.9312(6)	0.022(4)
N(1)	0.6667	0.3333	0.8333	0.014(10)

A.5.5: *IR spectrum for $Hf_2(AsO_4)_3(NH_4)$*

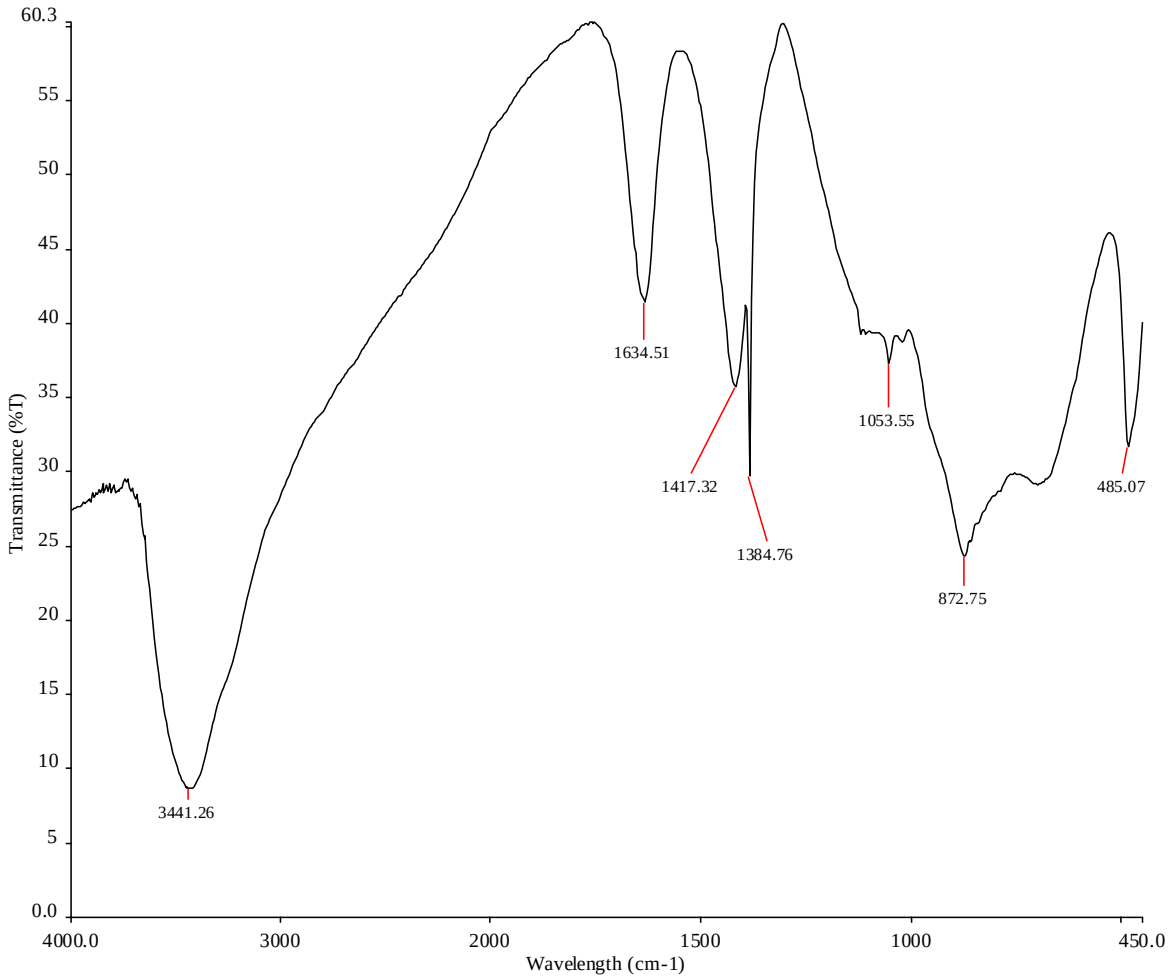

A.5.6: *Atomic weight percentages for $Hf_2(AsO_4)_3(NH_4)_3$*

Element	Atomic %	Calculated ratio of elements	Expected ratio of elements
O	62.51	3.69	12
As	20.56	1.21	3
Hf	16.93	1	2
Totals	100	5.9	17

Chapter 6:

***A.6.1**: Atomic Coordinates and U(eq) for $Hf^{IV}{}_2F(HAsO_4)(AsO_4)_2[(C_2H_8N_2)\text{-}H_2]_{1/2}(H_2O)_{1.5}$*

Atom	x	y	z	U(eq)
Hf(1)	0.2845(1)	0.4945(1)	0.0750(1)	0.005(1)
Hf(2)	0.1407(1)	0.9977(1)	0.2006(1)	0.005(1)
As(1)	0.1942(1)	0.5008(2)	0.2076(1)	0.005(1)
As(2)	0.2329(1)	0.9972(2)	0.0695(1)	0.005(1)
As(3)	0.4448(1)	0.5786(2)	0.1645(1)	0.007(1)
F(1)	0.1767(4)	0.4853(13)	0.0450(4)	0.013(2)
O(1)	0.1732(5)	0.9771(16)	0.1201(4)	0.011(1)
O(2)	0.1342(5)	0.6889(16)	0.2093(4)	0.011(1)
O(3)	0.2503(5)	0.9926(16)	0.2321(4)	0.011(1)
O(4)	0.1411(5)	0.12984(16)	0.2006(4)	0.011(2)
O(5)	0.0316(5)	0.9906(16)	0.1623(4)	0.011(1)
O(6)	0.0930(5)	1.0054(17)	0.2777(4)	0.011(1)
O(7)	0.2489(5)	0.5262(16)	0.1542(4)	0.010(2)
O(8)	0.2875(5)	0.7980(15)	0.0674(4)	0.006(2)
O(9)	0.2896(6)	0.1897(15)	0.0810(4)	0.009(2)
O(10)	0.3970(5)	0.5090(16)	0.1053(4)	0.009(2)
O(11)	0.3175(5)	0.4821(16)	-0.0078(4)	0.008(2)
O(12)	0.4457(6)	0.8319(15)	0.1599(4)	0.011(1)
O(1W)	0.5390(11)	0.6540(30)	0.0340(9)	0.011(1)
O(2W)	0.5494(10)	1.1900(30)	0.0776(9)	0.011(1)
O(3W)	0	0.5340(20)	0.2500	0.011(1)
N(1A)	0.4359(7)	0.9588(19)	0.0386(5)	0.015(3)
N(1B)	0.4359(7)	0.9588(19)	0.0386(5)	0.015(3)
C(4)	0.4774(16)	0.7970(40)	0.0069(11)	0.019(8)
C(5)	0.4919(15)	1.1300(40)	0.0472(11)	0.019(7)

***A.6.2:** Atomic weight percentages for $Hf^{IV}{}_2F(HAsO_4)(AsO_4)_2[(C_2H_8N_2)\text{-}H_2]_{1/2}(H_2O)_{1.5}$ from EDX analysis*

Element	Atomic %	Calculated ratio of elements	Expected ratio of elements from stoichiometry
O	60.56	13.57	13.5
F	4.46	1	1
As	18.78	4.21	3
Hf	16.19	3.63	2
Totals	100	22.41	19.5

A.6.3: *IR spectrum for* $Hf^{IV}_2F(HAsO_4)(AsO_4)_2[(C_2H_8N_2)\text{-}H_2]_{1/2}(H_2O)_{1.5}$

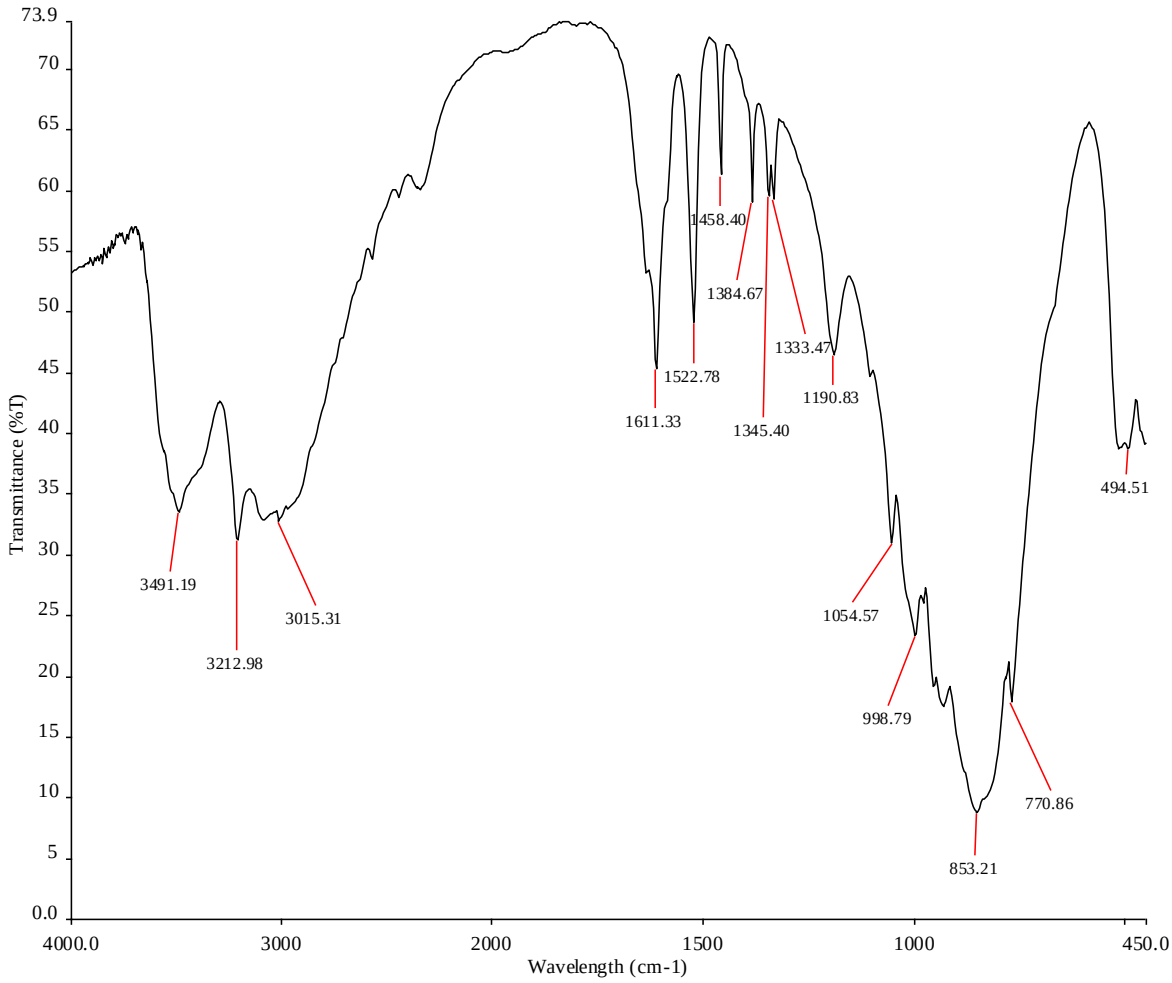

***A.6.4**: Atomic Coordinates and U(eq) for $Hf^{IV}_2F(HAsO_4)(AsO_4)_2[(C_4H_{14}N_3)\text{-}H_3]_{1/3}(H_2O)_{1.5}$*

Atom	x	y	z	U(eq)
Hf(1)	0.1748(1)	0.2820(1)	0.2088(1)	0.013(1)
Hf(2)	-0.0494(1)	0.2368(1)	0.0609(1)	0.012(1)
As(1)	0.3194(1)	0.2743(2)	0.3385(1)	0.013(1)
As(2)	0.0424(1)	0.2670(2)	-0.0136(1)	0.011(1)
As(3A)	0.0879(1)	0.1465(5)	0.2793(2)	0.014(1)
As(3B)	0.0792(1)	0.3322(5)	0.2735(2)	0.014(1)
O(1)	0.3231(6)	0.0862(18)	0.2803(9)	0.018(3)
O(2)	0.3277(6)	0.4822(18)	0.2960(10)	0.020(3)
O(3)	0.3696(5)	0.2520(20)	0.4483(8)	0.019(3)
O(4)	0.2561(5)	0.2727(18)	0.3266(8)	0.017(3)
O(5)	0.0954(5)	0.2980(20)	0.0944(9)	0.020(3)
O(6)	0.0400(6)	0.4610(18)	-0.0741(9)	0.018(3)
O(7)	0.0522(6)	0.0696(18)	-0.0599(9)	0.018(3)
O(8)	-0.0182(5)	0.2404(18)	-0.0199(8)	0.015(2)
O(9A)	0.1028(13)	-0.0900(40)	0.2980(20)	0.029(5)
O(9B)	0.0552(13)	0.5700(40)	0.2600(20)	0.029(5)
O(10)	0.0285(5)	0.1986(18)	0.1806(8)	0.017(3)
O(11)	0.0845(5)	0.2400(20)	0.3637(8)	0.019(3)
O(12A)	0.1430(20)	0.2650(70)	0.2900(60)	0.017(6)
O(12B)	0.1410(20)	0.3000(70)	0.2840(70)	0.017(6)
F(1)	0.2072(4)	0.2975(18)	0.1356(7)	0.024(2)

***A.6.5**: Bond valence calculations for **XIII** when n=3, where disorder is present, an average value * has been calculated for the Hf-O or As-O sites*

Atoms	F/O-Hf bond length (Å)	O-As bond length (Å)	Bond Valence F/O-Hf	Bond Valence O-As	Bond Valence Sum
O1	Hf1-2.07(12)	As1-1.68(12)	0.68	1.27	1.95
O2	Hf1-2.03(12)	As1-1.67(13)	0.75	1.29	2.04
O3	Hf2-2.03(11)	As1-1.66(12)	0.75	1.35	2.1
O4	Hf1-2.08(11)	As2-1.69(12)	0.65	1.23	1.88
O5	Hf1-2.03(13)	As2-1.66(13)	0.75	1.34	2.09
O6	Hf2-2.06(13)	As2-1.67(12)	0.69	1.30	1.99
O7	Hf2-2.08(12)	As2-1.67(13)	0.66	1.30	1.96
O8	Hf2-2.06(12)	As2-1.67(12)	0.69	1.29	1.98
O9a	n/a	As3a-1.65(3)		1.39	1.27*
O9b	n/a	As3b-1.71(3)		1.15	
O10	Hf2-2.06(12)	As3a-1.66(12)	0.69	1.35	1.94*
		As3b-1.72(12)		1.14	
O11	Hf2-2.06(11)	As3a-1.67(12)	0.68	1.29	1.90*
		As3b-1.64(12)		1.14	
O12a	Hf1-2.09(6)	As3a-1.67(2)	0.63	1.31	1.85*
		As3b-1.72(3)		1.13	
O12b	Hf1-2.04(6)	As3a-1.79(3)	0.73	1.31	1.86*
		As3b-1.67(2)		0.94	
F1	1.9638(1)	n/a	0.74	n/a	0.74

A.6.6:** Bond lengths and bond valence values for Hf within **XIII(3)

Atoms	Hf-O bond length (Å)	Hf-O Bond Valence
Hf1 – O1	2.06(12)	0.69
Hf1 – O2	2.03(12)	0.75
Hf1 – O4	2.08(11)	0.65
Hf1 – O5	2.03(12)	0.75
Hf1 – O12	2.05(10)	0.71
Hf1 – F1	1.96(10)	0.74
Total		4.3
Hf2 – O3	2.04(11)	0.73
Hf2 – O6	2.06(12)	0.69
Hf2 – O7	2.08(12)	0.65
Hf2 – O8	2.06(12)	0.69
Hf2 – O10	2.06(11)	0.69
Hf2 – O11	2.06(11)	0.69
Total		4.15

A.6.7: *Atomic weight percentages for $Hf^{IV}_2F(HAsO_4)(AsO_4)_2[(C_4H_{14}N_3)\text{-}H_3]_{1/3}(H_2O)_{1.5}$ from EDX analysis*

Element	Atomic %	Calculated ratio of elements	Expected ratio of elements from stoichiometry
O	60.07	11.49	13.5
F	5.23	1	1
As	18.65	3.57	3
Hf	16.05	3.07	2
Totals	100	19.13	19.5

A.6.8: *IR spectrum for $Hf^{IV}_2F(HAsO_4)(AsO_4)_2[(C_4H_{14}N_3)\text{-}H_3]_{1/3}(H_2O)$*

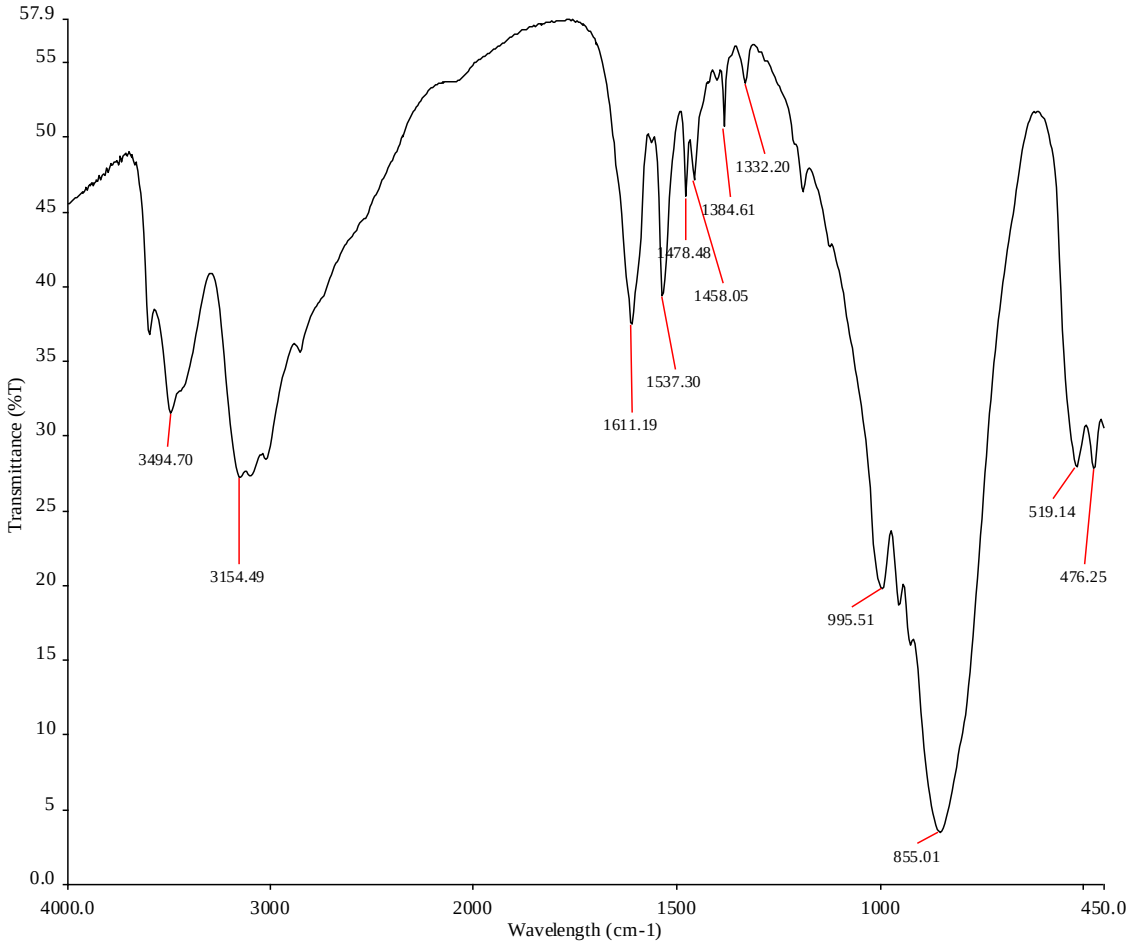

***A.6.9**: Atomic Coordinates and U(eq) for $Zr^{IV}_2(AsO_4)_2F_4(H_2O)_2[(C_2H_8N_2)\text{-}H_2]$*

Atom	x	y	z	U(eq)
Zr(1)	0.2012(2)	0.2387(2)	0.6194(1)	0.011(1)
As(1)	-0.2467(2)	0.2537(2)	0.4918(2)	0.012(1)
F(1)	0.1047(11)	0.2066(9)	0.8664(8)	0.016(1)
F(2)	0.3023(10)	0.2490(9)	0.3750(8)	0.014(1)
O(1)	0.5059(11)	0.2807(11)	0.6140(9)	0.013(2)
O(2)	0.2328(12)	-0.0675(11)	0.6317(9)	0.013(2)
O(3)	0.1569(11)	0.5433(11)	0.6327(9)	0.014(2)
O(4)	-0.1018(12)	0.2102(11)	0.6137(9)	0.014(2)
O(5)	-0.2267(13)	0.5713(12)	0.9260(10)	0.021(2)
N(1)	-0.3796(15)	0.2046(15)	1.0802(12)	0.021(2)
C(1)	-0.4184(19)	0.0834(17)	0.9532(16)	0.021(3)

***A.6.10:** Atomic weight percentages for $Zr^{IV}_2(AsO_4)_2F_4(H_2O)_2[(C_2H_8N_2)\text{-}H_2]$ from EDX analysis*

Element	Atomic %	Calculated ratio of elements	Expected ratio of elements from stoichiometry
O	51.07	3.87	10
F	20.09	1.52	4
As	13.19	1	2
Zr	15.64	1.19	2
Totals	100	7.58	18

A.6.11: *IR spectrum for $Zr^{IV}_2(AsO_4)_2F_4(H_2O)_2[(C_2H_8N_2)\text{-}H_2]$*

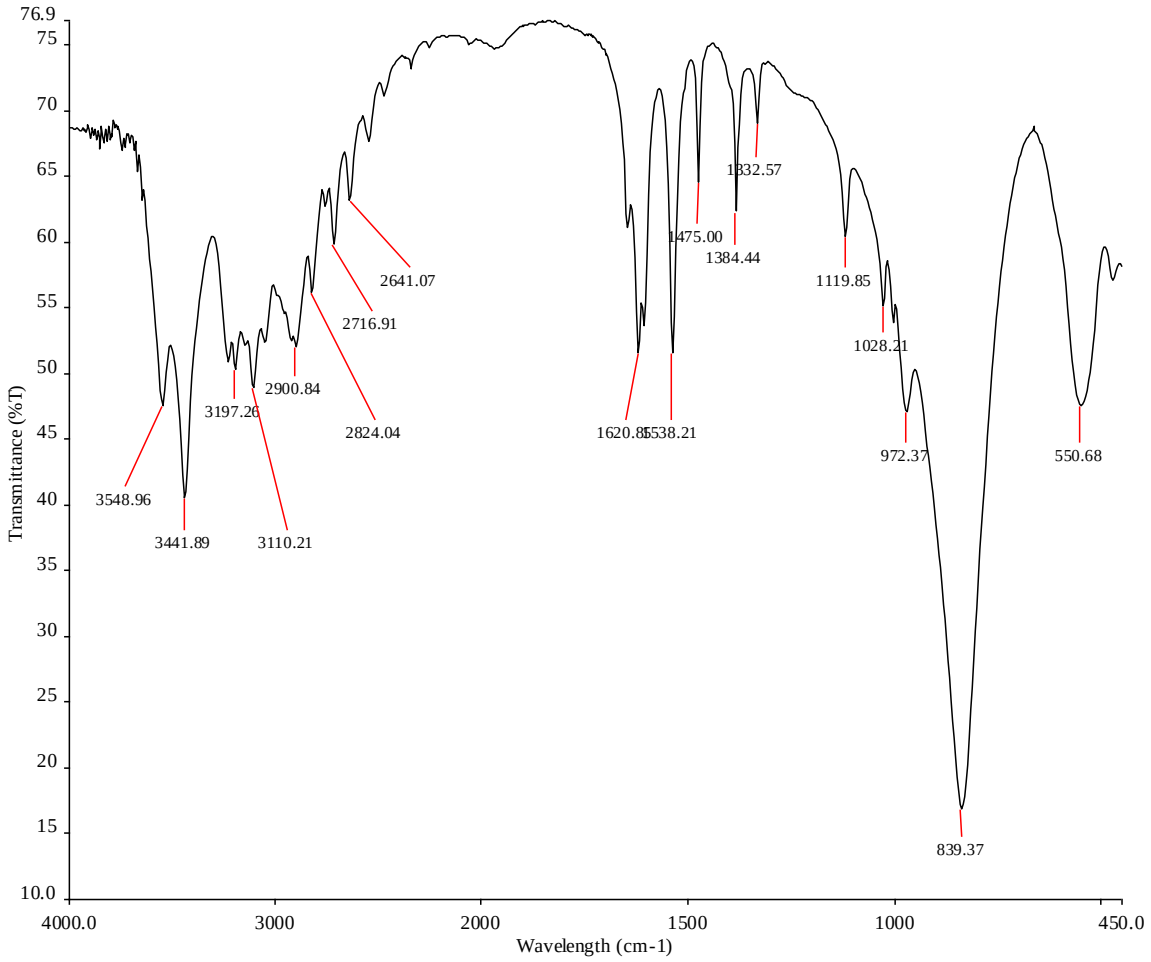

Chapter 7:

The parameters that were refined were the unit cell dimensions (*a*, *b*, *c*, α, β and γ), scale, atomic *x*,*y*,*z*, isotropic thermals, peak shape (GU, GV, GW, LX and asym), background, no. of cycles (10).

A.7.1: *Rietveld refinement of $NdPO_4.nH_2O$ (hydrated sample, 30°C)*

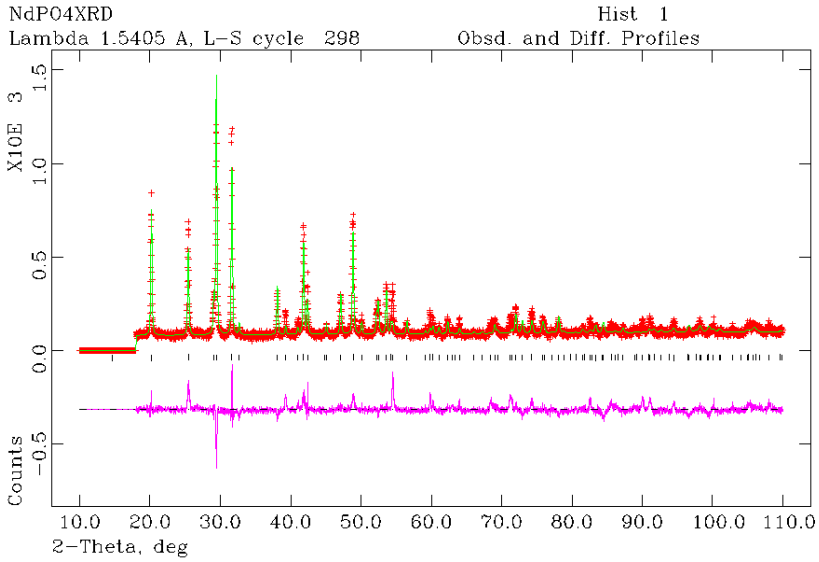

$\chi^2 = 2.8$, $R_p = 0.11$, $wR_p = 0.15$

A.7.2: *Rietveld refinement of $NdPO_4$ (dehydrated 180°C)*

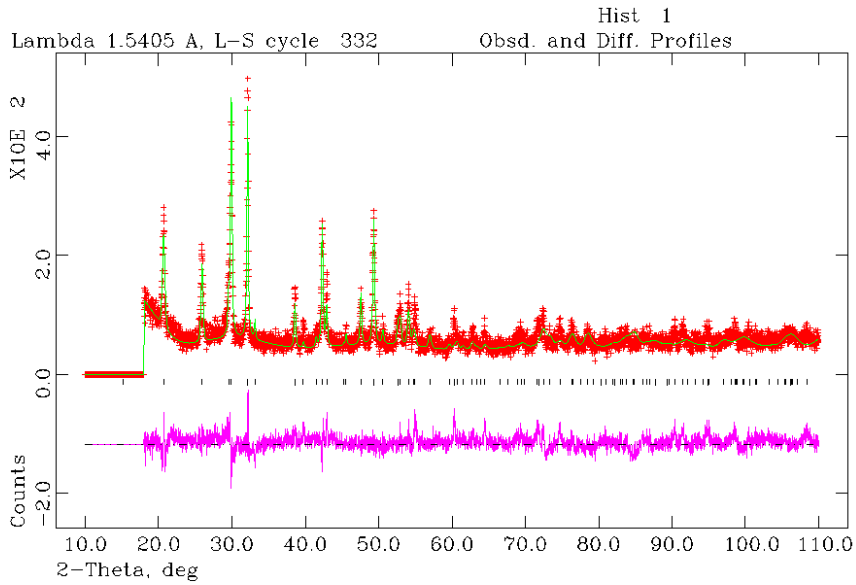

$\chi^2 = 1.9$, $R_p = 0.13$, $wR_p = 0.17$

A.7.3: *Rietveld refinement of $TbPO_4.nH_2O$ (hydrated sample, 30°C)*

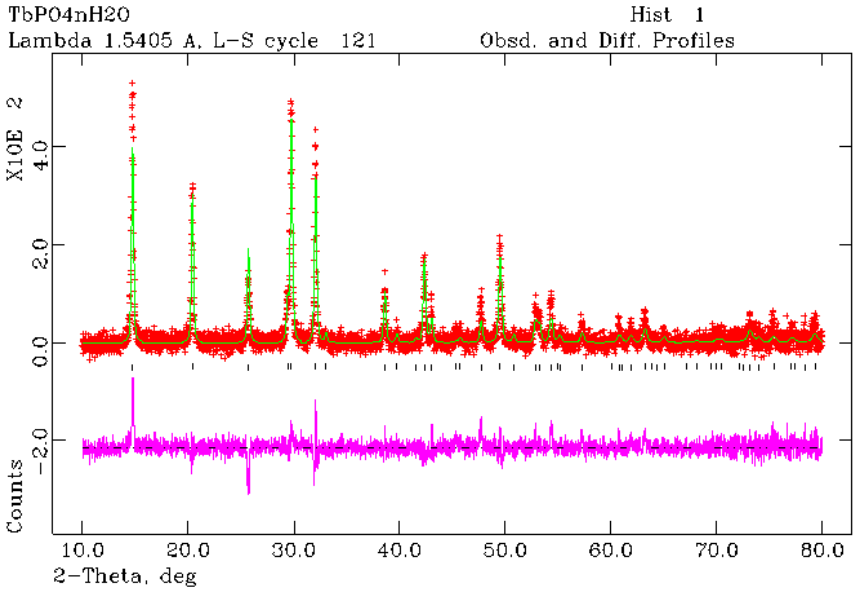

$\chi^2 = 1.6$, $R_p = 0.09$, $wR_p = 0.13$

A.7.4: *Rietveld refinement of $TbPO_4$ (dehydrated sample, 180°C)*

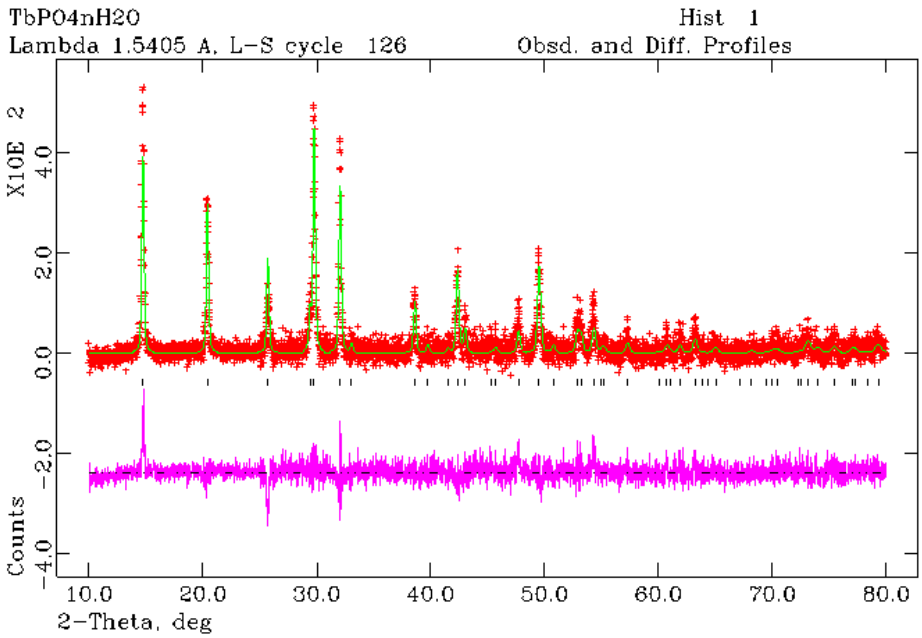

$\chi^2 = 2.29$, $R_p = 0.11$, $wR_p = 0.15$

The enclosed CD contains CIF data for the structures reported within this thesis.